

## **Copyright Notices**

### **Notice 1**

Under the Copyright Act 1968, this thesis must be used only under the normal conditions of scholarly fair dealing. In particular no results or conclusions should be extracted from it, nor should it be copied or closely paraphrased in whole or in part without the written consent of the author. Proper written acknowledgement should be made for any assistance obtained from this thesis.

### **Notice 2**

I certify that I have made all reasonable efforts to secure copyright permissions for third-party content included in this thesis and have not knowingly added copyright content to my work without the owner's permission.

# **The Phase Field Simulation of Autocatalytic Nucleation**

A thesis submitted in fulfilment of the requirements  
for the degree of Doctor of Philosophy

by  
Yury Kryvasheyev  
B.Sc. (Hons.)

School of Physics  
Monash University

January 2012



# Contents

Abstract .....	xiii
Acknowledgements .....	xv
Statement .....	xvii
1. Introduction .....	1
1.1. Overview .....	1
1.2. Outline of the thesis structure .....	3
2. Precipitation in solids .....	5
2.1. Nucleation theory .....	5
2.1.1. Introduction.....	5
2.1.2. Basic formulation of classical nucleation theory .....	6
2.1.3. Transient nucleation.....	10
2.1.4. Classification of nucleation processes .....	11
2.1.5. Heterogeneous nucleation and the influence of defects .....	12
2.1.5.1. Vacancies .....	12
2.1.5.2. Dislocations.....	14
2.1.5.3. Other defects .....	16
2.1.6. Limitations of the theory and its experimental support .....	16
2.1.7. Interfacial energy .....	18
2.1.8. Strain energy .....	21
2.1.8.1. Khachaturyan’s microelasticity theory.....	26
2.1.8.2. Energy of nucleus-microstructure elastic interaction.....	31
2.2. Classification of solid state transformations.....	33
2.3. Model system – $\theta'$ phase in Al-Cu.....	35

2.4.	Research direction and questions .....	39
3.	Magnitude of the activation barriers for platelike precipitates .....	41
3.1.	Method for finding critical parameters of platelike inclusions .....	41
3.2.	Interfacial energy estimates.....	44
3.3.	Chemical driving forces .....	46
3.4.	Results for the size, shape and activation energy of the critical nucleus .....	51
4.	Elastic interaction model of strain assisted nucleation .....	55
4.1.	Background .....	55
4.2.	Interaction energy calculation by a dislocation loop method.....	57
4.3.	Interaction of tetragonal transformation strain inclusions.....	59
4.4.	Shear strain effect on the interaction energy of plates .....	66
4.5.	Interaction of generalised transformation strain inclusions .....	68
4.6.	Interaction of tetragonal strain plates with sheared nuclei .....	75
4.7.	Conclusions .....	78
5.	Phase field model.....	79
5.1.	Basics of the phase field approach .....	79
5.2.	Energy functional .....	81
5.2.1.	Local free energy.....	81
5.2.2.	Gradient energy terms .....	83
5.2.3.	Elastic energy .....	85
5.3.	Evolution equations.....	86
5.4.	Treatment of thermally activated processes .....	87
5.4.1.	Langevin noise approach.....	87
5.4.2.	Explicit nucleation algorithm .....	88

5.5.	Kim-Kim-Suzuki construction of the local free energy function .....	89
5.6.	Typical parameters of the Al-Cu phase field model.....	95
5.7.	Transitional behaviour and rescaling of the interface width .....	98
5.8.	Limitations of the Kim-Kim-Suzuki model.....	101
5.9.	Interface kinetics.....	106
5.10.	Implementation of interfacial energy anisotropy.....	108
5.10.1.	The modified Allen-Cahn equation .....	109
5.10.2.	Regularisation of anisotropic interfacial energy functions .....	111
5.10.3.	Numerical scheme stable in presence of corner discontinuities .....	116
5.11.	Implementation of anisotropy in interface mobility .....	122
5.12.	Summary of the phase field model and its numerical implementation .....	123
5.12.1.	Semi-Implicit Fourier Spectral scheme for the Cahn-Hilliard equation.....	125
5.12.2.	Alternating Direction Implicit scheme for the Allen-Cahn equation .....	125
5.13.	Morphology of an isolated precipitate in two dimensions .....	128
6.	Driving forces for nucleation in the environment of pre-existing $\theta'$ precipitates.....	137
6.1.	Formation of a nucleus with tetragonal transformation strain.....	138
6.2.	Formation of a nucleus with shear component in the transformation strain.....	146
6.3.	Strain assisted nucleation.....	153
6.3.1.	Effect of the nucleation rate.....	155
6.3.2.	Effect of the type of the transformation strain. Tetragonal nucleus .....	167
6.3.3.	Evolution at larger scale at low nucleation rates .....	170
6.3.4.	Discussion of results .....	175
7.	Conclusions and directions for future research .....	177
	References .....	181

## List of Figures

- Fig. 1 Schematic variation of the change in the Gibbs free energy of the system associated with the formation of a new-phase domain, as a function of domain's size. The concept of critical size is illustrated as point B on the graph..... 7
- Fig. 2 Transient homogeneous nucleation rate in an arbitrary system with critical cluster comprising 25 atoms and the initial condition for the nucleation rate of 12-atom clusters equal to 0.01. Adapted from Turnbull [14]..... 11
- Fig. 3 Wulff construction in a hypothetical two-dimensional crystal. Polar plot of an interfacial energy gives the energy as a function of direction. Interfacial energy for a plane with a normal in a given direction (Wulff plane shown by the dashed line in the diagram) is defined by the length of the corresponding vector  $r$ , ending on the  $\gamma$ -plot. Cusps in the  $\gamma$ -plot identify low-energy directions and orientations of low-energy planes/facets of a crystal. According to the Wulff theorem, the inner envelope of all possible Wulff planes would give a lowest energy shape (adapted from [33]). ..... 19
- Fig. 4 Example of a semicoherent interface. The misfit between phases  $\alpha$  and  $\beta$  is in one dimension and is accommodated by the array of edge dislocations. .... 20
- Fig. 5 Shape factor in the expression (2.16) for the energy of an incoherent inclusion, after Nabarro [38]. ..... 22
- Fig. 6 Elastic energy of the ellipsoidal coherent precipitate, when both the matrix and the precipitate are isotropic, for different relative elastic moduli (from Barnett et al. [45]). The energy is normalised to the energy of the elastically homogeneous inclusion. .... 25
- Fig. 7 Normalised strain energy of anisotropic ellipsoidal inclusion embedded into an anisotropic matrix (from Lee et al. [46]). Various combination of anisotropy in either matrix (dotted curves), precipitate (dashed curves) or both (solid curves) are given.  $A = (2 C_{44})/(C_{11}-C_{12})$  is the Zener's anisotropy ratio (the star superscript corresponds to the precipitate phase). ..... 25
- Fig. 8 Aluminium-rich section of the Al-Cu phase diagram, adapted from Lorimer [68]. ..... 35
- Fig. 9  $\theta'$  structure, after Silcock et al. [71]. ..... 36
- Fig. 10 Conservative building block of the Dahmen-Westmacott [90] model for  $\theta'$  transformation mechanism. .... 38
- Fig. 11 Non-conservative building block of the Dahmen-Westmacott model. .... 38
- Fig. 12 The method for obtaining an estimate of chemical driving forces from a common tangent construction for the Al-Cu (left) and Al-Ag (right) systems. .... 49

Fig. 13 a) Aluminium-rich section of Al-Cu phase diagram (adapted from Lorimer [68]). Hatched region corresponds to the conditions for direct nucleation of $\theta'$ from solid solution. The red and blue paths outlined on the diagram are given to identify the upper limit and mid-range levels of the chemical driving force. Using the combination of composition and temperature along these paths the chemical driving force was calculated and plotted in b).....	50
Fig. 14 a) Aluminium-rich section of Al-Ag phase diagram (adapted from Baur [105] and Massalski [106]). The red path along the GP zones solvus corresponds to the maximum of the chemical driving force for direct nucleation of $\gamma$ phase; b) maximum driving force along the composition-temperature path outlined on the left.....	50
Fig. 15 Contour plot of the activation barrier (expressed in $k_B T$ ) for the nucleation of a circular disc. The barrier is presented as a function of the chemical driving force and the habit plane interfacial energy. The transformation temperature is taken as 520 K ( $\sim 250$ °C) which is representative of direct nucleation of $\theta'$ . The area shaded corresponds to the range of parameters where the activation barrier is lower than $60 k_B T$ . .....	51
Fig. 16 Interaction energy of two square plates in the face to face parallel orientation as a function of the vertical separation between their centres (red line – infinitesimal loops approximation, green line – plates modelled as rafts of smaller loops). Based on the method of Brown [107]. .....	60
Fig. 17 Interaction energy of two square plates in the edge to face perpendicular orientation as a function of the separation in $x$ -direction between their centres (red line – infinitesimal loops approximation, green line – plates modelled as rafts of smaller loops). Based on the method of Brown [107]. .....	60
Fig. 18 Diagrams of various linear arrays of precipitates, as considered in [92]. .....	61
Fig. 19 Interaction profiles for the small plate in the vicinity of a large one: a) small perpendicular plate next to the edge of a large plate, energy vs. $x$ -displacement; b) small plate parallel to the large one, displaced vertically by $Z = 0.1$ and $Z = 0.2$ , energy vs. $x$ -displacement. Adapted from Perovic et al. [92]. .....	62
Fig. 20 Interaction energy profile for the small parallel plate at the distance of closest approach to the large plate, plotted as a function of the displacement in $z$ -direction, away from the coplanar arrangement. Adapted from Perovic et al. [92]. .....	63
Fig. 21 Interaction energy density for the nucleus perpendicular to the primary plate.....	64
Fig. 22 Interaction energy density for the nucleus parallel to the primary plate.....	64
Fig. 23 Adapted from [110]: interactions between the large plate at the origin with a small plate next to its edge on $x$ -axis, while displaced vertically. Various characters of the transformation strains are considered: red – purely tetragonal with 5% misfit; green – 0.1 shear in $x$ -direction;	

blue and purple – mixture of the 5% tetragonal misfit and 0.1 shear, calculated without and with the cross terms from (4.9) respectively. ....	67
Fig. 24 Three-dimensional interaction energy density maps for parallel large and small plates with (001) and (001) habit planes and varying senses of shear in the secondary plate. ....	69
Fig. 25 Three-dimensional interaction energy density maps for perpendicular large and small plates with (001) and (100) habit planes and varying senses of shear in the secondary plate. ....	70
Fig. 26 Three-dimensional interaction energy density maps for perpendicular large and small plates with (001) and (010) habit planes and varying senses of shear in the secondary plate. ....	71
Fig. 27 Interaction energy density for parallel plates with similar senses of shear. ....	73
Fig. 28 Interaction energy density for parallel plates with opposite senses of shear. ....	73
Fig. 29 Interaction energy density for perpendicular plates with similar senses of shear. ....	74
Fig. 30 Interaction energy density for perpendicular plates with opposite senses of shear. ....	74
Fig. 31 Interaction energy density between the large plate of tetragonal strain and the nucleus of generalised strain. Plates are in the parallel orientation, with a positive shear in the nucleus. ....	76
Fig. 32 Interaction energy density between the large plate of tetragonal strain and the nucleus of generalised strain. Plates are in the parallel orientation, with a negative shear in the nucleus. ....	76
Fig. 33 Interaction energy density between the large plate of tetragonal strain and the nucleus of generalised strain. Plates are in the perpendicular orientation, with a positive shear in the nucleus. ....	77
Fig. 34 Interaction energy density between the large plate of tetragonal strain and the nucleus of generalised strain. Plates are in the perpendicular orientation, with a negative shear in the nucleus. ....	77
Fig. 35 Double-well potential. ....	82
Fig. 36 The local free energy density as a function of the field variable, and the interface established between two regions of equilibrium minimum values. The width of the interface is shown as $l$ . ....	84
Fig. 37 Landau polynomial free energy construction. ....	90
Fig. 38 Kim-Kim-Suzuki construction of the chemical free energy for the multiphase mixture of $\alpha$ and $\beta$ phases with $A(T) = B(T) = 1$ and $W = 0$ on the left, without double well potential imposed, and $W = 1$ on the right. Energy is minimised along the transformation path $c_{min}(\eta)$ exactly on the common tangent plane. ....	92

Fig. 39 Evolution of the compositional profile and the equilibrium distribution of phase variables across the interface.....	97
Fig. 40 Compositional and structural phase field variables across the equilibrium interface.....	98
Fig. 41 Comparison of the planar interface velocity, growing in diffusion controlled mode, with the analytical solution.....	99
Fig. 42 Effect of the variation in the interface width on the temporal behaviour of the phase field model.....	99
Fig. 43 Non-equilibrium interface composition profiles at $t = 500$ s.....	100
Fig. 44 Evolution of the planar interface with $200 \text{ mJ/m}^2$ energy compared to the $100 \text{ mJ/m}^2$ interface. The instability develops in the case of the low interfacial energy (with low height of the double well potential $W$ ).....	102
Fig. 45 Non-equilibrium interface in $c$ - $\eta$ representation.....	103
Fig. 46 Contour plots of $f(c, \eta)$ in the KKS model (5.24) with $A = 1$ and $W = 0.05$ on the left vs. $W = 1$ on the right. Contours are separated by 0.0025 increments. ....	104
Fig. 47 Effect of the transitional function on the energy landscape: slower transition in the vicinity of $\eta=0$ guarantees that a stable equilibrium with respect to $\eta$ is maintained for a wider range of solute concentrations.....	105
Fig. 48 The effect of a modified transition function on the stability of the simulation. Tenfold variation in the energy of the planar interface has no effect on its motion, as confirmed by the snapshots of the interface position at 2000 (on the left) and 10000 seconds (on the right). ....	105
Fig. 49 Variation of the interface growth regime with the value of mobility coefficient (as a function of the ageing time $t$ on the left and $\sqrt{t}$ on the right).....	107
Fig. 50 Growth kinetics of interfaces with different energy. ....	108
Fig. 51 Polar plots of the function (5.57) on the left and its inverse on the right, shown as solid red lines. Eggleston type regularisation produces “convexified” approximation to this function, shown as solid green lines.....	113
Fig. 52 $\xi$ -plots and $\sigma$ -plots of direct (red) and regularised (green) functions. ....	114
Fig. 53 Piecewise interfacial anisotropy function, its derivatives and interface stiffness with “missing orientations” replaced by the power series expansion (5.62).....	115
Fig. 54 Polar plots of $\sigma(\theta)$ and $\xi(n)$ in the case of power series expansion around the directions with minimum interfacial energies.....	116

Fig. 55 Schematics of a sharp corner, with a jump in the interface direction from $n_1$ to $n_2$ and a discontinuity in all spatial derivatives of field variable across the surface $\Sigma$ (adapted from Wheeler and McFadden [144]).	117
Fig. 56 Profile of the phase variable in the vicinity of a sharp corner.	119
Fig. 57 Contour plot of the phase variable in the vicinity of a sharp corner. Interface normals and angle gradients are also shown within missing orientations range.	119
Fig. 58 Laplacian term in the variational derivative. Note the sharp spike across the discontinuity line.	120
Fig. 59 Torque term of the variational derivative.	120
Fig. 60 Mutual compensation of the discontinuities in the Laplacian and the torque terms of the variational derivative.	121
Fig. 61 Chemical potential in the vicinity of the sharp corner, note the smooth character of the transition across the corner.	121
Fig. 62 Angular part of the anisotropic interface mobility $L_\eta(\theta)$ .	122
Fig. 63 Simulated evolution of the $\theta'$ particle under the influence of the interfacial energy anisotropy (elliptic anisotropy is assumed).	128
Fig. 64 Simulated evolution of the $\theta'$ particle under the combined influence of the interfacial energy and the elastic energy.	129
Fig. 65 Simulated evolution of the $\theta'$ particle in the larger periodic system with a) only interfacial energy; b) interfacial and strain energies and c) interfacial, strain energies and anisotropy in the interfacial mobility.	130
Fig. 66 Nucleation driving forces around the growing $\theta'$ precipitate. On the left – smooth elliptical anisotropy, on the right – sharp corners rectangular anisotropy.	132
Fig. 67 Nucleation driving forces around $\theta'$ plates growing under the influence of strain, interfacial energy anisotropy and interface mobility anisotropy (mixed control mode for habit plane growth).	133
Fig. 68 Nucleation driving forces around $\theta'$ plates modelled under different conditions: on the left fully resolved interfaces and anisotropic mobility, on the right – unresolved and numerically pinned habit planes.	134
Fig. 69 Al-2 wt. % Cu, $T = 200^\circ\text{C}$ . Distributions of a) chemical driving force, b) total driving force for the formation of a nucleus with a tetragonal misfit in the [01] direction and c) total driving force for the formation of the tetragonal nucleus with a [10] misfit.	140

Fig. 70 Al-2 wt. % Cu, $T = 225^{\circ}\text{C}$ . Distributions of a) chemical driving force, b) total driving force for the formation of a nucleus with a tetragonal misfit in the [01] direction and c) total driving force for the formation of the tetragonal nucleus with a [10] misfit.....	141
Fig. 71 Al-2 wt. % Cu, $T = 250^{\circ}\text{C}$ . Distributions of a) chemical driving force, b) total driving force for the formation of a nucleus with a tetragonal misfit in the [01] direction and c) total driving force for the formation of the tetragonal nucleus with a [10] misfit.....	142
Fig. 72 Al-4 wt. % Cu, $T = 200^{\circ}\text{C}$ . Distributions of a) chemical driving force, b) total driving force for the formation of a nucleus with a tetragonal misfit in the [01] direction and c) total driving force for the formation of the tetragonal nucleus with a [10] misfit.....	143
Fig. 73 Al-4 wt. % Cu, $T = 225^{\circ}\text{C}$ . Distributions of a) chemical driving force, b) total driving force for the formation of a nucleus with a tetragonal misfit in the [01] direction and c) total driving force for the formation of the tetragonal nucleus with a [10] misfit.....	144
Fig. 74 Al-4 wt. % Cu, $T = 250^{\circ}\text{C}$ . Distributions of a) chemical driving force, b) total driving force for the formation of a nucleus with a tetragonal misfit in the [01] direction and c) total driving force for the formation of the tetragonal nucleus with a [10] misfit.....	145
Fig. 75 Al-2 wt. % Cu, $T = 200^{\circ}\text{C}$ . Distributions of a) chemical driving force, b) total driving force for the formation of a nucleus with tetragonal misfit in the [01] direction and positive shear along [10]; c) total driving force for the formation of a nucleus with tetragonal misfit in the [01] direction and negative shear along [10]. .....	147
Fig. 76 Al-2 wt. % Cu, $T = 225^{\circ}\text{C}$ . Distributions of a) chemical driving force, b) total driving force for the formation of a nucleus with tetragonal misfit in the [01] direction and positive shear along [10]; c) total driving force for the formation of a nucleus with tetragonal misfit in the [01] direction and negative shear along [10]. .....	148
Fig. 77 Al-2 wt. % Cu, $T = 250^{\circ}\text{C}$ . Distributions of a) chemical driving force, b) total driving force for the formation of a nucleus with tetragonal misfit in the [01] direction and positive shear along [10]; c) total driving force for the formation of a nucleus with tetragonal misfit in the [01] direction and negative shear along [10]. .....	149
Fig. 78 Al-4 wt. % Cu, $T = 200^{\circ}\text{C}$ . Distributions of a) chemical driving force, b) total driving force for the formation of a nucleus with tetragonal misfit in the [01] direction and positive shear along [10]; c) total driving force for the formation of a nucleus with tetragonal misfit in the [01] direction and negative shear along [10]. .....	150
Fig. 79 Al-4 wt. % Cu, $T = 225^{\circ}\text{C}$ . Distributions of a) chemical driving force, b) total driving force for the formation of a nucleus with tetragonal misfit in the [01] direction and positive shear along [10]; c) total driving force for the formation of a nucleus with tetragonal misfit in the [01] direction and negative shear along [10]. .....	151
Fig. 80 Al-4 wt. % Cu, $T = 250^{\circ}\text{C}$ . Distributions of a) chemical driving force, b) total driving force for the formation of a nucleus with tetragonal misfit in the [01] direction and positive shear	

along [10]; c) total driving force for the formation of a nucleus with tetragonal misfit in the [01] direction and negative shear along [10]. .....	152
Fig. 81 Evolution of the system with nucleation barrier of $30 k_B T$ and $N_{nuc} = 0.5$ . .....	156
Fig. 82 Evolution of the system with nucleation barrier of $50 k_B T$ and $N_{nuc} = 0.5$ . .....	157
Fig. 83 Evolution of the system with nucleation barrier of $30 k_B T$ and $N_{nuc} = 4$ . .....	158
Fig. 84 Evolution of the system with nucleation barrier of $30 k_B T$ and $N_{nuc} = 1$ . .....	160
Fig. 85 Evolution of the system with nucleation barrier of $40 k_B T$ and $N_{nuc} = 1$ . .....	161
Fig. 86 Evolution of the system with nucleation barrier of $50 k_B T$ and $N_{nuc} = 1$ . .....	162
Fig. 87 Evolution of the system with nucleation barrier of $60 k_B T$ and $N_{nuc} = 1$ . .....	163
Fig. 88 Evolution of the system with nucleation barrier of $30 k_B T$ and $N_{nuc} = 2$ . .....	164
Fig. 89 Evolution of the system with nucleation barrier of $40 k_B T$ and $N_{nuc} = 2$ . .....	165
Fig. 90 Evolution of the system with nucleation barrier of $50 k_B T$ and $N_{nuc} = 2$ . .....	166
Fig. 91 Evolution of the system with nucleation barrier of $50 k_B T$ and $N_{nuc} = 2$ . Tetragonal nucleus. ....	168
Fig. 92 Evolution of the system with nucleation barrier of $50 k_B T$ and $N_{nuc} = 2$ . Tetragonal nucleus. ....	169
Fig. 93 Evolution of the Al-4 wt. % Cu system with nucleation barrier of $50 k_B T$ and $N_{nuc} = 0.2$ . Mixed type nucleus. ....	171
Fig. 94 Evolution of the Al-4 wt. % Cu system with nucleation barrier of $50 k_B T$ and $N_{nuc} = 0.2$ . Tetragonal nucleus. ....	172
Fig. 95 Evolution of the Al-2 wt. % Cu system with nucleation barrier of $50 k_B T$ and $N_{nuc} = 0.2$ . Mixed type nucleus. ....	173
Fig. 96 Evolution of the Al-2 wt. % Cu system with nucleation barrier of $50 k_B T$ and $N_{nuc} = 0.2$ . Tetragonal nucleus. ....	174

## List of Tables

Table 1 Estimates of interfacial energies of various matrix : precipitate interfaces in binary Al-Cu and Al-Ag alloys.....	46
Table 2 Polynomial coefficients (selected to return the energy in J/mol) of equation (3.9) for the Gibbs energy of pure elements for Al, Cu and Ag.....	47
Table 3 Polynomial expansion of Redlich-Kister coefficients (from Witusiewicz et al. [104])...	48
Table 4 The parameters of disc shaped critical nucleus as a function of chemical driving force, interfacial energy and uniaxial strain in the direction normal to the habit plane. The ranges of driving force and interfacial energies cover platelike precipitates in Al-based systems. The threefold anisotropy for the interfacial energy corresponds to the best estimates for $\theta'$ . ....	52
Table 5 Effect of the shear component ( $\tau = 0.3$ ) in transformation strain on nucleus parameters.	53
Table 6 Parameters of the parabolic approximation to the solid solution free energy, assuming the temperature of $T = 500$ K and fitting to the transformation driving force at the composition $c = 0.0172$ .....	96
Table 7 Variation of scaling parameter for the imposed double well potential $Wg(\eta)$ with the interfacial energy $\sigma$ and desired interface width $l$ of the phase field simulation. ....	96



## Abstract

Precipitation of metastable  $\theta'$  phase is a well known process that underlies age-hardening of Al-Cu alloys. The strength acquired is very sensitive to the morphology and spatial distribution of  $\theta'$ , with the peak hardness corresponding to a fine distribution of precipitates with high length-to-thickness aspect ratio. Therefore, an understanding of the transformation mechanism between the matrix and  $\theta'$  and the factors affecting the nucleation barriers associated with its formation are crucial for an effective alloy design.

Although the behaviour of the Al-Cu system has been a focus of intensive research for the large part of a century, the need still exists to elucidate the atomic mechanism of transformation.  $\theta'$  was traditionally considered to be a purely diffusional transformation product; however, several mechanisms have been proposed (Dahmen and Westmacott, Nie and Muddle) that recognised the existence of lattice correspondence between the Al-Cu matrix and  $\theta'$ . The important feature of these mechanisms was a large shear component in the transformation strain, suggesting that the transformation may be diffusional-displacive in nature.

This project was undertaken to investigate the special mode of transformation, autocatalytic nucleation, which features distinctive clusters of precipitates arranged into linear inclined stacks and cross-like arrays. The hypothesis tested was that such clustering of precipitates is the result of interaction between the shear component of the strain of the nucleus with the pre-existing microstructure, and that autocatalytic structures potentially reveal the nature of transformation strain.

The thesis presents an assessment of the nucleation barriers associated with the formation of platelike inclusions, representative of a wide class of strengthening precipitates ( $\theta'$  and  $T_1$  in Al-Cu and Al-Cu-Li,  $\gamma/\gamma'$  in Al-Ag). It is demonstrated that existing estimates of interfacial energies and chemical driving forces do not explain the difficulty of precipitation in these systems, and that the influence of the shear component on the magnitude of the nucleation barrier is crucial and must be accounted in the model of the transformation mechanism.

Further, a simple elastic interaction model based on earlier work of Perovic, Purdy and Brown is employed to demonstrate that the elastic interaction energy between the sheared nucleus and pre-existing large precipitate has the symmetry consistent with the distribution of  $\theta'$  in autocatalytic arrays.

Finally, a diffuse interface phase field model is developed for the coherent nucleation and microstructure evolution in Al-Cu. The model takes into account the effect of local stress on the nucleation rate in an attempt to dynamically track how the nucleation of subsequent precipitates is facilitated by elastic interaction with the pre-existing microstructure. It is demonstrated that the traditional model of purely tetragonal transformation strain rules out the possibility of strain induced nucleation, due to weak interaction and the effective suppression of driving forces by matrix depletion. In the case of a sheared nucleus it was not possible to answer conclusively whether autocatalysis may be caused by the elastic interaction. Some precipitate clustering was evident, but characteristic linear stacks and cross-like arrays observed in experiments were not reproduced in the simulations.

The results suggest that inhomogeneous distributions, when they occur, are the product of association with inhomogeneities, such as dislocations or grain boundaries, rather than a self-stimulating chain of strain induced nucleation events.

## Acknowledgements

The research carried out and presented in this thesis would not be possible without the guidance and help of many people. Since my background was primarily in the field of computational physics, I greatly appreciate the support from metallurgists, physicists and material scientists at Monash University and Ohio State University.

In the first place I would like to express my sincere gratitude to my supervisor - Professor Barrington Muddle. His lifelong interest in the crystallography of phase transformations and the nature of nucleation mechanism has inspired and directed this project from the beginning. I appreciate his much needed support in every aspect of research and management of my project. I am grateful for the opportunity to learn from the renowned experts on the technique of phase field modelling - Professor Yunzhi Wang (Department of Material Science and Engineering, Ohio State University) and Dr. Chen Shen (GE Global Research). Although experimental work did not eventually become an integral part of my project, I am thankful for the efforts that Dr. Brian Gable and Dr. Laure Bourgeois invested in my training with heat treatment, sample preparation and transmission electron microscopy. I would also like to acknowledge the enormous help with the preparation and editing of the manuscript provided to me by Dr. Andrew Smith (School of Physics, Monash University).

I would like to pay respects to my *alma mater*, Belarusian State University, and my first mentor in research, Dr. Stanislav Shabunya (Heat and Mass Transfer Institute, Minsk, Belarus).

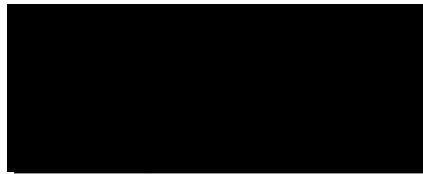
I greatly appreciate the financial support from the Commonwealth of Australia in the form of an International Postgraduate Research Scholarship and a Monash Graduate Scholarship, provided to me by Monash University. Many thanks to the academic and administrative staff at the ARC Centre of Excellence for Design in Light Metals, School of Physics and Monash Research Graduate School. I have truly enjoyed my time at Monash University especially because of the people I met here.

I take this chance to thank my parents, Elena and Nickolay, for their love and encouragement. My deepest gratitude goes to my dear wife Iryna and son Kiryll, who were constant support on this long journey. We also look forward to welcoming our little daughter Sophie into the world and I want to dedicate this work to all my family.



## Statement

I hereby declare that this thesis contains no material which has been accepted for the award of any other degree or diploma at any university or equivalent institution and that, to the best of my knowledge and belief, this thesis contains no material previously published or written by another person, except where due reference is made in the text of the thesis.



Yury Kryvasheyev

Melbourne, January 2012



# 1. Introduction

## 1.1. Overview

Phase transformations in metals and alloys form a broad fundamental scientific field, which is of great technological importance for the design of advanced engineering alloys. High-strength alloys of light metals, such as those of aluminium and magnesium, often acquire their peak hardness through the formation of the fine distribution of precipitates of one or more strengthening phases. Optimal mechanical properties of these alloys are directly controlled by the identity, size and spatial distribution of the nanoscale precipitates. Formation of such a population of particles within the initially uniform matrix is what constitutes the process of precipitation- or age-hardening.

Precipitation hardening requires an alloy system with the solubility decreasing with decreasing temperature. Solute introduced into solid solution at an elevated temperature tends to form aggregates of new phase during controlled ageing at lower temperature. Decomposition of the supersaturated matrix normally proceeds as a first-order heterogeneous phase transformation, which involves nucleation and further growth of new-phase embryos from the initially uniform metastable solid solution. Understanding the transformation mechanism and the factors affecting nucleation is therefore crucial for the effective design of advanced materials.

The research undertaken and presented in this thesis is focused on the traditional and well studied binary Al-Cu system. In this system, and in many commercial heat-treatable alloys based on it (2xxx series), the strengthening is achieved primarily due to the formation of an intermediate  $\theta'$  phase via heterogeneous nucleation and growth. These precipitates form as thin plates of high length-to-thickness aspect ratio, are rationally oriented within the matrix and have nearly perfect coherent matching to the matrix lattice across their broad faces. High aspect ratio, almost full coherency of broad faces and significant compositional difference between the matrix and precipitates are also common in some other strengthening products, such as  $\gamma'$  in Al-Ag and  $T_1$  in Al-Cu-Li. These phases do not fit easily into the traditional classification of phase transformations as being either diffusional or displacive, and exhibit some important characteristics of both classes. The compositional difference with the matrix clearly requires long range diffusion of the solute, but on the other hand the crystallography of these phases allows one to identify a simple lattice correspondence that is common for displacive transformations. The lattice correspondence, or the matrix-product stress free transformation strain for  $\theta'$ ,  $\gamma'$ ,  $T_1$

and other presumably mixed-mode products, invariably features a significant shear component. It has been suggested by some authors that many important transformation features, namely the apparent difficulty in nucleation, the nature of the association with matrix defects and clusters of vacancies and/or microalloying additions and finally the specific discrete thicknesses of the plates observed, might all be explained in terms of the accommodation of this shear component of transformation strain.

At the core of this project is an attempt to study the manifestation of the shear component of transformation strain through the special mode of precipitation - an autocatalytic nucleation. There is some experimental observation of  $\theta'$  colonies without any obvious association with defects. Such colonies are comprised of either a single variant of precipitates, arranged into inclined stacks of plates, or cross-like arrays of two perpendicular variants of  $\theta'$ . Early models of this process suggested that such short-range ordering is due to the elastic interactions between precipitates, with subsequent nuclei being formed in the solute depletion and elastic strain fields of previously formed plates. The work presented in this thesis is a natural extension of the elastic interaction models; it is based on a consideration of the generalised transformation strain with a significant shear component and uses state of the art simulation techniques. The catalytic effect of a coherent precipitate can be determined by the specific structure of the depletion field surrounding the particle and the local magnitude of the interaction energy between the pre-existing microstructure and the nucleus that is formed. As an extension of the early models an approach developed in this work uses the phase field model to simultaneously monitor both the compositional chemical and elastic driving forces. Rigorous analysis of the total nucleation driving forces in the environment of the pre-existing plates is presented for the different types of underlying transformation strains in both nuclei and mature precipitates.

Phase field modelling was selected as the primary simulation technique for this research project, as it is an extremely versatile and powerful tool for studying microstructure evolution in material systems on a mesoscale. The microstructure is represented by a set of continuous field variables related to the composition and structure of the matrix and product phases, with the evolution governed by minimisation of the free energy of the system. Phase field models are particularly useful in studying multiphase systems, since there is no need to track interfaces explicitly and various energy contributions (chemical and elastic) can be naturally incorporated into a model within a single simulation framework. This thesis presents such a phase field model for the precipitation of  $\theta'$  in Al-Cu and studies the precipitation at various levels of supersaturation, corresponding to different alloy compositions and ageing conditions. Nucleation is also incorporated into the model with new nuclei being randomly introduced at a rate sensitive

to the local composition and stress in the matrix. The study systematically looks at how the type of the transformation strain in the mature plates and nuclei affects the patterns in the precipitate distribution that develops dynamically during the alloy ageing.

The purpose of the study is to elucidate the atomistic details of the transformation mechanism for a whole class of phases that have important technological applications. An understanding of the role of the shear component of transformation strain and the way the strain energy is accommodated during nucleation of the strengthening phases has the potential to improve mechanical properties of the advanced materials by optimising the processing.

On the technical level this work is intended to fill the gap that exists in the field of mesoscale models in recognising the importance of shear. The phase field model presented in this thesis is an intermediate step in the direction of more physically realistic models of nucleation and microstructure evolution. The study also considers several important issues regarding the particular formulation of the phase field model for  $\theta'$  evolution. These include the construction of the free energy functional, scalability of the model in terms of the simulation domain size, the numerical stability and the efficiency of the finite difference schemes and the representation of interfacial energy and kinetic anisotropy.

## **1.2. Outline of the thesis structure**

Chapter 2 gives a detailed literature review of the fundamentals of nucleation theory as applied to solid-solid transformations. Classical nucleation theory is presented in some detail, both homogeneous and heterogeneous. The influence of various defects of real materials on the rate of the nucleation is discussed. Specific attention is paid to the role of interfacial and strain energies associated with the formation of the new phase embryos. Khachaturyan's microelasticity theory is presented at length, since it is incorporated into the phase field model to treat the elastic energy and also to account for the strain-induced modification of the nucleation driving force. The chapter closes with an overview of the binary Al-Cu system, the  $\theta'$  strengthening phase and the related diffusional-displacive products.

Chapter 3 presents a review of the thermodynamical data available for selected product phases, like  $\theta'$  in Al-Cu and  $\gamma'$  in Al-Ag, and uses typical interfacial energies and chemical driving force as inputs in the parametric analysis of critical sizes and activation barriers during the nucleation of platelike diffusional-displacive products. It demonstrates that current estimates,

especially those of interfacial energies, do not adequately explain the difficulty in nucleation of these phases and emphasizes the crucial importance of strain energy accommodation in the nucleation of the sheared product phases.

Chapter 4 reviews and extends the earlier models based on the application of a dislocation loop method to the analysis of the elastic interaction energy. The model is revisited to include the results of interaction between plates of various sizes and mutual orientations, with a specific focus on the role of the shear component in the stress-free transformation strain. Interactions between mature precipitates of tetragonal misfit and nuclei of generalised (having both dilatational and shear components) transformation strain are identified as having symmetry consistent with autocatalytic arrays.

Chapter 5 systematically introduces the basics of the phase field technique and details aspects of developing a phase field model for a specific system of interest. Special attention is given to the connection of the field variables and kinetic coefficients with the thermodynamic parameters of the system. The construction of the free energy functional and the treatment of various anisotropies, interfacial and kinetic, are discussed thoroughly. Simple one- and two-dimensional test cases are presented to illustrate the behaviour of the model against selected analytical solutions for the growth of planar interfaces and evolution of isolated particles in two dimensions. The chapter closes with the summary of the particular model used for Al-Cu and a description of its numerical implementation.

Chapter 6 presents the results of the phase field simulations in two dimensions with the focus on the chemical driving forces for the nucleation in the environment of an isolated precipitate. Driving forces are analysed for two alloy compositions and three transformation temperatures in an attempt to capture the effect of the magnitude of the chemical driving forces versus the catalytic effect of the elastic interaction. Finally, results of the simulations for concurrent strain-affected nucleation and growth are presented and analysed in terms of an autocatalytic nucleation. Conclusions and directions for further research are summarised and outlined in Chapter 7.

## **2. Precipitation in solids**

In this chapter the basics of nucleation theory and its applications to solid-solid transformations are discussed. The role of interfacial and strain energy is explained. The methods of estimating strain energy that accompanies solid-solid transformations are presented in detail. Classification of solid-solid transformation is given with the focus on the importance of mixed mode diffusional-displacive transformations. Al-Cu binary system and precipitation of  $\theta'$  is introduced as the model system within the scope of this project.

### **2.1. Nucleation theory**

#### **2.1.1. Introduction**

The process of precipitation in alloys is one of many technologically important examples of first order phase transformations. Its practical importance in material science stems from the crucial dependence of the material's mechanical properties on the type of microstructure that forms in the course of transition. The properties of a system, most notably its strength, are controlled by the size, morphology and distribution of second phase particles embedded into the parent phase matrix.

Nucleation is an initial stage of first-order transformations; therefore, understanding and controlling the nucleation is of crucial importance for the design of advanced materials. The following review is focused on the theory of nucleation and specifically on its application to solid-solid transformations.

The foundation of nucleation theory has been laid in the classical thermodynamics developed by Gibbs, who identified that the work required to form a nucleus of the new phase in unstable equilibrium with the parent phase is a measure of system stability. Based on these ideas the theory was further developed by Volmer, Weber, Farkas, Becker, Döring, Zeldovich and others. Developed initially for the condensation of vapour, and subsequently extended to processes like cavitation, melting and eventually transformations in solids, this theory of nucleation proved to be qualitatively correct, although extremely challenging both in terms of the fine details of the rate equations for specific applications and in terms of the experimental confirmation of key controlling variables.

Classical nucleation theory has its limitations (which will be discussed further) but it nonetheless describes the process of transformation well and can serve as a basis for theoretical analysis, provided that a realistic physical model of the transformation is identified. Thus in this review the basics of the classical nucleation theory will be presented and complications specific to solid-solid transformations, such as anisotropic interfacial energies, strain energy effects and the presence of structural singularities will also be discussed.

### **2.1.2. Basic formulation of classical nucleation theory**

Nucleation theory describes the initial stage of a large class of first order phase transformations. When a system is subject to external conditions outside the stability range of a given phase a transformation is expected to proceed. In the course of this transformation a new state develops, which could be a new aggregate state or a mixture of more stable phases. Decrease in the total energy of the system provides the driving force for the transformation.

The rate of the transition is limited because of an energy barrier associated with formation of domains of the new phase. The barrier originates primarily from the additional energy required to create an interface between the parent and product phases. Small embryos of the new phase have large ratios of the surface area to the volume, and thus can produce an overall energy increase when the interfacial energy penalty outweighs the volumetric energy decrease. Instability of such small embryos in the parent phase makes the system resistant to growth of new phase domains.

The energy change associated with formation of embryos is illustrated in Fig. 1. Two regions may be identified based on the value of the derivative of the total energy with respect to the size of an embryo. In the region A the energy increases with embryo size and therefore decay of the embryo is preferred to its growth. This consideration is reversed for the region C. The point B represents the critical size that is characterised by an unstable equilibrium of a nucleus with a parent phase.

Thermal fluctuations constantly generate the embryos of the new phase and the random processes of growth and decay of these embryos eventually produce a population of critical nuclei, which become viable and grow into stable volumes of equilibrium product. This process constitutes nucleation. Nucleation theory in general addresses the kinetics of the process, namely the rate of formation of product phase nuclei with the ability to grow continuously.

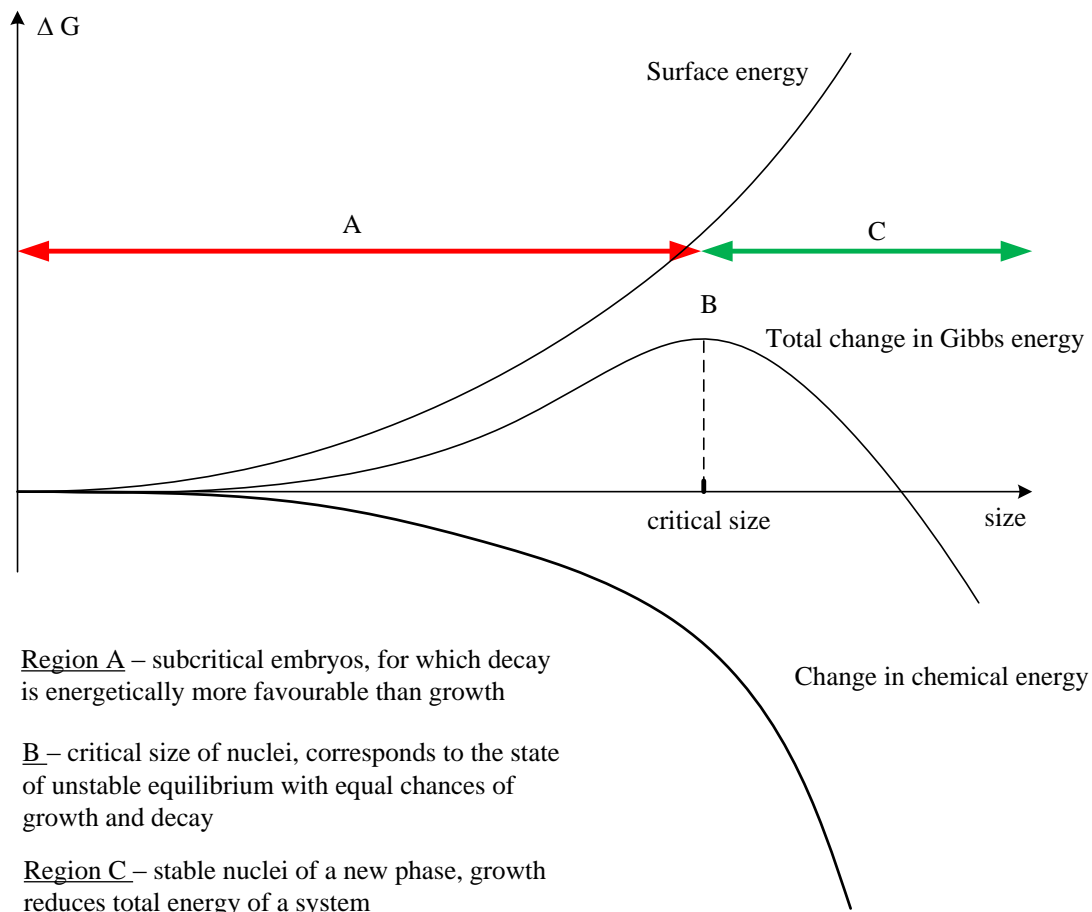


Fig. 1 Schematic variation of the change in the Gibbs free energy of the system associated with the formation of a new-phase domain, as a function of domain's size. The concept of critical size is illustrated as point B on the graph.

Quantitative development of nucleation theory arguably began with work by Volmer and Weber [1] on condensation in vapours. Building on the ideas of von Smoluchowski [2] and Einstein [3], who addressed critical opalescence in terms of thermal fluctuations, the authors related concentration of liquid or crystalline clusters to the energy required for their formation. This energy was obtained as work against extra pressure produced by the Gibbs-Thomson effect. Volmer and Weber derived the formulae for the work of critical cluster formation via the supersaturation of the vapour with respect to the equilibrium pressure, thus introducing the key concepts of critical size and activation barrier for nucleation.

In the developments that followed Farkas [4], Kaischew and Stranski [5] together with Becker and Döring [6] presented more rigorous analysis of vapour condensation on a kinetic rather than thermodynamic basis. The problem was treated via the probabilities of both condensation on and evaporation from the surface of the clusters. Kinetics of transformation was

analysed as a “diffusional flux” of clusters with respect to their size (number of clusters passing through particular size per unit time) under the influence of an external driving force. Steady state solutions for such a problem were derived with more exact expressions for the pre-exponential factor in the concentration of critical nuclei. A similar solution also appeared in the theory by Zeldovich [7] for cavitation in liquids. Zeldovich must also be credited for introducing a factor that gives the probability of a critical nucleus in unstable equilibrium with the parent phase to actually grow instead of decay.

The concepts of thermally activated fluctuations and their random growth and decay were also employed for the explanation of various pre-transition phenomena, like anomalously high specific heat capacity and the expansion coefficient in the vicinity of the transition temperatures in pre-melting of solids and pre-crystallisation. This has been developed by Frenkel [8] into a general theory of heterophase fluctuations and effectively expanded nucleation theory formalism into systems other than vapours.

Approximately at the same time the theory of nucleation was applied to solid-solid transformations. Becker [9, 10] analysed precipitation in binary alloys and obtained expressions for the activation energy for nucleation of cubical precipitates, assuming sharp interfaces and basing the derivation on the energy of the bonds broken. Becker also realised that the nucleation rate should depend on the diffusion rate, thus introducing a second Arrhenius exponent factor into the rate equation. However, the pre-exponential factor was not determined.

Further development of solid-specific theory was due to Turnbull and Fisher [11] who considered the rate of nucleation in condensed systems, primarily for processes that do not require long-range diffusion. Their treatment was based on absolute reaction rate theory and led to the classical form of the exponential factor in the rate equation, and also approximated the pre-exponential term as the product of lattice site density and the frequency of diffusional jumps across the nucleus interface.

It would be now appropriate to summarise formally the ideas of classical nucleation theory. This has been done by Russell in his review on nucleation in solids [12] by formulating basic principles sufficient to obtain a solution to the nucleation problem:

- Principle I: The probability of nucleation is proportional to the  $\exp(-\Delta G^*/k_B T)$ , where  $\Delta G^*$  is the work required to generate the critical nucleus, in other words make a system unstable with respect to the transformation.

- Principle II: Time reversal, which postulates that for equilibrium systems any state with inversed velocities of particles is equally probable. The approximate application of this principle to non-equilibrium systems allows equating the path of the fluctuation's growth and decay and easily deducing the activation path by tracing spontaneous deterministic decay, rather than random growth.

The steady-state nucleation rate in its most general form is then given by

$$J = Z\beta^*N \exp\left(-\frac{\Delta G^*}{k_B T}\right) \quad (2.1)$$

where  $\Delta G^*$  is the change in Gibbs free energy associated with critical nucleus formation,  $Z$  is the non-equilibrium Zeldovich factor ( $\sim 0.01 - 0.1$ ),  $\beta^*$  is an attachment frequency factor (the rate at which atoms or molecules are added to the critical nucleus) and  $N$  is the concentration of nucleation sites of a particular type available in the system. The product of this concentration and the exponential factor gives the total number of critical nuclei that exist in a system.

As pointed out by Russell in [12], while the general form and the meaning of the variables in equation (2.1) do not change, exact expressions should be developed on an individual basis depending on the system and the exact mechanism of transformation. Consider a simple example of the spherical particle of the new phase characterised by a sharp interface with isotropic interfacial energy  $\gamma$  and the chemical driving force  $\Delta G_V$  (the volumetric Gibbs free energy reduction upon transformation from parent to product phase). The change in Gibbs energy of the system brought about by the formation of the particle would be

$$\Delta G^* = -\frac{4}{3}\Delta G_V\pi r^3 + 4\pi r^2\gamma \quad (2.2)$$

where  $r$  is the radius of the sphere. Differentiation of expression (2.2) by the size variable gives an extremum at the critical size  $r = r^*$ , which is given by

$$r^* = \frac{2\gamma}{\Delta G_V} \quad (2.3)$$

Substitution of (2.3) into (2.2) gives an expression for the activation energy or the energy barrier for nucleation as

$$\Delta G^* = 16 \frac{\pi\gamma^3}{3\Delta G_V^2} \quad (2.4)$$

However, in more complex systems derivations analogous to (2.2) - (2.4) are complicated by the interfacial anisotropy and/or the effect of elastic strain energy in condensed systems. This introduces the shape dependence of the nucleus energy and the problem of identifying the critical nucleus and its parameters becomes multivariate. Instead of differentiation only with respect to size, the equation analogous to (2.2) must be differentiated with respect to size and shape. The critical nucleus then is the one defined by the saddle point in the free energy profile.

### 2.1.3. Transient nucleation

Expressions of the form (2.1) for the nucleation rate are obtained as steady state solutions and are applicable only when the equilibrium distribution of embryos is established. For some systems such as gases the treatment is a very good approximation; however, for condensed phases with slow diffusion the chain monomer attachments and detachments leading to the formation of a critical nucleus may take a considerable time.

It has been observed in some systems [13] (the transformation of austenite to pearlite in steels, the recrystallisation in aluminium and silicon ferrite) that there is a period initially when no nuclei are observed and then the nucleation rate starts to increase, rapidly approaching the steady-state value, as demonstrated in Fig. 2.

Turnbull explained the phenomenon qualitatively by pointing out that whenever the distribution of nuclei deviates from the equilibrium an incubation time should be expected and presented simulations of incubation time [14]. Fisher, Hollomon and Turnbull [15, 16] expanded the ideas to treat athermal nucleation and a systematic analytical solution was given.

The transient nucleation rate for isothermal reaction is obtained as

$$J(t) = J_s \exp\left(-\frac{\tau}{t}\right) \quad (2.5)$$

where  $J_s$  is a steady-state nucleation rate and  $\tau$  is a characteristic incubation time.

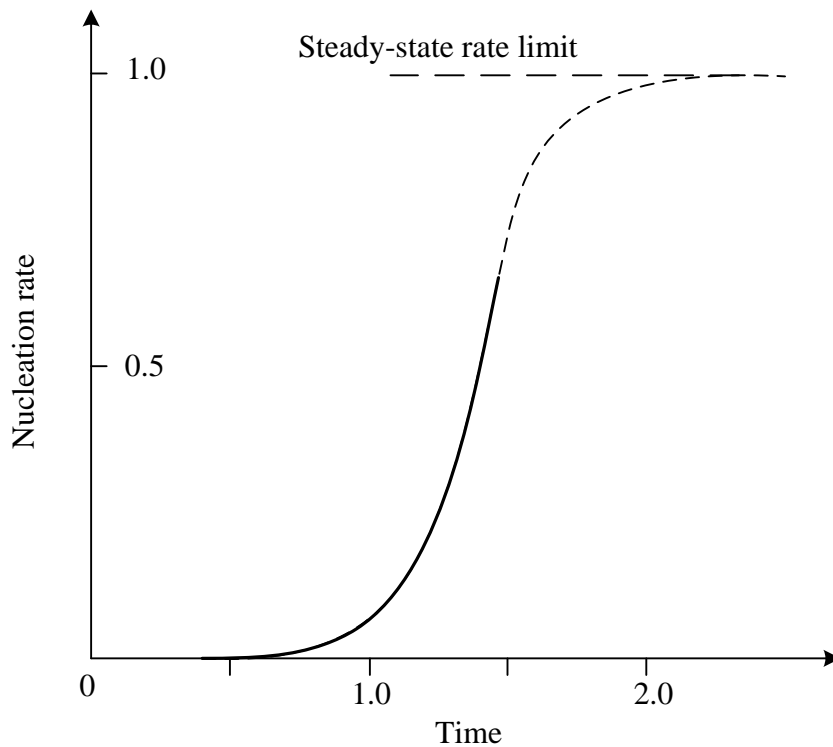


Fig. 2 Transient homogeneous nucleation rate in an arbitrary system with critical cluster comprising 25 atoms and the initial condition for the nucleation rate of 12-atom clusters equal to 0.01. Adapted from Turnbull [14].

#### 2.1.4. Classification of nucleation processes

Nucleation in solids is usually classified, in terms of the nature of the process of nuclei formation, as either homogeneous or heterogeneous. Distinction is made according to whether the formation of the embryo that evolves to become a critical nucleus occurs randomly in space or at some singularity in the structure. Such singularities usually serve as nucleation sites due to the reduced activation barrier associated with the nucleus formation. All of the general nucleation theory conclusions remain true, with the only adjustment being the number of nucleation sites in the rate equation (2.1), which obviously should be replaced from the total number of lattice sites in the case of homogeneous nucleation to the number of the sites preferred for heterogeneous nucleation.

Homogeneous and heterogeneous nucleation may be regarded as competing processes, with homogeneous nucleation having more theoretical than practical interest for solid-solid transformations. This is as long as the real structure of the material provides an array of suitable

nucleation sites such as dislocations, grain boundaries, stacking faults, inclusions and free surfaces.

In solids classification is also possible with respect to the type of the interface that is created between parent and product phases. According to this, the process may be classified as coherent, semicoherent or incoherent. Interfacial structure develops as a result of a balance between interfacial and strain energy contributions. Coherent structures, where matrix and product are coupled continuously and crystal planes are not interrupted, have the lowest interfacial energies but may produce significant elastic strains in the matrix and/or precipitate phases. On the other hand, incoherent interfaces show no continuity and typically have high interfacial energies, but low elastic strains. For the intermediate cases of semicoherent interfaces, structural misfit and accumulating strains are partially relieved by the array of dislocations within the otherwise coherent interface.

### **2.1.5. Heterogeneous nucleation and the influence of defects**

The structure of the real material provides imperfections of various kinds in abundance. These imperfections can serve as nucleation sites and commonly the effect of imperfections is to favour heterogeneous nucleation over the homogeneous pathway. In this section a brief description will be given for the effects of particular defects on the nucleation process.

#### **2.1.5.1. Vacancies**

In the equilibrium state the system has a certain concentration of vacant lattice sites, because from the total energy viewpoint the minimum is attained when the increase in the enthalpy of the broken bonds associated with vacancy formation is compensated by the increase in configurational entropy of mixing vacancies and atoms. The equilibrium concentration of vacancies is given by the expression

$$c_{vac}^{eq} = A \exp\left(-\frac{\Delta H_{vac}}{k_B T}\right) \quad (2.6)$$

where  $\Delta H_{vac}$  is the vacancy formation enthalpy (~0.2-0.3 eV) and  $A$  is a material constant close to unity.

The equilibrium vacancy population does not affect the nucleation because at equilibrium the change in energy associated with the small change in vacancy concentration is zero. Also for a coherent nucleation, when lattice continuity is maintained between parent and product phases, there is no effect of vacancies on stresses.

For incoherent and semicoherent nucleation equilibrium vacancies play a part in relieving the transformation strains, providing the flux of material in the direction required to compensate for transformation strains. Non-equilibrium vacancies produced by rapid quench from high temperature down to the transformation temperature will be involved in the same process. However, the destruction of non-equilibrium vacancies in strain relief will also affect both the chemical energy of the system, and the elastic strain energy (for instance when annihilation of non-equilibrium vacancies strains the nucleus in tension, as suggested by Cahn in [17]). An analysis of the effect of excess vacancies was presented by Russell [18] who considered the precipitation of the  $\beta$  phase from the  $\alpha$  matrix in a binary solution and arrived at the modified form of the equation (2.4) for the nucleation barrier:

$$\Delta G^* = \frac{16\pi\gamma^3}{3(\Delta G_V + \Delta G_{vac})^2} = \frac{16\pi\gamma^3}{3\left(\Delta G_V + \varepsilon^T \frac{\Delta\mu_{vac}}{V_\beta} + 9\Delta\mu_{vac}^2 \frac{(1-\nu)}{4EV_\beta^2}\right)^2} \quad (2.7)$$

Here, the chemical potential of excess vacancies may be expressed via the supersaturation of vacancies as

$$\Delta\mu_{vac} = k_B T \ln\left(\frac{c_{vac}}{c_{vac}^{eq}}\right) \quad (2.8)$$

where  $c_{vac}$  is the actual and  $c_{vac}^{eq}$  the equilibrium vacancy concentrations. Transformation strain is expressed via atomic volumes of the matrix  $V_\alpha$  and the precipitate  $V_\beta$  as  $\varepsilon^T = (V_\beta - V_\alpha)/V_\alpha$ ;  $E$  is the Young's modulus and  $\nu$  is the Poisson's ratio.

It can be seen from expression (2.7) that depending on the type of transformation strain the term linear in  $\Delta\mu_{vac}$  may increase or reduce the activation barrier for nucleation. For precipitates with atomic volume larger than that of a matrix ( $\varepsilon^T > 0$ ) the driving force is increased and the barrier is lowered. The quadratic term (associated with annihilation of more or fewer vacancies, than required for the exact strain relief) always reduces the barrier.

Another obvious effect of excess vacancies on nucleation is the increase of diffusion rates and as such the proportional increase of the frequency factor  $\beta^*$  in the pre-exponential part of the nucleation rate equation (2.1). This is true for all transformations that involve compositional change and require long-range diffusion, regardless of the interface type.

The combined effect of the factors discussed above leads to enhanced nucleation of semi- or incoherent phases with positive volumetric misfit, both due to faster diffusion and reduction of the nucleation barrier. The precipitation of phases associated with the reduction in volume should be suppressed to some extent by the reduced driving force and the increased activation barrier.

### 2.1.5.2. Dislocations

Dislocations have strong effect on nucleation via several different mechanisms, and their influence is different for coherent and incoherent precipitation. One may identify several areas where the influence of the dislocation may affect the precipitation process: enhanced diffusion along the disordered dislocation core, the interaction of complex strain fields surrounding dislocations with the transformation strain of a precipitate and finally the effect of the dislocation on the population of vacancies and on the diffusion of solute atoms. Also, precipitation directly on the dislocation line may be preferred due to the destruction of the high-energy disordered dislocation segment, replaced by the precipitate, which thus reduces the barrier for its formation.

The latter mechanism was investigated by Cahn [17] who analysed the process of incoherent precipitation on the dislocation core. Cahn assumed that the highly strained region of the dislocation core would be decorated with solute in a way analogous to the Cottrell atmosphere and be a metastable subcritical cylinder of a new phase, characterised by the radius  $r_0$ . The process of nucleation is a formation of a bulge on the metastable tube by a thermal fluctuation.

The catalytic power of the dislocation in this model can be estimated by the parameter

$$\alpha = \frac{\mu b}{2\pi^2} \frac{\Delta G_V}{\gamma^2} \quad (2.9)$$

where  $\mu$  is a shear modulus,  $b$  is the magnitude of the dislocation's Burgers vector,  $\Delta G_V$  is a nucleation driving force and  $\gamma$  is the interfacial energy.

Cahn demonstrated that for increasing  $\alpha$  the barrier for nucleation continuously decreases, until for  $\alpha \geq 1$  it effectively disappears. It was estimated that for a range of systems  $\alpha$  is between 0.4 and 0.7, thus significantly reducing the activation energy. Gomez-Ramirez and Pound [19] also studied similar problems with different morphologies of the bulge and found no strong dependence of barrier on the shape. They also concluded that metastable embryos may exist on dislocations even in undersaturated systems.

Thus for incoherent nucleation dislocations provide a catalytic effect that is stronger for larger Burgers vector, and for higher supersaturation. It is also concluded that edge dislocations are more effective than screw dislocations.

For coherent precipitates the benefit in association with the dislocation line is of a different nature. It is a partial relief of the transformation strain, when the particle forms in the stress field of a dislocation line. Such an interaction has been analysed by Lyubov and Solov'ev [20], Dollins [21] and later by Barnett [22] and reviewed by Larche [23]. Analysis has been restricted to ellipsoidal shapes and dilatational transformation strain  $\varepsilon_{ij} = \delta_{ij}\varepsilon$ . It was found that strain relief is equivalent to the reduction of the "effective" interfacial energy, which lowers the activation barrier and the size of the critical nucleus:

$$\gamma_{eff} = \gamma - \frac{\mu b (1 + \nu)}{9\pi (1 - \nu)} |\varepsilon| \quad (2.10)$$

Dollins also suggested that the elastic properties of a precipitate play a role, with soft precipitates reducing the energy of a dislocation line and hard ones increasing it. It should thus be expected that coherent precipitates of lower elastic moduli should be preferred, while those of higher modulus are suppressed in the vicinity of dislocations.

Besides affecting the magnitude of the nucleation barrier for the precipitates, dislocations can also modify other factors in the rate equation (2.1). Transport is enhanced along the core, and as such the frequency factor  $\beta$  is increased according to the dislocation core diffusivity. This is of great importance for the nucleation of incoherent precipitates directly on dislocations.

Finally, the nucleation site density  $N$  should be modified to reflect that only those lattice sites in the neighbourhood of the dislocation line that are now available for nucleation. Russell estimates this number as

$$N \approx \frac{\rho_d}{a} \quad (2.11)$$

where  $\rho_d$  is the dislocation line density (length per unit volume) and  $a$  is the lattice constant. It is estimated that for annealed metals  $N$  is about  $10^{-14} \text{ cm}^{-3}$ , which is a reduction by a factor of  $10^9$  compared to a homogeneous nucleation. For an incoherent nucleation this is usually compensated by enhanced transport; however, for coherent nucleation it must be taken into account that the frequency factor is still the same as defined by the volume diffusion.

### 2.1.5.3. Other defects

Other defects also have the potential to enhance the nucleation of particular phases. Internal boundaries may provide enhanced transport in the same way as highly disordered dislocation line cores. They also serve as effective sources and sinks for the vacancies, and may enhance or suppress nucleation by affecting vacancy population. Reduction in the activation energy is similar to incoherent nucleation on the dislocation line – for example it can be found by replacing an area of a grain boundary and recovering an extra surface energy associated with this area. The effect is particularly strong for grain edges and corners (Cahn [24]).

Assistance can also be provided by stacking faults [12], which can either be replaced in a process of coherent nucleation, or constitute a pre-existing embryo with a structure different to that of the matrix, thus reducing the structural part of the transformation barrier. The influence of microalloying additions is also manifold – it may be a lowered interfacial energy due to the absorption of a microalloying component in the interface, reduction in strains or the provision of pre-existing sites in the form of solute or solute-vacancy clusters.

### 2.1.6. Limitations of the theory and its experimental support

Classical nucleation theory has its obvious limitations. The rate equations are developed for the steady-state approximation, when the distribution of nuclei of various sizes is close to equilibrium at the given transformation temperature. The transient equations for a nucleation rate account for an incubation time, which is required to establish this distribution after a system is brought to a transformation temperature; however, effects of a slow approach to transformation conditions are usually ignored.

It is a matter of serious debate whether the macroscopic thermodynamic quantities can be extrapolated into the nanoscopically small domains of the new phase and as such what is the actual additional energy penalty associated with embryo formation.

Also, it is unclear if the structure of the embryo is well defined and the interface between the product and parent phases is sharp. A number of improvements to the theory have been considered, like the diffuse interface treatment of Cahn and Hilliard [25-27] or the multi-flux analysis of Russell [28]. These theories do provide new insights into the structure of the nucleus, its immediate surroundings and the magnitude of the activation barrier and non-equilibrium Zeldovich factor, induction time, etc. Nonetheless the broad picture formulated in rate equation (2.1) remains unchallenged and many improvements affect the results less than the actual uncertainty in key variables (interfacial energy and chemical driving force).

Classical nucleation theory has been confirmed to describe well the kinetics of condensation of supersaturated vapours within the limits of experimental uncertainties. Volmer and Flood [29] and Flood [30] have studied drop formation in various systems and found good agreement with Volmer-Weber rate equations.

In more complex condensed systems comparison of transformation kinetics with the theoretical treatment becomes very difficult. It is usually done by comparison of the interfacial energy or chemical driving force, as estimated from the experimentally observed nucleation rates, with their counterparts as measured for macroscopic interfaces or obtained from alternative methods. Therefore, systematic interpretation of results also suffers from the lack of reliable experimental information on the magnitude of interfacial energies and driving forces.

It is widely accepted and confirmed by observation that nucleation in condensed systems is rarely homogeneous, due to the relatively high interfacial energies and strains involved. The strong influence of imperfections (vacancies, dislocations, stacking faults, grain boundaries, clusters of microalloying additions, etc.) makes the process heterogeneous in almost all systems and unfortunately the exact mechanism of transformation is often poorly understood.

However, in some systems solid-solid homogeneous nucleation is considered possible (see Russell [12] for review) and a satisfactory explanation of kinetics is given for Al-Si and Al-Ge alloys. Servi and Turnbull [31] also explained precipitation in Cu-Co at low supersaturation in terms of homogeneous nucleation and growth.

The ideas of classical nucleation theory proved to be correct and applicable for a wide range of physical systems and transformations and continue to provide an important theoretical framework for the interpretation of phase transition kinetics.

The next part of this review gives more details on the role of interfaces and coherency strains during nucleation and leads to the subject of the thesis, i.e. the role of displacive transformation strains in diffusional transformations. This role will be analysed by studying the effect of shear strain in the specific mode of dynamic heterogeneous nucleation, assisted by the elastic interaction energy.

### **2.1.7. Interfacial energy**

The energy of the interface between matrix and product phase is one of the most important variables that enter equations (2.2) - (2.4) and their analogous forms for any nucleation problem. By definition  $\gamma$  is the reversible work required to create a unit surface interface under the existing constraints. In the case of solids, with constant pressure, temperature and mass of the system  $\gamma$  becomes an extra Gibbs free energy associated with the interface.

Although the qualitative role of  $\gamma$  in the nucleation process is well understood and confirmed experimentally, there are still doubts about whether it is possible to describe surfaces of very small new phase embryos in terms of classical surface thermodynamics. It is uncertain if the surface of the nanosized particle can be assigned the value of energy measured or theoretically estimated for the macroscopic interface. Moreover, the interfacial energies in solids are hard to measure experimentally or estimate theoretically.

Interfaces are classified into three categories based on the continuity and matching of lattice planes across them – coherent, incoherent and semicoherent (or partially coherent) interfaces are identified. The character of the interface depends on the crystallography of the phases involved and also on the scaling factor brought by the influence of elastic coherency strains. If the product phase is very different in structure from the matrix, incoherent interfaces usually develop, characterised by the high interfacial energy with little or no elastic strains. For the phases with little difference in structure coherent, well-matched interfaces are possible, especially for small particles. Semicoherent structures develop under the combined influence of elastic strain energy and interfacial energy, and are essentially coherent interfaces with an overlapped network of misfit dislocations that relieve stress.

Solid interfaces are highly anisotropic, which is reflected in the faceted shapes of crystals. Wulff [32] suggested that the length of the vector from the crystal centre to the facet is proportional to the interfacial energy of this facet. This is known as the Gibbs-Wulff theorem and serves a basis for the Wulff construction, the method for determining an equilibrium shape of a crystal in liquid or vapour from the polar plot of the interfacial energy ( $\gamma$ -plot), as for example in Fig. 3.

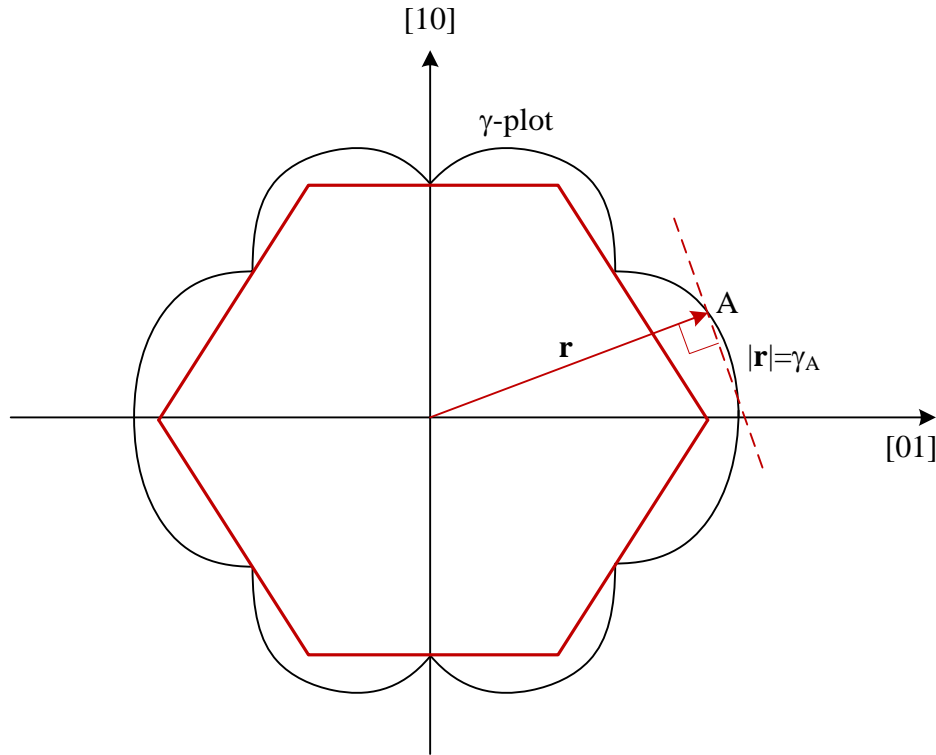


Fig. 3 Wulff construction in a hypothetical two-dimensional crystal. Polar plot of an interfacial energy gives the energy as a function of direction. Interfacial energy for a plane with a normal in a given direction (Wulff plane shown by the dashed line in the diagram) is defined by the length of the corresponding vector  $\mathbf{r}$ , ending on the  $\gamma$ -plot. Cusps in the  $\gamma$ -plot identify low-energy directions and orientations of low-energy planes/facets of a crystal. According to the Wulff theorem, the inner envelope of all possible Wulff planes would give a lowest energy shape (adapted from [33]).

A simple method of theoretical prediction of interfacial energy magnitude has been proposed by Turnbull in [34]. The process of creating the planar interface is seen as cutting two crystals A and B, which represent phases  $\alpha$  and  $\beta$  of different composition across the interface, and rejoining them together to create two pieces with an  $\alpha$ - $\beta$  interface. The energy can be estimated by the difference of the energies of bonds destroyed in cutting and created in rejoining. Interfacial energy is given as

$$\gamma = \frac{n_s z_s \Delta E^0 (x_\alpha - x_\beta)^2}{N_A z_l} \quad (2.12)$$

where  $n_s$  is the number of atoms per unit area in the interface plane,  $z_s$  is the number of bonds per interface atom,  $z_l$  is the lattice coordination number,  $x_\alpha$  and  $x_\beta$  are the compositions of the phases across the interface,  $\Delta E^0$  is the heat of solution of  $\alpha$  in  $\beta$  and  $N_A$  is the Avogadro's number. A modification of equation (2.12) that includes the entropic part has been developed by Aaronson et al. [35]. Typical values for this purely chemical part of the interfacial energy lie in the range 20 - 200 mJ/m<sup>2</sup> [12].

The analysis above is valid for coherent interfaces. In the case of partial coherency Turnbull proposes to view the interfacial energy  $\gamma$  as a combination of chemical and structural parts

$$\gamma \approx \gamma_{chem} + \gamma_{struct} \quad (2.13)$$

For the simplest case of identical lattices in similar orientation but with different lattice constants the misfit can be accommodated by a planar array of edge dislocations, as in Fig. 4:

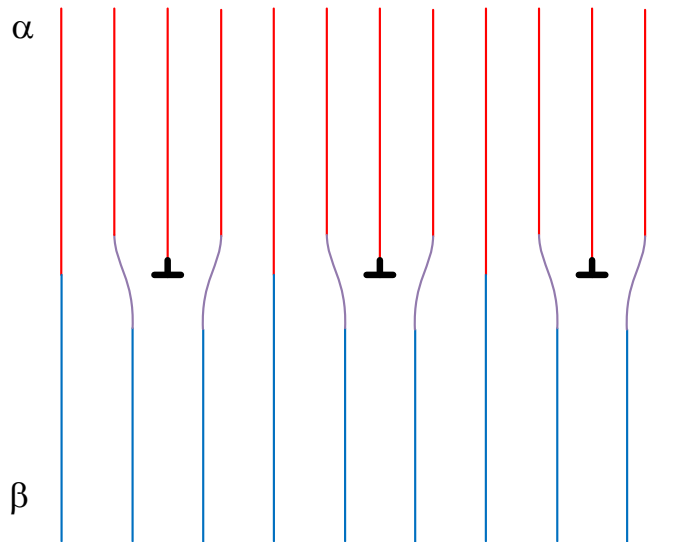


Fig. 4 Example of a semicoherent interface. The misfit between phases  $\alpha$  and  $\beta$  is in one dimension and is accommodated by the array of edge dislocations.

The coherency strain part of the interfacial energy in this case can be estimated from van der Merwe's [36] expression:

$$\gamma_{struct} = \frac{\mu a}{2\pi^2} \left( 1 + \psi - \sqrt{1 + \psi^2} \right) \quad (2.14)$$

where  $\mu$  is the shear modulus,  $a$  is the lattice constant and the function  $\psi$  is defined via the linear misfit in the interface  $\varepsilon^T$  and the Poisson's ratio  $\nu$  as

$$\psi = \frac{2\pi\varepsilon^T}{1-\nu} \quad (2.15)$$

Experimental data on the interfacial energy can be obtained by calorimetry studies supplemented with microstructure observation and also by coarsening analysis. Hondros [37] summarised selected data in various systems and gave an energy of several hundreds of  $\text{mJ/m}^2$  for incoherent interfaces, tens of  $\text{mJ/m}^2$  for coherent interfaces between phases with compositional difference and as low as a few  $\text{mJ/m}^2$  for stacking faults and twin boundaries.

The data for platelike precipitates in Al alloys, which are the focus of this thesis, will be discussed in detail in the relevant section of the chapter 3 “Magnitude of the activation barriers for platelike precipitates”.

### 2.1.8. Strain energy

From the very early stages of embryo formation, its growth towards critical size and development into a stable particle of the new phase, there is a strain energy contribution to the Gibbs energy of a system. Strain energy plays its role regardless of an interface type and typically both matrix and product lattices are strained, with the unusual exception of a hypothetical transformation between phases with identical crystal structures and lattice parameters.

The effect of strains, however, is quite different for coherent and incoherent precipitation and depends both on the type of the interface and the elastic properties of both matrix and inclusion.

As pointed out by Russell in [12], strain energy is irrelevant to incoherent nucleation. The critical nucleus is supposed to be in unstable equilibrium with the matrix; therefore, when it is strained, the flow of equilibrium vacancies will tend to eliminate strain and decrease the energy. As such by definition this unstable equilibrium is impossible to sustain with strains involved. In the presence of excess vacancies the critical size nucleus may be strained, but this energy may be accounted for separately in the expression for the energy of excess vacancies, as in (2.7). Beyond the nucleation stage the incoherent precipitate may produce strain energy that can be calculated. Nabarro [38] and Kröner [39] analysed the problem of strain energy for an incoherent ellipsoid, with purely dilatational strain and elastically homogeneous with the matrix. It was found that

such a precipitate is stressed in hydrostatic fashion and the strain energy becomes a function of the inclusion shape:

$$E_{el} = 6\mu V \varepsilon^2 f\left(\frac{c}{a}\right) \quad (2.16)$$

The shape factor  $f(c/a)$  has a minimum for thin discs, maximum for a sphere and an intermediate value for a prolate needle-like shape, as demonstrated in Fig. 5:

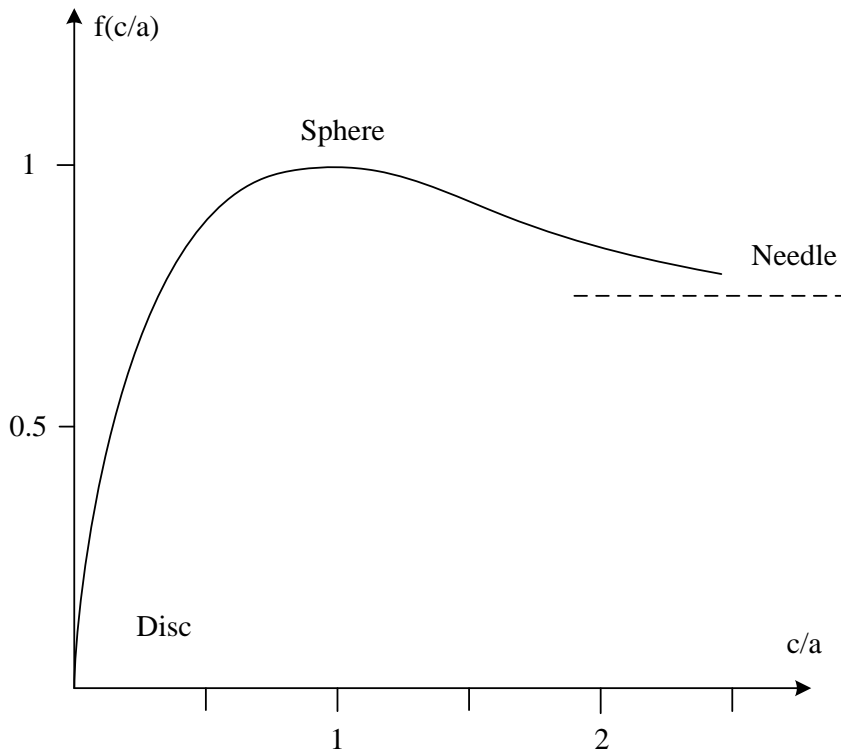


Fig. 5 Shape factor in the expression (2.16) for the energy of an incoherent inclusion, after Nabarro [38].

The strain energy of coherent precipitates on the contrary is very important for nucleation. It enters directly into the expression for the Gibbs free energy change analogous to (2.2) and affects all the parameters of the critical nucleus.

In the case of simple dilatation and an elastically homogeneous matrix the inclusion of the strain energy takes the particularly simple form, derived by Crum and reported by Nabarro in [38]:

$$E_{el} = 2\mu\varepsilon^2 \frac{(1+\nu)}{(1-\nu)} V \quad (2.17)$$

where  $\mu$  is the shear modulus of the matrix/inclusion,  $\nu$  is the Poisson's ratio,  $V$  is the inclusion volume and  $\varepsilon = \varepsilon_{11} = \varepsilon_{22} = \varepsilon_{33}$  and are the principal strains of a dilatational stress-free transformation strain. The strain energy of such an inclusion is independent of the inclusion's shape and proportional only to the volume. Expression (2.17) also implies coherency across the interface.

The first general treatment of the strain energy problem for a coherent inclusion has been developed by Eshelby [40, 41]. It addressed the problems of: a) coherent inclusion with the same elastic constants as the matrix and arbitrary stress-free transformation strain and b) coherent inclusion with elastic constants that differ from the matrix elastic constants, provided that both phases are elastically isotropic. The latter problem has been proven to have an analytical solution for an ellipsoidal shape of inclusion.

Eshelby's approach included a separation of the transformation process into imaginary stages. Firstly, of cutting out the region and allowing it to be transformed without the constraints of the matrix. Secondly, of applying a layer of surface forces to restore the shape of inclusion for re-insertion back into the matrix (at this stage stress is produced in the transformed region). Finally, of inserting the region back and allowing it to relax. This process generally produces strains both in the inclusion and the matrix. The solutions for the stresses, strains and elastic energies are complex and lengthy, so only some important results are discussed below.

Eshelby confirmed the conclusions of Crum for coherent dilatational centres that are elastically homogeneous with the matrix, namely that the elastic energy density is independent of inclusion shape and there is no elastic interaction between such centres.

It was also demonstrated that the elastic energy may be represented as a sum of independent terms corresponding to dilatation and shear. Christian [42, 43] and Kaufman [44] developed this argument and specified the solution for elastic energy of a martensite plate as a sum of dilatational and shear components. Further simplifying their results for the case of a thin oblate ellipsoid (representative of many disc-like and platelike precipitates) one may obtain the solution for elastic energy of such ellipsoid as:

$$E_{el} = E_{shear} + E_{dil} = V \left[ \frac{\pi}{8} \frac{(2 - \nu)}{(1 - \nu)} \mu \alpha \tau^2 + \frac{\pi}{4(1 - \nu)} \mu \alpha \xi^2 \right] \quad (2.18)$$

where  $\alpha$  is the aspect ratio of the ellipsoid (thickness to diameter),  $V$  is its volume,  $\tau$  is the shear and  $\xi$  is an expansion/contraction in the direction of ellipsoid's thickness. This result demonstrates that the strain energy is minimised for low aspect ratio inclusions, since both terms are linear with respect to  $\alpha$ .

Eshelby's method has also been applied to the inhomogeneous problem by Barnett et al. [45] to study the shape dependence of the precipitate formed by uniform expansion, when both matrix and precipitate are isotropic but have different elastic moduli (elastically inhomogeneous). The shape dependence of the strain energy density per unit volume of precipitate was found as shown in Fig. 6. The nature of shape dependence is different for hard precipitates, when strain energy is minimised for spherical inclusions, and soft ones, with energy minimum for disc-shaped inclusions.

Lee et al. [46] further extended the method to include the anisotropy of either the matrix, the precipitate or both. As can be seen from Fig. 7, the previous conclusions for isotropic media still hold true in the case of soft inclusions, which minimise the energy in the form of discs regardless of anisotropy (see bottom three curves). However, for homogeneous and elastically hard inclusions the exact result will depend on the degree of anisotropy in both phases and the minimum in strain energy can be achieved either for discs or spheres, depending on the degree of anisotropy in both phases.

Shapes that differ from ellipsoidal have also been analysed both in isotropic and anisotropic matrices. In the isotropic matrix Sass, Mura and Cohen [47] proposed a Fourier series solution for the cuboidal precipitate, Faivre [48] obtained an exact solution for the rectangular parallelepiped and Sankaran and Laird [49] for the square plate. Lee and Johnson [50] proposed a solution for the cuboidal precipitate in an anisotropic matrix.

Also more general forms of transformation strain, including those with non-zero deviatoric components, have been considered by Onaka et al. [51] for ellipsoidal inclusions with elastic moduli different from the matrix.

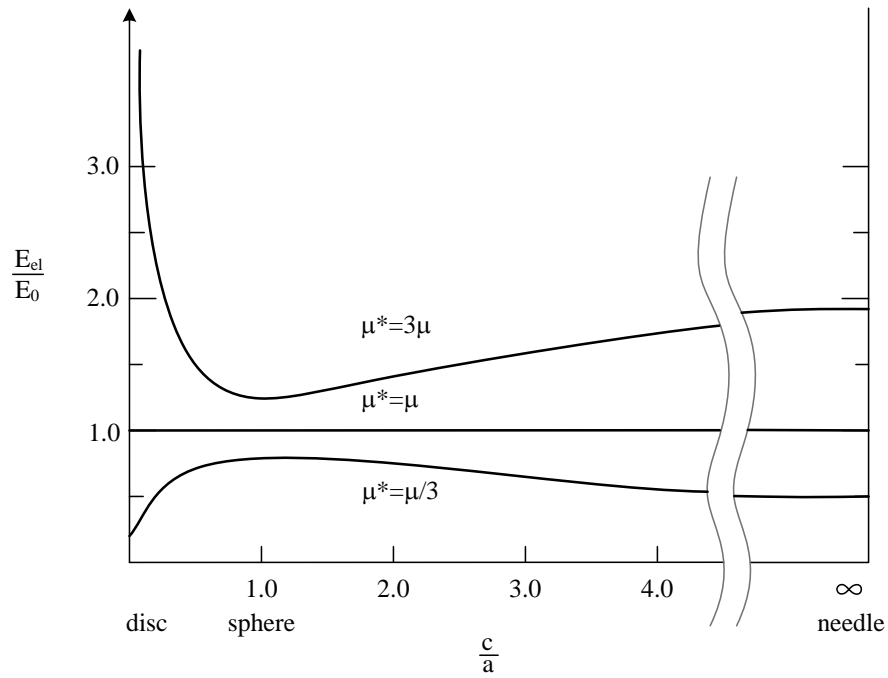


Fig. 6 Elastic energy of the ellipsoidal coherent precipitate, when both the matrix and the precipitate are isotropic, for different relative elastic moduli (from Barnett et al. [45]). The energy is normalised to the energy of the elastically homogeneous inclusion.

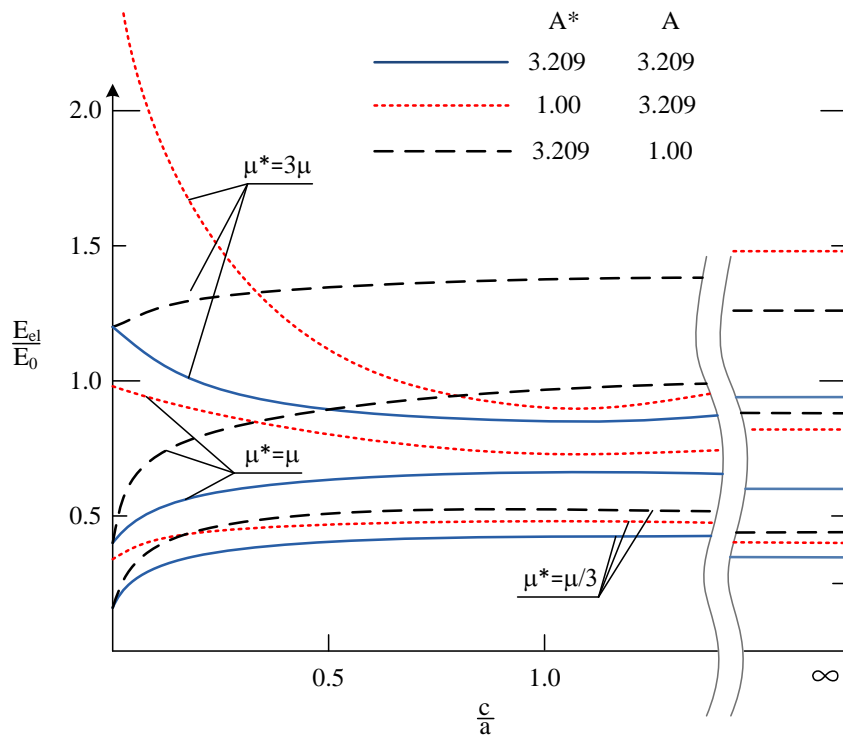


Fig. 7 Normalised strain energy of anisotropic ellipsoidal inclusion embedded into an anisotropic matrix (from Lee et al. [46]). Various combination of anisotropy in either matrix (dotted curves), precipitate (dashed curves) or both (solid curves) are given.  $A = (2 C_{44}) / (C_{11} - C_{12})$  is the Zener's anisotropy ratio (the star superscript corresponds to the precipitate phase).

The theories mentioned above are all limited to special cases, either of a simple inclusion shape that allows an exact solution of the elastic problem (like the ellipsoid or parallelepiped) or the assumption of an elastically isotropic medium and/or homogeneous elastic properties of the matrix and the inclusion. It should also be noted that the treatment of the elastic problem is commonly restricted to an isolated inclusion embedded into an infinite matrix, and as such complex mixtures of inclusions, especially of different types, are not covered by the theory.

The general theory applicable to the multiphase coherent mixture was first developed by Khachaturyan and Shatalov [52, 53] and described in detail by Khachaturyan [54]. The solution is obtained under the assumption of uniform elastic moduli; however, it is perfectly general with respect to the number of phases in the mixture, the shapes of the inclusions and the elastic properties of the medium. A variation of the theory to address the case of inhomogeneous elastic moduli was described by Khachaturyan, Semenovskaya and Tsakalakos [55].

Khachaturyan's theory presents a Fourier-space solution for a mechanical equilibrium problem and can be easily integrated into the energy functional for diffuse interface models. Phase field models almost exclusively use the theory, so in the next two sections the formalism is presented in detail.

### **2.1.8.1. Khachaturyan's microelasticity theory**

Khachaturyan's original treatment as summarised in [54] follows the logic proposed by Eshelby and identifies imaginary steps of structural transformation. In the first step regions of the material are "removed" from the matrix and allowed to undergo a stress-free homogeneous transformation. In the second step new phase inclusions are brought back to the original shape. This stage introduces the elastic self energy of the constrained transformation. Finally, the system is allowed to relax, with inhomogeneous strains established throughout the system to remove the internal stress gradients.

A solution for the elastic problem was proved to be possible in the homogeneous modulus approximation, by representing the strain as a sum of homogeneous and inhomogeneous parts. The original solution was also obtained under assumption of vanishing external forces at the system boundaries, which allowed the finding of a particularly simple form of the homogeneous part of strain. Recent developments [55] saw the theory extended to a more general form, to include the systems under various boundary conditions (constant external strain or stress) and

also to elastically inhomogeneous systems. In the following section the most general formulation of the theory is presented and the types of boundary conditions that usually occur are discussed.

In most general terms the goal is to find a solution to the equation of mechanical equilibrium for a given spatial distribution of coherent inclusions described by the transformation (stress-free) strain when the system is under specified boundary conditions. Both matrix and inclusions are described by the same set of elastic constants  $C_{ijkl}$ .

Mechanical equilibrium is described by the equation

$$\frac{\partial \sigma_{ij}(\vec{r})}{\partial \vec{r}} = 0 \quad (2.19)$$

where  $\sigma_{ij}(\vec{r})$  is the stress at the point with radius vector  $\vec{r}$  in a selected coordinate system. Elastic stress is related to the elastic strain  $\varepsilon_{kl}^{el}(\vec{r})$  by the constitutive equation

$$\sigma_{ij}(\vec{r}) = C_{ijkl} \varepsilon_{kl}^{el}(\vec{r}) \quad (2.20)$$

In equation (2.20) and later throughout the text, unless specified otherwise, Einstein's tensor notation is used with summations carried out over repeated indices.

The local elastic strain  $\varepsilon_{kl}^{el}(\vec{r})$  is the difference between the total strain and the stress-free transformation strain:

$$\varepsilon_{kl}^{el}(\vec{r}) = \varepsilon_{ij}(\vec{r}) - \varepsilon_{kl}^T(\vec{r}) \quad (2.21)$$

In terms of the displacement vector  $\vec{u}$ , defined with respect to the matrix phase, the total strain can be expressed as

$$\varepsilon_{ij}(\vec{r}) = \frac{1}{2} \left( \frac{\partial u_i(\vec{r})}{\partial r_j} + \frac{\partial u_j(\vec{r})}{\partial r_i} \right) \quad (2.22)$$

Applying equations (2.20) - (2.22) to the mechanical equilibrium equation (2.19) one gets

$$\frac{1}{2} \frac{\partial}{\partial r_j} C_{ijkl} \left( \frac{\partial u_k(\vec{r})}{\partial r_l} + \frac{\partial u_l(\vec{r})}{\partial r_k} \right) = \frac{\partial}{\partial r_j} C_{ijkl} \varepsilon_{kl}^T(\vec{r}) \quad (2.23)$$

Equation (2.23) is a second-order partial differential equation in real space, and has a Fourier space analogue which is a simple algebraic equation. However, to ensure this, the argument of the Fourier transform must satisfy certain conditions imposed by the existence of the transform itself, namely it should be an analytical function vanishing at the boundaries of the system. Generally this condition is not satisfied for a displacement vector  $\vec{u}$ , but the problem can be overcome by separating the total strain into homogeneous and heterogeneous components:

$$\varepsilon_{ij}(\vec{r}) = \overline{\varepsilon_{ij}} + \delta\varepsilon_{ij}(\vec{r}) \quad (2.24)$$

with a homogeneous part  $\overline{\varepsilon_{ij}}$  uniform everywhere in the system and an inhomogeneous part  $\delta\varepsilon_{ij}(\vec{r})$  that vanishes on the macroscopic level:

$$\int \delta\varepsilon_{ij}(\vec{r})d^3r = 0 \quad (2.25)$$

By the very definition of the inhomogeneous part of the total strain it does not affect the dimensions of the system, thus the displacements  $\delta u(\vec{r})$  that corresponds to the  $\delta\varepsilon_{ij}(\vec{r})$  should vanish at the external boundary. This fact is sufficient to guarantee the existence of the Fourier counterpart of the equation (2.23) when applied only to inhomogeneous displacement:

$$C_{ijkl} \frac{\partial^2 \delta u_j(\vec{r})}{\partial r_k \partial r_l} = \frac{\partial}{\partial r_j} C_{ijkl} \varepsilon_{kl}^T(\vec{r}) \quad (2.26)$$

The transformation strain in its most general form is a sum over all different types of inclusions present in the system. It may be described as

$$\varepsilon_{kl}^T(\vec{r}) = \sum_p \varepsilon_{kl}^T(p) \Theta_p(\vec{r}) \quad (2.27)$$

In this equation  $\varepsilon_{kl}^T(p)$  is a homogeneous stress-free transformation strain that converts a lattice from matrix into type- $p$  inclusion,  $\Theta_p(\vec{r})$  is a shape function, equal to unity inside a type- $p$  inclusion and zero elsewhere.

In the inverse (Fourier) space equation (2.26) can be solved to obtain

$$\{\delta u_i\}_g = -i \Omega_{ij}(\vec{n}) \sum_p \sigma_{jk}^T(p) g_k \{\Delta \Theta_p(\vec{r})\}_g \quad (2.28)$$

where  $\vec{g}$  is a reciprocal space vector and  $\vec{n} = \vec{g}/|\vec{g}|$  is its corresponding unit vector;  $\Delta\Theta_p(\vec{r}) = (\Theta_p(\vec{r}) - w_p)$  is an adjusted shape function ( $w_p$  is the volume fraction of type- $p$  inclusion);  $\sigma_{ij}^T(p) = C_{ijkl}\varepsilon_{kl}^T(p)$  is a constrained transformation stress;  $\Omega_{jk}(\vec{n})$  is the inverse of  $\Omega_{jk}^{-1}(\vec{n}) = n_i C_{ijkl} n_l$  and the Fourier transforms are expressed as  $\{f\}_g = \int f(\vec{r}) \exp(-i\vec{g}\vec{r}) d^3r$ .

Substitution of the solution (2.28) into (2.24) gives the total strain and finally by the application of (2.21) the elastic strain in the system. At this point the total elastic energy of the system may be found:

$$\begin{aligned}
E_{el} &= \int C_{ijkl} \varepsilon_{ij}^{el}(\vec{r}) \varepsilon_{kl}^{el}(\vec{r}) d^3r = \\
&= \frac{V}{2} C_{ijkl} \overline{\varepsilon_{ij}} \overline{\varepsilon_{kl}} - \overline{\varepsilon_{ij}} \int C_{ijkl} \sum_p \varepsilon_{kl}^T(p) \Theta_p(\vec{r}) d^3r \\
&+ \frac{1}{2} \int C_{ijkl} \sum_p \varepsilon_{ij}^T(p) \Theta_p(\vec{r}) \sum_q \varepsilon_{kl}^T(q) \Theta_q(\vec{r}) d^3r \\
&- \frac{1}{2} \sum_p \sum_q \int_{P.V.} n_i \sigma_{ij}^T(p) \Omega_{jk}(\vec{n}) \sigma_{kl}^T(q) n_l \{\Theta_p(\vec{r})\} \{\Theta_q(\vec{r})\}^* \frac{d^3g}{(2\pi)^3}
\end{aligned} \tag{2.29}$$

The integral in the last term is a Cauchy principal value, meaning that the integration excludes the small region of volume  $2\pi/V$  in the vicinity of the origin of inverse space at  $\vec{g} = 0$ . In the expression for the total energy above one can identify physically distinct contributions from the energy of: macroscopic external loading in the first term, coupling between the macroscopic and local eigenstrains in the second term, self energy of the transformation from the matrix to the inclusion lattice in the third term and finally the configurational energy term, which depends on the spatial distribution of inclusions.

The macroscopic strain  $\overline{\varepsilon_{ij}}$  is defined according to the boundary conditions to which the system is subjected. Strain or stress may be specified on the external boundary of the system and modify the form of total energy equation according to these conditions [56, 57].

In the case of strain controlled conditions one defines explicitly the strain at the boundaries (macroscopic shape change of the system). One example of such conditions is a free external surface or relaxed boundary condition with zero external normal forces. The homogeneous strain is easily defined from the mechanical equilibrium stress-free conditions as the volume average of transformation strain:

$$\overline{\varepsilon}_{ij} = \frac{1}{V} \int d^3r \sum_p \varepsilon_{ij}^T(p) \Theta_p(\vec{r}) \quad (2.30)$$

In this case the equation for total energy simplifies to

$$E_{el} = \frac{1}{2} \sum_p \sum_q \int B'_{pq}(\vec{n}) \{\Theta_p(\vec{r})\} \{\Theta_q(\vec{r})\}^* \frac{d^3g}{(2\pi)^3} \quad (2.31)$$

with

$$B'_{pq}(\vec{n}) = \begin{cases} 0 & , \text{if } \vec{g} \in \frac{2\pi}{V} \Big|_{\vec{g}=0} \\ C_{ijkl} \varepsilon_{ij}^T(p) \varepsilon_{kl}^T(q) - n_i \sigma_{ij}^T(p) \Omega_{jk}(\vec{n}) \sigma_{kl}^T(q) n_l & , \text{if } \vec{g} \notin \frac{2\pi}{V} \Big|_{\vec{g}=0} \end{cases} \quad (2.32)$$

Another special case is a rigidly constrained system with  $\overline{\varepsilon}_{ij} = 0$ . The total energy is again expressed by equation (2.31), but with a different matrix  $B'_{pq}(\vec{n})$ :

$$B'_{pq}(\vec{n}) = \begin{cases} C_{ijkl} \varepsilon_{ij}^T(p) \varepsilon_{kl}^T(q) & , \text{if } \vec{g} \in \frac{2\pi}{V} \Big|_{\vec{g}=0} \\ C_{ijkl} \varepsilon_{ij}^T(p) \varepsilon_{kl}^T(q) - n_i \sigma_{ij}^T(p) \Omega_{jk}(\vec{n}) \sigma_{kl}^T(q) n_l & , \text{if } \vec{g} \notin \frac{2\pi}{V} \Big|_{\vec{g}=0} \end{cases} \quad (2.33)$$

It is also possible to specify external forces for stress-controlled boundary conditions. Assume that applied stress is introduced as  $\sigma_{ij}^{appl}$ . The macroscopic strain would then be

$$\overline{\varepsilon}_{ij} = S_{ijkl} \sigma_{kl}^{appl} + \frac{1}{V} \int d^3r \sum_p \varepsilon_{ij}^T(p) \Theta_p(\vec{r}) \quad (2.34)$$

where  $S_{ijkl} = C_{ijkl}^{-1}$  is a compliance tensor. Substituting (2.34) into the energy equation (2.29) an expression for the elastic energy of the system under applied stress may be obtained in the following form:

$$\begin{aligned}
E_{el} = & \frac{V}{2} S_{ijkl} \sigma_{ij}^{appl} \sigma_{kl}^{appl} \\
& - \frac{1}{2V} C_{ijkl} \int d^3r \sum_p \varepsilon_{ij}^T(p) \Theta_p(\vec{r}) \int d^3r' \sum_p \varepsilon_{kl}^T(p) \Theta_p(\vec{r}') \\
& + \frac{1}{2} \int C_{ijkl} \sum_p \varepsilon_{ij}^T(p) \Theta_p(\vec{r}) \sum_q \varepsilon_{kl}^T(q) \Theta_q(\vec{r}) d^3r \\
& - \frac{1}{2} \sum_p \sum_q \int_{P.V.} n_i \sigma_{ij}^T(p) \Omega_{jk}(\vec{n}) \sigma_{kl}^T(q) n_l \{ \Theta_p(\vec{r}) \} \{ \Theta_q(\vec{r}) \}^* \frac{d^3g}{(2\pi)^3}
\end{aligned} \tag{2.35}$$

It is also possible to modify the theory to describe elastically inhomogeneous systems, with different elastic constants  $C_{ijkl}$  for a matrix and inclusions. This has been done for example in [58] by recognising an elastically homogeneous system that is equivalent to the inhomogeneous system in terms of the stress in a state of mechanical equilibrium.

Depending on the type of boundary conditions, either Helmholtz (strain-controlled boundary conditions) or Gibbs free energy (stress-controlled boundary conditions) becomes a governing potential for the minimisation of the system's energy. Khachaturyan's solutions provide an explicit form of elastic energy terms of such potentials, as  $E_{el}$  given by equation (2.31) for strain controlled conditions and  $(E_{el} - V \sigma_{ij}^{appl} \overline{\varepsilon_{ij}})$  described by (2.34) and (2.35) for the stress-controlled conditions.

Khachaturyan's theory provides a powerful and flexible formalism for an analysis of various elastic problems. Its generality and ability to treat simultaneously different types of elastic defects makes it extremely attractive for application to mesoscopic microstructure simulations. This application will be later described in the chapter 5 "Phase field model".

### 2.1.8.2. Energy of nucleus-microstructure elastic interaction

One of the important applications of Khachaturyan's theory is the ability to calculate in a simple and efficient way the volumetric interaction energy between an arbitrary microstructure and a nucleus that forms in a system.

The solution to this problem was developed by Shen et al. [59] and is based on the expression for the total elastic energy of a coherent multiphase system (2.31). Let the microstructure before the nucleation event be described by the set of shape functions  $\Theta_i$  and after nucleation by the modified set  $\Theta_i = \Delta\Theta_i$ . The change in total elastic energy may be expressed as:

$$\begin{aligned}\Delta E_{el} &= \Delta E^{int} + \Delta E^{self} = \\ &= \sum_p \sum_q \int B'_{pq}(\vec{n}) \{\Theta_p(\vec{r})\} \{\Delta\Theta_q(\vec{r})\}^* \frac{d^3g}{(2\pi)^3} \\ &+ \frac{1}{2} \sum_p \sum_q \int B'_{pq}(\vec{n}) \{\Delta\Theta_p(\vec{r})\} \{\Delta\Theta_q(\vec{r})\}^* \frac{d^3g}{(2\pi)^3}\end{aligned}\quad (2.36)$$

The first term in (2.36) represents the interaction energy, which under assumptions of central symmetry of the nucleus shape and of constant stress field in the matrix at the location  $\vec{R}$  of the nucleus of type- $l$  simplifies to:

$$\Delta E_l^{int} = V_0 \sum_p \int B'_{pl}(\vec{n}) \{\Theta_p\} e^{i\vec{g}\vec{R}} \frac{d^3g}{(2\pi)^3}\quad (2.37)$$

It is obvious that expression (2.37) depends only on the pre-existing microstructure described by the set of shape functions  $\Theta_p$  and the volume of the nucleus, making it possible to represent the interaction energy in a volumetric form as the interaction energy density via the following backward Fourier transform:

$$\frac{\Delta E_l^{int}}{V_0} = \sum_p \{B'_{pl}(\vec{n}) \{\Theta_p\}\}\quad (2.38)$$

This solution allows one to include the interaction energy density directly into the driving force for the nucleation and estimate the local, strain modified nucleation rate in a system containing a distribution of coherent precipitates.

## 2.2. Classification of solid state transformations

Solid-solid phase transformations have been traditionally classified into two broad classes [13], with the distinction based on the type of growth exhibited by the product phase – thermally activated or athermal growth.

The first class encompasses those transformations where the product differs from the matrix in composition and/or structure and its growth requires thermal activation, with atoms crossing the interface one by one during diffusive jumps. These transformations can be interface controlled or restricted by the long-range atom transport. The term “diffusional transformations” is also a widely used term for this class.

Athermal transformations on the other hand imply that the growth of the product phase does not require thermal activation and proceeds relatively easily and rapidly, even at low temperatures and with interface velocities approaching the speed of sound in the material. The growth happens through the migration of coherent or semicoherent glissile interfaces, which move conservatively. Atoms cross the interface in co-ordinated, “military” fashion, and there is a lattice correspondence (a unique relationship between planes, vectors and unit cells of the two structures) maintained between parent and product phases. These transformations are also known as “displacive”, martensitic or shear transformations.

The traditional view of such a classification was that these two groups are largely mutually exclusive, because long-range diffusion and random atomic interchange between phases would cancel any shape strain and lattice correspondence characteristic of displacive transformations.

However, in recent decades experimental evidence in a variety of systems proved that the “diffusional-vs.-displacive” classification of solid-solid transformations is not universal. A range of products was proven to exhibit not only important characteristics of displacive transformations, for instance the shape change in the transformed volume and the identifiable lattice correspondence, but also significant composition difference with the matrix. Some of the notable examples are presented by Muddle et al. in [60] and include  $\text{Ag}_2\text{Al}$   $\gamma'$  precipitates in Al-Ag, ordered AuCu II plates in disordered equiatomic Au-Cu alloys and metastable  $9R$   $\alpha_1$  plates in ordered Cu-Zn and Ag-Cd alloys. It was demonstrated that these precipitates produce surface relief consistent with invariant plain strain shape change and that a lattice correspondence may be identified between parent and product phases, making it possible to apply a phenomenological theory of martensite crystallography to these diffusional transformations.

Such shortcomings of the traditional classification became a focus of extended discussion during the 1992 “Pacific Rim Conference on the Roles of Shear and Diffusion in the Formation of Plate-Shaped Transformation Products” [61, 62]. It has been suggested that diffusional-displacive transformations should be recognised in their own right.

Christian [63] illustrated that maintenance of lattice correspondence between matrix and product is not necessarily destroyed by long-range diffusion, provided that no lattice sites are created or destroyed in the interface migration. Consequently, a transformation with significant composition change may still maintain a lattice correspondence and exhibit the features of displacive transformations.

Subsequently phenomenological theory of martensite crystallography (PTMC) has been applied to several more diffusional plate-shaped products. Nie and Muddle [64, 65] demonstrated the application of PTMC and identified lattice correspondence for  $\text{Al}_2\text{Cu}$   $\theta'$  in Al-Cu,  $\Omega$  phase in microalloyed (Mg and Ag) Al-Cu and  $T_1$  phase in Al-Cu-Li. In all these systems the common feature of the identified lattice correspondence was a significant ( $\sim 0.18$ - $0.35$ ) shear component accompanying the transformation. It was assumed that accommodation of the strain energy associated with this shear plays a major role in controlling the nucleation and growth of such precipitates.

Because of the technological importance of rationally-oriented coherent plate or lath shaped precipitates for the strengthening of engineering light alloys, the understanding of the mechanism of transformation is crucial for the control of precipitation and alloy design.

In the course of the present work the focus is concentrated on one such precipitate in the relatively well studied model system –  $\theta'$  in Al-Cu. In the next section the properties of this system will be discussed in detail, along with some other examples of diffusional-displacive plate-shaped precipitates. In the final part of this review the scope of the thesis will be outlined.

### 2.3. Model system – $\theta'$ phase in Al-Cu

Al-Cu has been selected as a primary model system for the study of the transformation mechanism and autocatalytic nucleation of metastable  $\theta'$ . The formation of this intermediate precipitate is a classical example of a transformation that proceeds via heterogeneous nucleation and growth of platelike particles. There is a significant technological interest in such precipitates in age-hardenable alloys, because coherent inclusions of high aspect ratio of thickness to length are very effective for the strengthening. Al-Cu system with  $\theta'$  as a primary strengthening constituent is a basis of the 2xxx series of commercial, heat-treatable alloys.

Fig. 8 shows the aluminium-rich end of the Al-Cu phase diagram with approximate solvus lines of various intermediate precipitates. For low ageing temperatures (below  $\theta''$  solvus) precipitation follows the well documented sequence [66, 67]:

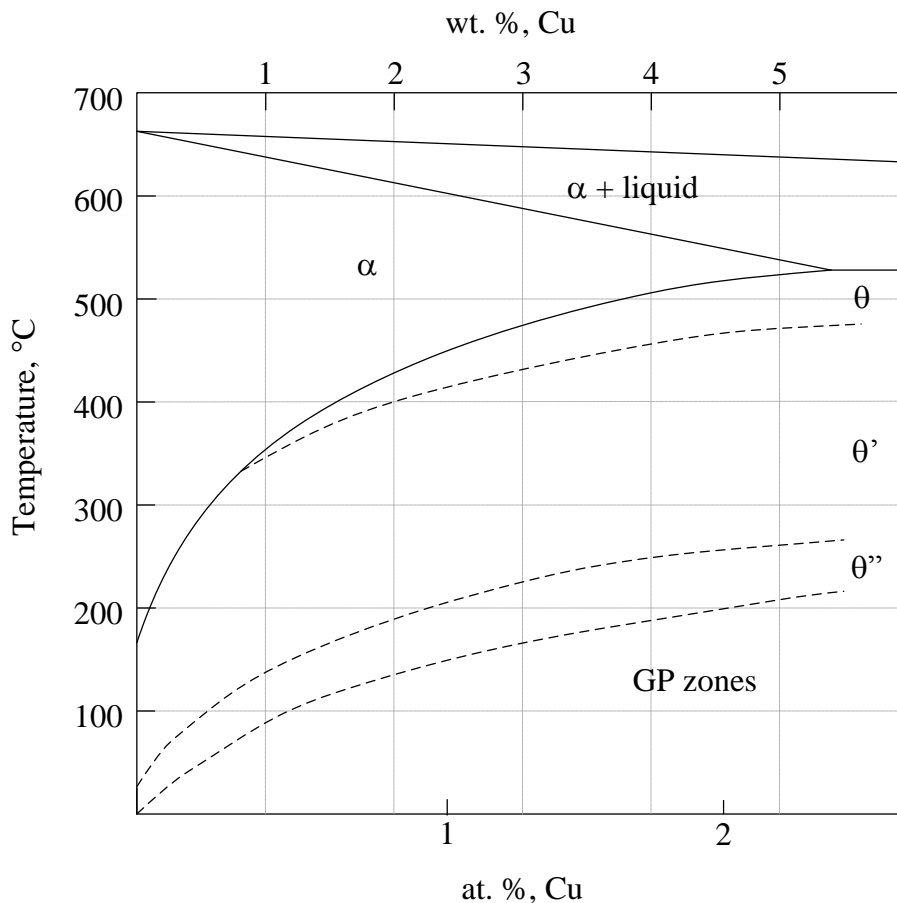
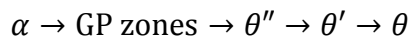


Fig. 8 Aluminium-rich section of the Al-Cu phase diagram, adapted from Lorimer [68].

With the temperature of ageing above 190 - 220°C for 2 - 4 wt. % Cu alloys  $\theta'$  precipitates directly from solid solution. The structure of the unit cell was studied by Preston [69], Guinier [70] and Silcock et al. [71, 72] and found to be a distorted  $\text{CaF}_2$  structure, which is tetragonal with  $a=b=4.04 \text{ \AA}$  and  $c=5.8 \text{ \AA}$ . Alternatively the structure may be considered as body centred tetragonal with respect to Cu atoms, having 2 Al atoms in side faces. The composition of the phase is approximately  $\text{Al}_2\text{Cu}$  and the structure is shown in Fig. 9.

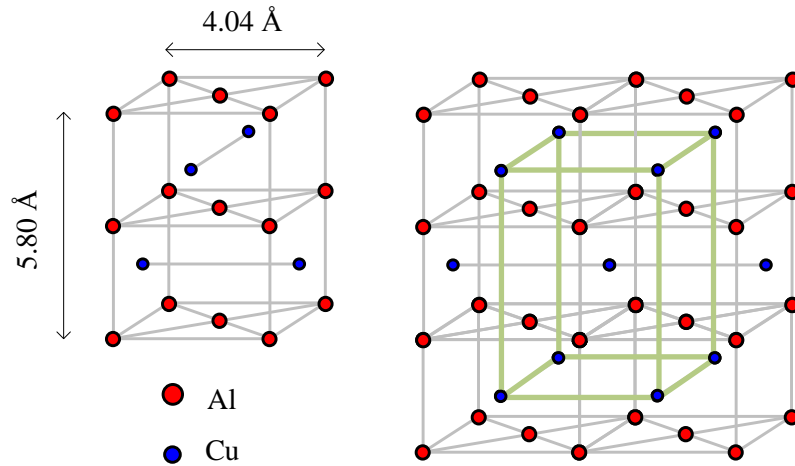


Fig. 9  $\theta'$  structure, after Silcock et al. [71].

Plates of  $\theta'$  form parallel to the  $\{100\}_\alpha$  planes of the fcc matrix with nearly full coherence of the broad plate faces. The edges of the  $\theta'$  plates are usually considered to be incoherent [33] and a suggested precipitate thickening/thinning mechanism is by the propagation of ledges [73]. Dissolution ledges are reported to contain misfit dislocations with Burgers vector  $a[001]$  perpendicular to the habit plane and their height varies somewhere between 1.5 and 6.5 nm (Laird and Aaronson [74, 75], Weatherly and Sargent [76]). Thinner ledges are observed for growth by Stobbs and Purdy [77] and Bouazra and Reynaud [78]. Depending on the thickness of plates, moderate tetragonal misfit is maintained between the matrix and product, usually between -4.3% and +7.7%.

Intragranular nucleation of  $\theta'$  is heterogeneous and a number of studies suggested that precipitation is facilitated by defects. Preferential nucleation of  $\theta'$  on various defects, for instance on edge sections of helical dislocation, in slip bands, on dislocation loops and near sub-boundaries has been reported by Thomas and Whelan [79], Nicholson et al. [80, 81]. Precipitation of selected variants was also observed in cold-worked alloys near slip planes by Silcock [82]. Selective precipitation of the particular variants was also observed by Hosford and Agrawal [83] under the influence of applied stress. The mechanisms proposed to explain this

association are mostly based on accommodation of the strain energy arising from tetragonal misfit between  $\theta'$  and the matrix.

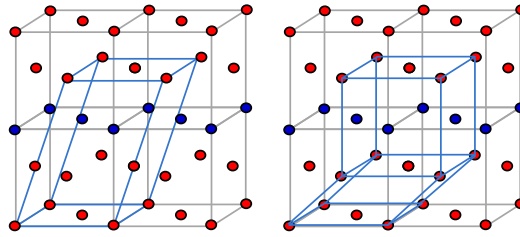
Precipitation of  $\theta'$  is also affected by microalloying additions. Trace amounts of In, Sn or Cd increases the number density of  $\theta'$ , and if the ageing temperature allows formation of other intermediate products (GP zones,  $\theta''$ ) their formation is suppressed [84, 85]. Plates of  $\theta'$  appear with a larger number density and in association with precipitates or clusters of microalloying additions (see Gao et al. [86], Bourgeois et al. [87]). The mechanism for enhanced precipitation number density is not clear; however, it has been suggested by Muddle that the “vacancy-trace element” co-clusters may be a very effective catalyst due to the potential relief of shear strain if such strain is involved in the transformation mechanism [65, 88, 89].

Several authors have proposed to consider  $\theta'$  as an example of diffusional-displacive products, discussed in the previous section. Based on the experimental observations of Stobbs and Purdy [77] who reported that the thickness of  $\theta'$  plates follows a well defined sequence of discrete number of half-unit cells with corresponding sign of elastic stress between matrix and product, Dahmen and Westmacott [90] suggested an elegant model based on the simple lattice correspondence of  $\theta'$  and  $\alpha$ -Al. Their explanation of the observed thicknesses is based on the principle of minimisation of both dilatational stress associated with the tetragonal misfit and the self-accommodation of the large shear strain component of the transformation strain. The authors identified two basic building blocks of the transformation: the conservative mechanism, based on the shear of the 1.5  $\alpha$ -Al unit cell by the  $a/2 \langle 100 \rangle$  vector with the further shuffle of Cu atoms; and the non-conservative mechanism that involves the similar shear of the half-unit cell of  $\alpha$ -Al and the external diffusion of Cu. The process is illustrated schematically in Fig. 10 and Fig. 11. The authors suggested that nucleation of ledges combine building blocks so that the shear is self-accommodated and the total dilatational strain is minimised. A similar lattice correspondence is also considered by Nie and Muddle [64, 65] along with other examples of plate-shaped diffusional-displacive products.

Precipitation of  $\theta'$  is also reportedly occurs in autocatalytic fashion [77, 91, 92] when precipitates are observed in close groups or arrays, seemingly without any association with dislocation or any other defects. It has been suggested that a tetragonal misfit is responsible for the strong long-range elastic interactions between the precipitate plates, and once an initial  $\theta'$  plate has nucleated it may stimulate formation of subsequent plates in its surroundings. The process has been analysed assuming tetragonal transformation strain. Results and extensions of this approach would be discussed later in relevant chapters.

Conservative mechanism - produces single unit cell of  $\theta'$

Lattice correspondence:



Transformation sequence -

- 1) Shear of a skewed cell by the vector  $a/2\langle 100 \rangle$  into rectangular cell (equivalent to the passage of a corresponding dislocation)
- 2) Shuffles of Cu atoms within the rectangular cell to produce bct structure of  $\theta'$

NB: Number of atomic sites is conserved within the cell

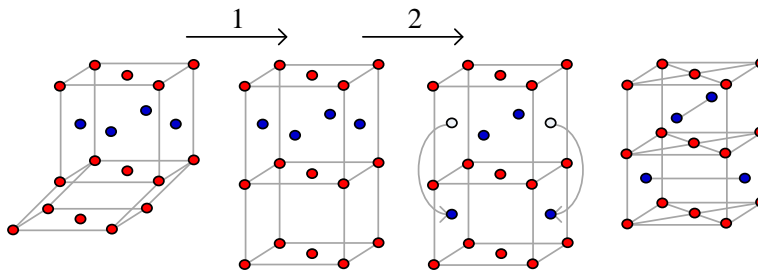
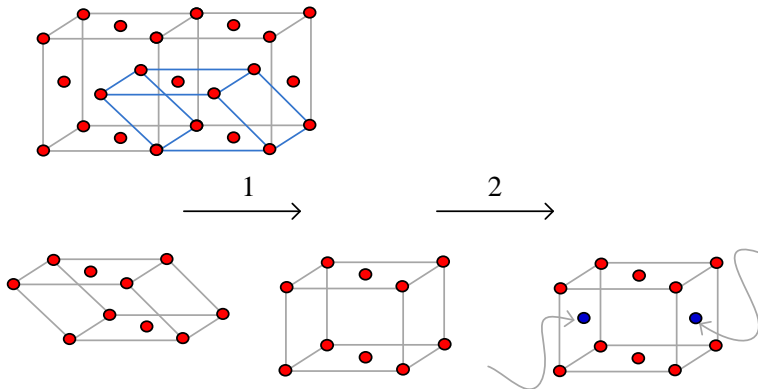


Fig. 10 Conservative building block of the Dahmen-Westmacott [90] model for  $\theta'$  transformation mechanism.

Non-conservative mechanism - produces half-unit cell of  $\theta'$



- 1) Skewed cell is sheared by the vector  $a/2\langle 100 \rangle$
- 2) Cell is expanded by adding Cu atoms to complete  $\theta'$  bct structure

NB: Number of atomic sites is not conserved. Diffusion of Cu from fcc lattice is required.

Fig. 11 Non-conservative building block of the Dahmen-Westmacott model.

## 2.4. Research direction and questions

As discussed above, there is still little clarity in the exact atomic mechanism of many important phase transformations of mixed diffusional-displacive character. Although in a broad sense many such system as Al-Cu are well studied with the precipitate structure, kinetics of transformation and association with defects documented, some doubt still remains about the nature of this association. On a deeper level this doubt reflects the need for better understanding of the transformation mechanism.

Existence of shear in the transformation strain of many platelike products ( $\theta'$ ,  $\gamma'$ ,  $T_1$  and others) still needs to be confirmed. In the present work the autocatalytic mode of nucleation has been selected as an interesting and relatively little studied example of a strain-dependent, dynamic heterogeneous nucleation process. An attempt is made to develop a mesoscopic model that takes into account a general type of transformation strain (including shear component) and estimate how the type of strain affects the microstructure patterns that develop in autocatalytic mode.



### 3. Magnitude of the activation barriers for platelike precipitates

As discussed before, there is a range of solid state systems where the strength is primarily defined by the fine distribution of rationally-oriented plate or lath-shaped precipitates of high aspect ratio. It has been demonstrated [60, 64] that for such precipitates it is possible to identify a lattice correspondence with a significant shear component in the transformation strain. It is assumed that accommodation of the shear strain energy strongly affects nucleation and microstructure evolution.

In this chapter the standard expressions of classical nucleation theory are used to estimate quantitatively (based on the data available for selected systems) the effect of the shear component of the transformation strain on the magnitude of the nucleation barrier and the shape of a critical nucleus. The calculations presented are carried out for the  $\text{Ag}_2\text{Al}$   $\gamma/\gamma'$  in Al-Ag and  $\text{Al}_2\text{Cu}$   $\theta'$  in Al-Cu alloys.

The intention of the case studies presented below is to illustrate that shear strain energy should be recognised as a part of the activation barrier in the formation of coherent plate-shaped precipitates.

#### 3.1. Method for finding critical parameters of platelike inclusions

The rate of nucleation, as shown in the chapter 2 “Precipitation in solids”, is controlled by several factors, the strongest of which is the magnitude of the activation barrier associated with the formation of a critical nucleus. This energy is related to the concentration of critical nuclei by an exponential Boltzmann type distribution and as such becomes the most critical term affecting overall kinetics of transformation.

The problem of calculating critical parameters is that of finding extrema in the Gibbs free energy change of the system, considering this change as a function of the nucleus size and shape. The saddle point in the free energy change profile represents the critical configuration.

Consider a platelike nucleus of arbitrary shape. Let it have broad parallel faces with interfacial energy  $\gamma_h$  and edges with interfacial energy  $\gamma_e$ . The geometry of the nucleus can be described by the characteristic linear parameter  $l$ , which may represent the diameter of a circular disc or the side length of a square plate, and the shape coefficients  $K_p$  and  $K_s$ . These coefficients describe the shape by relating the perimeter of a plate and the surface area of its broad face to the

linear dimension  $l$  as  $P = K_p l$  and  $S = K_s l^2$  respectively. For a square plate  $K_p = 4$  and  $K_s = 1$ , for a circular disc  $K_p = \pi$  and  $K_s = \pi/4$ . The aspect ratio of the plate is defined as the ratio of the thickness  $t$  to the linear dimension  $\alpha = t/l$ .

The change in the Gibbs free energy associated with formation of such a nucleus is composed of the reduction due to the change in the chemical free energy per unit volume of the inclusion and the positive contributions of the strain energy and the energy of the interface created between the parent and product phases:

$$\Delta G = [-\Delta G_V + W(\alpha)]V + 2S\gamma_h + Pt\gamma_e \quad (3.1)$$

where  $\Delta G_V$  is the chemical driving force (chemical free energy reduction per unit volume),  $W(\alpha)$  is the strain energy as a function of the inclusion shape and the surface energy is given as a sum of the energies for the broad faces and edges of the plate. Substitution of the volume, surface area and perimeter by the linear dimension and aspect ratio gives

$$\Delta G = [-\Delta G_V + W(\alpha)]K_s \alpha l^3 + 2K_s l^2 \gamma_h + K_p \alpha l^2 \gamma_e \quad (3.2)$$

The critical configuration is a solution for the system of equations of the form

$$\begin{cases} \left. \frac{\partial \Delta G}{\partial \alpha} \right|_l = 0 \\ \left. \frac{\partial \Delta G}{\partial l} \right|_\alpha = 0 \end{cases} \quad (3.3)$$

The second equation in the system (3.3) results in the expression for critical size

$$l^* = \frac{2}{3} \frac{2K_s \gamma_h + K_p \alpha^* \gamma_e}{K_s \alpha^* [\Delta G_V - W(\alpha^*)]} \quad (3.4)$$

which can be substituted into the first equation of (3.3) to get the shape of a critical nucleus. If the functional dependence of strain energy on the shape parameter is known the solution can be obtained analytically.

In the limit of vanishing elastic energy density, when  $W(\alpha) \rightarrow 0$ , or for the case when the strain energy density is independent of the shape and its only effect is to offset the chemical driving force, equations (3.3) - (3.4) can be simplified to give the set of equations (3.5):

$$\begin{cases} \alpha^* = \frac{4K_s \gamma_h}{K_p \gamma_e} \\ l^* = \frac{K_p \gamma_e}{K_s \Delta G_V} \\ \Delta G^* = 2 \frac{K_p^2}{K_s} \frac{\alpha^* \gamma_e^3}{\Delta G_V^2} \end{cases} \xrightarrow{\text{disc or cuboid}} \begin{cases} \alpha^* = \frac{\gamma_h}{\gamma_e} \\ l^* = 4 \frac{\gamma_e}{\Delta G_V} \\ \Delta G_{disc}^* = 8\pi \frac{\alpha^* \gamma_e^3}{\Delta G_V^2}; \quad \Delta G_{cuboid}^* = 32 \frac{\alpha^* \gamma_e^3}{\Delta G_V^2} \end{cases} \quad (3.5)$$

For the coherent precipitate the influence of the strain energy would be to alter the critical nucleus shape towards the one that minimises the strain energy. Analysis of the strain influence on diffusional nucleation was carried out by Lee and Johnson [93] and is based on their earlier treatment of coherency strains for ellipsoidal precipitates [45]. It is demonstrated that the effect of strain on the shape of the critical nucleus is relatively weak. Only for strain energy densities exceeding at least 75% of the chemical driving force does the deviation of the shape from the one controlled by the interfacial energy minimum start to be noticeable. However, the effect on the magnitude of the nucleation barrier is quite profound.

Based on this relative insensitivity of the critical shape to the magnitude of strain energy, one way to treat the influence of the coherency strain is to ignore its effect on the critical nucleus shape. In this case the elastic energy density may be calculated for the equilibrium shape that is yielded by the interfacial energy anisotropy and accounted for in the modified chemical driving force. This approach was taken by Shiflet et al. [94] and leads to results identical to those in (3.5).

However, in the case of transformation strain with significant shear component ( $\sim 0.3$ ) this simplification is not easily justified. Instead, the Eshelby's solution [40] for the elastic energy of a thin ellipsoid constrained by the isotropic matrix is included into (3.3) - (3.4). Although this solution is only valid for the specific form of inclusion ( $\theta'$  or  $\gamma/\gamma'$  plates have planar broad interfaces and would be better represented by parallelepipeds), it is nonetheless a good approximation. Parallelepiped or disc plates with sharp edges can be expected to yield coherency strains higher than ellipsoids, but on the other hand excess vacancies may partially relieve the strains, as argued by Russel [18].

Thus, following Eshelby, the strain energy is divided into the components  $W_\tau$  and  $W_\xi$ , which arise respectively from the shear and non-shear parts of the transformation strain. If the stress-free transformation strain consists of a uniaxial expansion  $\xi$  normal to the habit plane and a shear  $\tau$ , parallel to the habit plane then expressions for the strain energy per unit volume of ellipsoid are:

$$W_{\tau} = \frac{\pi}{8} \frac{(2 - \nu)}{(1 - \nu)} \mu \alpha \tau^2 \quad (3.6)$$

$$W_{\xi} = \frac{\pi}{4(1 - \nu)} \mu \alpha \xi^2 \quad (3.7)$$

where  $\mu$  is the shear modulus and  $\nu$  is the Poisson's ratio,  $\alpha$  is the ellipsoid's aspect ratio. The total strain energy per unit volume of precipitate is  $W(\alpha) = W_{\tau}(\alpha) + W_{\xi}(\alpha)$  is substituted into expressions (3.3) - (3.4). An analytical solution for the critical nucleus parameters can be obtained, but lengthy expressions are omitted here for the sake of simplicity.

The data available on the interfacial energies and chemical driving forces are presented next and followed by results of the calculations of critical nucleus parameters in Al-Cu and Al-Ag systems.

### 3.2. Interfacial energy estimates

In the expressions above for the critical parameters the magnitude of the interfacial energy between the nucleus and the matrix is the most significant variable. Unfortunately at the same time it remains the one known with the least confidence. This is because of the difficulty of unambiguous direct measurements and theoretical estimates.

Directly measured values available for Al-alloys are based on isothermal calorimetry measurements of heat evolution during the coarsening stage of precipitation. The heat produced is then normalised by the change in the interfacial area, obtained from transmission electron metallography. The value measured in such experiments by Boyd and Nicholson [95] for  $\theta'$  is  $1.53 \text{ J/m}^2$ . The decomposition of this averaged interfacial energy into the energies of the broad habit plane and that of the semicoherent edges based on the observed aspect ratio (diameter-to-thickness of  $\sim 45$ ) gives  $0.51 \text{ J/m}^2$  for the habit plane and  $21.5 \text{ J/m}^2$  for the edges. It is recognised by the authors that these results are very high compared to those predicted by theory.

Theoretical estimates in their simplest form take their origin from the works of Becker [9] and Turnbull [34]. The chemical contribution to the interfacial energy in this approach is obtained from the energies of the nearest neighbour interatomic bonds that were broken and replaced in the process of creating the interface. The structural contribution to the energy arises

due to the energy of coherency dislocations. A detailed analysis by this approach was given by Aaronson, Clark and Laird in [35] who considered both fully coherent habit plane interfaces in  $\theta'$  Al-Cu and semicoherent dislocation boundaries of  $\gamma$  plates in Al-Ag. They predicted the energies of  $40 \text{ mJ/m}^2$  for coherent  $\theta'$  interfaces and  $175 \text{ mJ/m}^2$  for dislocation-based interfaces of  $\gamma$  particles. It has also been suggested that these values need to be scaled down by 20-25% on the basis of the comparison between estimated and measured energies of disordered boundaries in corresponding alloys.

In the last decade a new class of estimates has emerged, based on the application of ab initio density functional theory (DFT) calculations. Results of such calculations are currently limited to the 0 K values, due to the inherent complexities arising in the treatment of configurational entropy. Direct first principle calculations by Vaithyanathan, Wolverton and Chen [96, 97] give values in the range  $190\text{-}235 \text{ mJ/m}^2$  for the coherent boundary and approximately  $600 \text{ mJ/m}^2$  for the edges. Empirical potentials molecular dynamic simulations by Hu et al. [98] give close results of  $156$  and  $694 \text{ mJ/m}^2$  respectively. The differences are attributed to the different boundary conditions employed.

Interfacial energy data obtained as first principle estimates at 0 K do not reflect the temperature dependence of the enthalpy for both phases and completely ignore the contribution of entropy. Although the role of configurational entropy may be insignificant for a coherent boundary [35], vibrational entropy has been proved to be an important factor in the stability of  $\theta$  vs.  $\theta'$  at elevated temperatures [99] and may equally prove to have an important role in the interfacial energy. Hondros [37] gives an estimate for a grain boundary vibrational entropy of  $0.09 \text{ mJ}/(\text{m}^2\text{K})$  and configurational entropy of  $0.4 \text{ mJ}/(\text{m}^2\text{K})$ . An influence of the same order of magnitude should be expected for disordered edge interfaces, giving a reduction in their interfacial energy of a few tens  $\text{mJ/m}^2$  for every 100 K temperature increase.

Table 1 summarises the values discussed above for both  $\theta'$  in Al-Cu and  $\gamma$  in Al-Ag alloys. Also given are results for the metastable  $\gamma'$  in Al-Ag, as reviewed in [100].

Table 1 Estimates of interfacial energies of various matrix : precipitate interfaces in binary Al-Cu and Al-Ag alloys.

Interface	$\gamma$ , mJ/m <sup>2</sup>	Method/Ref.
$\alpha/\theta'$ , habit plane	30	Nearest neighbour, regular solution model [35]
	156	MEAM (MD, empirical potentials calculations) [98]
	190	Ab initio, DFT [97]
	235	Ab initio, DFT [96]
	<i>510</i>	Experiment, isothermal calorimetry [95]
$\alpha/\theta'$ , semicoherent edges	360	Nearest neighbour, regular solution model [101]
	615	Ab initio, DFT [96]
	694	MEAM [98]
	<i>21500</i>	Experiment, isothermal calorimetry [95]
$\alpha/\gamma$ , habit plane	115	Nearest neighbour, regular solution model [35]
	150	Discrete-lattice plane, regular solution model [100]
$\alpha/\gamma'$ , habit plane	4-7	Discrete-lattice plane, regular solution model [100]
	60	Nearest neighbour, regular solution model [35]
	117	Discrete-lattice plane, regular solution model [100]

For the purpose of further analysis we will treat the interfacial energy as a parameter in the broad range of 30-230 mJ/m<sup>2</sup> for the habit plane and 100-700 mJ/m<sup>2</sup> for the edges of platelike precipitates. These limits reflect the most reliable values available in the literature, with results by Boyd and Nicholson (*italicised in Table 1*) discarded as overestimates.

### 3.3. Chemical driving forces

To obtain chemical driving forces for the nucleation of  $\theta'$  and  $\gamma/\gamma'$  (no distinction is made between the two at the nucleation stage) the COST507 thermodynamical database for light metal alloys [102] is used. It allows extracting free-energy curves for the binary solid solutions and precipitating phases. The common tangent construction is applied to the free-energy profiles in order to obtain the driving force as a function of temperature and composition.

For the disordered solid solutions of a particular crystal structure the free energy  $G(T, x_A, x_B)$  is expressed as a combination of the reference parts of the Gibbs energy, the ideal entropy of mixing and the excess free energy:

$$G(T, x_A, x_B) = x_A {}^0G_A + x_B {}^0G_B + RT(x_A \ln x_A + x_B \ln x_B) + {}^eG(x_A, x_B) \quad (3.8)$$

where  $x_i$  is the molar concentration of the element,  ${}^0G_i$  is its molar Gibbs energy with respect to the standard reference state,  $R$  is the gas constant and  ${}^eG(x_A, x_B)$  is the excess part of mixing energy.

The temperature dependence of the molar Gibbs energies for pure elements referred to the standard state is taken from the compilation by Scientific Group Thermodata Europe (SGTE) [103]:

$${}^0G_i = A + BT + CT \ln T + DT^2 + \frac{E}{T} + FT^3 + IT^7 - \frac{J}{T^9} \quad (3.9)$$

A summary of the coefficients in the expression (3.9) for Gibbs energies of Al, Cu and Ag in fcc and hcp lattices is given in Table 2:

Table 2 Polynomial coefficients (selected to return the energy in J/mol) of equation (3.9) for the Gibbs energy of pure elements for Al, Cu and Ag.

	Al, fcc 298.14-700 K	Al, hcp 298.14-700 K	Ag, fcc 298.14-1235.1 K	Ag, hcp 298.14-1235.1 K	Cu, fcc 298.14-1357.8 K
<i>A</i>	-7976.15	-2495.15	-7209.512	-6909.512	-7770.458
<i>B</i>	137.093038	135.293038	118.202013	118.502013	130.485235
<i>C</i>	-24.3671976	-24.3671976	-23.8463314	-23.8463314	-24.112392
<i>D</i>	-0.001884662	-0.001884662	-0.001790585	-0.001790585	-0.00265684
<i>E</i>	74092.0	74092.0	-12011.0	-12011.0	52478.0
<i>F</i>	-8.77664 $10^{-7}$	-8.77664 $10^{-7}$	-3.98587 $10^{-7}$	-3.98587 $10^{-7}$	1.29223 $10^{-7}$
<i>I</i>	0.0	0.0	0.0	0.0	0.0
<i>J</i>	0.0	0.0	0.0	0.0	0.0

The excess Gibbs free-energy is described by Redlich-Kister polynomials of the form

$${}^eG(x_A, x_B) = x_A x_B \sum_{\nu=0}^n L_{A,B}^{\nu} (x_A - x_B)^{\nu} \quad (3.10)$$

with the Taylor expansion coefficients  $L_{A,B}^n$  being temperature dependent functions expressed as

$$L_{A,B}^n = a_n + b_n T \quad (3.11)$$

and coefficients  $a_n$  and  $b_n$  for equation (3.11) compiled in Table 3.

Table 3 Polynomial expansion of Redlich-Kister coefficients (from Witusiewicz et al. [104]).

$n$	fcc Al-Cu		fcc Ag-Al		hcp Ag-Al	
	$a_n$	$b_n$	$a_n$	$b_n$	$a_n$	$b_n$
0	-53520.0	2.0	-7154.0	-19.562	10711.0	-24.223
1	38590.0	-2.0	-16541.0	-21.694	-328502.0	27.206
2	1170.0	0.0	4274.0	-27.839	973510.0	0.0
3			-8100.0	0.0	-1386465.0	-175.760
4					881518.0	0.0

In the case of  $\theta'$  the data available from COST507 are completely sufficient to extract the driving force, as metastable  $\theta'$  is represented in the database as a stoichiometric phase (line compound of fixed composition). The free energy of  $\theta'$  is expressed as

$$G_{\theta'} = -46500 + 6.5T + 2 {}^0G_{\text{Al}}^{fcc} + {}^0G_{\text{Cu}}^{fcc} \quad (3.12)$$

Unfortunately there are no data available for  $\gamma/\gamma'$  in the database and thus the driving force for the formation of the hcp Al-Ag in the fcc Al-Ag solid solution is used instead.

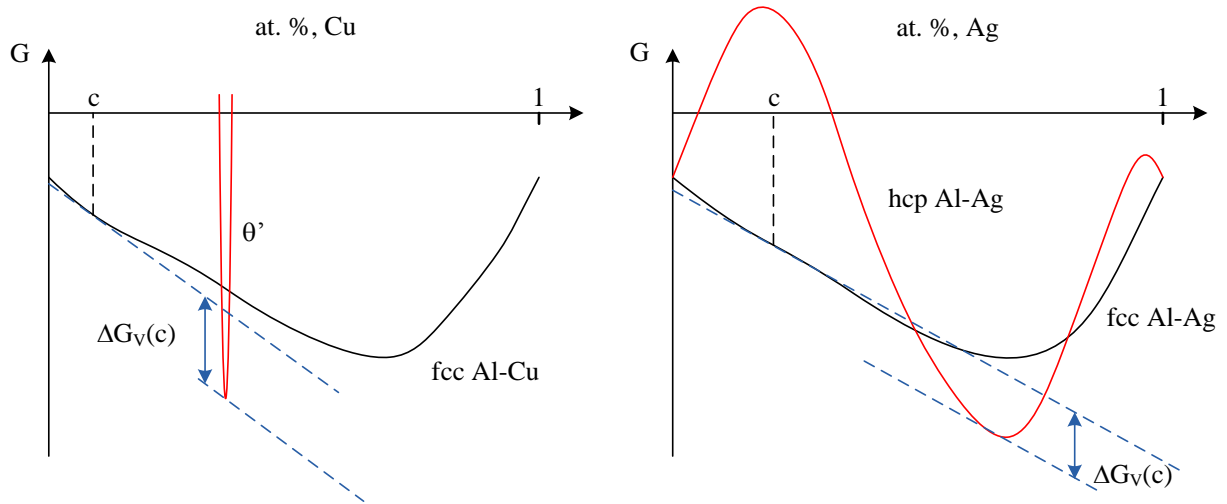


Fig. 12 The method for obtaining an estimate of chemical driving forces from a common tangent construction for the Al-Cu (left) and Al-Ag (right) systems.

Fig. 12 shows schematically Gibbs free energy curves of the phases under consideration in the Al-Cu and Al-Ag systems. With complete information for the polynomial approximations for the Gibbs energies it is possible to obtain the chemical driving force as a function of alloy composition and temperature.

The phase diagrams of the alloys under consideration serve as a guide for identifying an upper limit of the chemical driving force. This force would be maximised in the vicinity of the boundary between the metastable phase nucleating and the one that is more stable at lower temperatures (for example along the  $\theta''$  solvus for the direct nucleation of  $\theta'$  in Al-Cu, or along the GP zones solvus in Al-Ag). Corresponding sections of phase diagrams are given in Fig. 13 and Fig. 14, accompanied by the driving force calculated for the conditions shown in the diagrams.

Thus for the estimates of the activation energy and critical nucleus parameters the driving force will be taken in the range from  $2$  to  $4 \cdot 10^8$  J/m<sup>3</sup> in Al-Cu and from  $1$  to  $5 \cdot 10^8$  J/m<sup>3</sup> in Al-Ag systems.

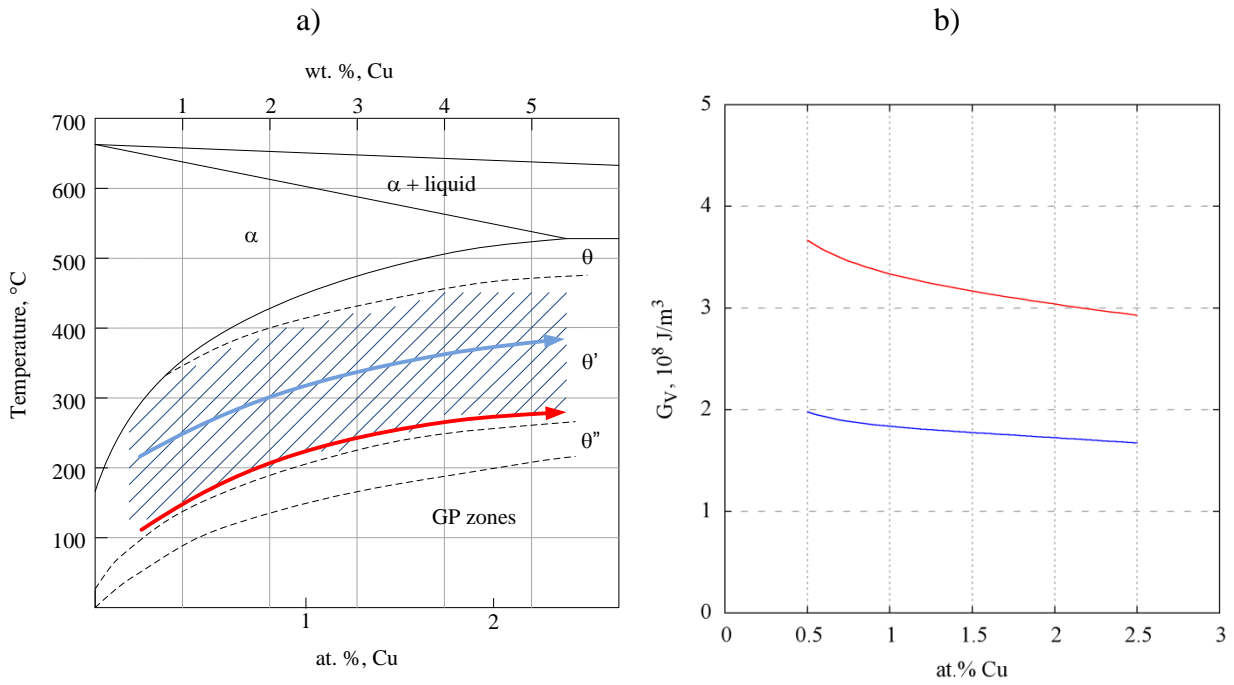


Fig. 13 a) Aluminium-rich section of Al-Cu phase diagram (adapted from Lorimer [68]). Hatched region corresponds to the conditions for direct nucleation of  $\theta'$  from solid solution. The red and blue paths outlined on the diagram are given to identify the upper limit and mid-range levels of the chemical driving force. Using the combination of composition and temperature along these paths the chemical driving force was calculated and plotted in b).

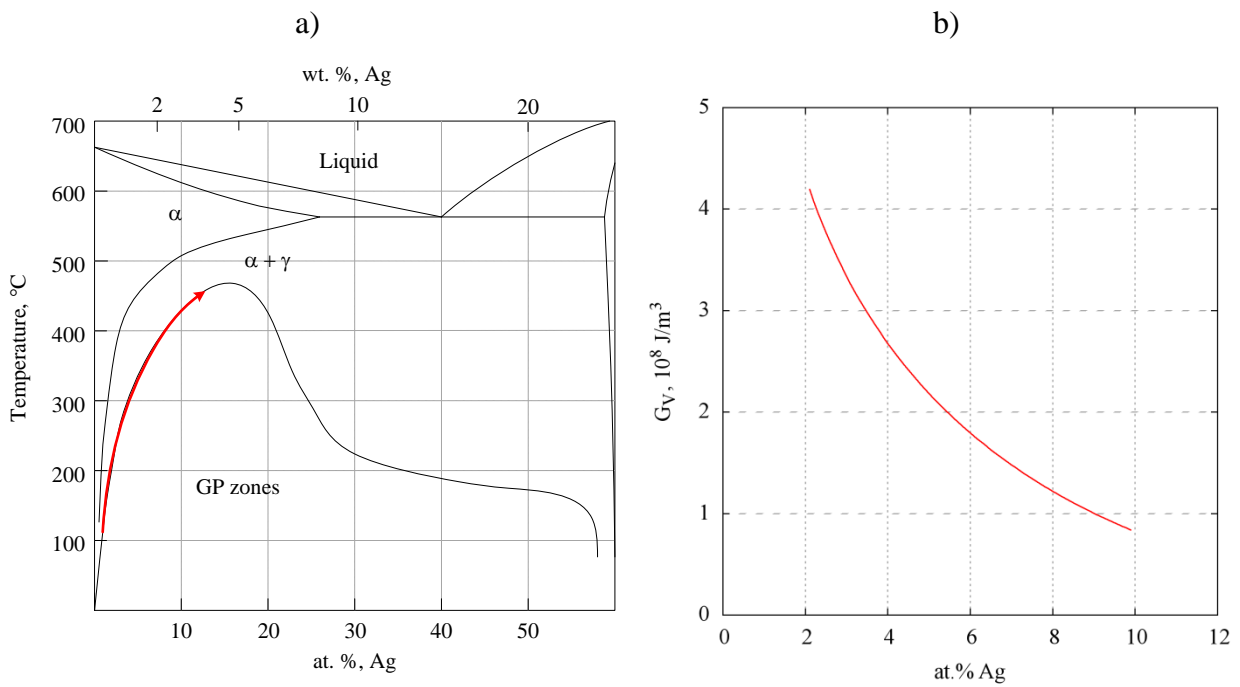


Fig. 14 a) Aluminium-rich section of Al-Ag phase diagram (adapted from Baur [105] and Massalski [106]). The red path along the GP zones solvus corresponds to the maximum of the chemical driving force for direct nucleation of  $\gamma$  phase; b) maximum driving force along the composition-temperature path outlined on the left.

### 3.4. Results for the size, shape and activation energy of the critical nucleus

The uncertainty range in both of the key variables controlling nucleation kinetics (especially the magnitude of the interfacial energy) makes it necessary to consider critical nuclei characteristics parametrically. Varying both the interfacial energy and chemical driving force within the ranges discussed above one may obtain estimates for size, shape and energy barrier on the basis of equations (3.2) and (3.3), with the elastic energy density given by Eshelby's solution (3.6) and (3.7) for a thin ellipsoid.

The map of the activation barrier for the nucleation of a disc-shaped nucleus with 4.5% tetragonal compression strain normal to the habit plane is given in Fig. 15.

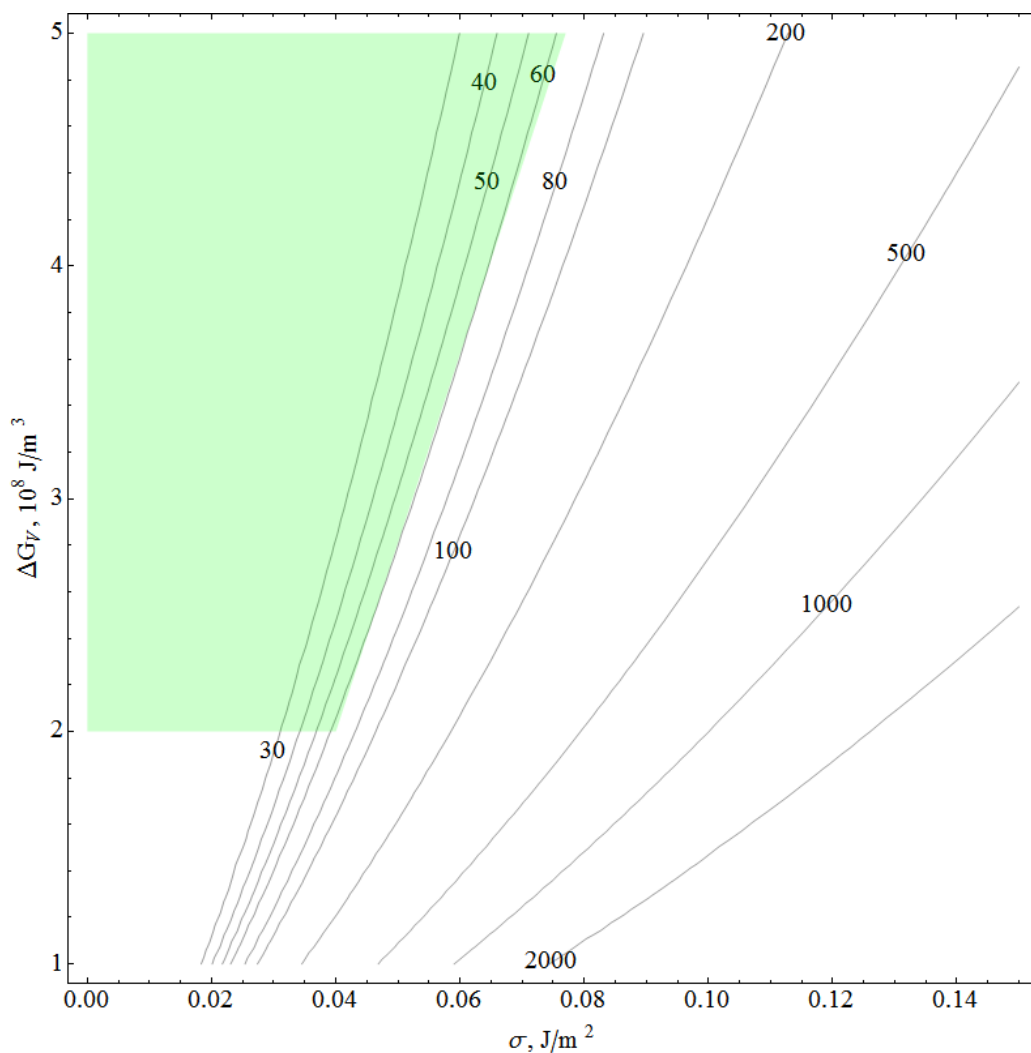


Fig. 15 Contour plot of the activation barrier (expressed in  $k_B T$ ) for the nucleation of a circular disc. The barrier is presented as a function of the chemical driving force and the habit plane interfacial energy. The transformation temperature is taken as 520 K ( $\sim 250$  °C) which is representative of direct nucleation of  $\theta'$ . The area shaded corresponds to the range of parameters where the activation barrier is lower than  $60 k_B T$ .

Table 4 The parameters of disc shaped critical nucleus as a function of chemical driving force, interfacial energy and uniaxial strain in the direction normal to the habit plane. The ranges of driving force and interfacial energies cover platelike precipitates in Al-based systems. The threefold anisotropy for the interfacial energy corresponds to the best estimates for  $\theta'$ .

$G_V, 10^8 \frac{J}{m^3}$	$\xi = 0, \tau = 0$			$\xi = 0.025, \tau = 0$			$\xi = 0.05, \tau = 0$		
	$l^*, \text{nm}$	$\alpha^*$	$\Delta G^*, k_B T$	$l^*, \text{nm}$	$\alpha^*$	$\Delta G^*, k_B T$	$l^*, \text{nm}$	$\alpha^*$	$\Delta G^*, k_B T$
$\gamma_h = 30 \text{ mJ/m}^2; \gamma_e = 3\gamma_h$									
1	3.6	0.33	85.1	4.05	0.28	96.3	5.23	0.199	131.2
2	1.8	0.33	21.3	1.91	0.30	22.7	2.23	0.245	26.9
3	1.2	0.33	9.5	1.25	0.31	9.9	1.40	0.268	11.1
4	0.9	0.33	5.3	0.93	0.32	5.5	1.01	0.281	6.0
5	0.7	0.33	3.4	0.74	0.32	3.5	0.79	0.290	3.8
$\gamma_h = 50 \text{ mJ/m}^2; \gamma_e = 3\gamma_h$									
1	6.0	0.33	394.0	6.74	0.28	445.8	8.72	0.199	607.4
2	3.0	0.33	98.5	3.19	0.30	105.0	3.72	0.245	124.6
3	2.0	0.33	<b>43.8</b>	2.09	0.31	45.7	2.33	0.268	<b>51.5</b>
4	1.5	0.33	24.6	1.55	0.32	25.4	1.69	0.281	27.9
5	1.2	0.33	15.8	1.23	0.32	16.7	1.32	0.290	17.4
$\gamma_h = 100 \text{ mJ/m}^2; \gamma_e = 3\gamma_h$									
1	12.0	0.33	3152.1	13.5	0.28	3566.9	17.44	0.199	4859.8
2	6.0	0.33	788.0	6.38	0.30	839.5	7.43	0.245	996.7
3	4.0	0.33	350.2	4.17	0.31	365.5	4.65	0.268	411.7
4	3.0	0.33	197.0	3.10	0.32	203.5	3.37	0.281	222.9
5	2.4	0.33	126.1	2.46	0.32	129.4	2.64	0.290	139.3

Table 4 illustrates the importance of the interfacial energy. The activation barrier follows a  $\gamma^3$  law for the stress-free case, and this function becomes stronger with increasing strain energy. However, for low interfacial energies and intermediate chemical driving forces the nucleation barrier may be as low as several tens of  $k_B T$  at temperatures characteristic of direct  $\theta'$  nucleation ( $T \sim 520 \text{ K}$ ). Such combinations of controlling parameters are highlighted in light green.

It is noteworthy that for those cases where the predicted barrier is of the moderate magnitude (below  $100 k_B T$ ) the role of strain energy contribution is not strong. Because a strain

is a volumetric term its contribution increases strongly with the size of nuclei, but for small particles the interfacial energy dominates. In the range of activation barriers from 20 to 60  $k_B T$  a uniaxial strain of 5% increases the barrier by approximately 10 to 20%. One example highlighted in the Table 4 is that of  $3 \cdot 10^8 \text{ J/m}^3$  driving force and  $50 \text{ mJ/m}^2$  interfacial energy. As shown in bold font, the tetragonal strain of 5% increases the barrier from 44 to 52  $k_B T$ . In terms of concentration of critical nuclei it is equivalent to a reduction factor of just  $10^{-2}$ . Meanwhile for heterogeneous formation even complete recovery of the strain energy in the vicinity of a dislocation line carries a penalty in the pre-exponential factor, because of the fraction of solute available in the proximity to the dislocations (up to  $10^{-6}$  [34]).

One may conclude that the level of confidence in the key variables does not exclude homogeneous nucleation of  $\theta'$  in the first place. Moreover, the effect of the catalysis provided by the dislocation lines, with which heterogeneous nucleation of  $\theta'$  is usually associated, is not clearly understood.

On the contrary when the transformation strain contains shear component the role of strain energy increases dramatically, as illustrated in Table 5:

Table 5 Effect of the shear component ( $\tau = 0.3$ ) in transformation strain on nucleus parameters.

$G_V, 10^8 \frac{\text{J}}{\text{m}^3}$	$\xi = 0, \tau = 0$			$\xi = 0.05, \tau = 0.3$		
	$l^*, \text{nm}$	$\alpha^*$	$\Delta G^*, k_B T$	$l^*, \text{nm}$	$\alpha^*$	$\Delta G^*, k_B T$
1	6.0	0.33	394.0	72.1	0.019	21147.1
2	3.0	0.33	98.5	19.9	0.035	1754.3
3	2.0	0.33	<b>43.8</b>	9.7	0.049	<b>442.4</b>
4	1.5	0.33	24.6	5.9	0.062	173.6
5	1.2	0.33	15.8	4.1	0.073	86.2

It is obvious that shear strain makes an otherwise relatively easy process become virtually forbidden. In this case accommodation of the shear strain energy becomes crucial for the nucleation of the precipitates. Thus the role of possible shear in transformation strain should not be discarded and needs to be considered in transformation kinetics models.



## 4. Elastic interaction model of strain assisted nucleation

This chapter focuses on the formalism and applications of a simple dislocation loop model to a treatment of elastic interactions between platelike precipitates. The approach presented here provides a useful framework for the analysis of phenomena influenced by elastic energy, such as assisted nucleation, growth and coarsening during phase transformations in solids.

The chapter reviews a series of publications based on applications of this method to the formation, growth and stabilisation of linear arrays of precipitates. An extension of the method that considers the generalised form of transformation strain between parent and product phases is presented in detail. Particular attention is given to the role that the shear component of a transformation strain plays in the development of precipitate arrays and autocatalytic nucleation.

The chapter concludes by discussing the limitations of the approach, which in the context of the project have led to the introduction of the phase field method as the primary research technique.

### 4.1. Background

The importance of the strain energy in solid-solid phase transformations has long been recognised. The matrix imposes elastic constraints on the domain of a new phase and thus introduces the elastic energy contribution into the activation energy of a transformation.

However, besides the energy of a nucleus itself, it is also important to address the interaction energy between precipitates. The problem was first analysed by Khachaturyan and Shatalov [53] for the interaction of spherical inclusions. It was demonstrated that interactions could be of complex symmetry and character, both attractive and repulsive. Attractive interaction may potentially promote selective growth or assist in the formation of new precipitates. Therefore, certain forms of a short range order in the arrangement of the precipitates may develop.

Brown et al. in [107] speculated that the attractive elastic interaction between precipitates with tetragonal stress-free transformation strain leads to the stabilisation of precipitate arrays against coarsening. It was shown that unlike surface energy, which is minimised when a large precipitate consumes a smaller one, the elastic energy of an interacting pair attains its minimum for equally sized particles. Provided that the elastic interaction is strong and negative, and the

surface energy is relatively low it was suggested that a pair of precipitates may be stabilised against competitive growth. Therefore, an array of precipitates could be stabilised against Ostwald ripening. A simple criterion for stability was introduced in the form of a critical value of a dimensionless parameter that is proportional to the average size and volume fraction of precipitates and inversely proportional to the effective surface energy. This confirmed the general assumption that stability is promoted by a low interfacial energy, a large elastic misfit and a high volume fraction of precipitates.

In a subsequent contribution Perovic et al. [108] proceeded with the analysis of finite precipitate interactions and introduced the dislocation loop model to treat platelike precipitates with tetragonal transformation strain. Pairwise interactions of finite plates were modelled and in contrast to the infinitesimal approximation a stable minimum in the interaction energy of the perpendicular plates was found. A particular type of the regular precipitate array, namely the one studied by Eurin [109], has been tested for stability against coarsening and confirmed to have an energy minimum that corresponds to the minimum in the pairwise interactions of nearest neighbours, as predicted by Khachaturyan and Shatalov. The stability criterion has been defined more precisely, generally confirming the previous estimate, and supported by selected experimental results in various alloy systems (Co-Pt, Cu-Be and Al-Cu).

Emergence of the quasi-regular arrangements of precipitates has been observed in the Al-Cu system by Lorimer [91] and Stobbs and Purdy [77]. It has been suggested that the process of nucleation that leads to the formation of such arrays could be autocatalytic in nature. Developing this idea Perovic et al. [92] applied the dislocation loop formalism to study in detail the interactions between  $\theta'$  precipitates of various sizes, mutual orientations and separation between plates. Interactions of small particles with large ones were used to analyse the effect of the pre-existing coherent precipitate on the nucleation of subsequent particles. Several types of precipitate arrangements have been tested for stability and demonstrated to have the energy minimum in the configurations observed experimentally.

The case with shear component in transformation strain has also been analysed by Perovic et al. in [110]. The same dislocation loop methodology was used and both interactions between the plates with pure shear, and those with shear accompanied by dilatation were studied. However, the range of the configurations studied was limited and requires further attention. In this chapter the details of the method are introduced. Major results and conclusions from the original papers are discussed and the analysis is extended to several important cases of transformations with shear.

## 4.2. Interaction energy calculation by a dislocation loop method

As pointed out by Khachaturyan and Shatalov [53] from the elasticity point of view the field of a dislocation loop can be considered as the limiting case of the field produced by a planar coherent inclusion. The relationship between the transformation strain, which describes the transition from matrix to precipitate, and the parameters of the corresponding dislocation loop is of the form

$$\varepsilon_{ij} = \frac{1}{2d}(b_i n_j + b_j n_i) \quad (4.1)$$

where  $\vec{b}$  is the Burgers vector of the dislocation loop,  $\vec{n}$  is a unit vector normal to the loop plane and  $d$  is the thickness of the inclusion.

Following Brown [107] and Perovic et al. [108] the interaction energy between two platelike precipitates can be replaced with the interaction energy of the corresponding dislocation loops. The latter is by definition the energy required to create a second dislocation loop in the stress field of the first one. For infinitesimal loops this energy is given via the product of the transformation strain of the second precipitate and the local stress created by first one

$$E_{int} = \varepsilon_{ij}^{(2)} \sigma_{ij}^{(1)} V^{(2)} = n_i^{(2)} \sigma_{ij}^{(1)} b_j^{(2)} \delta A^{(2)} \quad (4.2)$$

here, expression (4.1) is used to replace  $\varepsilon_{ij}^{(2)}$ ,  $\sigma_{ij}^{(1)}$  is a stress tensor for the first loop and  $\delta A^{(2)}$  represents the area of the second loop.

Stresses  $\sigma_{ij}^{(1)}$  in equation (4.2) were given by Kroupa [111] for a loop with an arbitrary orientation of Burgers vector. The stress tensor of such a loop is separated into the terms that correspond to the displacements created by the glide (lying in the plane of the loop)  $b^G$  and the perpendicular  $b^P$  components of the Burgers vector  $\vec{b}$ . The total stress is a simple superposition of the glide and perpendicular parts:

$$\sigma_{ij} = \sigma_{ij}^G + \sigma_{ij}^P \quad (4.3)$$

For the glide dislocation loop centred at the origin of the coordinate system  $(x, y, z)$  with Burgers vector  $b^G$  in the  $x$ -direction the stress components are given in equation (4.4), where  $r = \sqrt{x^2 + y^2 + z^2}$  is the distance from the loop to the point of interest, and  $K^G = -\delta A b^G [3\mu/4\pi(1 - \nu)]$  ( $\delta A$  is the loop area,  $\mu$  is the shear modulus and  $\nu$  is the Poisson's ratio):

$$\left\{ \begin{array}{l} \sigma_{11}^G = K^G \frac{xz}{r^5} \left( 1 - \frac{5x^2}{r^2} \right) \\ \sigma_{22}^G = K^G \frac{xz}{r^5} \left( 1 - 2\nu - \frac{5y^2}{r^2} \right) \\ \sigma_{33}^G = K^G \frac{xz}{r^5} \left( 1 - \frac{5z^2}{r^2} \right) \\ \sigma_{12}^G = K^G \frac{yz}{r^5} \left( \nu - \frac{5x^2}{r^2} \right) \\ \sigma_{13}^G = K^G \frac{1}{r^3} \left( \frac{1 + \nu}{3} - \nu \frac{y^2}{r^2} - \frac{5x^2 z^2}{r^4} \right) \\ \sigma_{23}^G = K^G \frac{xy}{r^5} \left( \nu - \frac{5z^2}{r^2} \right) \end{array} \right. \quad (4.4)$$

In a similar way for the perpendicular loop at the origin with  $b^P$  in the  $z$ -direction the stresses are given below, with  $K^P = -\delta A b^P [3\mu/4\pi(1 - \nu)]$ :

$$\left\{ \begin{array}{l} \sigma_{11}^P = K^P \frac{1}{r^3} \left( \frac{4\nu - 1}{3} + (1 - 2\nu) \frac{x^2 + z^2}{r^2} - \frac{5x^2 z^2}{r^4} \right) \\ \sigma_{22}^P = K^P \frac{1}{r^3} \left( \frac{4\nu - 1}{3} + (1 - 2\nu) \frac{y^2 + z^2}{r^2} - \frac{5y^2 z^2}{r^4} \right) \\ \sigma_{33}^P = K^P \frac{1}{r^3} \left( \frac{1}{3} + \frac{2z^2}{r^2} - \frac{5z^4}{r^4} \right) \\ \sigma_{12}^P = K^P \frac{xy}{r^5} \left( 1 - 2\nu - \frac{5z^2}{r^2} \right) \\ \sigma_{13}^P = K^P \frac{xz}{r^5} \left( 1 - \frac{5z^2}{r^2} \right) \\ \sigma_{23}^P = K^P \frac{yz}{r^5} \left( 1 - \frac{5z^2}{r^2} \right) \end{array} \right. \quad (4.5)$$

Equation (4.2) allows one to calculate the interaction energy between precipitates with arbitrary natures of transformation strain and of arbitrary mutual orientation. It is only applicable in the infinitesimal approximation, i.e. for loops separation large compared to their characteristic size. In order to describe precipitates of finite size with acceptable accuracy it is necessary to

overcome the restrictions of large separation. This can be done as proposed by Brown et al. [107] by representing a large loop as an array of smaller loops. Then interactions between all the elements of such arrays are added up to give the total interaction energy.

### 4.3. Interaction of tetragonal transformation strain inclusions

The method described above was initially applied (Brown et al. in [107] and later Perovic et al. in [92, 108]) to study the interactions between platelike inclusions with tetragonal transformation strain. The results obtained are briefly discussed here before proceeding to the more general case of transformations involving the shear component.

Consider two interacting plates embedded coherently into the elastically isotropic matrix. Assume that the transformation strain from parent to product phase is purely dilatational and in our case is limited to expansion (or contraction) in the direction normal to the habit plane. The situation is representative of an Al-Cu  $\theta'$  precipitates with -4.3% misfit strain. Taking into account the orientation relationship observed for the plates with habit planes parallel to  $\{100\}$  planes of the fcc matrix it is sufficient to analyse only the interactions between mutually perpendicular or parallel plates.

The most prominent result of Brown et al. [107] was the demonstrated discrepancy between the interaction profiles in the infinitesimal approximation and that of the finite plates. Naturally, the former failed to describe close range interactions between the precipitates. Examples are presented in Fig. 16 and Fig. 17<sup>1</sup>, which show the interaction energy profiles between two equally sized square plates as a function of their centre-to-centre separation. The magnitude of the interaction energy is normalised here by the factor  $\mu V_0 \varepsilon^2$ , where  $\varepsilon$  is a misfit parameter (tetragonal expansion or contraction) and  $V_0$  is the volume of the precipitate. Distance is normalised by the scaling factor  $L$ , which is the side length of the plates.

Two orientations were considered – parallel plates one on top of the other in Fig. 16 and perpendicular plates in the edge to face orientation in Fig. 17. It can be seen that both cases show significant difference between the raft representation of finite plates and the infinitesimal approximation, especially at small separation of interacting plates.

---

<sup>1</sup> In all diagrams of this section that illustrate the mutual orientation of precipitates the components of transformation strain are shown as blue arrows in the direction of tetragonal misfit, and red arrows in the direction of shear.

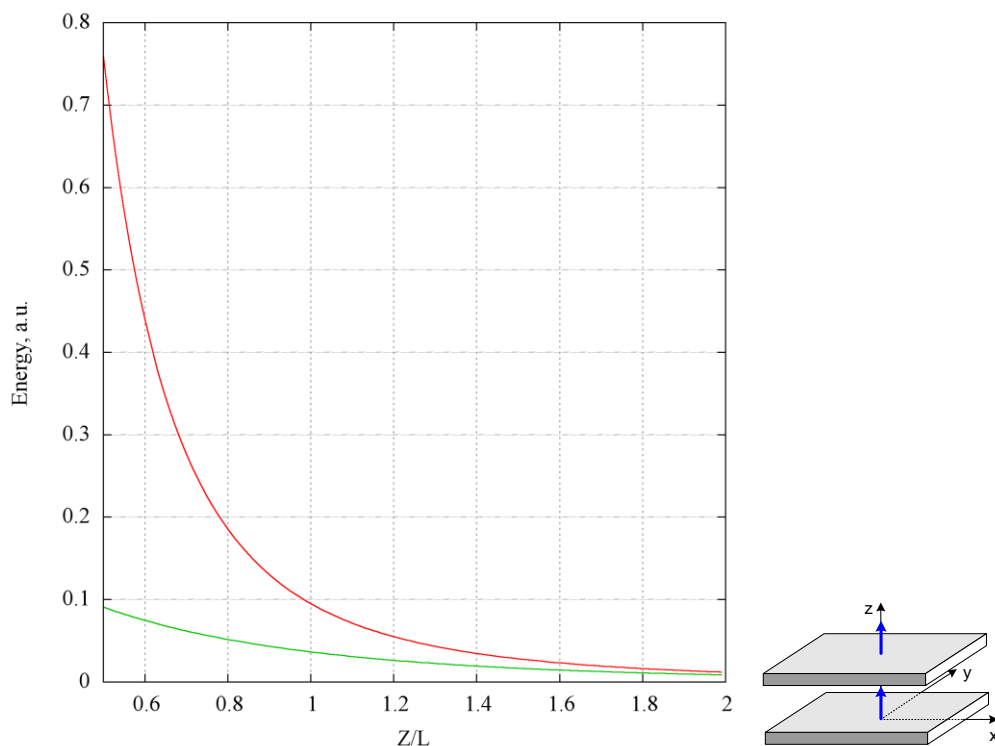


Fig. 16 Interaction energy of two square plates in the face to face parallel orientation as a function of the vertical separation between their centres (red line – infinitesimal loops approximation, green line – plates modelled as rafts of smaller loops). Based on the method of Brown [107].

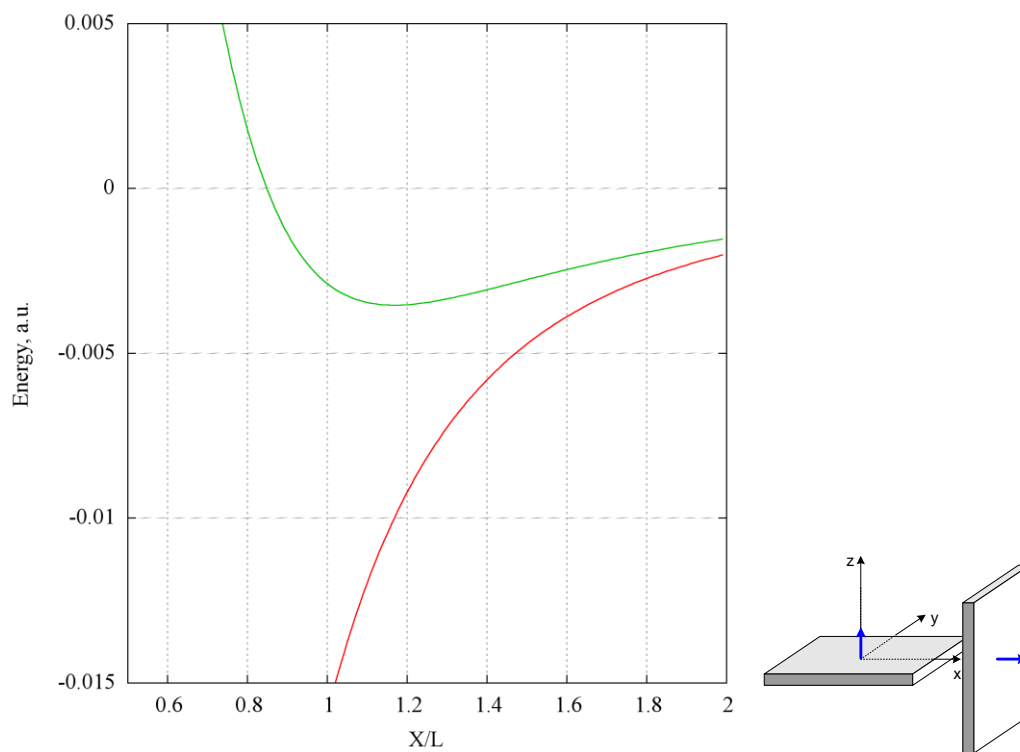


Fig. 17 Interaction energy of two square plates in the edge to face perpendicular orientation as a function of the separation in  $x$ -direction between their centres (red line – infinitesimal loops approximation, green line – plates modelled as rafts of smaller loops). Based on the method of Brown [107].

The difference is strongly pronounced in the case of the edge to face orientation, when the monotonic attractive potential is replaced with a one that demonstrates a stable minimum. The minimum is achieved at the separation of centres of approximately  $1.1 L$ . As suggested by Khachatryan and Shatalov [53] this stable minimum in the interaction energy may affect the distribution of precipitates and lead to the short-range order in their arrangement.

Based on pairwise interaction potentials, repulsive for parallel plates as in Fig. 16 and attractive for perpendicular plates as in Fig. 17, several types of array structures have been analysed in terms of their stability. Configurations considered by Perovic et al. in [92] are presented in Fig. 18:

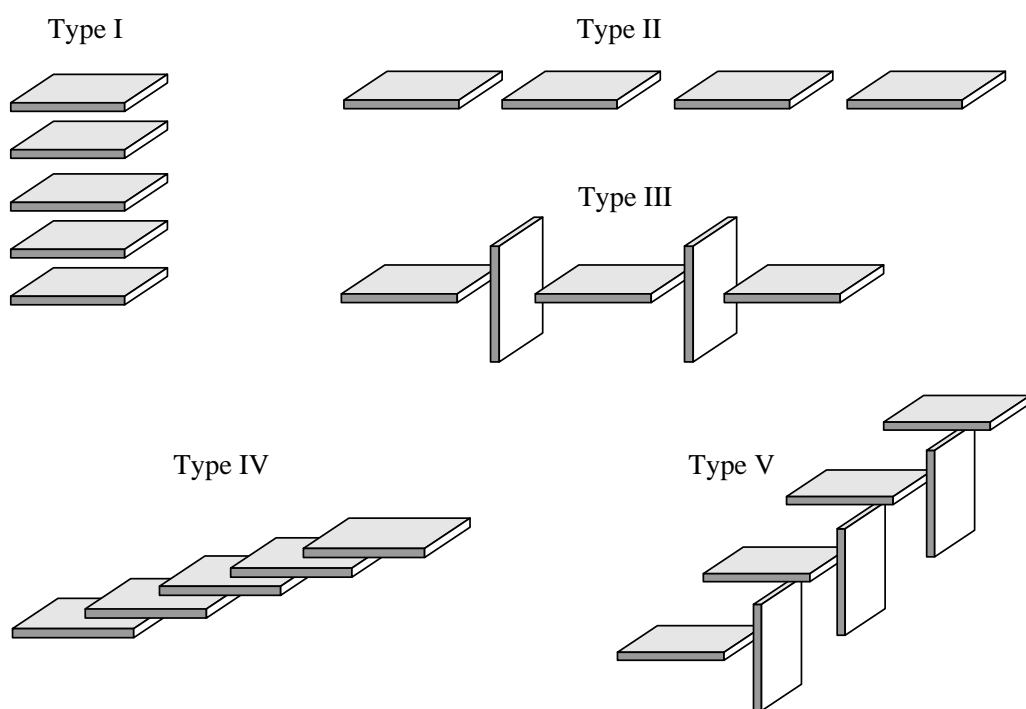


Fig. 18 Diagrams of various linear arrays of precipitates, as considered in [92].

The structure of Type I is energetically unfavourable, as all the nearest neighbour interactions are repulsive. On the other hand, an array with all the plates in the same plane, like that of Type II, is based on attractive interactions between all elements. Arrays of these types are never observed in experiment.

Type III arrangement is more complex. It has attractive interactions between the nearest neighbours and between second nearest neighbours for horizontal plates lying in the same plane. However, this energy benefit is counterbalanced by the repulsive second neighbour interaction between vertical parallel plates.

The two types of arrays that are most commonly observed in experiment are those of Type IV and Type V. The Type IV structure is an intermediate case between the two extremes of Type I and Type II. As the inclination of the array varies from  $0^\circ$  (all plates are in one plane) to  $90^\circ$  (plates on top of each other) the interaction potential changes from attractive to repulsive. The variation of the particle spacing and the inclination angle of the array show a minimum of interaction energy for small inclination angles ( $15^\circ - 20^\circ$ ). As for the Type V structures they were found to be with neighbour separations that correspond to the edge-face interaction minimum, as can be easily predicted.

The evolution sequence has been analysed by assessing the interactions of a large plate with a smaller one. This was done in an attempt to mimic the effect of the stress field surrounding the mature precipitate on the formation of a nucleus. Fig. 19 illustrates the interaction profiles in two configurations. There are several important features to be noticed. The edge to face interactions between the large and small particles show a potential similar to that between equally sized particles. It has a stable minimum, but the minimum is closer to the edge of the large plate (Fig. 19a), compared to the  $1.1L$  separation predicted for the plates of equal size.

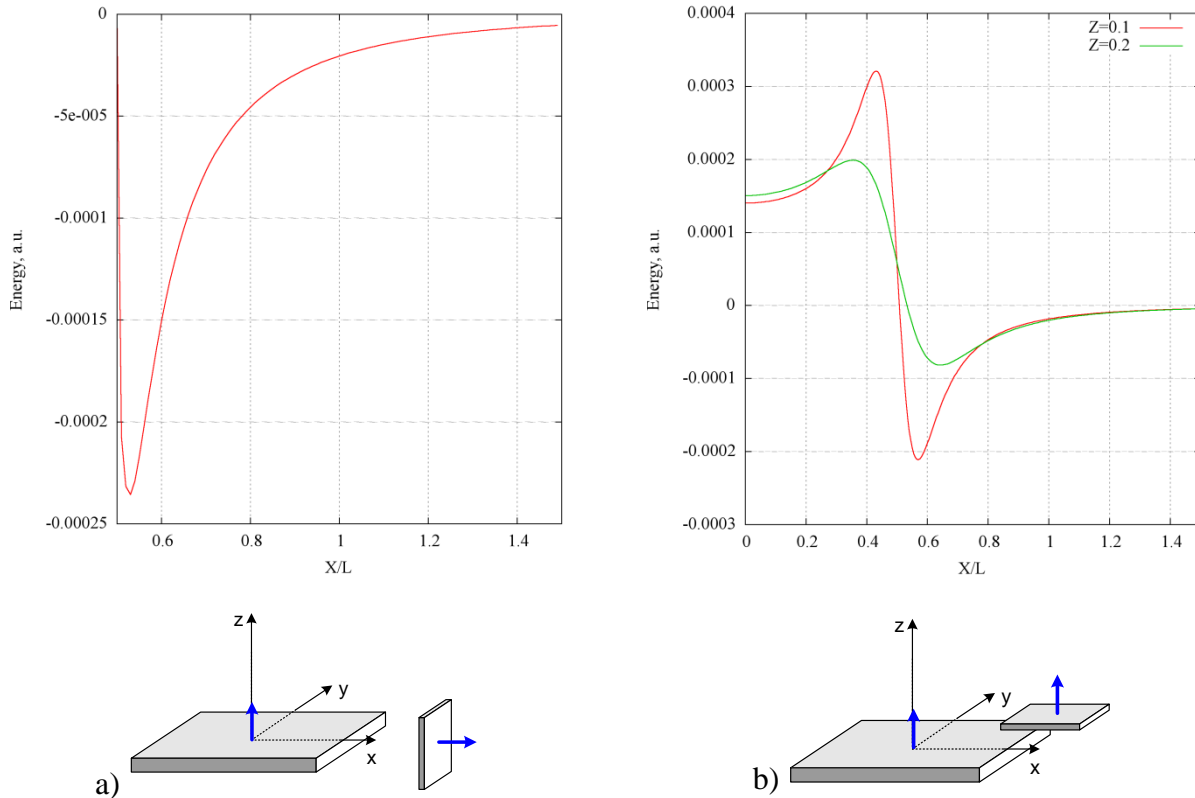


Fig. 19 Interaction profiles for the small plate in the vicinity of a large one: a) small perpendicular plate next to the edge of a large plate, energy vs.  $x$ -displacement; b) small plate parallel to the large one, displaced vertically by  $Z = 0.1$  and  $Z = 0.2$ , energy vs.  $x$ -displacement. Adapted from Perovic et al. [92].

For the parallel plates (Fig. 19b) the region of stress concentration above the edges of the large plate is a place where the character of the interaction changes abruptly from repulsive to attractive within limited spatial region. This supposedly gives a possibility for the nucleus to form above or below the edge of the large plate.

An interesting result is also obtained for the parallel nucleus displaced away from the coplanar position. A small vertical displacement results in the drop of interaction energy, as shown in Fig. 20. The authors initially claimed that the effect could be due to the restrictions of the calculation method. The result was attributed to inadequate treatment of the dislocation interaction at small distances, when segments of loops touch and are supposed to cancel. However, it has been speculated later [110] that the minimum could be responsible for the formation of inclined linear arrays in autocatalytic fashion by forming nuclei close to precursor, but shifted away from the common plane.

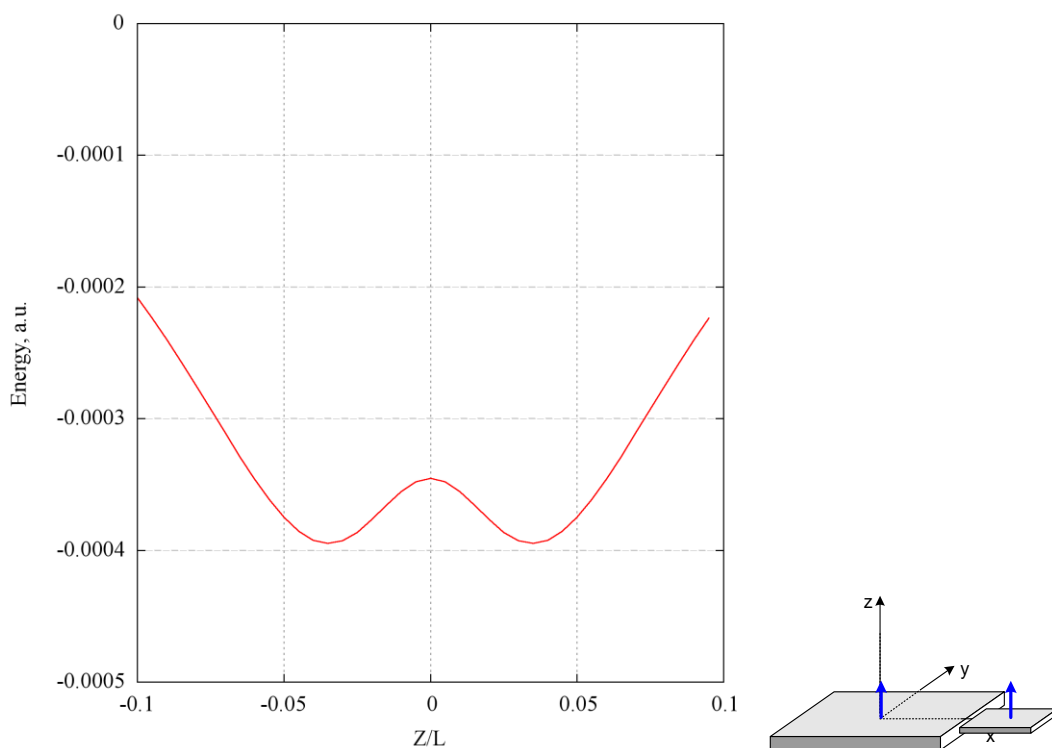


Fig. 20 Interaction energy profile for the small parallel plate at the distance of closest approach to the large plate, plotted as a function of the displacement in  $z$ -direction, away from the coplanar arrangement. Adapted from Perovic et al. [92].

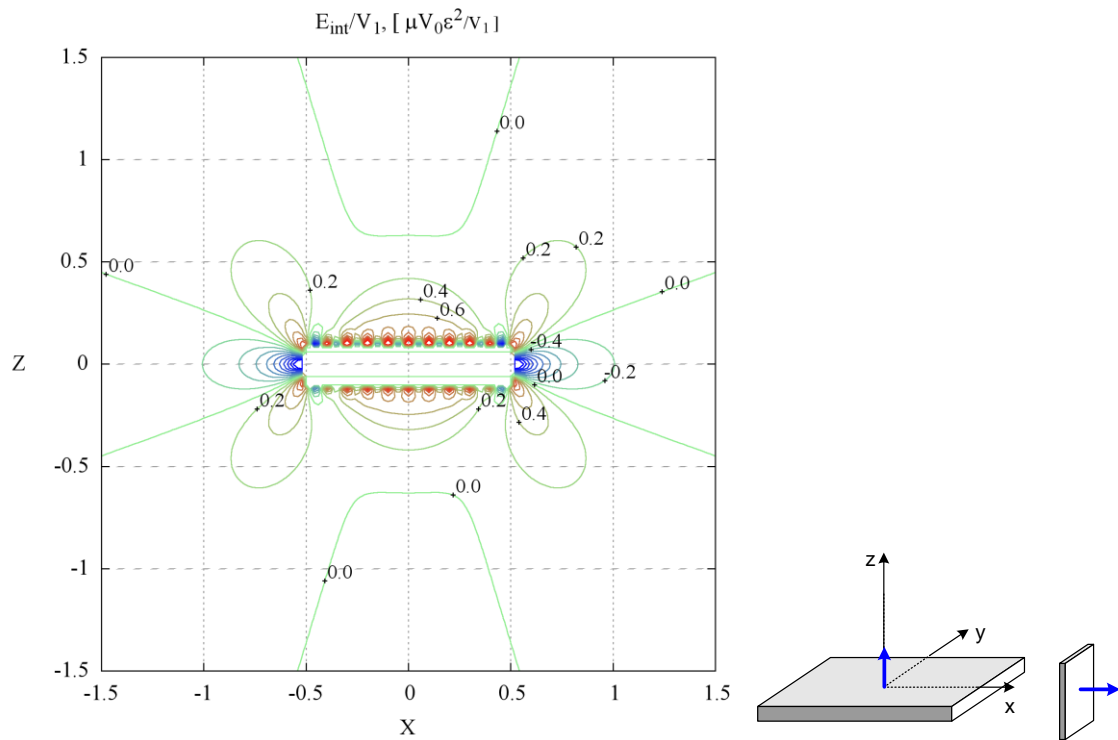


Fig. 21 Interaction energy density for the nucleus perpendicular to the primary plate.

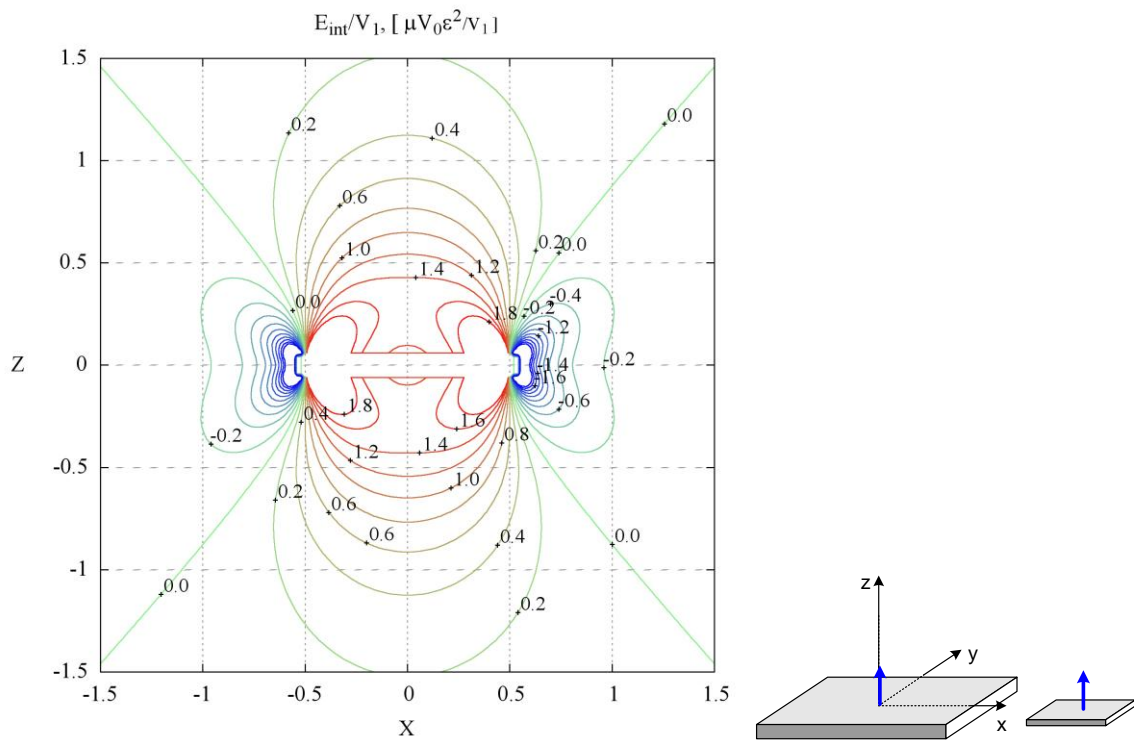


Fig. 22 Interaction energy density for the nucleus parallel to the primary plate.

To illustrate the interactions at the stage of nucleation in detail two-dimensional interaction energy density maps are presented in Fig. 21 for the nucleus perpendicular to the primary plate and Fig. 22 for a nucleus parallel to the primary plate. It is obvious that the perpendicular nucleus is bound to be formed next to the edge, where the interaction energy is attractive and strongest.

Fig. 22 on the other hand indicates that the parallel nucleus may indeed be formed with slight vertical displacement away from the plane of the primary plate. The minimum that appears with vertical offset is actually caused by the  $\sigma_{33}^P$  component of the large plate's stress (it is the only component that remains in the energy expression, as selected by this orientation of plates). As can be derived from (4.5):

$$\sigma_{33}^P = K^P \frac{1}{r^3} \left( \frac{1}{3} + \frac{2z^2}{r^2} - \frac{5z^4}{r^4} \right) \quad (4.6)$$

this stress component has minima at two locations (polynomial roots of the expression above):

$$z_{min} = \pm \frac{\sqrt{x^2 + y^2}}{2} \quad (4.7)$$

However, because the stress is a strong inverse function of the distance, the negative interaction and its detailed structure are only noticeable in immediate proximity to the edge of the large plate.

In summary, the application of the dislocation loop model demonstrated that elastic interaction between precipitates has the potential to explain certain experimentally observed microstructural features, namely arrays of types IV and V. The stability of inclined stacks is in agreement with the predictions of the model. Cross like arrays may be explained by the defining role of the minimum in the interaction of nearest neighbours. Finally, within the plausibility of the mathematical model, an explanation is suggested for the evolution of the structure in an autocatalytic way.

#### 4.4. Shear strain effect on the interaction energy of plates

In their latest paper from the series Perovic et al. [110] attempted to analyse how the shear component of the transformation strain affects the elastic interaction between plates. They considered various situations, including the interaction of plates characterised by the pure shear and those with the mixture of tetragonal and shear components in the transformation strain. Unfortunately, the latter calculations were carried out erroneously, which will be demonstrated below, thus the case requires reassessment. Some interesting examples of interactions between inclusions of different types have not been assessed, for instance the interaction of the large tetragonal defect with the sheared nucleus.

The geometrical configurations considered in [110] were restricted to those with only parallel plates. Various cases of large interacting sheared plates showed complex symmetry of the interaction potentials, in some cases with stable minima. Interactions of large and small particles, representative of the nucleation stage, revealed that the sheared nucleus invariably shows an energy minimum when formed in the same plane as the large plate. This fact was stressed as a significant difference to the tetragonal case, where the nucleus was predicted to form with a displacement away from the coplanar position.

The case of the mixed character transformation strain requires additional attention. Consider the transformation strain of the following form, with the shear  $\tau$  and the tetragonal misfit  $\xi$ :

$$\varepsilon_{ij} = \begin{pmatrix} 0 & 0 & \varepsilon_{13} \\ 0 & 0 & 0 \\ \varepsilon_{31} & 0 & \varepsilon_{33} \end{pmatrix} = \begin{pmatrix} 0 & 0 & \tau/2 \\ 0 & 0 & 0 \\ \tau/2 & 0 & \xi \end{pmatrix} \quad (4.8)$$

Orientation of the precipitates is described by the habit plane normal vector  $\vec{n} = (0,0,1)$  aligned with the  $z$ -axis in the Cartesian system. The Burgers vector, similar for both loops, is related to the strain tensor components as  $\vec{b} = (b_1, b_2, b_3) = d(\tau, 0, \xi)$ , i.e. with shear in the positive  $x$ -direction and compression (or expansion) in the  $z$ -direction. In accordance with (4.2) the interaction energy between two such precipitates can be expanded as

$$\begin{aligned} E_{int} &= n_i^{(2)} \sigma_{ij}^{(1)} b_j^{(2)} \delta A^{(2)} = \delta A^{(2)} \left[ \sigma_{31}^{(1)} b_1^{(2)} + \sigma_{33}^{(1)} b_3^{(2)} \right] = \\ &= \delta A^{(2)} \left[ \sigma_{31}^{(1G)} b_1^{(2)} + \sigma_{31}^{(1P)} b_1^{(2)} + \sigma_{33}^{(1G)} b_3^{(2)} + \sigma_{33}^{(1P)} b_3^{(2)} \right] \end{aligned} \quad (4.9)$$

and is essentially composed of four terms that represent interactions due to pure tetragonal distortions, pure shear distortions and two cross-terms of mixed character interactions (products of shear strain and tetragonal stress and vice versa – tetragonal strain and shear stress). It is thus important to recognise that unlike the stress itself the energy of interaction is not merely a superposition of tetragonal and shear parts of the interaction energy.

To verify the results from [110] for the mixed-character strain selected examples from this paper were repeated. Fig. 23 reproduces the interaction profiles between the large central plate and small plate in its vicinity as a function of the small plate displacement away from the coplanar position. Two simplified cases of purely tetragonal and purely sheared transformation strain are presented on this graph in red and in green respectively. The interaction of the tetragonal plates has a stable minimum when the small plate is offset away from the plane of the large plate. Sheared plates, on the contrary, minimise interaction energy when they are coplanar.

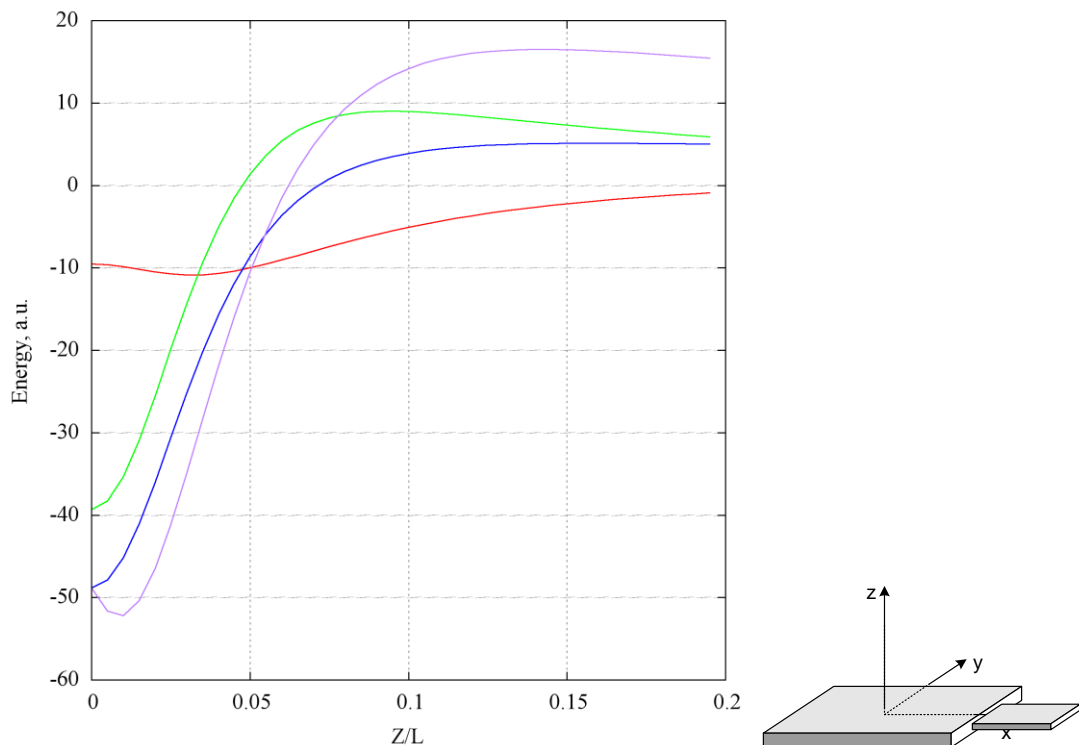


Fig. 23 Adapted from [110]: interactions between the large plate at the origin with a small plate next to its edge on x-axis, while displaced vertically. Various characters of the transformation strains are considered: red – purely tetragonal with 5% misfit; green – 0.1 shear in x-direction; blue and purple – mixture of the 5% tetragonal misfit and 0.1 shear, calculated without and with the cross terms from (4.9) respectively.

The blue line shows the profile calculated in [110] for the mixed strain type. It is obvious that the interaction energy from the original paper (solid blue line) for the mixed plates is an exact superposition of the two profiles for purely tetragonal and purely sheared strains, thus confirming that the cross-terms from equation (4.9) were neglected in the calculations.

The correct profile, which accounts for all terms in the interaction energy, is given on the same graph in purple. Not only is it asymmetrical with respect to displacement sign, but it also does not have a minimum at zero displacement.

Perovic et al. have concluded on the basis of the blue profile that the role of shear component in the transformation strain is to promote coplanar configurations, while the tetragonal component tends to displace the plates away from it. Inclined stacks of plates thus supposedly should appear when the tetragonal part dominates the shear. These results, however, must be revisited.

#### **4.5. Interaction of generalised transformation strain inclusions**

The pairwise interaction energies presented in this section were calculated for square plates with the thickness-to-length aspect ratio of 0.1. Three different orientations of habit plane and four senses of shear were tested. The magnitude of the shear component was taken to be 0.3, which is representative of several examples of diffusional-displacive transformations (for example  $\gamma'$  and  $\theta'$  - [64, 90]). In each of the cases the coordinate system is defined with respect to the body centre-point of one plate which is sheared in the positive  $x$ -direction, and the energy is calculated as function of the second plate coordinates. Results of the calculations are scaled as discussed before by the factor  $\mu V_0 \varepsilon^2 / V_1$  ( $V_1$  is the volume of the secondary plate) and represent the distribution of the normalised interaction energy density.

The interaction between the large plate at the origin and the smaller plate was calculated and results presented with the orientation of the plates and the direction of the shear for the secondary plates shown schematically. For each of the possible 12 variants three-dimensional maps were calculated and regions with negative interaction energy were identified. Fig. 24, Fig. 25 and Fig. 26 show isosurface plots of interaction energy levels from -5 to 5. The opacity of isosurfaces and their colour represent the sign and strength of interaction, with negative interaction shown in blue and positive in red.

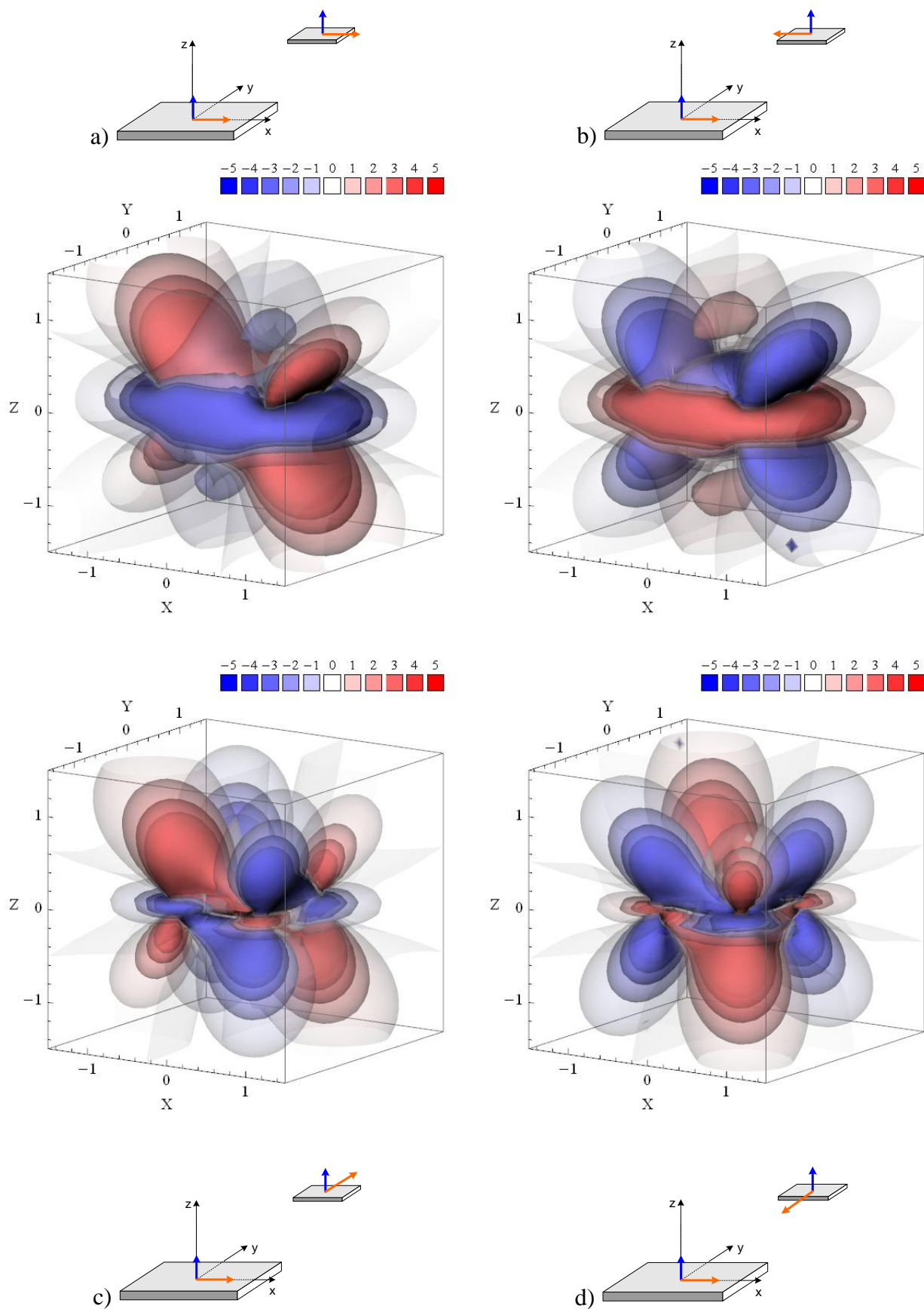


Fig. 24 Three-dimensional interaction energy density maps for parallel large and small plates with (001) and (001) habit planes and varying senses of shear in the secondary plate.

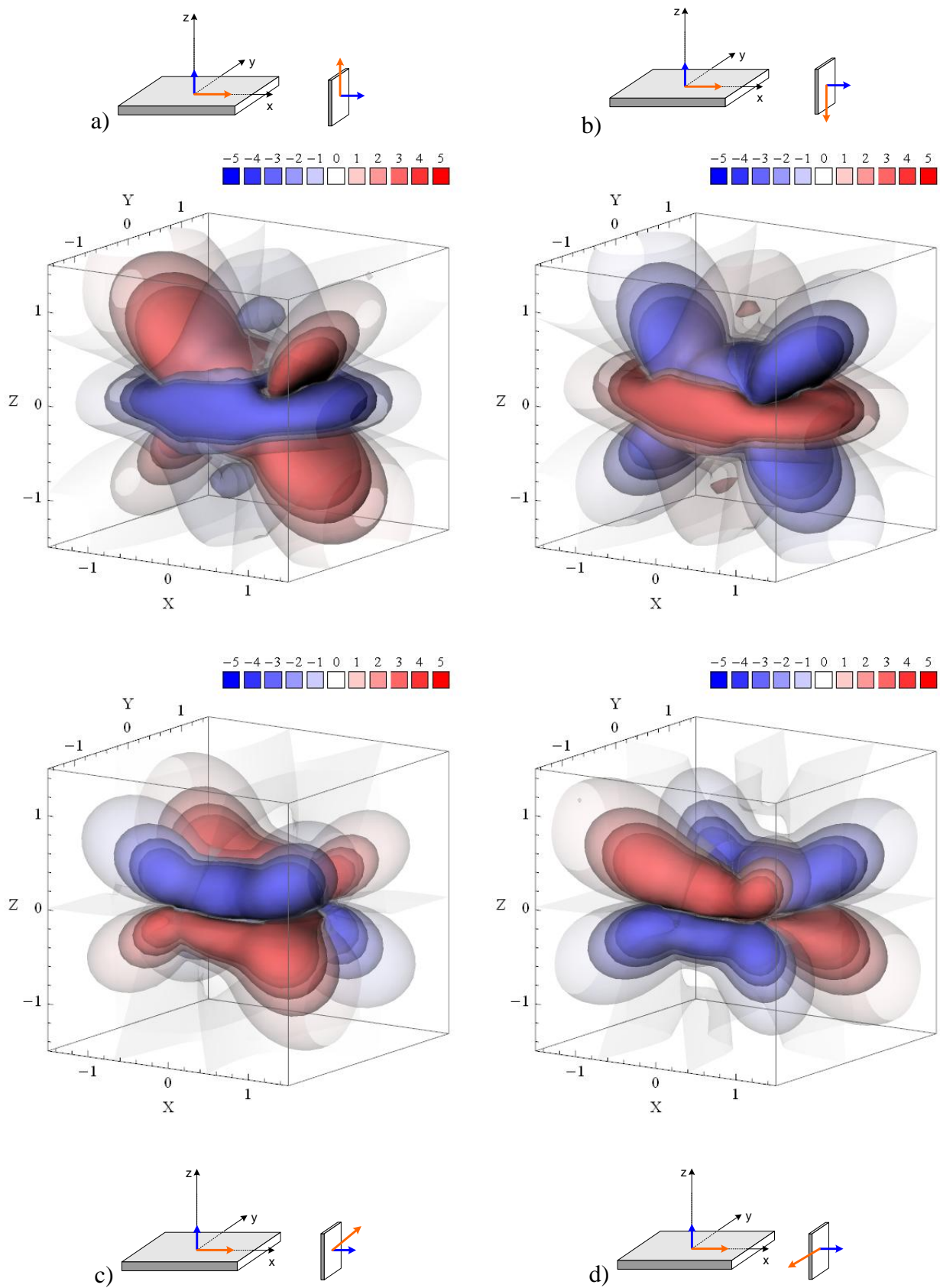


Fig. 25 Three-dimensional interaction energy density maps for perpendicular large and small plates with (001) and (100) habit planes and varying senses of shear in the secondary plate.

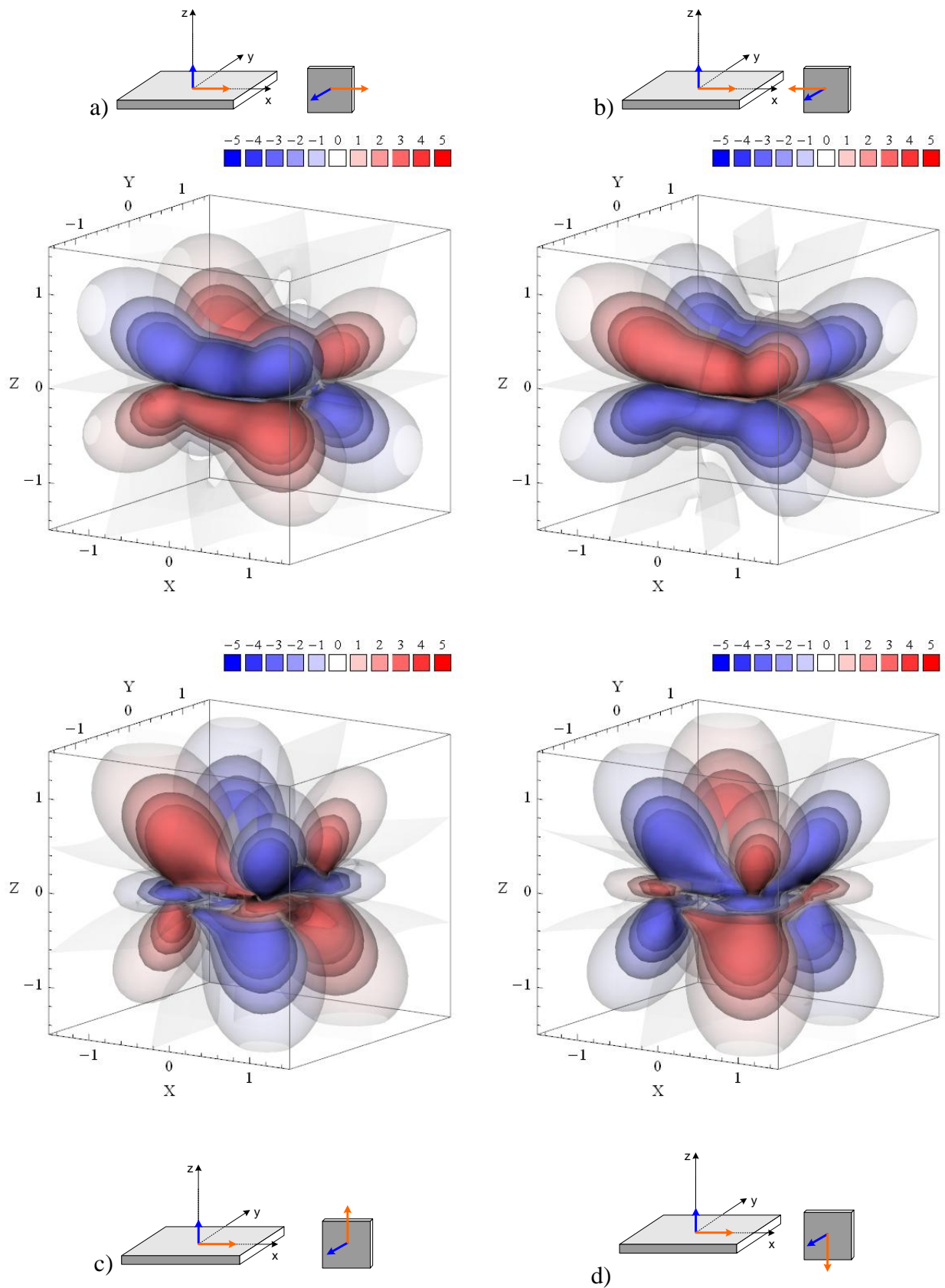


Fig. 26 Three-dimensional interaction energy density maps for perpendicular large and small plates with (001) and (010) habit planes and varying senses of shear in the secondary plate.

Particularly strong effect of the interaction may be noticed in Fig. 24a, Fig. 24b, Fig. 25a and Fig. 25b. These variants have the following common characteristics:

- The plane of mirror symmetry for the distribution of interaction energy can be identified. For the arrangements considered (with one plate centred at the origin and with shear along the  $x$ -axis positive direction) this plane is  $XZ$  ( $Y = 0$ ). The maximum strength of interaction is achieved when the centre of the secondary plate lies in the same  $XZ$  plane.
- The components of the Burgers vector for the second loop, which is related to its transformation strain and orientation in space, belong to the same  $XZ$  plane.

The configurations mentioned above are considered in more details in the following section. Two dimensional energy distribution maps are given for the  $XZ$  plane of the maximum interaction strength ( $Y = 0$ ). The cases of strongest interaction energy density are presented in Fig. 27 - Fig. 30.

The interaction of the large plate with the parallel nucleus strongly depends on the sense of the shear. For the same shear direction in primary and secondary plates the interaction is primarily repulsive, except for the coplanar configuration of large and small precipitates, as shown in Fig. 27. Therefore, the elastic interaction is expected to either facilitate a growth of the existing plate, or stimulate the formation of a nucleus in the same plane as the primary plate.

The parallel variant with opposite shears in Fig. 28 features regions of negative interaction energy immediately above and below the primary plate, and also above and below the rim of the plate. It is expected that the interaction would either promote formation of new shear accommodating layers on top of the existing plate or lead to formation of a nucleus close to the rim of the plate.

The interaction with the perpendicular nucleus, shown in Fig. 29 and Fig. 30, is essentially the same, suggesting the dominant role of the shear component in the examples considered.

It must be emphasised that the effect of shear is obviously more complicated than was suggested in [110]. It does not generally stabilise coplanar arrangement of precipitates. On the contrary, it may either stimulate the formation of self-accommodating layers (similar to twinning) or promote the nucleation in the regions above or below the edges of the primary plate.

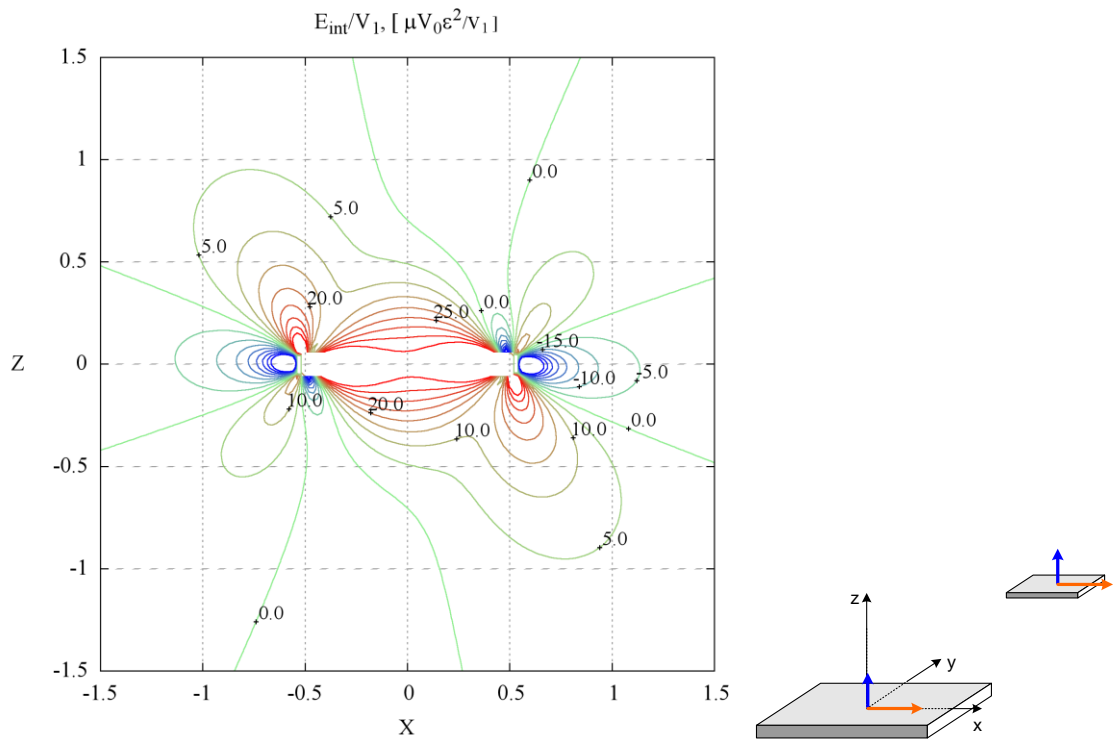


Fig. 27 Interaction energy density for parallel plates with similar senses of shear.

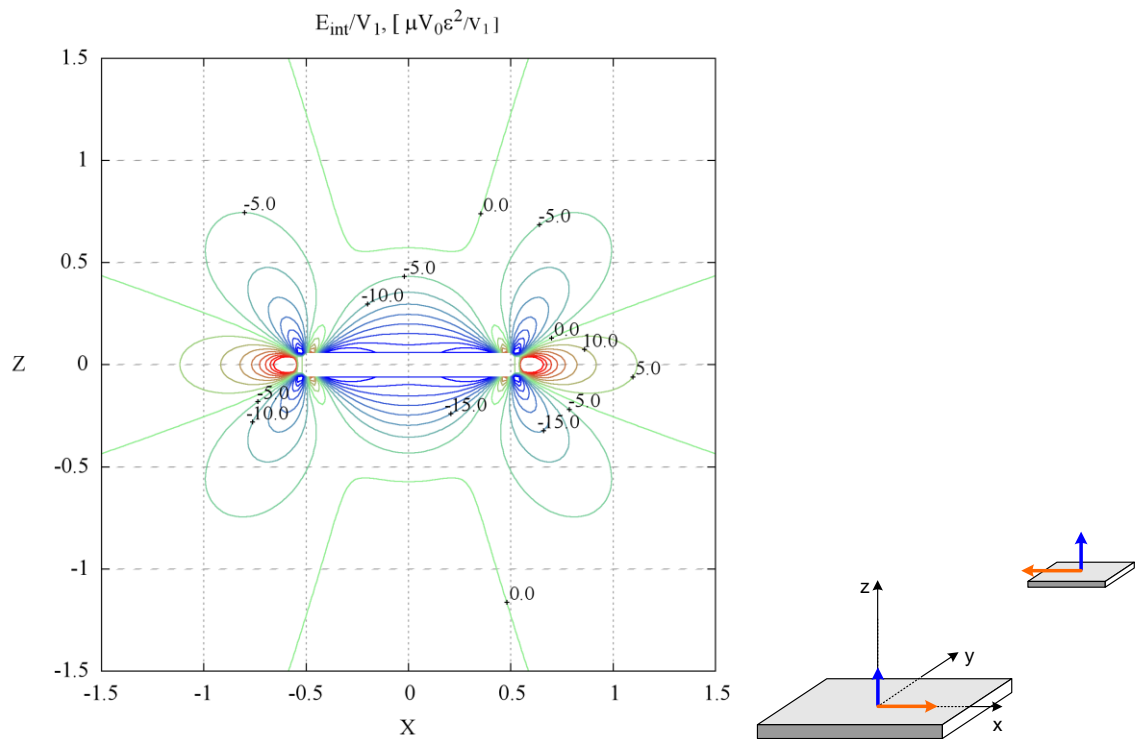


Fig. 28 Interaction energy density for parallel plates with opposite senses of shear.

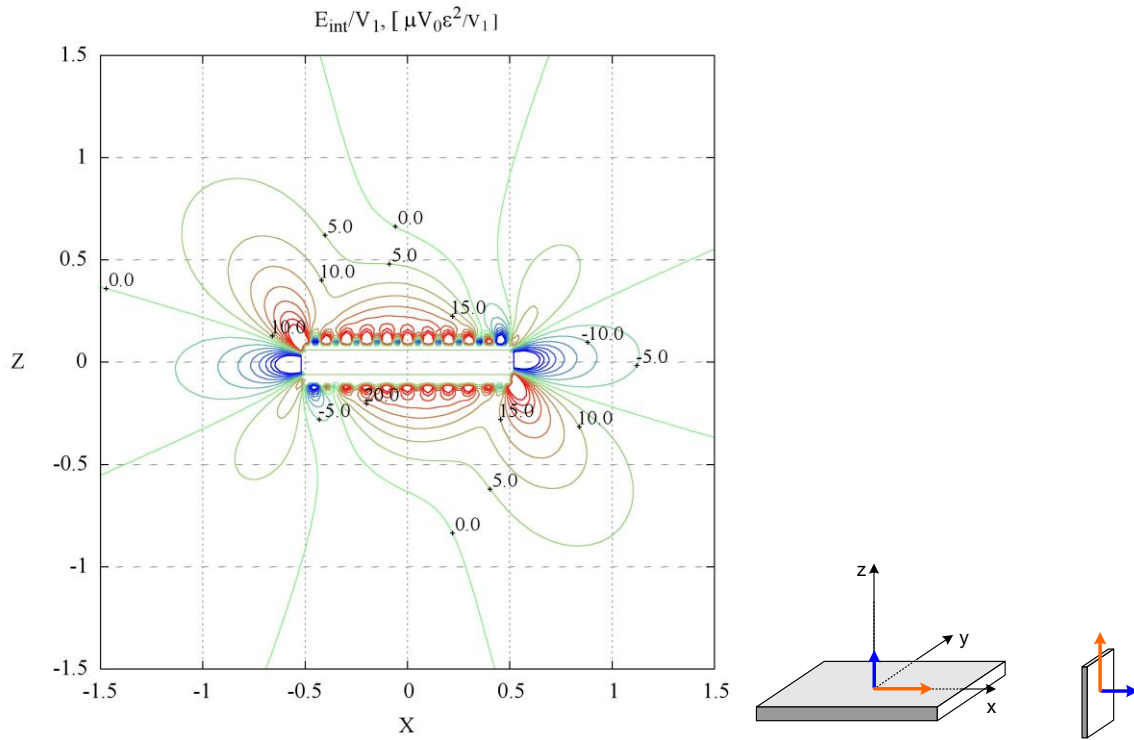


Fig. 29 Interaction energy density for perpendicular plates with similar senses of shear.

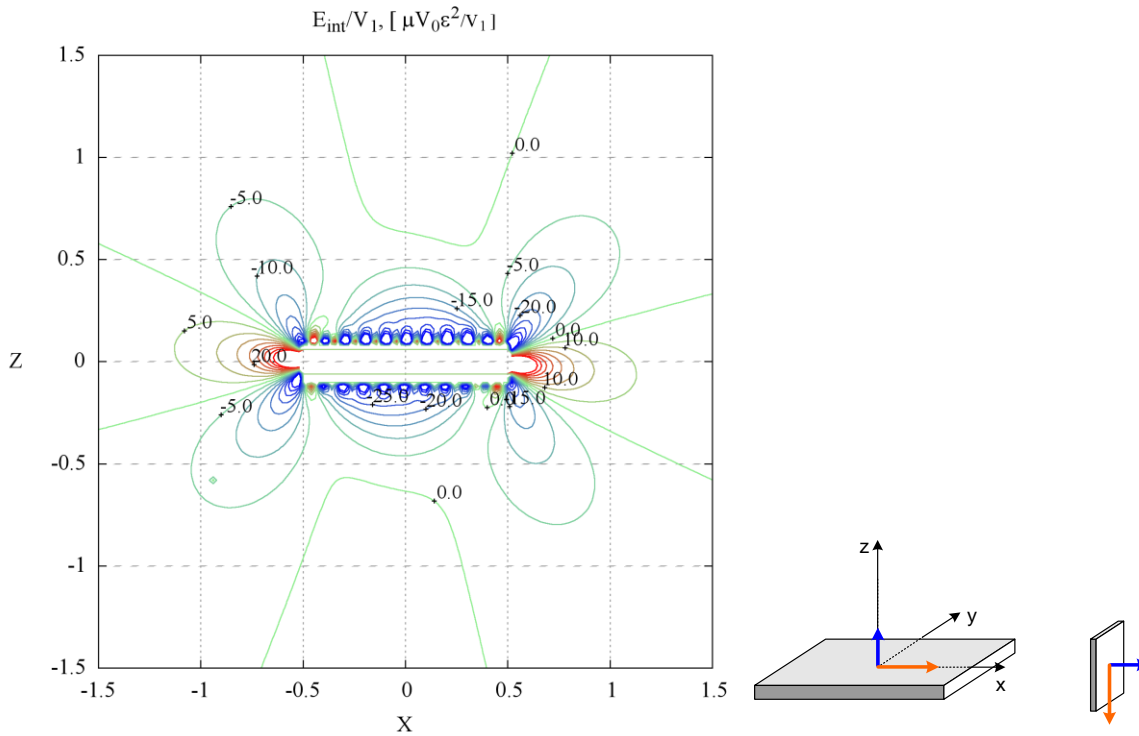


Fig. 30 Interaction energy density for perpendicular plates with opposite senses of shear.

## 4.6. Interaction of tetragonal strain plates with sheared nuclei

The twinning of the precipitate with the shear component of the transformation strain provides a way to accommodate the shear strains for the precipitate and, as the interaction energy confirms, the plate of opposite sense of shear is most likely to be formed on top of the precursor. In such a case the character of the strain maintained between the matrix and the layered precipitate would be purely tetragonal. However, there is a probability for the nucleus to be formed as a sheared platelet. Therefore, it is instructive to consider the interaction between a large plate of tetragonal transformation strain and a nucleus with mixed character strain.

Results of calculations for two dimensional maps of interaction energy between the large plate at the origin and a small nucleus are given in Fig. 31 - Fig. 34. The strength of interaction is noticeably less than when both large plate and nucleus have a shear in their transformation strain. On the other hand it is stronger than in the case of pure dilatational transformation strain presented in Fig. 21 and Fig. 22.

It should be noticed that in the simulations presented here the shear was taken as 0.3 and plays greater role compared to the dilatational component of -0.05. As a result of such a choice there is a relatively weak effect of the tetragonal component on the symmetry of the interaction energy distribution. For instance, the maps in Fig. 31 and Fig. 33 (and likewise Fig. 32 and Fig. 34) are quite similar. This happens because 90° rotation of the nucleus habit plane selects the same combination of the shear component of the nucleus Burgers vector and deviatoric component in the stress large plate tensor  $\sigma_{13}^P \tau$ , which preserves the symmetry of the energy part that arises due to the shear. The other part of the energy arising from the tetragonal part of the strain is less in magnitude, and does not noticeably changes the picture. If, however, the relative magnitude of the shear and tetragonal components should change, it would be reflected in the symmetry of the interaction.

The spatial distribution of interaction energy is particularly interesting. In all orientations considered, the regions of negative interaction are located close to the edges of the primary plates. They extend as lobes vertically up or down the edge (depending on the sign of shear) with a lobe in the opposite direction on the opposite edge of the plate. Such symmetry provides an attractive explanation for the autocatalytic formation of precipitate arrays. It is consistent both with the stacks of parallel plates and for the cross-like arrays of alternating (100) and (001) habit planes. In conclusion it should be stressed that the interaction energy of the sheared nucleus and the tetragonal defect promotes nucleation above or below the edges of the primary plate.

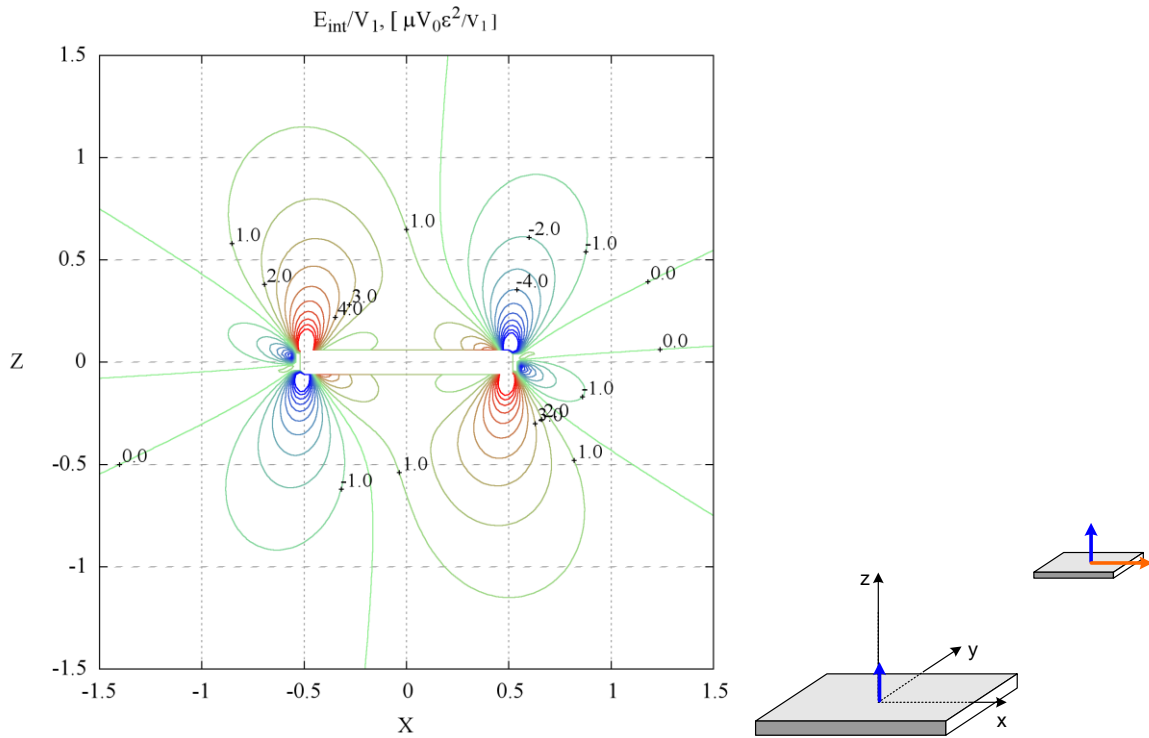


Fig. 31 Interaction energy density between the large plate of tetragonal strain and the nucleus of generalised strain. Plates are in the parallel orientation, with a positive shear in the nucleus.

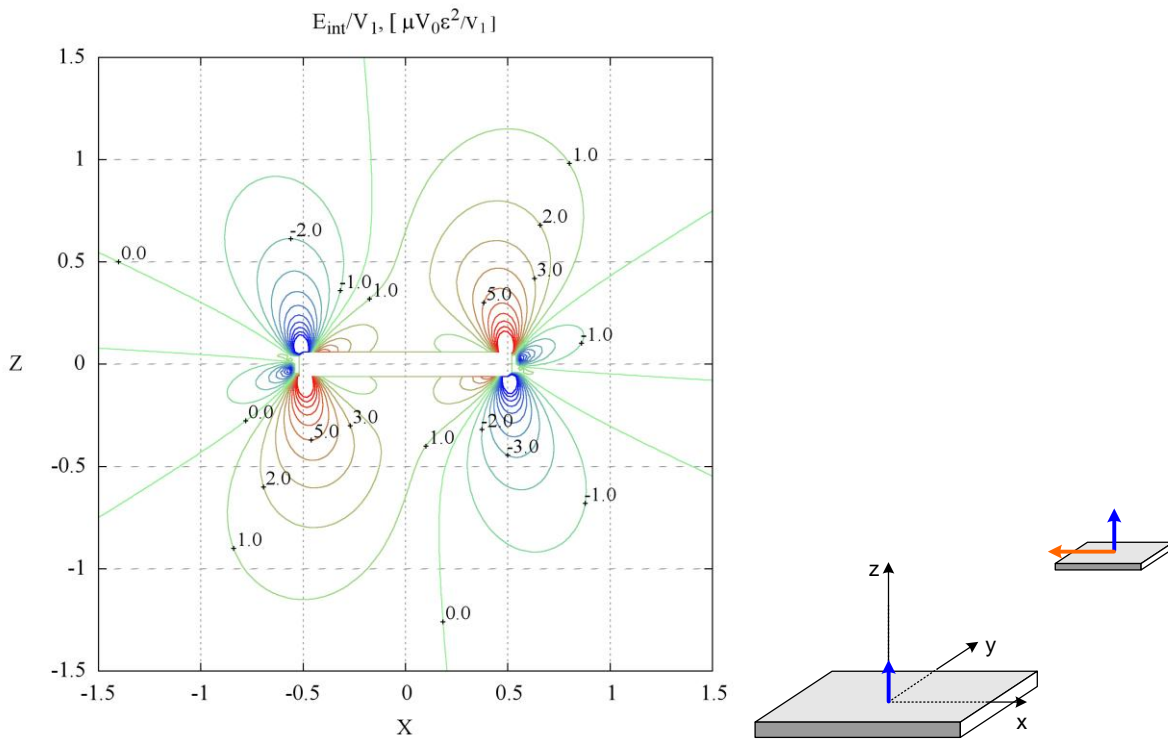


Fig. 32 Interaction energy density between the large plate of tetragonal strain and the nucleus of generalised strain. Plates are in the parallel orientation, with a negative shear in the nucleus.

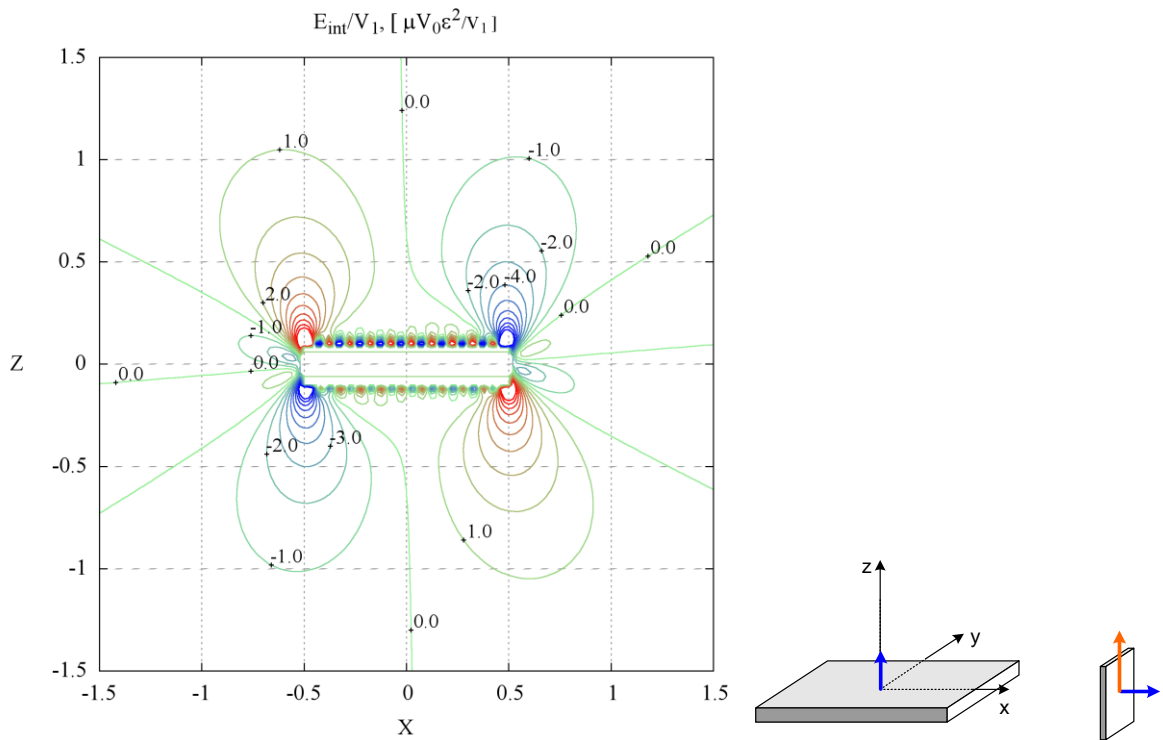


Fig. 33 Interaction energy density between the large plate of tetragonal strain and the nucleus of generalised strain. Plates are in the perpendicular orientation, with a positive shear in the nucleus.

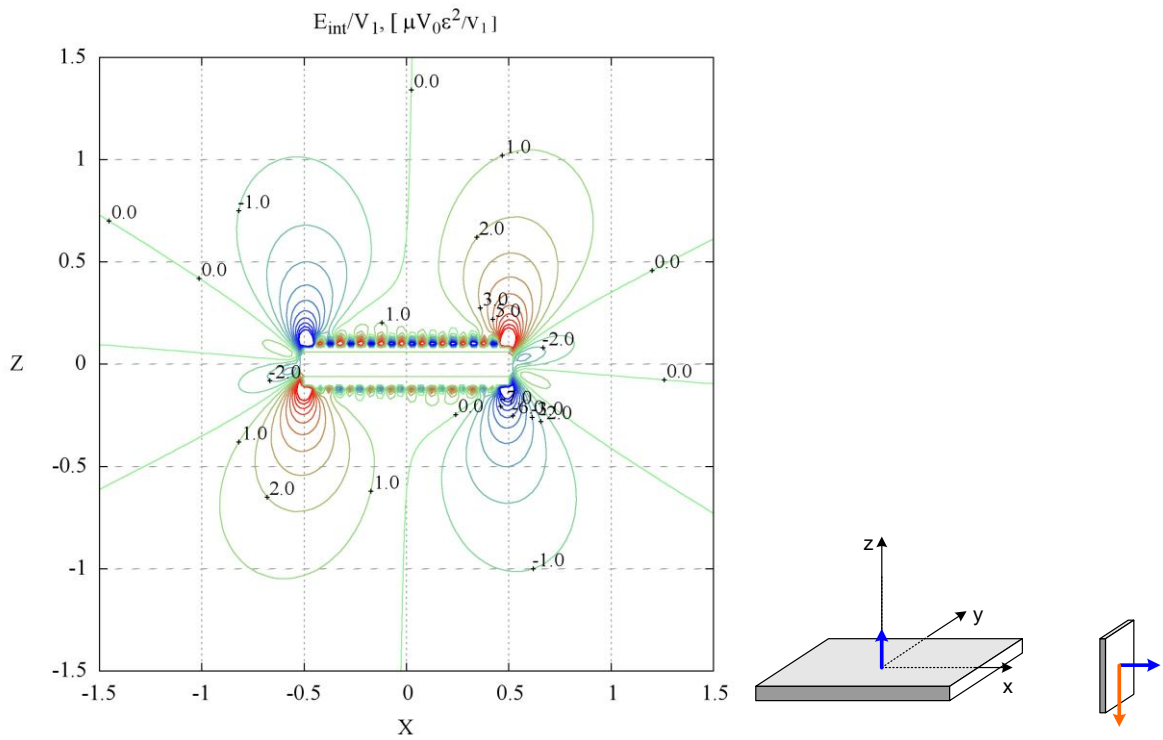


Fig. 34 Interaction energy density between the large plate of tetragonal strain and the nucleus of generalised strain. Plates are in the perpendicular orientation, with a negative shear in the nucleus.

## 4.7. Conclusions

In this chapter the application of the dislocation loop model to calculations of the interactions between platelike precipitates was considered. Various types of transformation strain and mutual orientation of precipitates have been analysed. The method was proved to be useful and an insightful tool for estimating the effect of elastic interactions on the formation of simple precipitate arrangements.

The method, however, has certain shortcomings. It only gives a distribution of the interaction energy that corresponds to the specific sizes of the plates considered. It is hard to obtain a variational derivative of the elastic energy in order to predict the evolution of the microstructure. Also, being only the mechanical part of the free energy uncoupled from chemical driving forces, it remains of limited use in actually predicting the evolution. For example, it is noteworthy that the interaction between two large precipitates generally differs from the large-to-small interaction. Although the character of the interaction energy map remains the same, the distance scale changes. This poses a problem in explaining stable arrangements because the link between the initial position of the nucleus and the final position of two or more mature plates is obscure.

The explanation of the inclined stacks of the nuclei formed with a slight displacement away from the plane containing the primary particle is questionable; because once the plate is formed, it may only thicken and grow laterally, but not move in the direction normal to the habit plane. In experimental micrographs the offset is relatively large, in the order of tens of nanometres, whereas the dislocation loop model predicts the initial offset of the nucleus comparable with the thickness of the plates. In the same way it is hard to trace how the nucleus of the perpendicular variant, which is supposed to form very close to the edge of a large plate, may later on develop into a secondary plate of comparable size and at a distance approximately equal to length of the plates.

Thus in order to estimate the effect of the elastic interactions on precipitate distributions one needs to account simultaneously for the chemical driving forces, interfacial energy and elastic energy in a unified approach. Such a method, based on the diffuse-interface theory will be presented in the next chapter.

## 5. Phase field model

In this chapter the diffuse-interface phase field model is presented, as applied to the study of the autocatalytic nucleation of platelike precipitates with the generalised form of transformation strain.

The basics of the method are discussed in the most general terms, together with its applications to phase transformations. Representation of chemical, gradient and elastic energy terms is given in detail. The method of incorporating nucleation events into simulation is described. Finally, the evolution equations and numerical aspects of their solution are discussed.

### 5.1. Basics of the phase field approach

Real material systems are usually inhomogeneous, with domains that can be distinguished by one or another characteristic. Domains may be different in their structure and/or composition. This description is broadly applicable to a variety of structures like spatially distributed phases of different composition and/or crystallography, distributions of domains in different aggregate states (in melting and solidification), grains of different orientations, domains of electrical or magnetic polarisations, etc. Evolution of a microstructure is a process driven by the reduction in total energy of a system.

Analysis of microstructure evolution is often complex and requires a numerical approach. In a conventional, sharp-interface approach, the interfaces that separate domains are treated as infinitely thin, and their local velocity is determined via local driving forces and interface mobility. Such an approach is extremely demanding computationally due to the need to track explicitly all the interfaces present in the system.

The phase field method provides an alternative proven to be a flexible and powerful technique of numerical simulations. It is based on the diffuse interface description from the classical works of Cahn and Hilliard [25-27] where the energy of the non-uniform system has been described as a functional of local energy density and gradient terms, which account for the additional energy in the transition regions. Allen and Cahn [112] later applied the formalism to systems with only structural, rather than compositional inhomogeneities. Once the form of the free energy functional is established via field variables, the evolution of a system towards equilibrium is described by the set of continuum equations: the Cahn-Hilliard nonlinear diffusion

equation for conserved variables [113] and the Allen-Cahn equation for non-conserved field variables [112]. With random thermal noise terms in the evolution equations they become stochastic and can describe metastable systems and critical phenomena [114].

Field variables on which the energy functional depends could represent a certain physical characteristic like composition of the phase or a long-range order parameter. Alternatively the field variable may be introduced just to distinguish domains logically, for instance liquid from solid in solidification and melting models. In both cases the mapping of the phase field model parameters to real physical quantities can either possibly be found directly (derived from thermodynamic and kinetic characteristics of the system) or done by asymptotic analysis.

The phase field method is based on the coarse-grain representation of the free-energy density, and as such models the system on the mesoscale. Sharp interface descriptions of microstructure evolution may be derived from phase field equations as a limiting transition.

The phase field formalism often perceived as phenomenological has been proved by Cahn [26] to be completely analogous to the thermodynamic treatment of inhomogeneous systems [115]. It has also been demonstrated that the evolution equations may be derived directly from the statistical mechanics description of a metastable system, see Langer [116, 117] and Shen [118].

The phase field method provides a number of advantages over sharp interface models, because there is no need to track interfaces explicitly and the whole microstructure is described in a unified approach by the solution to the evolution equations. There is also a great flexibility to account for difficult long-range interactions, built into the energy minimisation process. These advantages have made phase field simulations a very popular technique applied to a variety of systems and processes, from solidification and solid-state transformations to grain growth, dislocation dynamics and many others [119].

In the following sections the ingredients of the phase field model will be presented in detail in context of coherent precipitation in solids. Components of a free energy functional will be introduced, gradient terms and their influence on interfacial properties will be explained and the evolution equations described.

## 5.2. Energy functional

The diffuse interface approach describes a system as a whole with a set of continuous variables, or phase fields. Phase fields are smooth continuous functions throughout the system. There are two types of field variables, conserved and non-conserved. Conserved variables must satisfy local conservation conditions and are related to compositional fields, i.e. the concentration of a particular component in alloy system. Non-conserved fields are those free from conservation conditions and may represent physically defined order parameters or are introduced arbitrarily as a mean to distinguish structurally different domains (phases of similar composition but different structure, grains of different orientation, etc.).

The total free energy of the system is then defined by the Ginzburg-Landau type functional via  $N$  conserved variables  $c_n$  and  $M$  non-conserved variables  $\eta_m$  as [119]

$$F = \int \left[ f(c_1, \dots, c_N, \eta_1, \dots, \eta_M) + \sum_{n=1}^N \frac{\kappa_n}{2} (\nabla c_n)^2 + \sum_{i=1}^3 \sum_{j=1}^3 \sum_{m=1}^M \frac{k_{ij}}{2} \nabla_i \eta_m \nabla_j \eta_m \right] d^3r + E_{nonlocal} \quad (5.1)$$

where  $f(c_1, \dots, c_N, \eta_1, \dots, \eta_M)$  is the local energy density defined as a function of field variables,  $\kappa_n$  and  $k_{ij}$  are gradient energy coefficients, and the integration is over the volume of a system. The first term is a volume integral that covers the local chemical contributions and the gradient energy terms. The gradient terms add an additional energy of interfaces and fluctuations; they deviate from zero only at or in the vicinity of the interfaces. The second term is the energy associated with long range interactions present in the system, such as elastic, electrostatic, magnetic or others.

### 5.2.1. Local free energy

The central component of any phase field model is a local energy density, which is defined as a function of field variables. This function may be related directly to the chemical free energy of the system, defined via physically meaningful field variables (composition, long-range order parameter, electric polarisation, etc.) and matched to thermodynamic databases. Alternatively the local energy density may be any function of field variables with minima that correspond to

distinct domains in the microstructure, and the choice of parameters will control the driving forces for interface motion.

One widely used example, especially in solidification models, is a double-well potential presented in Fig. 35:

$$f(\eta) = 4\Delta f\left(\frac{\eta^4}{4} - \frac{\eta^2}{2}\right) \quad (5.2)$$

where  $\eta$  is a field variable and  $\Delta f$  is a scaling parameter.

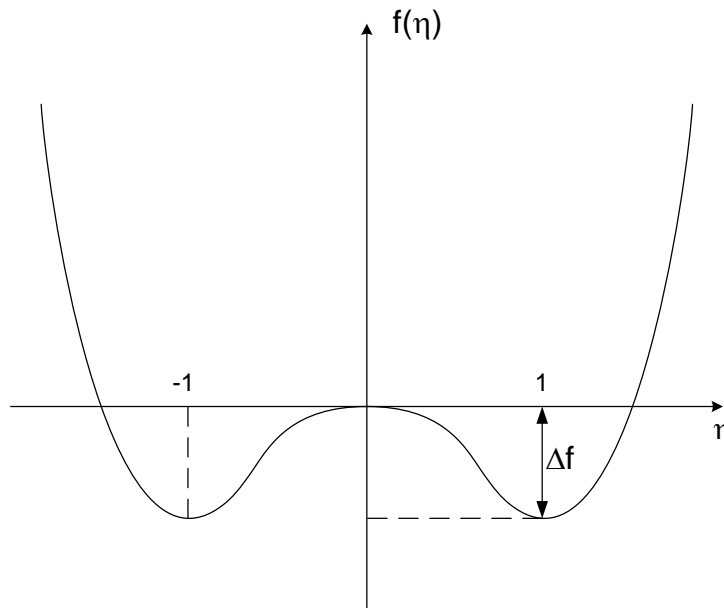


Fig. 35 Double-well potential.

The double-well potential has two minima at  $\eta = -1$  and  $\eta = 1$ . The character (conserved or non-conserved) and the meaning of  $\eta$  can be different in particular models and may represent solid and liquid states, phases with different composition or two antiphase domains. The common feature is that the energy is minimised for the microstructure in either of the two minimum states of the field variable, and the magnitude of the scaling parameter  $\Delta f$  defines the driving force for the decomposition and also affects the properties of the interface.

For solid-solid transformations Landau type polynomial expansions in long-range order parameters are often used to approximate the free-energy [56, 57, 120, 121]. The polynomial should be invariant with respect to the symmetry operations of the parent phase and must have

degenerate minima that represent energetically equivalent orientations of the product phase. An example of such a polynomial expansion for the  $\theta'$  phase in the fcc Al-Cu system is given by Li and Chen [56] as

$$\begin{aligned}
f(c, \eta_1, \dots, \eta_M) &= A_1(c - c_1)^2 + A_2(c - c_2) \sum_{p=1}^M \eta_p^2 + A_3 \sum_{p=1}^M \eta_p^4 + A_4 \sum_{p=1}^M \eta_p^6 \\
&+ A_5 \sum_{p \neq q}^M \eta_p^2 \eta_q^2 + A_6 \sum_{p \neq q, p \neq r}^M \eta_p^4 (\eta_q^2 + \eta_r^2) + A_7 \sum_{p \neq q \neq r}^M \eta_p^2 \eta_q^2 \eta_r^2
\end{aligned} \tag{5.3}$$

The coefficients in the polynomial expansions are fitted to the thermodynamical databases for the free energy of the phases considered. The temperature dependence of the free-energy can also be accounted for by temperature dependent coefficients.

### 5.2.2. Gradient energy terms

The free energy functional given in equation (5.1) includes the local-density function as an integrand, and also the gradient terms. Gradient terms are essentially the Taylor expansion required to account for non-uniformity in the local energy density. The functional is usually limited to the second-order in field variables gradients, with higher orders neglected.

Coefficients  $\kappa_n$  and  $k_{ij}$  define the “weight” of the contribution from regions of strong change in field variables and directly affect the properties of interfaces in the system, namely the thickness of the interface and its energy.

In a simplified example of the single field variable  $\eta$  in the one-dimension system, and the free-energy functional of the following form

$$F = \int \left[ f(\eta) + \frac{k}{2} (\nabla \eta)^2 \right] d^3r \tag{5.4}$$

the parameters of the flat interface may be derived according to Cahn [25] as

$$\sigma = 2 \int_{\eta_1}^{\eta_2} d\eta \sqrt{\frac{k \Delta f(\eta)}{2}} \quad (5.5)$$

for the interfacial energy, and

$$l = (\eta_2 - \eta_1) \sqrt{\frac{k}{2 \Delta f_{max}}} \quad (5.6)$$

for the width of the interface.

The parameters of the equations (5.5) and (5.6) are explained in Fig. 36. The local energy density has two minima corresponding to the field variable equilibrium values  $\eta_1$  and  $\eta_2$ . The difference between the local energy density and the common tangent construction is designated as  $\Delta f(\eta)$ , with its maximum value being  $\Delta f_{max}$

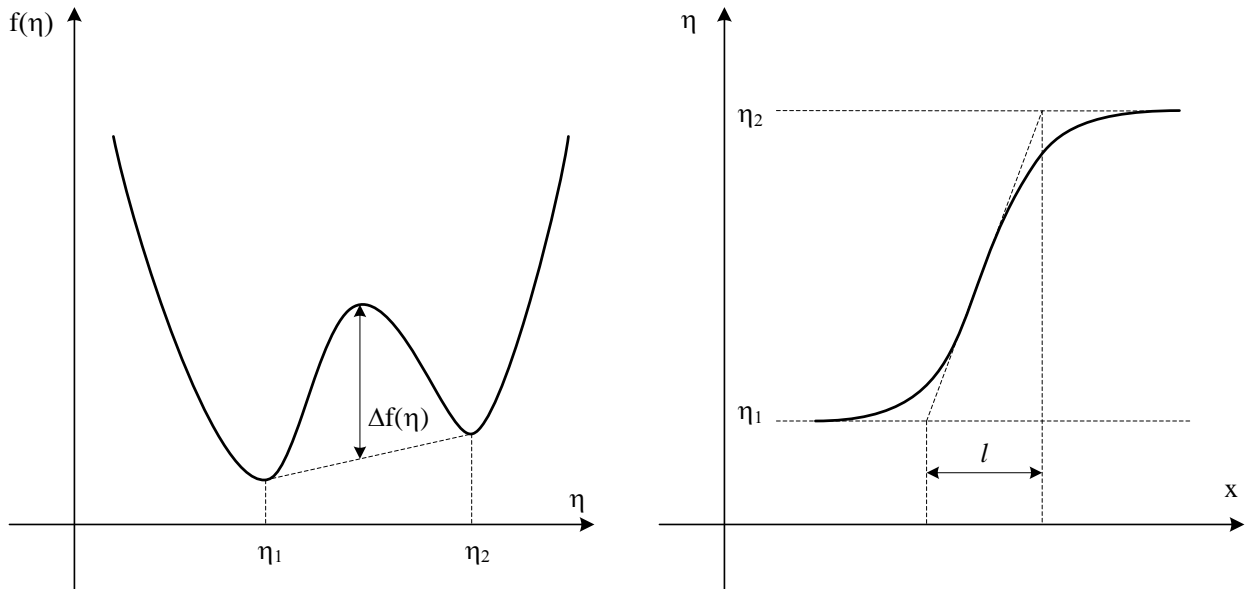


Fig. 36 The local free energy density as a function of the field variable, and the interface established between two regions of equilibrium minimum values. The width of the interface is shown as  $l$ .

In systems where the local energy density becomes a function of more than one phase field expressions for interfacial energy and width become more complicated, but the general dependence of  $\sigma \approx \sqrt{k \Delta f_{max}}$  and  $l \approx \sqrt{k / \Delta f_{max}}$  still holds true.

### 5.2.3. Elastic energy

The section on Khachaturyan's theory of elasticity has discussed earlier how the elastic energy of an arbitrary microstructure can be derived. The solution obtained is expressed via the Fourier transform of a shape function, which is equal to unity inside the coherent inclusion and equal to zero elsewhere in the system, and was given in equation (2.31) as:

$$E_{el} = \frac{1}{2} \sum_p \sum_q \int B'_{pq}(\vec{n}) \{\Theta_p(\vec{r})\} \{\Theta_q(\vec{r})\}^* \frac{d^3g}{(2\pi)^3} \quad (5.7)$$

The shape function presents a natural choice for the non-conserved field variable, which distinguishes structurally the matrix and the inclusions. It is generally possible to relate the shape function to field variables in some trivial way.

Assuming that the shape function for a certain type of product phase is expressed uniquely via single conserved or non-conserved field variable as

$$\Theta_p = g(\psi_p) \quad (5.8)$$

one may obtain the variational derivatives of elastic energy in the following form (there is no implicit Einstein summation over index  $p$ , which represents one particular inclusion type):

$$\frac{\delta E_{el}}{\delta \psi_p} = \frac{\partial E_{el}}{\partial \Theta_p} \frac{\partial \Theta_p}{\partial \psi_p} = \frac{\partial g(\psi_p)}{\partial \psi_p} \sum_q \{B'_{pq}(\vec{n}) \{\Theta_q\}\} \quad (5.9)$$

In the expression (5.9)  $\psi_p$  represents the field variables ( $c$  or  $\eta$ ), the summation by  $q$  is carried over all different types of inclusions in the system and the external parentheses under summation represent backward Fourier transform.

### 5.3. Evolution equations

Once the free energy of the system has been defined in the form (5.1), the dynamic evolution of the field variables is obtained by solving the corresponding evolution equation. According to the type of the field variable there are two types of dynamic equations: the Cahn-Hilliard equation for conserved variables [113]; and the Allen-Cahn equation, otherwise known as time-dependent Ginzburg-Landau, for non-conserved variables [112].

The Cahn-Hilliard equation, initially derived for spinodal decomposition, is a generalised form of the diffusion equation and has a form

$$\frac{\partial c_i(\vec{r}, t)}{\partial t} = \nabla M_c \nabla \frac{\delta F}{\delta c_i(\vec{r}, t)} \quad (5.10)$$

Where  $c_i$  is a conserved field variable,  $M_c$  is a mobility coefficient (which is related to atomic mobility or diffusion coefficient if the field variable represents concentration) and the variational derivative under the differential operator is a chemical potential of the  $i$ -th component.

The evolution of non-conserved variables is governed by the Allen-Cahn equation, first introduced to describe a motion of an antiphase boundary

$$\frac{\partial \eta_i(\vec{r}, t)}{\partial t} = -L_\eta \frac{\delta F}{\delta \eta_i(\vec{r}, t)} \quad (5.11)$$

that suggests a linear response of the evolution rate to the driving force, given again as a variational derivative of the free energy.  $L_\eta$  is an interface mobility coefficient.

The problem of microstructure evolution reduces to the solution of equations (5.10) and (5.11), which is usually obtained numerically by various methods, most often with simple finite-difference schemes on a uniform grid with explicit time-stepping.

Spectral methods are widely used in the case of periodic boundary conditions. One of the computational techniques successfully employed is a Semi-Implicit Fourier Spectral method [122]. This method benefits from a number of advantages; it allows, for example, the use of relatively sparse grids, and increased time intervals, and it treats the elastic energy term conveniently using an existing analytical solution in Fourier space.

## 5.4. Treatment of thermally activated processes

The set of Cahn-Hilliard and Allen-Cahn equations is sufficient to follow the changes that develop in the arbitrary microstructure, given that there is a non-equilibrium and inhomogeneous distribution present in the system as an initial condition. However, often the goal of the simulation is to model an activated process, like the phase transformation in a metastable system. To mimic the effect of thermal fluctuations it is required to disturb the initially homogeneous metastable system by some stochastic process, variations of which are discussed next.

### 5.4.1. Langevin noise approach

The most widely applied method of simulating thermal fluctuations is to introduce random Langevin noise terms into the evolution equations [123]:

$$\frac{\partial c_i(\vec{r}, t)}{\partial t} = \nabla M_c \nabla \frac{\delta F}{\delta c_i(\vec{r}, t)} + \xi_c(\vec{r}, t) \quad (5.12)$$

$$\frac{\partial \eta_i(\vec{r}, t)}{\partial t} = -L_\eta \frac{\delta F}{\delta \eta_i(\vec{r}, t)} + \xi_\eta(\vec{r}, t) \quad (5.13)$$

Noise terms in (5.12) and (5.13) should have Gaussian distributions and must satisfy the requirements of the fluctuation-dissipation theorem [124] for the mean values, spatial and temporal correlation of random force (noise), given below

$$\begin{aligned} \langle \xi_c(\vec{r}, t) \rangle &= 0 \\ \langle \xi_\eta(\vec{r}, t) \rangle &= 0 \\ \langle \xi_c(\vec{r}, t) \xi_c(\vec{r}', t') \rangle &= -2k_B T M_c \delta(t - t') \nabla^2 \delta(\vec{r} - \vec{r}') \\ \langle \xi_\eta(\vec{r}, t) \xi_\eta(\vec{r}', t') \rangle &= 2k_B T L_\eta \delta(t - t') \delta(\vec{r} - \vec{r}') \end{aligned} \quad (5.14)$$

where  $k_B$  is the Boltzmann constant,  $T$  the temperature,  $\delta$  is a delta-function and  $M_c$  and  $L_\eta$  are mobility coefficients. In discrete form on a uniform spatial and temporal grids the conditions (5.14) may be expressed as (Shen et al. [125] and Rogers et al. [126]):

$$\begin{aligned} \langle \xi_c(n, m) \rangle &= 0 \\ \langle \xi_\eta(n, m) \rangle &= 0 \\ \langle \xi_c(n, m) \xi_c(n', m') \rangle &= -2k_B T M_c \frac{\delta_{mm'}}{\Delta t} \nabla^2 \frac{\delta_{nn'}}{\lambda^d} \\ \langle \xi_\eta(n, m) \xi_\eta(n', m') \rangle &= 2k_B T L_\eta \frac{\delta_{mm'}}{\Delta t} \frac{\delta_{nn'}}{\lambda^d} \end{aligned} \quad (5.15)$$

where  $n$  and  $m$  are indices of discrete positions in space in time,  $\lambda$  and  $\Delta t$  are grid steps and  $d$  is the dimensionality of the problem,  $\delta$  is Kronecker's delta. During a simulation noise terms may be introduced using a random number generator, for example following the procedure given by Shen et al. in [125].

Langevin equations (5.12) and (5.13) in theory provide a solid basis for simulation of all thermally activated processes in a microstructure, including nucleation. However, quantitative phase field simulations of nucleation by noise terms in the evolution equations have certain limitations [118, 125]. These limitations arise from the differences in time and length scales of the phase field simulation, which occurs on the mesoscale, and the characteristic times and length involved in the nucleation event, which often takes place on the atomic scale. In essence the coarse-grained energy functional should by definition be “blind” towards any events smaller in scale than the grid step of the phase field model. Similar considerations are applicable to the time step, which needs to be impractically small to allow for tracking nucleation events.

To overcome these difficulties an alternative procedure of introducing overcritical nuclei into phase field simulation has been developed recently and is described in the next section.

#### **5.4.2. Explicit nucleation algorithm**

The explicit nucleation algorithm was developed by Simmons, Shen and Wang [127] and is presented in detail in [118]. In contrast to the Langevin approach, where noise terms in the phase field evolution equations are used to disturb the metastable equilibrium in the initial stages of simulation and are turned off later on, the explicit nucleation algorithm is a procedure that works in parallel with phase field time stepping.

Explicit algorithm is a stochastic model, which introduces the nuclei into a microstructure explicitly, with the nucleation rate predicted by nucleation theory (homogeneous or heterogeneous) or calibrated to experimental data.

Assume that the nucleation rate  $J$  at the given point in time is defined as a function of field parameters. Let  $\Delta t$  be the time step of the phase field simulation and  $\Delta V$  be the volume of the phase field simulation cell. Under assumptions that the time required for the nucleation event is much less than  $\Delta t$ , and that the nucleation event anywhere within the phase field cell transforms the whole cell the probability of the phase field cell to be transformed is given by

$$P = 1 - \exp(-J \Delta t \Delta V) \quad (5.16)$$

During the simulation the uniformly distributed random variable is generated in every phase field cell and compared to the probability of nucleation at this location, which is given by (5.16). If the random variable is less than  $P$  the cell is considered transformed and the nucleus is introduced manually at this location.

This procedure is non-trivial because of possible nuclei overlap and requirements of mass balance. In the current work nuclei are seeded without adjusting the conserved phase field that represents solute composition. As demonstrated by Russell [28], sub-critical clusters on average are surrounded by a matrix enriched in solute, with critical size clusters surrounded by a matrix of average composition. The depletion field around a nucleus introduced by the explicit nucleation algorithm has a timeframe for development less or equal to  $\Delta t$  and therefore may be neglected for simplicity.

Specific choice of the nucleation rate expression is described later in the section 6.3 “Strain assisted nucleation”.

## 5.5. Kim-Kim-Suzuki construction of the local free energy function

The formulation of a phase field model for a particular material system starts from an expansion of its chemical free energy as a function of field variables. Such an expansion could be done in the form of a Landau polynomial (5.3). The polynomial must reflect the symmetry of a parent phase and have degenerate minima representing various orientations of the transformation product.

Consider the following free energy polynomial, used in phase field models of precipitation in Al-Cu and Ti-Ni alloys [56, 57] and illustrated with an example presented in Fig. 37:

$$f(c, \eta) = A_1(c - c_\alpha)^2 + A_2(c - c_\beta)\eta^2 + A_4\eta^4 + A_6\eta^6 \quad (5.17)$$

$$\begin{aligned} c_\alpha &= 0.001, c_\beta = 0.33 \\ A_2 &= -0.658 A_1, A_4 = -0.3257 A_1, A_6 = 0.2165 A_1 \end{aligned} \quad (5.18)$$

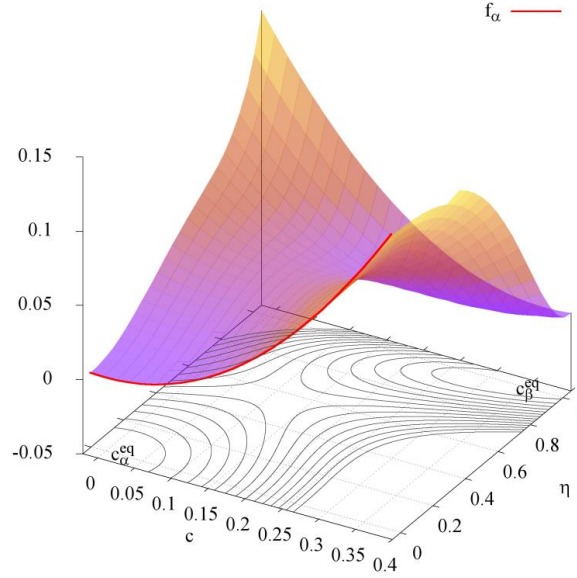


Fig. 37 Landau polynomial free energy construction.

The coefficient  $A_1$  is selected to approximate the solid solution free energy at  $\eta = 0$  as  $f_\alpha = f(c, 0)$  and the product phase is represented by minimizing the energy with respect to the structural order parameter  $f(c, \eta^*(c))$ . The equilibrium interface traces the minimum excess energy transformation path in  $c - \eta$  space, passing through the saddle point. Based on the value of the saddle point energy barrier  $\Delta f_{max}$  the gradient coefficient  $k_\eta$  is selected to obtain the interfacial energy as  $\sigma \approx \sqrt{k_\eta \Delta f_{max}}$ . The interface width would then be fixed as  $l \approx \sqrt{k_\eta / \Delta f_{max}}$  dictating the grid step of the numerical scheme. This procedure leaves no degrees of freedom for scaling a model to improve computational efficiency by diffusing the interface and employing sparser grids. Any attempts to change the gradient coefficients and/or energy barrier would also affect the interfacial energy and/or full energy landscape, therefore representing different material systems.

These constraints were analysed in detail by Shen [118]. It has been suggested that for simulations focused on one particular aspect of microstructure evolution it is possible to model a different system, which has an identical rate controlling parameter. For example for anti-phase domain coarsening and grain growth the rate is controlled by the gradient coefficient, thus a phase field model with lower  $\Delta f_{max}$  exhibits the same morphology, albeit with a different interfacial energy, which must be mapped back to the actual energy  $\sigma = \sigma^{sim} \sqrt{\Delta f_{max} / \Delta f_{max}^{sim}}$  for an interpretation of results. While modelling precipitate growth the gradient coefficient may be increased, and  $\Delta f_{max}$  kept constant for maintaining the same energy landscape to keep the

diffusion behaviour unaltered. Finally, in simulating coarsening, which is governed by interfacial energy, one may keep the  $k_\eta \Delta f_{max}$  product constant but increase the  $k_\eta / \Delta f_{max}$  ratio.

For a simulation of processes with constraints on both the interface properties and bulk phase processes (concurrent growth and coarsening) special measures are required if interface width change is needed. Shen [118] suggests employing a selective rescaling of the energy landscape to reduce  $f(c, \eta)$  specifically in the vicinity of the transformation path. In doing so the interface becomes wider; however, diffusion in the bulk phase is unchanged. Although an effective way to overcome the effect of  $\Delta f_{max}$  on bulk behaviour, this makes the model more demanding in terms of numerical stability because the characteristic curvature of the energy landscape becomes higher in the vicinity of the transformation path.

An alternative method of constructing the chemical free energy expansion is the Kim-Kim-Suzuki (KKS) model [128], originally developed in the context of solidification modelling and later applied by Hu [129] to precipitation. Consider a transition between matrix phase  $\alpha$  and product phase  $\beta$ . The free energy of the bulk phases may be available from thermodynamical databases or represented by a regular solution model and would be a function of temperature and composition, or even only temperature for stoichiometric phases like  $\theta'$ . These functions  $f_\alpha(c, T)$  and  $f_\beta(c, T)$  serve as the basis for  $f(c, \eta_i)$ . The KKS model represents the interfacial transitional region as mixture of the two phases with different compositions of equal chemical potential, i.e. satisfying the following conditions:

$$c = [1 - h(\eta)]c_\alpha + h(\eta)c_\beta \quad (5.19)$$

$$\frac{\partial f_\alpha(c_\alpha, T)}{\partial c_\alpha} = \frac{\partial f_\beta(c_\beta, T)}{\partial c_\beta} \quad (5.20)$$

The structural non-conserved variable  $\eta$  is employed to combine  $f_\alpha(c, T)$  and  $f_\beta(c, T)$  into the singular chemical free energy polynomial  $f(c, \eta, T)$ , with  $\eta = 0$  and  $\eta = 1$  energy minima distinguishing the two:

$$f(c, \eta, T) = [1 - h(\eta)]f_\alpha(c_\alpha, T) + h(\eta)f_\beta(c_\beta, T) + Wg(\eta) \quad (5.21)$$

The function  $h(\eta)$  is a smooth transition function changing between 0 and 1 as  $\eta$  changes between the minima distinguishing the two phases. The physical meaning of this function is a volume fraction of the product phase in a mixture of matrix and product of equal chemical potential. One example of the transition function, employed by Hu [129, 130] is

$$h(\eta) = 3\eta^2 - 2\eta^3 \quad (5.22)$$

Generally, to evaluate the chemical free energy at some composition  $c$  and structural order parameter  $\eta$  it is required additionally to solve the system of equations (5.19) - (5.20) and obtain  $c_\alpha$  and  $c_\beta$ . However, for the simple parabolic approximation of bulk chemical energies in the vicinity of equilibrium compositions

$$\begin{aligned} f_\alpha &= A(T)(c - c_\alpha^{eq})^2 \\ f_\beta &= B(T)(c - c_\beta^{eq})^2 \end{aligned} \quad (5.23)$$

there exists an analytical solution:

$$f(c, \eta, T) = \frac{A(T)B(T) \left[ c - c_\alpha^{eq} - (c_\beta^{eq} - c_\alpha^{eq})h(\eta) \right]^2}{B(T) + [A(T) - B(T)]h(\eta)} + Wg(\eta) \quad (5.24)$$

It is obvious from (5.24) that in the absence of a second term the energy is minimised on the common tangent plane between  $f_\alpha(c, T)$  and  $f_\beta(c, T)$  exactly along the following  $c - \eta$  path (Fig. 38):

$$c_{min}(\eta) = c_\alpha^{eq} + (c_\beta^{eq} - c_\alpha^{eq})h(\eta) \quad (5.25)$$

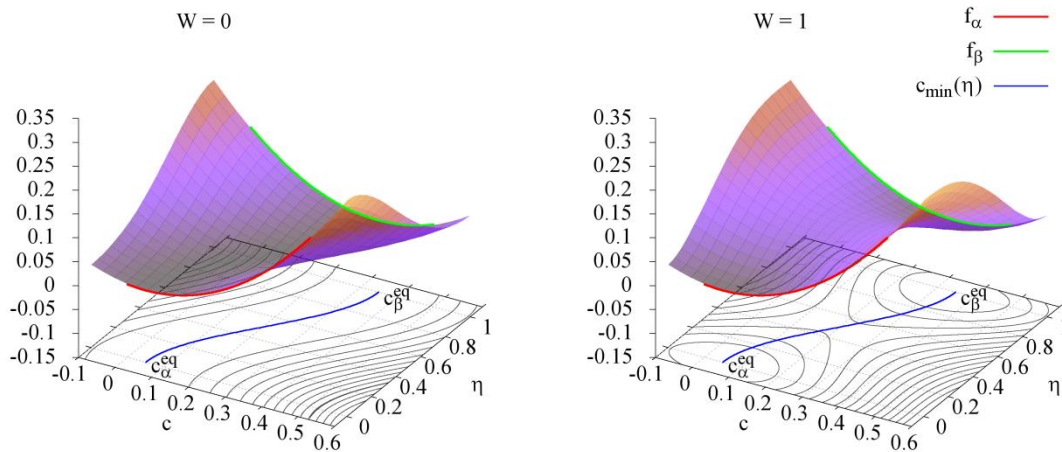


Fig. 38 Kim-Kim-Suzuki construction of the chemical free energy for the multiphase mixture of  $\alpha$  and  $\beta$  phases with  $A(T) = B(T) = 1$  and  $W = 0$  on the left, without double well potential imposed, and  $W = 1$  on the right. Energy is minimised along the transformation path  $c_{min}(\eta)$  exactly on the common tangent plane.

The double well potential  $Wg(\eta)$  introduces an energy barrier to separate the  $\alpha$  and  $\beta$  phases. The height of this barrier is determined by  $W$  but does not affect the branches that correspond to bulk matrix and precipitate phases,  $f(c, \eta = 0, T)$  and  $f(c, \eta = 1, T)$ , as illustrated in Fig. 38. Interface properties in such a model become separated from bulk properties to a certain extent, which will be discussed in more details in the next section.

Thus, as explained above, the Kim-Kim-Suzuki representation of chemical free energy offers several advantages over Landau type polynomials:

- Firstly, it allows breaking the link between the properties of a diffuse interface (its energy and thickness) from the description of free energies of bulk phases. In doing so one degree of freedom becomes available for the scaling of the phase field model independently of diffusion in the bulk, i.e. the interface could be made more diffuse without affecting transformation driving forces.
- Secondly, evolution equations are simplified because there is no gradient energy term for a conserved field variable. Consequently, the Cahn-Hilliard equation order is lowered from fourth to second. This significantly relaxes the stability constraints on the time step of the numerical scheme employed ( $\Delta t_{max} \sim \Delta x^n$  where  $n$  is the differential equation order).

Based on the relative advantages of the KKS model the approach was adopted exclusively for all phase field simulations in this project. Since it was demonstrated by Hu [130] that growth kinetics are insensitive to the particular approximation used for the precipitate phase, for the sake of simplicity bulk free energies are approximated by parabolic functions (5.23) with similar curvatures:

$$f(c, \eta, T) = A(T) \left[ c - c_{\alpha}^{eq} - (c_{\beta}^{eq} - c_{\alpha}^{eq})h(\eta) \right]^2 + Wg(\eta) \quad (5.26)$$

The parabolic approximation is fitted to reproduce the overall driving force at the initial composition and appropriate transformation temperature. Based on a common tangent construction between the Gibbs free energies of the binary solid solution and  $\theta'$  phase (estimated from SGTE [103] or Murray assessment [131]) the driving force  $G(c_0, T)$  translates into the curvature of a parabolic fit as

$$A(T) = \frac{G(c_0, T)}{(c_0 - c_{\alpha}^{eq})^2} \quad (5.27)$$

The double well potential employed is given by

$$g(\eta) = \eta^2(1 - \eta)^2 \quad (5.28)$$

In the absence of elastic energy the variational derivatives reduce to

$$\begin{aligned} \frac{\delta F}{\delta c} &= \frac{\partial f}{\partial c} = 2A(T) \left[ c - c_\alpha^{eq} - (c_\beta^{eq} - c_\alpha^{eq})h(\eta) \right] \\ \frac{\delta F}{\delta \eta} &= \frac{\partial f}{\partial \eta} - k_\eta \nabla^2 \eta = \\ &= -2A(T) \left[ c - c_\alpha^{eq} - (c_\beta^{eq} - c_\alpha^{eq})h(\eta) \right] (c_\beta^{eq} - c_\alpha^{eq}) \frac{\partial h(\eta)}{\partial \eta} \\ &\quad + W \frac{\partial g(\eta)}{\partial \eta} - k_\eta \nabla^2 \eta \end{aligned} \quad (5.29)$$

Subsequently, the evolution equations transform to

$$\begin{aligned} \frac{\partial c}{\partial t} &= 2M_c A(T) \left[ \nabla^2 c - (c_\beta^{eq} - c_\alpha^{eq}) \nabla^2 h(\eta) \right] \\ \frac{\partial \eta}{\partial t} &= 2L_\eta A(T) \left[ c - c_\alpha^{eq} - (c_\beta^{eq} - c_\alpha^{eq})h(\eta) \right] (c_\beta^{eq} - c_\alpha^{eq}) \frac{\partial h(\eta)}{\partial \eta} - L_\eta W \frac{\partial g(\eta)}{\partial \eta} \\ &\quad + L_\eta k_\eta \nabla^2 \eta \end{aligned} \quad (5.30)$$

The mobility coefficient  $M_c$  in the Cahn-Hilliard equation is selected based on the value of the diffusion coefficient ( $Q=133.9$  kJ/mol and  $D_0=4.44 \cdot 10^{-5}$  m<sup>2</sup>/s [132]):

$$2M_c A(T) = D(T) = D_0 \exp\left(-\frac{Q}{RT}\right) \quad (5.31)$$

The value of the interface mobility coefficient  $L_\eta$  can be adjusted in order to simulate appropriate growth conditions of interface-controlled, diffusion-controlled or mixed type. Specific selection will be discussed later.

The model has gradients terms only in non-conserved variables and in the simplified one-dimensional example described above this is  $k_\eta$ . The interface energy and thickness can be obtained from the following expressions [128]:

$$\begin{aligned}
\sigma &= \frac{1}{3\sqrt{2}} \sqrt{k_\eta W} = \frac{4}{3\sqrt{2}} \sqrt{k_\eta \Delta f_{max}} \approx \sqrt{k_\eta \Delta f_{max}} \\
l &= \alpha^* \sqrt{2} \sqrt{\frac{k_\eta}{W}} = \frac{2.94}{2\sqrt{2}} \sqrt{\frac{k_\eta}{\Delta f_{max}}} \approx \sqrt{\frac{k_\eta}{\Delta f_{max}}}
\end{aligned} \tag{5.32}$$

where  $\alpha^*=2.94$  for the interface width defined as the distance between the  $\eta=0.05$  and  $\eta=0.95$  levels.

It is usually convenient to convert the evolution equations into their dimensionless form, by scaling the length, energy and time of a simulation. The characteristic units for scaling are usually grid step for length, height of the energy barrier  $\Delta f_{max}$  for all energy related terms and time is rescaled to bring the dimensionless equivalent of either  $M_c$  or  $L_\eta$  to unity, i.e.

$$\begin{aligned}
\tilde{x} &= \frac{x}{l_0}; \quad \tilde{f} = \frac{f}{\Delta f_{max}}; \quad \tilde{t} = \left( \frac{M_c \Delta f_{max}}{l_0^2} \right) t \\
\tilde{M}_c &= 1; \quad \tilde{L}_\eta = \frac{L_\eta l_0^2}{M_c}; \quad \tilde{k}_\eta = \frac{k_\eta}{l_0^2 \Delta f_{max}} \approx \frac{l^2}{l_0^2}
\end{aligned} \tag{5.33}$$

The dimensionless evolution equations then take the form:

$$\begin{aligned}
\frac{\partial c}{\partial \tilde{t}} &= \tilde{\nabla}^2 \frac{\partial \tilde{f}}{\partial c} \\
\frac{\partial \eta}{\partial \tilde{t}} &= -\tilde{L}_\eta \left( \frac{\partial \tilde{f}}{\partial \eta} - \tilde{k}_\eta \tilde{\nabla}^2 \eta \right)
\end{aligned} \tag{5.34}$$

The scaling of the energy densities by the height of an energy barrier has the advantage of giving a physically meaningful interpretation to the dimensionless gradient coefficient, which becomes the squared dimensionless interface width.

## 5.6. Typical parameters of the Al-Cu phase field model

For a system of a composition Al - 1.72 at. % Cu and typical transformation temperature of 500 K, which corresponds to direct nucleation of  $\theta'$  from Al-Cu solid solution, key parameters of the model are determined according to the following procedure.

The chemical driving force  $G(c_0, T)$  and the compositions  $c_\alpha^{eq}$  and  $c_{\theta'}^{eq}$  are estimated from the common tangent construction between the Al-Cu solid solution and  $\theta'$  Gibbs free energies.

Then, using the appropriate diffusion coefficient  $D(T)$  and expressions (5.27) and (5.31), the values for the atomic mobility coefficient  $M_c$  and curvature of parabolic approximation  $A(T)$  are obtained and presented in the Table 6:

Table 6 Parameters of the parabolic approximation to the solid solution free energy, assuming the temperature of  $T = 500$  K and fitting to the transformation driving force at the composition  $c = 0.0172$ .

$D(T)$	$G(c_0, T)$	$A(T)$	$M_c$
$4.55 \cdot 10^{-19} \text{ m}^2/\text{s}$	169 J/mol	460 kJ/mol	$4.95 \cdot 10^{-25} \text{ m}^2\text{mol}/(\text{J s})$

Finally, application of (5.32) determines the gradient coefficient  $k_\eta$  and scaling coefficient for the double-well potential  $W = 16\Delta f_{max}$  from the interfacial energy  $\sigma$  and width  $l$ . Every parameter of the model, except the interface width, is rigidly defined by the specific material system. There is, however, freedom to set  $l$  according to the needs of a simulation. This will change the scaling  $W$  of an imposed double-well potential, but provided that  $W$  is not too small [129] will not affect either interface energy, or diffusion in a matrix.

For the correct performance of the employed numerical scheme it is required to sufficiently resolve the interface, i.e. to have 4-6 grid points across the interface. It is therefore assumed that  $l_0 = 0.2l$  for the example given in Table 7. It is worth noting that the dimensionless gradient coefficient remains invariant if the same resolution is maintained.

Table 7 Variation of scaling parameter for the imposed double well potential  $Wg(\eta)$  with the interfacial energy  $\sigma$  and desired interface width  $l$  of the phase field simulation.

$\sigma, \text{ J/m}^2$	$l, \text{ nm}$	$W = 16\Delta f_{max}, \text{ kJ/mol}$	$k_\eta, 10^{-10} \text{ J/m}$	$\tilde{k}_\eta = \frac{k_\eta}{l_0^2 \Delta f_{max}}$
0.6	1	96	6	25
	2	48	12	
	3	32	18	
0.2	1	32	2	
	2	16	4	
	3	10.67	6	
0.05	1	8	0.5	
	2	4	1	
	3	2.67	1.5	

An example of a simple one dimensional simulation of  $\theta'$  growth in Al-2 at. % Cu at 500 K is presented in Fig. 39. It illustrates the evolution of the compositional profile and the distribution of simulation points in the  $c - \eta$  plane.

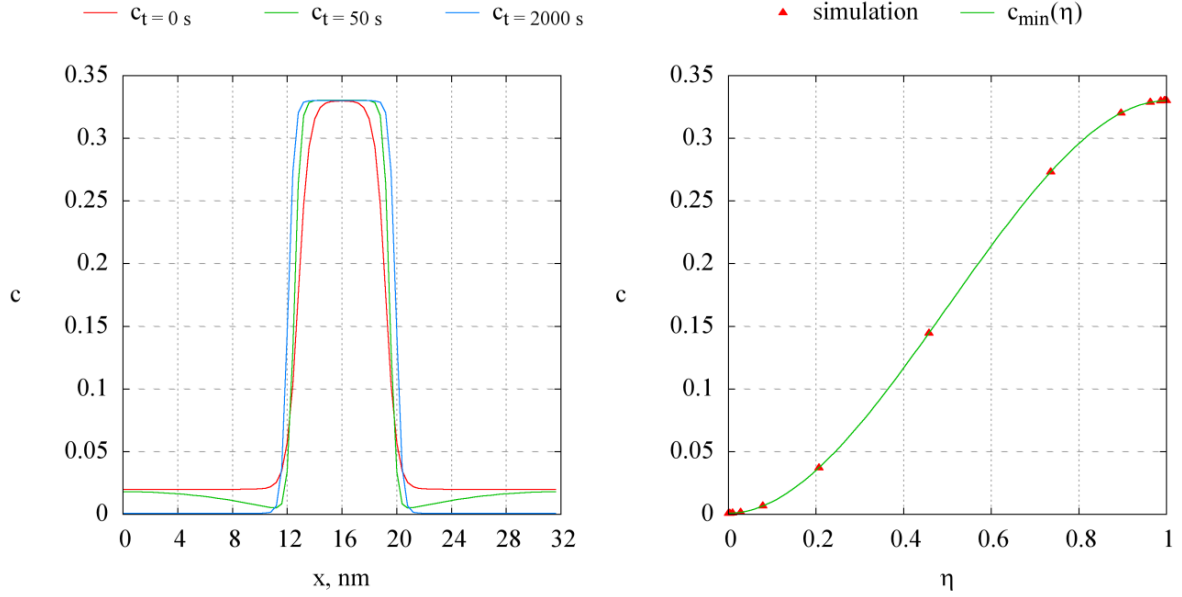


Fig. 39 Evolution of the compositional profile and the equilibrium distribution of phase variables across the interface.

The interfacial energy is assumed to be  $0.6 \text{ J/m}^2$  and the width is set to 2 nm. The system size is 32 nm with periodic boundary conditions employed and 80 grid points, giving 0.4 nm grid step and 5 grid points to resolve an interface. The initial conditions place the precipitate approximately 6.4 nm wide in the middle and then simulation follows its evolution. In the initial stage the depletion layer could be seen forming next to the interface and the interface itself assumes the shape close to an equilibrium one. At the end of the simulation (2000 s) the equilibrium composition is established both in the matrix and the precipitate. Mapping of the simulation points onto the  $c - \eta$  plane shows that within the interface the compositional and structural field variables change along the transformation path prescribed by the transitional function  $h(\eta)$ , i.e. all points are lying on the  $c_{min}(\eta)$  curve.

The equilibrium shape of the interface (Fig. 40) in the non-conserved variable follows the classical profile

$$\eta(x) = 0.5 \left( 1 - \tanh \left( x \sqrt{\frac{W}{2k_\eta}} \right) \right) \quad (5.35)$$

while the composition profile is slightly different and corresponds to the type of transition function  $h(\eta)$  used. For this reason the gradient of the compositional profile is higher and the interface is thinner. It is important to bear this in mind for appropriate selection of the grid step, as the resolution demands of the scheme used for solving the Cahn-Hilliard equation become more stringent.

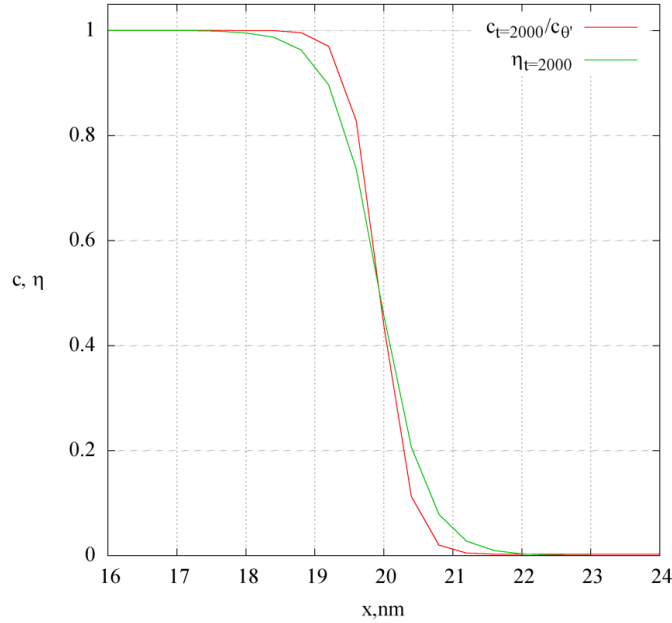


Fig. 40 Compositional and structural phase field variables across the equilibrium interface.

## 5.7. Transitional behaviour and rescaling of the interface width

The one dimensional problem of precipitate growth provides a convenient test case for the behaviour of the model. The position and velocity of a planar interface growing under conditions of diffusion control may be described by Zener's [133] analytical solution:

$$V(t) = \frac{c_0 - c_\alpha}{c_\beta - c_\alpha} \sqrt{\frac{D}{\pi t}} \quad (5.36)$$

The phase field simulation follows the analytical solution exactly, as demonstrated by the results in Fig. 41. Model rescaling does not affect the kinetic behaviour, with interface width variation between 1 nm and 5 nm having no effect on the interface position in medium to long term simulations, as illustrated in Fig. 42.

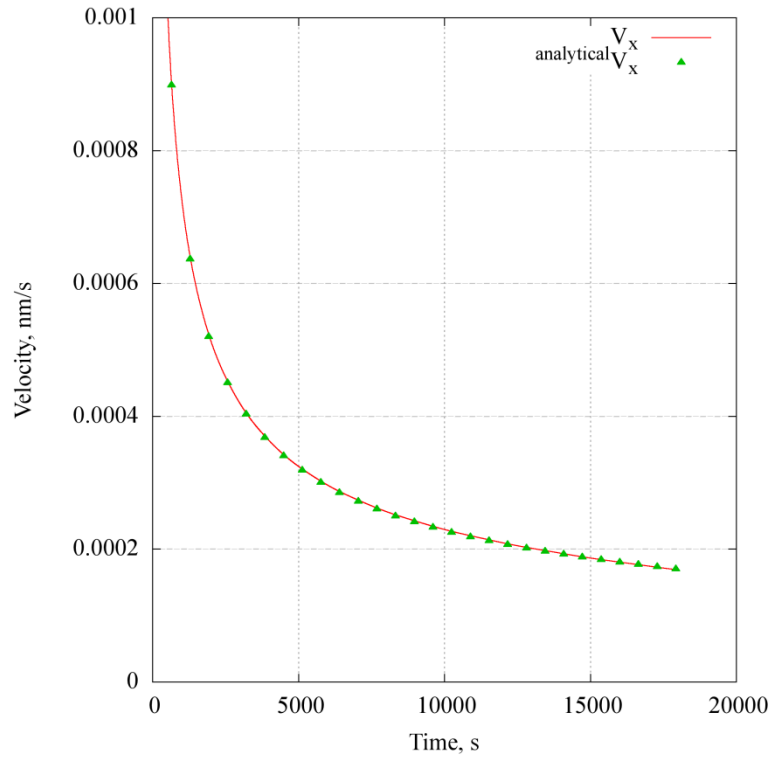


Fig. 41 Comparison of the planar interface velocity, growing in diffusion controlled mode, with the analytical solution.

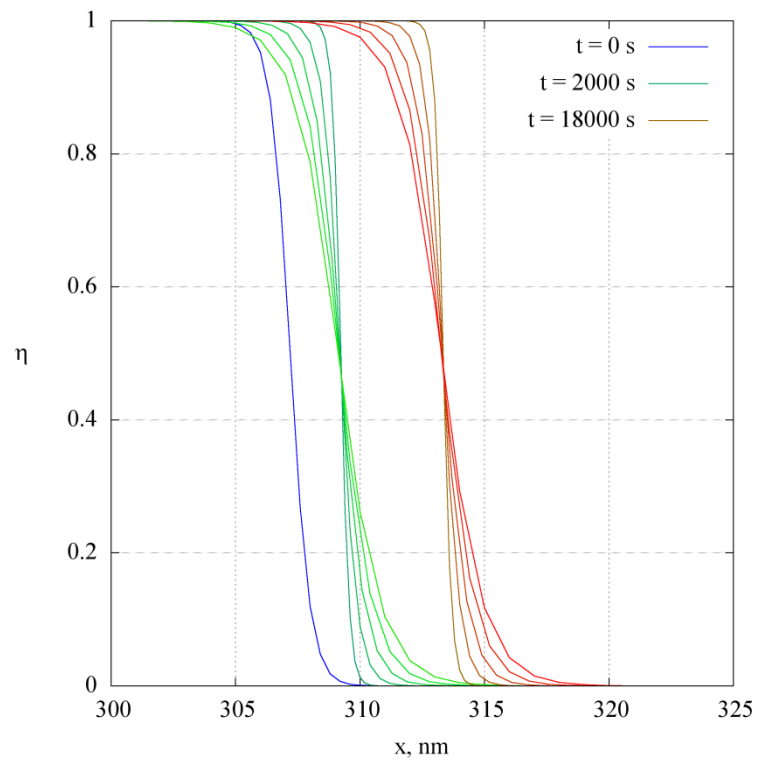


Fig. 42 Effect of the variation in the interface width on the temporal behaviour of the phase field model.

The transitional behaviour, before the equilibrium concentrations are reached both for the matrix and the precipitate, also closely follows the analytical solution [33]:

$$c(x, t) = c_0 + (c_\alpha^{eq} - c_0) \operatorname{erfc}\left(\frac{x - x_{int}}{2\sqrt{Dt}}\right) \quad (5.37)$$

Fig. 43 shows the simulation results after a relatively short ageing time of 500 s. The variation of the interface width has no effect on the interface location, and the composition profile away from the interface asymptotically approaches the analytical solution (5.37) for the sharp interface.

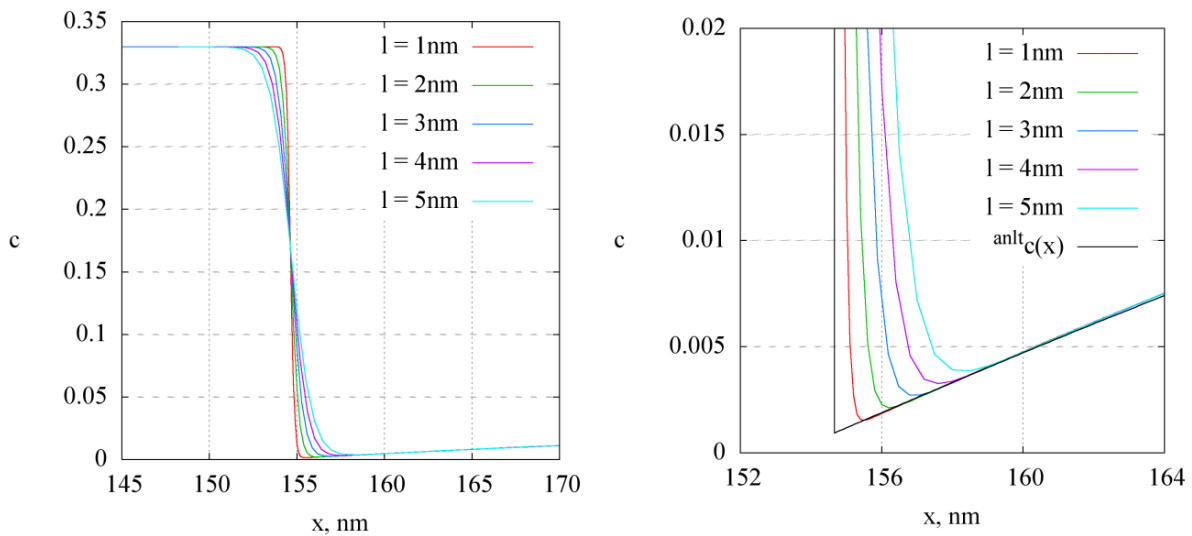


Fig. 43 Non-equilibrium interface composition profiles at  $t = 500$  s.

It is confirmed in the simple one dimensional example that Kim-Kim-Suzuki approach to the construction of the free energy density function is an easy and reliable method in excellent agreement with analytical solutions. The method, however, has certain limitations affecting numerical stability, which is discussed in the next section.

## 5.8. Limitations of the Kim-Kim-Suzuki model

Despite all the convenience offered by the KKS model in terms of simplicity in polynomial construction and flexibility in changing the length scale of the simulation, there are still limitations on the choice of the height of the imposed double well potential  $Wg(\eta)$ . Hu mentions in [129] that  $W$ , if set too small, may cause numerical instability for the model.

Unfortunately, in some cases this instability may potentially develop exactly in the range of parameters desired in a simulation. In all the examples presented in the previous section the interfacial energy was assumed to be  $600 \text{ mJ/m}^2$ , representative of semicoherent interfaces of  $\theta'$  edges. Variation of interface width from 1 to 5 nm produced no numerical artefacts. Consider now the energy of the broad faces of  $\theta'$  plates, which is estimated to be closer to 150 - 200  $\text{mJ/m}^2$ . Since  $W \approx 16 \sigma/l$  reduction in the interfacial energy and increase of the desired interface width (or both simultaneously) will result in a smaller  $W$ .

In Fig. 44 two simulations are compared side by side, with snapshots taken at the same points in time. On the left is the evolution of composition and structural order parameter for an interface of  $200 \text{ mJ/m}^2$  energy and 2 nm thickness, on the right – an interface of  $100 \text{ mJ/m}^2$  and similar thickness. Since the problem is one-dimensional without any influence from the Gibbs-Thomson effect, there should be no difference in the evolution of the system. However, in the case of low interface energy, the evolution is markedly different. A “wave” develops in the structural order parameter, which quickly propagates into the matrix with virtually no change in composition. Later this plateau breaks down into several peaks that eventually either develop into precipitate regions or dissolve. If these regions are not dissolved the position of the main interface is affected.

The ripple described above develops in the matrix close to the interface, suggesting that the  $c - \eta$  transformation path does not follow the equilibrium transformation pathway  $c_{min}(\eta)$ , which means that the fastest way for the system to minimise the energy deviates from keeping the structural order parameter at zero within the matrix. The system prefers to quickly descend into the trough of minimal energy almost at fixed composition, by changing only the structure variable.

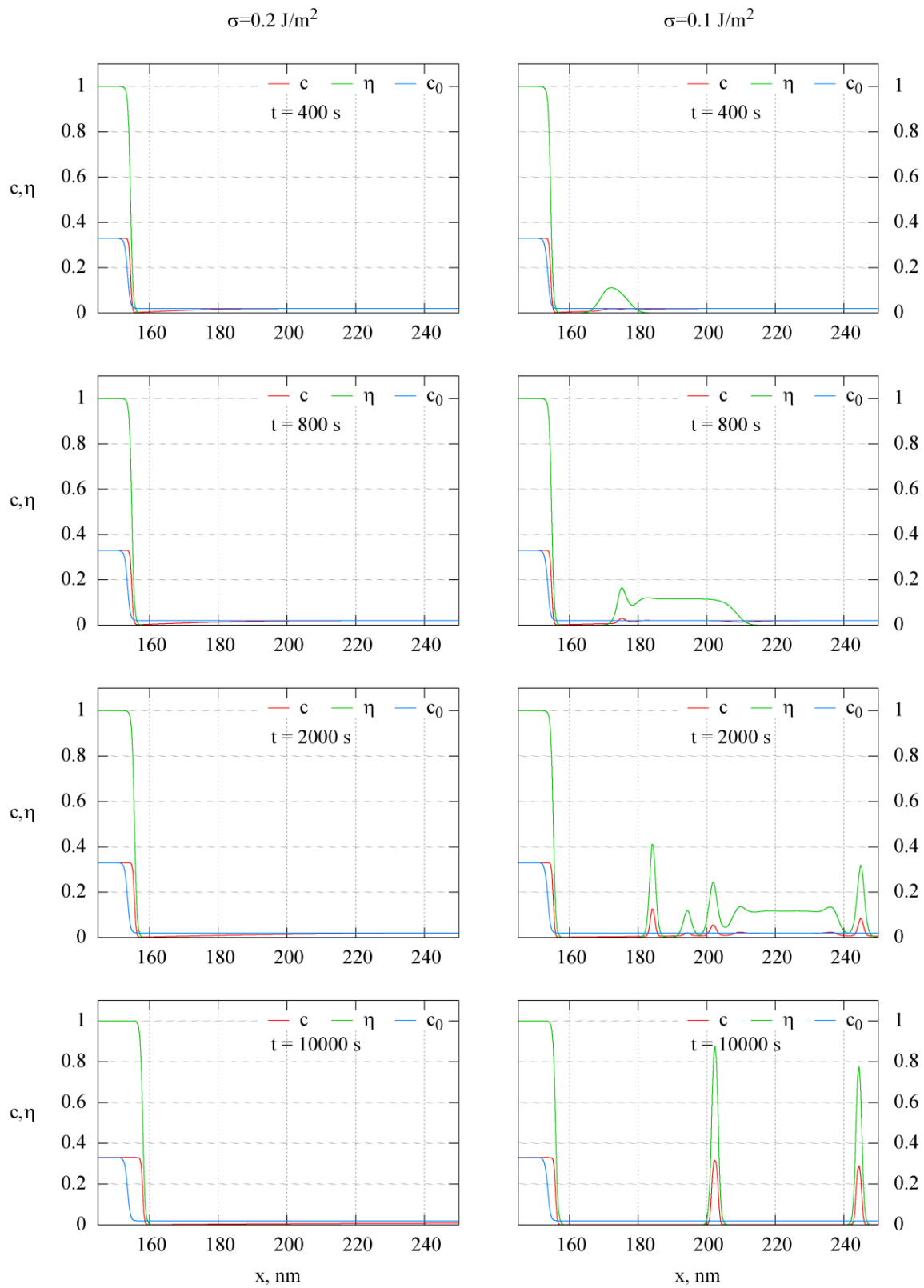


Fig. 44 Evolution of the planar interface with  $200 \text{ mJ/m}^2$  energy compared to the  $100 \text{ mJ/m}^2$  interface. The instability develops in the case of the low interfacial energy (with low height of the double well potential  $W$ ).

To understand the origin of this behaviour one needs to look at the chemical energy landscape in  $c - \eta$  space in the vicinity of  $(c_0, \eta = 0)$ .

Firstly, the non-equilibrium interface deviates from the  $c_{min}(\eta)$  pathway. As illustrated previously in Fig. 43, the compositional profile asymptotically approaches an analytical solution away from the sharp interface, and as such with a certain degree of diffuseness the actual change from precipitate to matrix starts at a composition higher than the equilibrium  $c_\alpha$ . For more diffuse interfaces the structural order parameter starts to change at higher concentrations, as shown in Fig. 45:

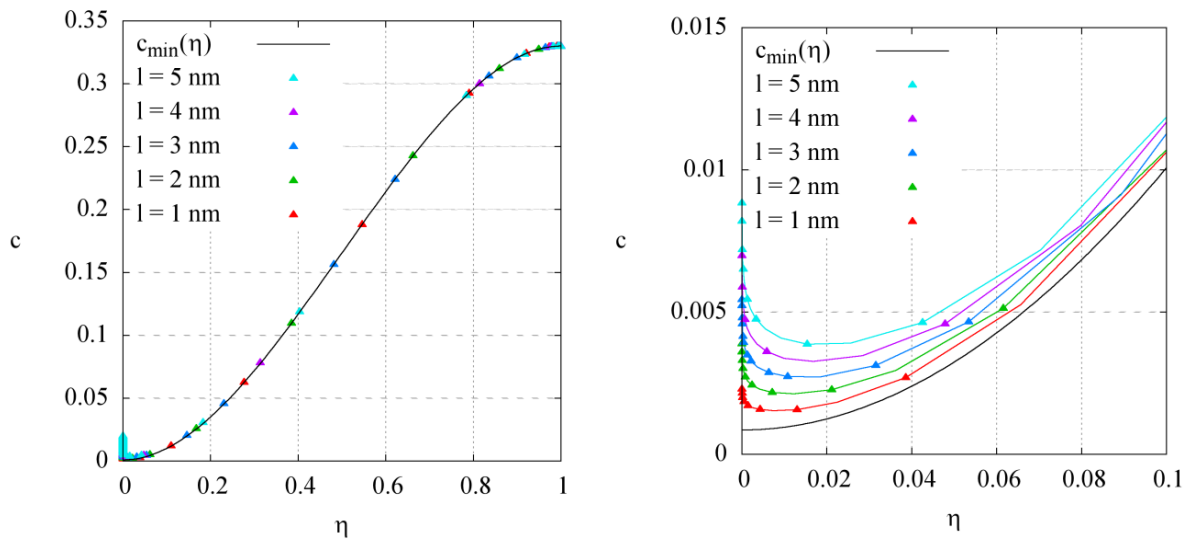


Fig. 45 Non-equilibrium interface in  $c$ - $\eta$  representation.

Secondly, once the system is disturbed from the local minimum of the matrix structural order parameter, its further evolution depends on whether the minimum was stable or unstable. Consider the difference between KKS energy landscapes with different heights of the imposed double-well potential  $W$ , presented in Fig. 46. It is obvious that when  $W$  is small ( $W = 0.05$ , on the left) the equilibrium with respect to change of  $\eta$  is unstable and therefore the system disturbed from equilibrium would “slide” towards  $c_{min}(\eta)$ , exactly the behaviour observed in Fig. 44.

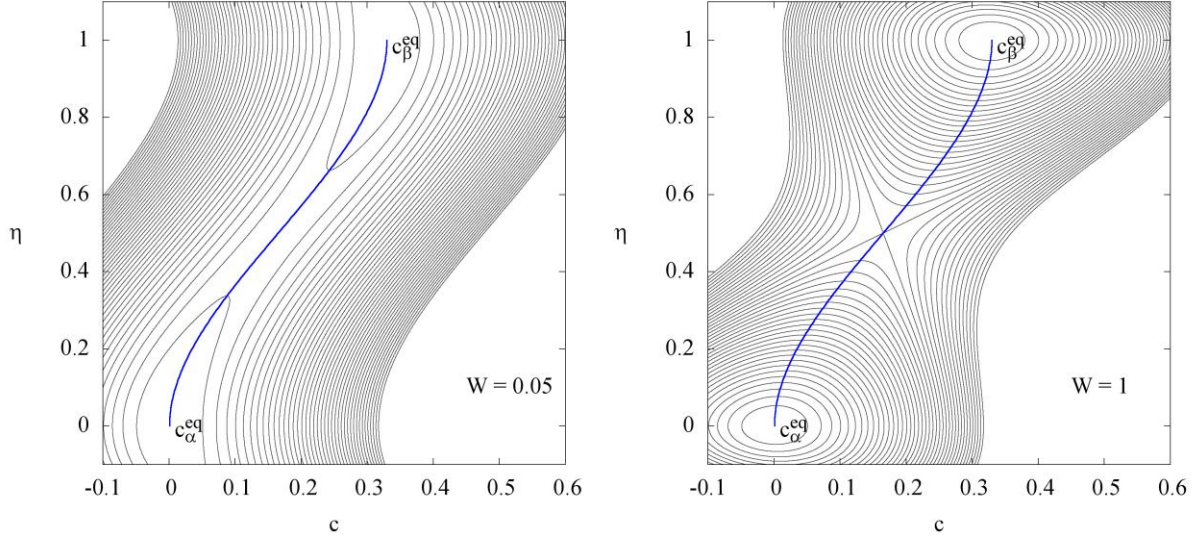


Fig. 46 Contour plots of  $f(c, \eta)$  in the KKS model (5.24) with  $A = 1$  and  $W = 0.05$  on the left vs.  $W = 1$  on the right. Contours are separated by 0.0025 increments.

To avoid this behaviour, which is not a numerical instability as suggested previously [129], one needs to guarantee that the equilibrium in the matrix is a stable one, at least in the composition range up to the initial composition of the matrix  $c_0$ , which is equivalent to

$$\left. \frac{\partial^2 f}{\partial \eta^2} \right|_{c \leq c_0} \geq 0 \quad (5.38)$$

In practical terms, this may be achieved by using a transitional function  $h(\eta)$  that changes slower around  $\eta = 0$  and  $\eta = 1$ , for instance

$$h(\eta) = 6\eta^5 - 15\eta^4 + 10\eta^3 \quad (5.39)$$

The effect of using different transition function is illustrated in Fig. 47. This change in the type of  $h(\eta)$  allows avoiding an unstable equilibrium for a wider range of matrix composition, and makes it possible to use lower  $W$  that is equivalent to wider interfaces. Repeating the simulation presented in Fig. 44 with  $h(\eta)$  from (5.39) allows the reduction of the interfacial energy (or the increase of interface width if required) tenfold, with no adverse effect on dynamic behaviour. Reduction of  $\sigma$  to 20 mJ/m<sup>2</sup> still places the interface exactly at the same position as the one with interface energy of 200 mJ/m<sup>2</sup>, as demonstrated in Fig. 48.

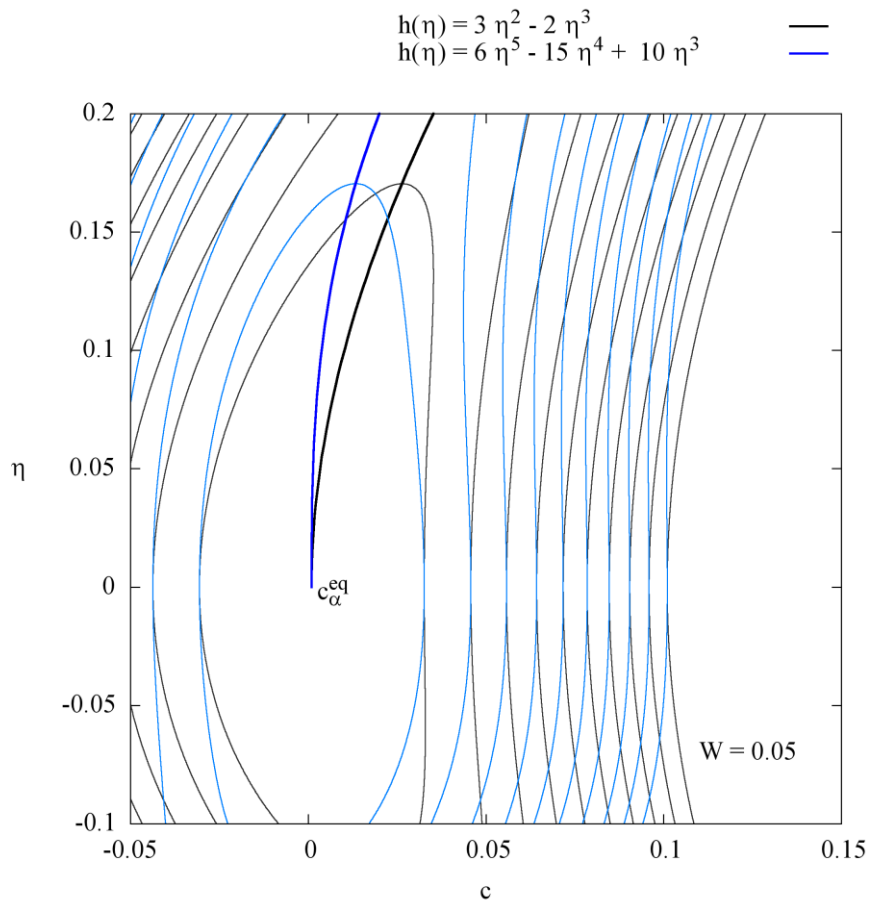


Fig. 47 Effect of the transitional function on the energy landscape: slower transition in the vicinity of  $\eta=0$  guarantees that a stable equilibrium with respect to  $\eta$  is maintained for a wider range of solute concentrations.

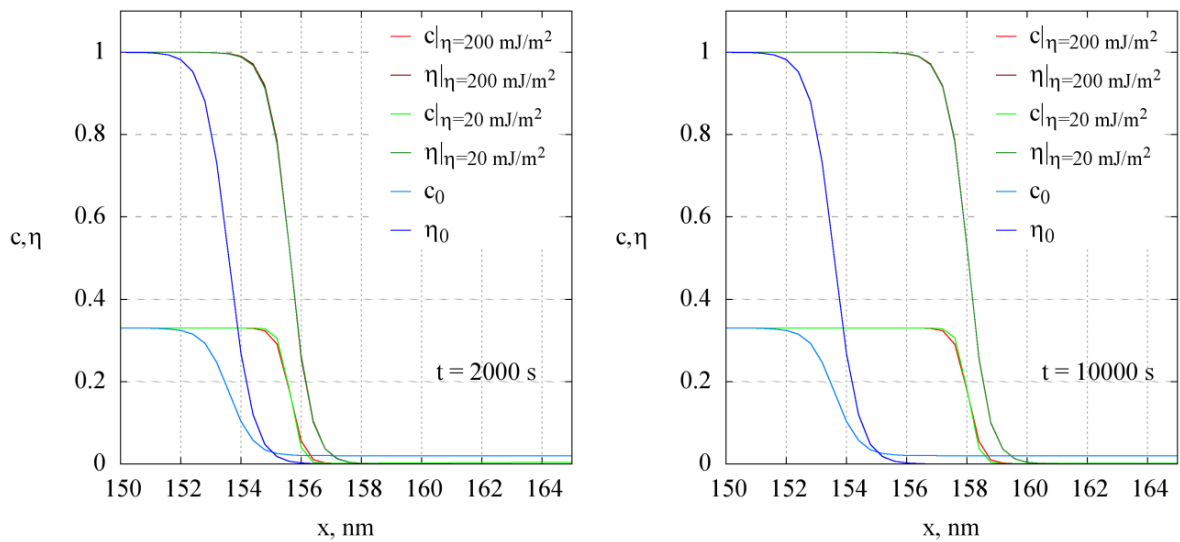


Fig. 48 The effect of a modified transition function on the stability of the simulation. Tenfold variation in the energy of the planar interface has no effect on its motion, as confirmed by the snapshots of the interface position at 2000 (on the left) and 10000 seconds (on the right).

## 5.9. Interface kinetics

Typical parameters of a phase field model (5.30) that correspond to a particular material system may be defined as described in section 5.6. Atomic mobility and gradient terms are based on the bulk diffusion properties and interfacial energy. The only other parameter that affects evolution behaviour and remains undefined is the interface mobility coefficient  $L_\eta$  in the Allen-Cahn equation. Since there are no experimental data available on the mobility of interfaces in our model Al-Cu system, this parameter must be defined based on its effect on interface dynamic properties.

The dimensionless form of the phase field equations (5.34) provides a convenient reference frame for analysing the effect of  $L_\eta$ . Scaling (5.33) is used and parametric analysis of one-dimensional precipitate growth is carried out in the range of the dimensionless kinetic coefficient  $\tilde{L}_\eta$  from 0.001 to 2. The interface resolution is kept the same, with  $\tilde{\beta}=25$ . The initial precipitate of equilibrium  $\theta'$  composition  $c_{\theta'}=0.33$  and width of approximately 10 nm is placed in the centre of the 512 nm simulation domain and its growth is observed for various  $\tilde{L}_\eta$  and  $\sigma$ .

It is widely recognised in the literature [56, 130, 134] that the relative magnitude of the kinetic coefficients  $M_c$  and  $L_\eta$  determine the mode of growth and by controlling the magnitude of  $L_\eta$  it is possible to reproduce parabolic diffusion controlled growth, linear interface controlled growth and intermediate regimes. However, since slightly different scaling procedures are applied by different authors it was important to establish the corresponding ranges in the present model. Dependence of kinetic behaviour on the magnitude of the interfacial energy was also tested, since  $\sigma$  affects the shape of the chemical energy landscape.

Fig. 49 shows how the magnitude of  $\tilde{L}_\eta$  affects the growth of precipitate with interfacial energy of 600 mJ/m<sup>2</sup>. Above  $\tilde{L}_\eta=0.5$  growth follows the analytical parabolic solution, which is consistent with the diffusion controlled mode of interface propagation. This is especially obvious if width is plotted as a function of  $\sqrt{t}$  producing perfectly linear and almost overlapping plots. For  $\tilde{L}_\eta<0.005$  the mode of growth starts to approach linear, and by  $\tilde{L}_\eta<0.001$  becomes a nearly perfect straight line, indicating that purely interface controlled mode of growth is observed.

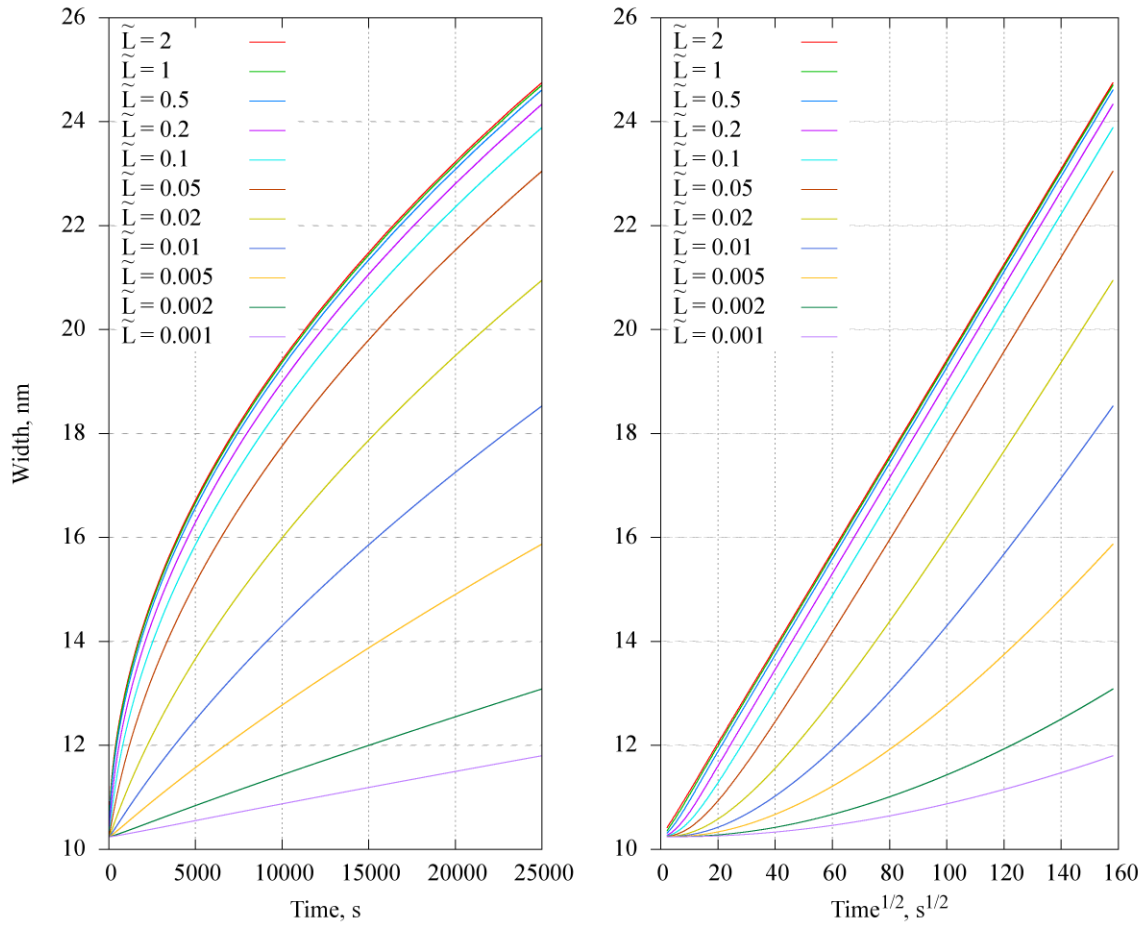


Fig. 49 Variation of the interface growth regime with the value of mobility coefficient (as a function of the ageing time  $t$  on the left and  $\sqrt{t}$  on the right).

Thus three specific regions in terms of  $\tilde{L}_\eta$  may be identified, each corresponding to the particular growth regime:

- Diffusion controlled growth for  $\tilde{L}_\eta > 0.5$
- Interface controlled growth for  $\tilde{L}_\eta < 0.005$
- Mixed mode for intermediate values

Very similar results are quoted by Hu [130], with critical values of  $\tilde{L}_\eta = 0.1$  and  $\tilde{L}_\eta = 0.001$ . The differences may be attributed to the particular scaling procedure used to switch to dimensionless equivalent equations.

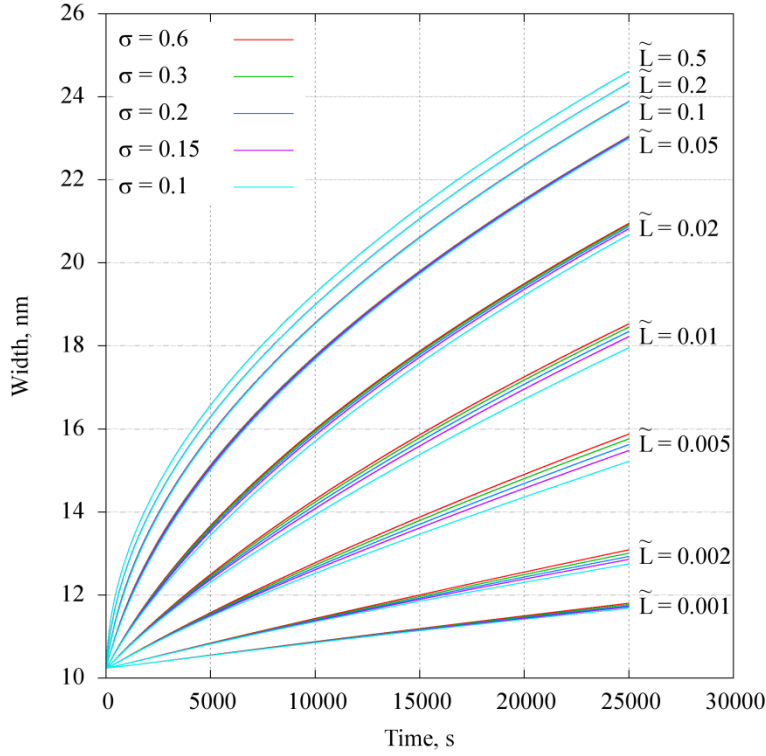


Fig. 50 Growth kinetics of interfaces with different energy.

Variation of interfacial energy has limited effect on kinetics of growth. The origin of this dependence lies in the procedure of the free energy construction within the KKS framework. Change in interfacial energy, desired interface width or both is translated into the change of magnitude of the imposed double well potential  $Wg(\eta)$  and its partial derivatives.

However, the actual effect is not particularly strong (as can be seen in Fig. 50), and mostly pronounced for mixed mode growth and interface controlled growth. For the diffusion controlled regime virtually no difference is observed in growth behaviour.

In all subsequent simulations  $\tilde{L}_\eta$  is kept equal to 2 for the semicoherent edges of  $\theta'$  plates. The choice of  $\tilde{L}_\eta$  for fully coherent broad faces is discussed later in the section on morphology of growing  $\theta'$  plates.

## 5.10. Implementation of interfacial energy anisotropy

The product of phase transformation in solids almost invariably differs in crystal structure from the parent phase. It is usually not only a change in lattice constants, but often of the Bravais lattice type itself. Because of this, interfaces that develop between matrix and product are highly anisotropic. In the case of the model Al-Cu system the difference in the interfacial energy

between precipitate faces and edges is estimated to be a factor of three to four. To reproduce the correct morphology of the individual plates, as well as the solute depletion field around them, it is necessary to account for this anisotropy in the formulation of the phase field model.

Anisotropy in the magnitude of the interfacial energy within the phase field model basically means anisotropy of gradient terms in the free energy functional. The most straightforward way to implement angular dependence  $\sigma(\theta)$  is to make  $\sqrt{k_\eta}$  the same angular function of the interface orientation [119] as  $\sigma(\theta)$  itself. Alternatively, instead of a single gradient term, one may use the form

$$\frac{1}{2}k_x(\nabla_x\eta)^2 + \frac{1}{2}k_y(\nabla_y\eta)^2 \quad (5.40)$$

with different coefficients in different principal directions. Although this method is particularly simple to implement numerically only elliptical anisotropy can be produced and no sharp corners can be implemented.

Finally, one may obtain cubic anisotropy by including higher order expansion terms into the energy functional [135, 136]; however, the model becomes significantly more complicated in terms of numerical implementation.

In the current model the first approach is chosen due to its generality. In the following sections anisotropic modification of the evolution equations, regularisation of  $\sigma(\theta)$  functions and numerical issues associated with having sharp corners will be discussed in detail.

### 5.10.1. The modified Allen-Cahn equation

Anisotropy of the gradient coefficient leads to additional terms in the variational derivative and the evolution equations. Following McFadden et al. [137], these terms are derived as follows. Consider the free energy functional integrand, where the gradient coefficient  $k_\eta$  is a function of interface orientation  $\theta$ :

$$F(c, \eta) = \int [f(c, \eta) + k_\eta(\theta)(\nabla\eta)^2] dV \quad (5.41)$$

With the interface orientation angle  $\theta$  defined via the gradient components<sup>2</sup> as

$$\theta = \arctan\left(\frac{\eta_y}{\eta_x}\right) \quad (5.42)$$

and the gradient coefficient in the form of

$$k_\eta = k_0 \Psi(\theta) \quad (5.43)$$

the variational derivative of (5.41) with respect to the structural order parameter becomes

$$\begin{aligned} \frac{\delta F}{\delta \eta} = \frac{\partial f}{\partial \eta} - k_0 \Psi(\theta) \Delta \eta - k_0 \Psi'(\theta) [\cos(2\theta) \eta_{xy} + 0.5 \sin(2\theta) (\eta_{yy} - \eta_{xx})] \\ - \frac{k_0 \Psi''(\theta)}{2} [\sin^2 \theta \eta_{xx} + \cos^2 \theta \eta_{yy} - \sin(2\theta) \eta_{xy}] \end{aligned} \quad (5.44)$$

or equivalently

$$\frac{\delta F}{\delta \eta} = \frac{\partial f}{\partial \eta} - k_0 \Psi(\theta) \Delta \eta - k_0 \Psi'(\theta) |\nabla \eta \cdot \nabla \theta| - \frac{k_0 \Psi''(\theta)}{2} |\nabla \eta \times \nabla \theta| \quad (5.45)$$

This expression features two additional terms responsible for the local torque acting on the interface element.

The interfacial energy  $\sigma$  will follow the underlying anisotropy of the gradient coefficient:

$$\sigma = \sqrt{k_0 \Psi(\theta) \Delta f_{max}} \quad (5.46)$$

Also, as a side-effect, similar anisotropy is introduced into the width of the interface:

$$l = \sqrt{k_0 \Psi(\theta) / \Delta f_{max}} \quad (5.47)$$

For highly anisotropic interfacial energies this may result in interfaces with significant differences in width. To avoid the complications of numerical pinning and incorrect equilibrium shapes it may also be preferred to maintain constant width of the interfaces, as proposed by Ma et al. [138]. Let us assume the same angular dependence for a barrier term in the chemical free energy density:

---

<sup>2</sup> In this section subscript indices of  $\eta$  represent partial spatial derivatives, e.g.  $\eta_x = \partial \eta / \partial x$  or  $\eta_{xy} = \partial^2 \eta / \partial x \partial y$

$$f(c, \eta) = f^*(c, t) + W(\theta)g(\eta) = f^*(c, t) + W_0\Psi(\theta)g(\eta) \quad (5.48)$$

This results in  $\Delta f_{max} = \Delta f_0\Psi(\theta)$  and as such a constant interface width and interfacial energy that follows the angular dependence of the gradient energy coefficient:

$$\begin{aligned} \sigma &= \sqrt{k_0\Delta f_0\Psi^2(\theta)} = \sigma_0\Psi(\theta) \\ l &= \sqrt{\frac{k_0\Psi(\theta)}{\Delta f_0\Psi(\theta)}} = l_0 \end{aligned} \quad (5.49)$$

With this final modification the variational derivative becomes

$$\begin{aligned} \frac{\delta F}{\delta \eta} &= \frac{\partial f^*}{\partial \eta} + W_0\Psi(\theta)g'(\eta) - k_0\Psi(\theta)\Delta\eta - \left[ k_0 - \frac{2W_0g(\eta)}{(\nabla\eta)^2} \right] \Psi'(\theta)|\nabla\eta \cdot \nabla\theta| \\ &\quad - \left[ \frac{k_0}{2} + \frac{W_0g(\eta)}{(\nabla\eta)^2} \right] \Psi''(\theta)|\nabla\eta \times \nabla\theta| \end{aligned} \quad (5.50)$$

### 5.10.2. Regularisation of anisotropic interfacial energy functions

According to the Gibbs-Wulff theorem, discussed earlier, the shape of the crystal is defined by the minimum in its surface energy. For simple two-fold symmetry shapes like rectangular or nearly rectangular plates it should be sufficient to define the angular dependence of the interfacial energy  $\sigma(\theta)$  with two strong local minima corresponding to habit plane and edges respectively.

Before discussing the specific implementation of  $\sigma(\theta)$ , several basic principles and results of vector thermodynamics of anisotropic surfaces will be introduced below to explain the specific choice of anisotropy functions, and illustrate the behaviour of the anisotropic phase field model.

Cahn and Hoffman [139, 140] proposed to use a vector function  $\vec{\xi}(\vec{n})$  as an alternative to the scalar function  $\sigma(\vec{n})$ . The function, the capillarity vector, is defined via the gradient of the scalar field, whose magnitude in the direction  $\vec{n}$  is a product of the radius vector length and the interfacial energy in this direction:

$$\vec{\xi} = \nabla(r \sigma(\vec{n})) \quad (5.51)$$

The capillarity vector by definition is a function of direction only. In a two dimensional representation for the cylindrical coordinate system  $(\rho, \theta)$  with radial unit vector  $\vec{\rho}$  and tangential unit vector  $\vec{\theta}$  the capillarity vector becomes:

$$\vec{\xi} = \sigma(\theta)\vec{\rho} + \frac{\partial\sigma(\theta)}{\partial\theta}\vec{\theta} \quad (5.52)$$

Hoffmann and Cahn [139] demonstrated that for an element of the surface characterised by the normal unit vector  $\vec{n}$  the negative of the capillarity vector  $(-\vec{\xi})$  represents a force exerted by the surface and acting on the surface element in order to reduce its energy. The projection of  $(-\vec{\xi})$  onto  $\vec{n}$  is a contraction force, and the projection onto the surface tangential vector  $\vec{\theta}$  is a torque that tends to rotate the surface element. Generally, the force acting upon the line element on the surface (with unit vector  $\vec{l}$ ) may then be defined as

$$\vec{f} = \vec{\xi} \times \vec{l} \quad (5.53)$$

One of the central findings is that the interface in equilibrium satisfies the condition

$$-\Delta\Omega = \nabla_S \vec{\xi} \quad (5.54)$$

where  $\Delta\Omega$  is the free energy difference across the interface. For an isolated particle with a surface described by the radius-vector  $\vec{R}$

$$\vec{R} = -\frac{2\vec{\xi}}{\Delta\Omega} \quad (5.55)$$

condition (5.54) is satisfied, therefore the equilibrium shape (Gibbs-Wulff form) must follow the trace of the  $\vec{\xi}$ -plot. For highly anisotropic surfaces the Gibbs-Wulff form may exhibit sharp corners or edges, which means that certain orientations of an interface are not represented in the equilibrium shape at all. This situation corresponds to the  $\vec{\xi}$ -plot with self-intersecting sections, the so-called extended Gibbs-Wulff shape. As proved by Mullins [141], the equilibrium shape is convex in two dimensions, thus the sections of the  $\vec{\xi}$ -plot beyond the intersections must be discarded. Cahn and Hoffman [140] subsequently proved that the sections of the capillarity vector plot extending beyond the points of self-intersections are unstable with respect to continuous faceting when the following condition for interface stiffness is satisfied:

$$\sigma(\theta) + \frac{\partial^2 \sigma(\theta)}{\partial \theta^2} < 0 \quad (5.56)$$

Whenever the instability condition (5.56) is satisfied locally the evolution equations based on variational derivative (5.44) or (5.50) become ill posed, leading to interface breakdown into multiple facets. This process usually leads both to the pinning of an interface and the development of numerical instability. It is therefore necessary to employ “regularisation” of  $\sigma(\theta)$  in order to prevent such faceting.

For  $\theta'$  precipitates in Al-Cu the interfacial energy of edges is estimated to be approximately 600 mJ/m<sup>2</sup>, while the energy of broad faces is about 200 mJ/m<sup>2</sup>. To introduce such a three-fold difference the following function may be used (analogous to Eggleston et al. [142]):

$$\sigma(\theta) = \sigma_0 [2 + 2 \sin^2(2\theta) + \cos(2\theta)] \quad (5.57)$$

where  $\sigma_0 = 200$  mJ/m<sup>2</sup>.

The function (5.57) is shown in Fig. 51 and it has two pronounced minima equal to  $3\sigma_0$  at  $\theta = 0$  and  $\sigma_0$  at  $\theta = \pi/2$ . The high degree of anisotropy produces concave sections in the inverse  $\sigma$ -plot. These regions of concave  $\sigma^{-1}(\theta)$  are the regions of “missing orientations” with condition (5.56) satisfied. The corresponding  $\vec{\xi}$ -plot exhibits self-intersecting sections, as shown with red lines in Fig. 52.

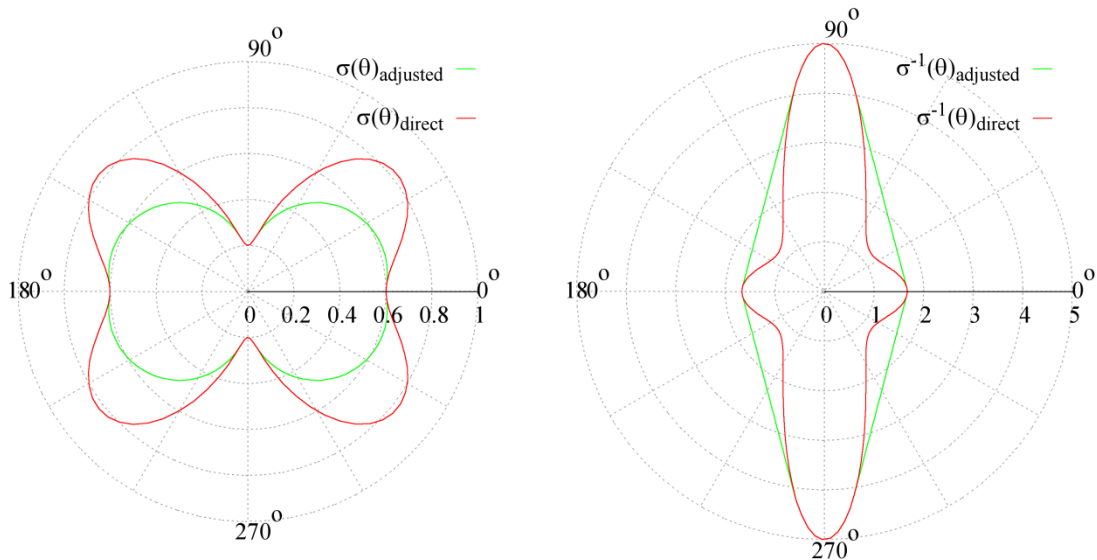


Fig. 51 Polar plots of the function (5.57) on the left and its inverse on the right, shown as solid red lines. Eggleston type regularisation produces “convexified” approximation to this function, shown as solid green lines.

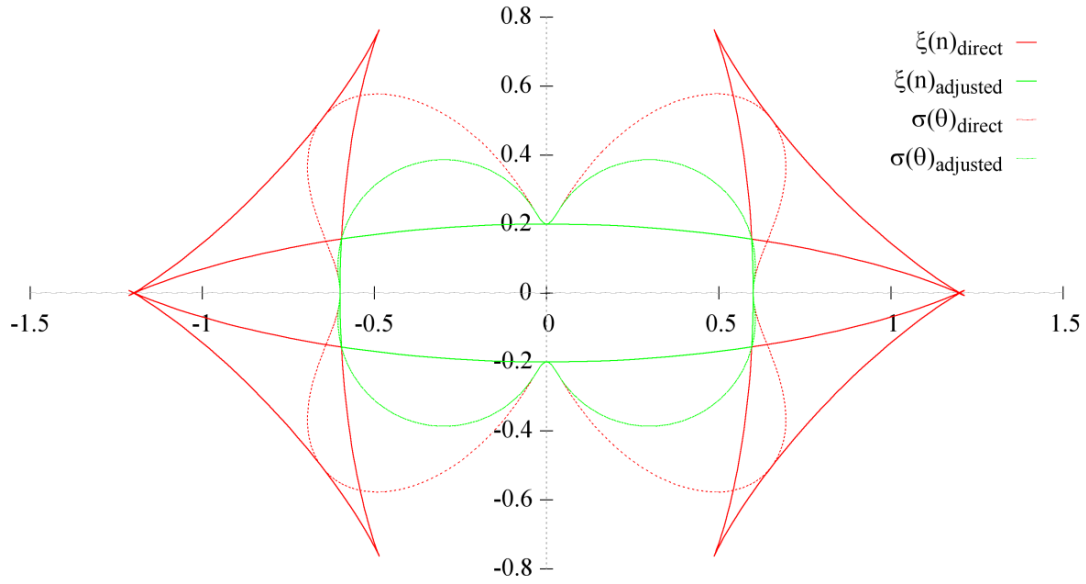


Fig. 52  $\xi$ -plots and  $\sigma$ -plots of direct (red) and regularised (green) functions.

The goal of the regularisation procedure is to avoid the appearance of unstable sections in the angular dependence of  $\sigma(\theta)$ . There are several modifications of such regularisation, all based on the replacement of the negative stiffness regions with a modified function of the following form:

$$\sigma(\theta) = A \sin \theta + B \cos \theta \quad (5.58)$$

This allows setting the stiffness to zero and the capillarity plot of the corresponding region is reduced to a single corner point. An extended Gibbs-Wulff shape is reduced to its inner envelope, with the unstable section being discarded. Eggleston et al. [142] used regularisation based directly on convexification of the inverse  $\sigma(\theta)$  plot and a replacement of concave sections with a tangential straight line, see solid green line in Fig. 52. Eggleston's regularisation is represented by the following piecewise function:

$$\begin{cases} 0.782858 \sin \theta + 2.97949 \cos \theta & ; 0.0552919 < \theta < \frac{\pi}{2} - 0.148876 \\ 2 + 2 \sin^2(2\theta) + \cos(2\theta) & ; \text{elsewhere} \end{cases} \quad (5.59)$$

Debierre [143] utilised a similar approach, but instead of using a two-fold symmetrical underlying function like (5.57) the piecewise construction was employed. Cusps in principal directions are represented by harmonic functions, where coefficients could be fitted in order to provide a smooth transition at critical angles:

$$\begin{cases} M + R \cos \theta & ; \theta < \theta_1 \\ G + F \sin \theta & ; \theta > \theta_2 \\ A \sin \theta + B \cos \theta & ; \theta_1 \leq \theta \leq \theta_2 \end{cases} \quad (5.60)$$

$$\begin{aligned} \theta_1 &= 0.1 & \theta_2 &= \frac{\pi}{2} - 0.15 \\ M &= 7.78798 & R &= -4.78798 \\ G &= 19.8148 & F &= -18.8148 \\ A &= 0.77751 & B &= 2.96109 \end{aligned} \quad (5.61)$$

Both Eggleston's and Debierre's approximations have discontinuities in  $\partial^2\sigma/\partial\theta^2$  at  $\theta_1$  and  $\theta_2$ . To avoid numerical instability issues associated with such discontinuities, in the current model a power series expansion was used to represent energy minima close to  $\theta = 0$  and  $\theta = \pi/2$ . Polynomials of fourth order were used in order to provide a transition into the "missing orientations" region with both first and second order continuous derivatives:

$$\begin{cases} 3 + a_2\theta^2 + a_4\theta^4 & ; \theta < \theta_1 \\ 1 + b_2\left(\frac{\pi}{2} - \theta\right)^2 + b_4\left(\frac{\pi}{2} - \theta\right)^4 & ; \theta > \theta_2 \\ A \sin \theta + B \cos \theta & ; \theta_1 \leq \theta \leq \theta_2 \end{cases} \quad (5.62)$$

$$\begin{aligned} \theta_1 &= 0.1 & \theta_2 &= \frac{\pi}{2} - 0.15 \\ a_2 &= 4.75119 & a_4 &= -104.495 \\ b_2 &= 14.3716 & b_4 &= -111.149 \\ A &= 0.832798 & B &= 2.96875 \end{aligned} \quad (5.63)$$

This power series approximation is shown in Fig. 53 in the angular range  $[0, \pi/2]$ .

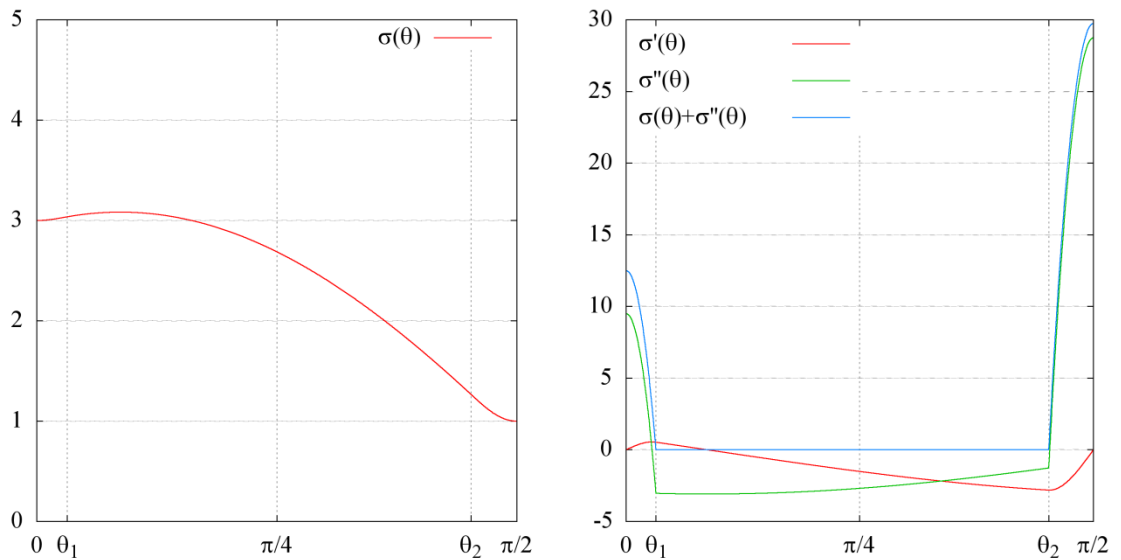


Fig. 53 Piecewise interfacial anisotropy function, its derivatives and interface stiffness with "missing orientations" replaced by the power series expansion (5.62).

The corresponding  $\vec{\xi}$ -plot that represents the equilibrium shape is shown in Fig. 54:

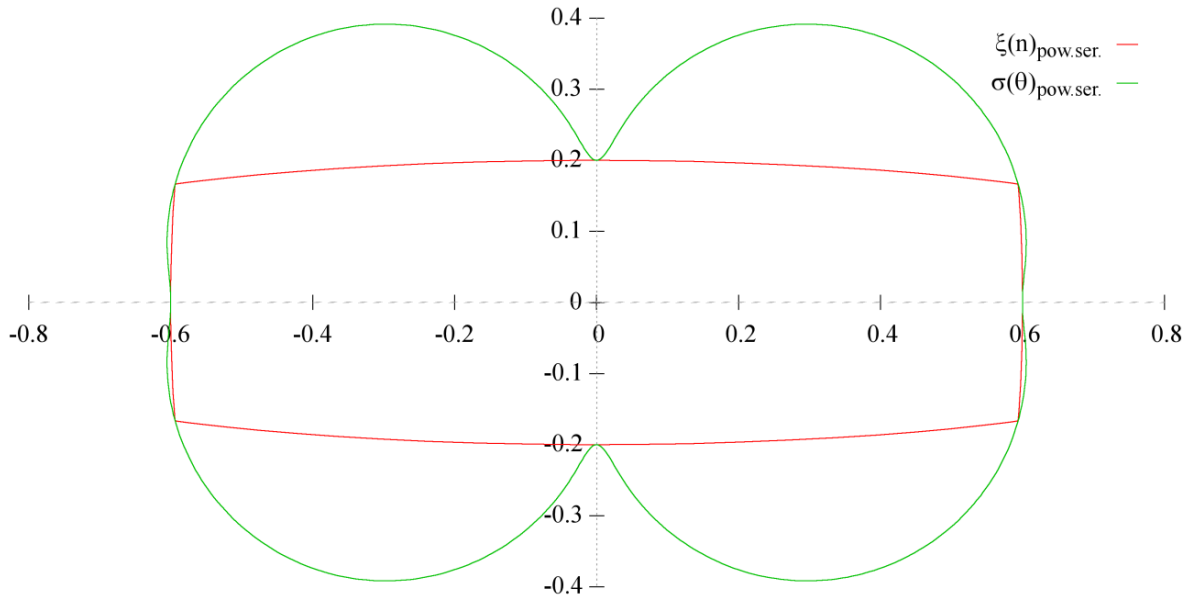


Fig. 54 Polar plots of  $\sigma(\theta)$  and  $\xi(n)$  in the case of power series expansion around the directions with minimum interfacial energies.

### 5.10.3. Numerical scheme stable in presence of corner discontinuities

Strong interfacial anisotropy that is sufficient to produce sharp corners in the  $\vec{\xi}$ -plot presents another challenge in the context of the diffuse model. Although the regularisation discussed above allows the avoidance of the natural instability associated with negative stiffness, the equilibrium shape must exhibit very sharp corners.

Wheeler and McFadden [144, 145] extended the Cahn-Hoffman capillarity vector formalism and presented the anisotropic phase field model directly in terms of  $\vec{\xi}$ . They demonstrated analytically that the negative stiffness range of “missing orientations” is represented by weak shock in the phase field variable, see Fig. 55. The phase field itself is continuous across the shock, but its spatial variables are discontinuous. Having such a discontinuity numerically resolved on a computational grid is problematic and the simulation may become unstable.

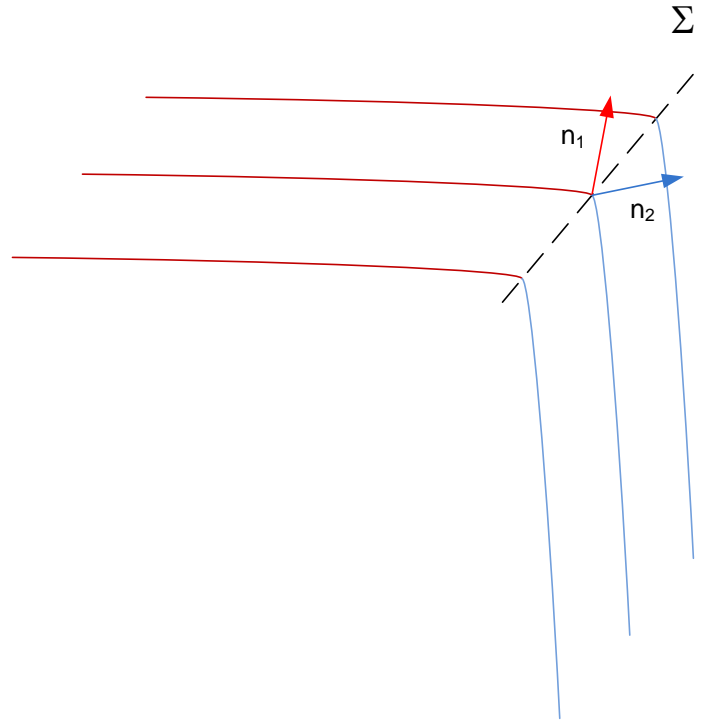


Fig. 55 Schematics of a sharp corner, with a jump in the interface direction from  $n_1$  to  $n_2$  and a discontinuity in all spatial derivatives of field variable across the surface  $\Sigma$  (adapted from Wheeler and McFadden [144]).

Wheeler [146] subsequently proposed a modification of the free energy functional that allows smooth and round sharp corners. It was demonstrated that an additional gradient term in the functional of the form  $\delta^2(\Delta\eta)^2$  diffuses the discontinuity plane  $\Sigma$  into the transitional region where the interface normal changes continuously. The method essentially introduces a penalty energy associated with sharp corner and the system tries to smooth it out.

The approach is similar to the model of interfaces with cubic anisotropy by Abinandanan and Haider [135] where higher order gradient terms were also included in the energy functional. However, these higher order expansions for gradient energy lead to the 4-th order Allen-Cahn evolution equation with significantly more stringent requirements for numerical stability.

Eggleston [142], while addressing the same issue, has noted that the problem is partially alleviated either by aligning the grid with interfaces or by using one-sided finite-difference approximations for first spatial derivatives. In this work the first approach is used, since the directions of interfacial energy minima are perpendicular and it is a natural choice to align a computational grid in the same directions.

Simple centred finite-difference stencils are used to estimate the gradient of phase variable. This allows keeping the “footprint” of the scheme localised to nearest neighbours and as such minimizing the region where the discontinuity may affect the solution. There is still a jump in second derivatives across the discontinuity line; however, the special method of assessing derivatives allows smoothing out its effect and achieving continuous chemical potential across the corner.

In the equation for the variational derivative (5.50) the following term is responsible for rotation of the interface towards the minimal energy direction:

$$-\left[\frac{k_0}{2} + \frac{W_0 g(\eta)}{(\nabla\eta)^2}\right] \Psi''(\theta) |\nabla\eta \times \nabla\theta| \quad (5.64)$$

The cross product  $|\nabla\eta \times \nabla\theta|$  may be expanded as

$$|\nabla\eta \times \nabla\theta| = -|\nabla\eta| \operatorname{div}(\vec{n}) = -|\nabla\eta| \left(\frac{\partial n_x}{\partial x} + \frac{\partial n_y}{\partial y}\right) \quad (5.65)$$

During the assessment of the variational derivatives the term above is evaluated in different ways, depending on the value of the interface orientation angle. If  $\theta \notin (\theta_1, \theta_2)$ , in other words the angle is out of the “missing orientations” range the  $\operatorname{div}(\vec{n})$  is estimated using one-sided approximations and the minimum value is selected. When the angle belongs to the missing orientation range the maximum possible value of the term is selected, based on the centred differencing.

The effect of the technique is illustrated in Fig. 56 - Fig. 61. The profile of the structural field variable  $\eta$  is shown in Fig. 56, demonstrating a sharp change across the corner. Corresponding interface normals and the angle gradient vectors  $\nabla\theta$  are shown in the contour plot in Fig. 57. Centred differencing for the second derivatives of  $\eta$  leads to the sharp spike in the Laplacian term  $k_0\Psi(\theta)\Delta\eta$ , as shown in Fig. 58. The procedure of maximisation for the torque term (5.64) within the “missing orientations” range of the interface angle leads to the localisation of a corresponding spike in the vicinity of the discontinuity line, as shown in Fig. 59. The two spikes cancel each other and as a result of this the combination of the Laplacian and the torque terms is relatively smooth across the corner, see Fig. 60. The chemical potential presented in Fig. 61 also demonstrates continuity across the corner.

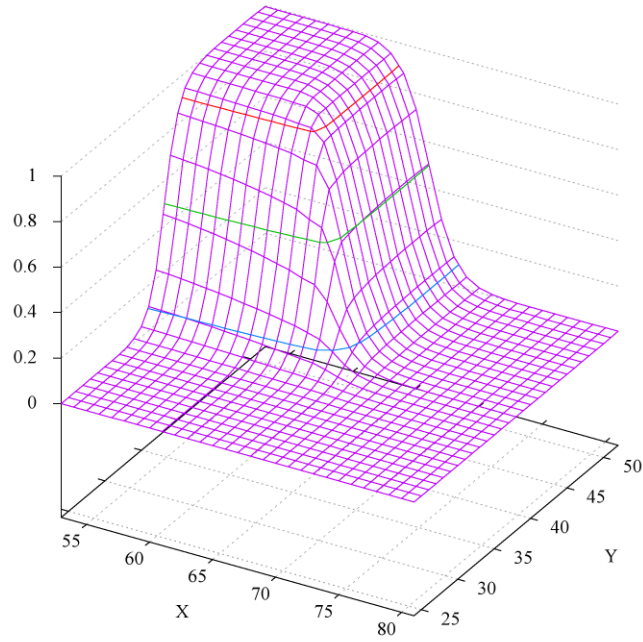


Fig. 56 Profile of the phase variable in the vicinity of a sharp corner.

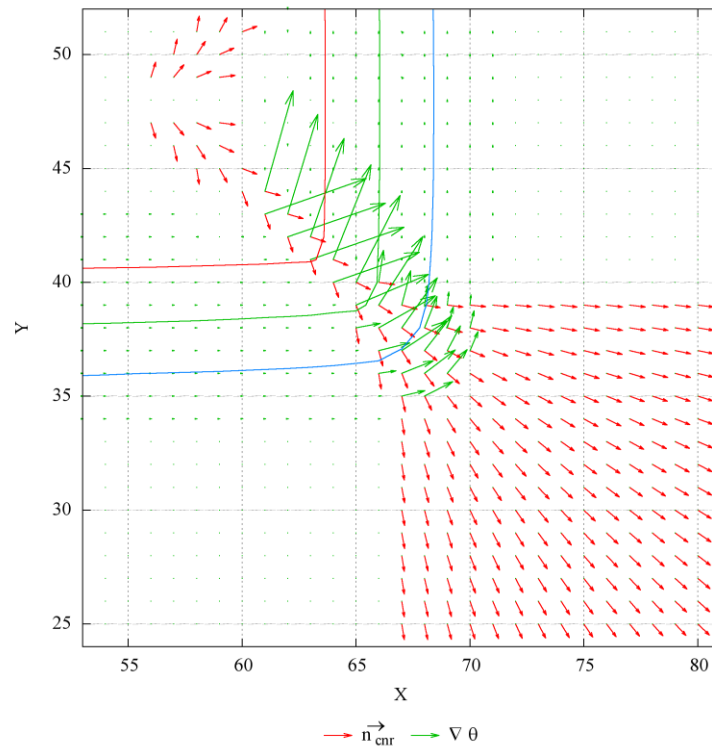


Fig. 57 Contour plot of the phase variable in the vicinity of a sharp corner. Interface normals and angle gradients are also shown within missing orientations range.

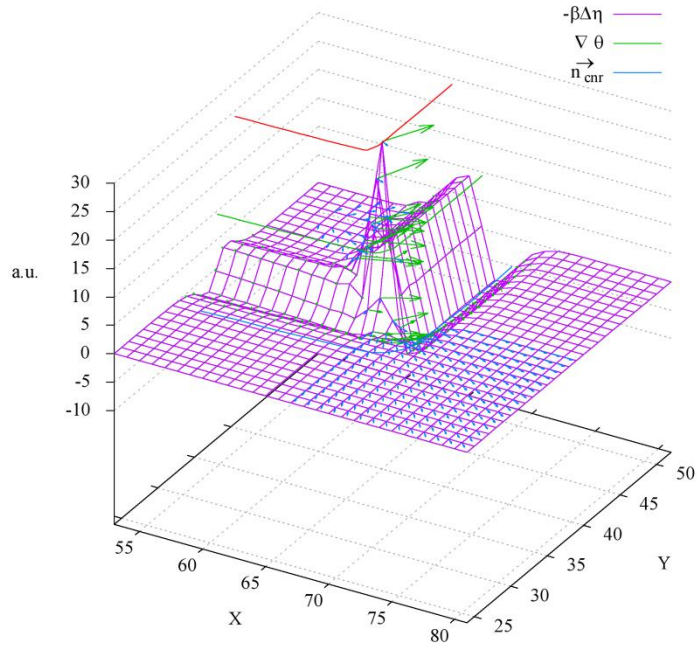


Fig. 58 Laplacian term in the variational derivative. Note the sharp spike across the discontinuity line.

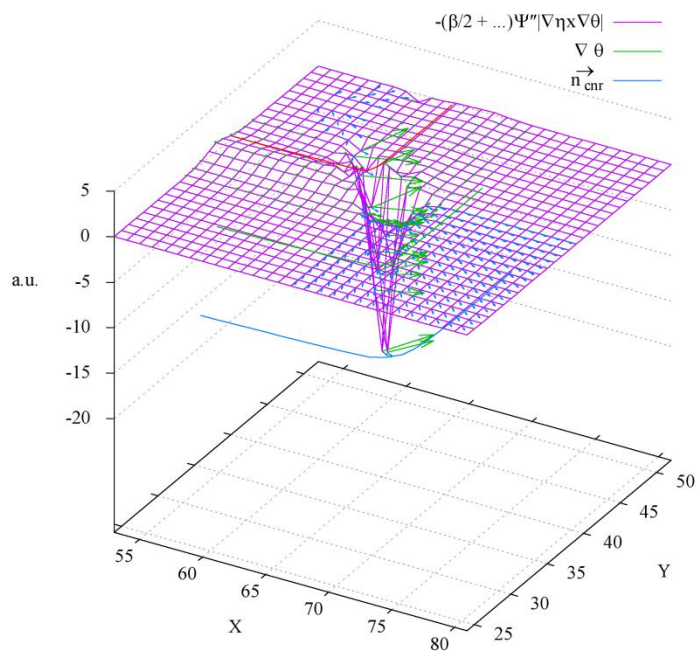


Fig. 59 Torque term of the variational derivative.

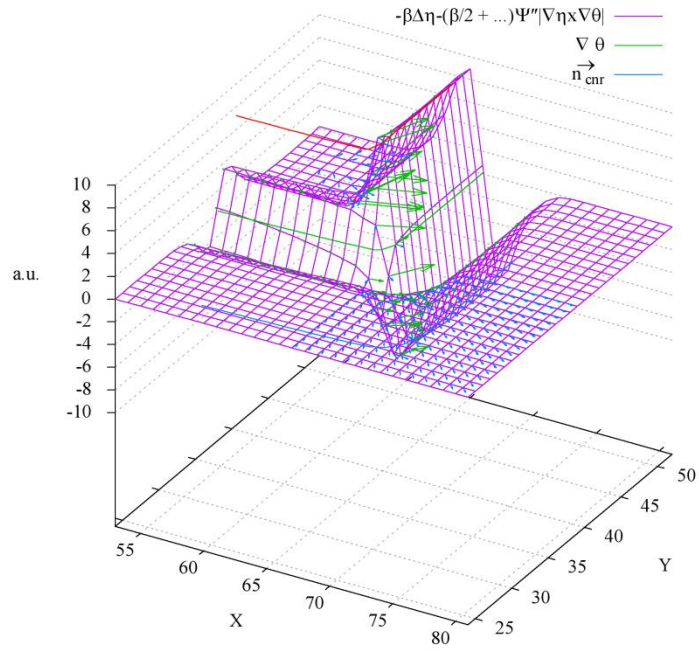


Fig. 60 Mutual compensation of the discontinuities in the Laplacian and the torque terms of the variational derivative.

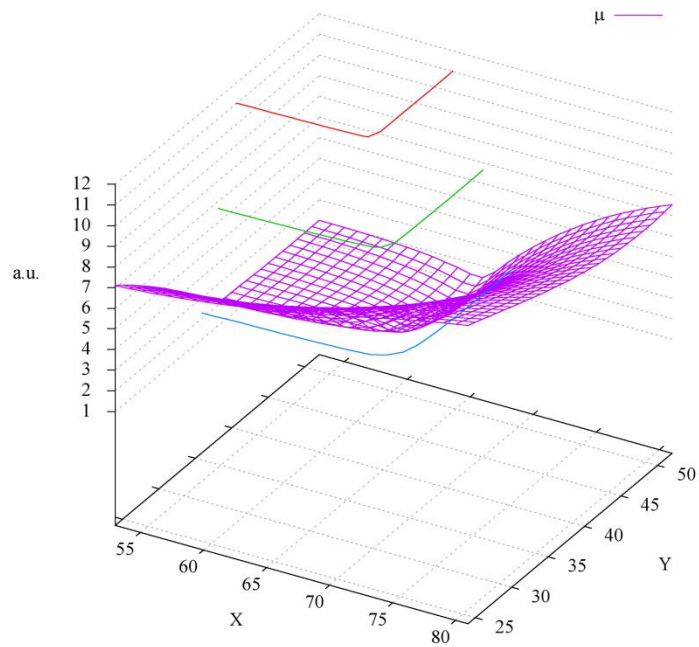


Fig. 61 Chemical potential in the vicinity of the sharp corner, note the smooth character of the transition across the corner.

### 5.11. Implementation of anisotropy in interface mobility

As discussed previously in the section 5.9 “Interface kinetics”, the rate coefficient in the Allen-Cahn equation, or interface mobility coefficient, controls the mode of growth of an interface. It was demonstrated how the relative magnitude of interface and atomic mobilities allow the reproduction of either diffusion or interface controlled growth, as well as intermediate modes.

For  $\theta'$  precipitates in the Al-Cu crystallography data suggest nearly perfect coherency of broad habit planes and semicoherent or even disordered edges. Kinetic behaviour of such interfaces should be markedly different, with slow mobility of coherent faces and high mobility of disordered ones. This anisotropy can be reflected in the phase field model via the angular dependence of the interface mobility coefficient  $L_\eta(\theta)$ . In the current model a simple dependence of the following form is assumed:

$$L_\eta(\theta) = L_0(\lambda \sin^2 \theta + \cos^2 \theta) \tag{5.66}$$

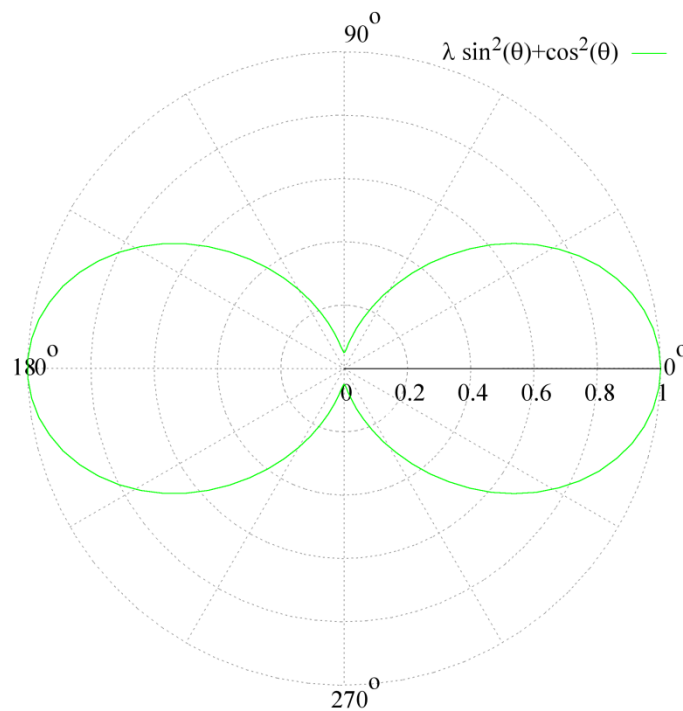


Fig. 62 Angular part of the anisotropic interface mobility  $L_\eta(\theta)$ .

This allows the mobility coefficient to change gradually from  $L_0$  for the edges to  $\lambda L_0$  for the broad faces, see Fig. 62. By controlling the parameter  $\lambda$  (the kinetic anisotropy ratio) the mobility of the different interfaces may be set independently and accordingly to their respective mode of growth.

## 5.12. Summary of the phase field model and its numerical implementation

This section presents the summary of the numerical implementation of a phase field model of  $\theta'$  precipitation in the Al-Cu system. The model is two dimensional, and based on one conserved phase field that represents the atomic concentration of Cu, and two non-conserved (structural) phase fields  $\eta_1$  and  $\eta_2$  that distinguish between the orientations of the precipitates.

The free energy functional used is of the following form:

$$F = \int \left[ f(c, \eta_1, \eta_2) + \frac{k_0}{2} \sum_{i=1}^2 \Psi_i(\theta_i) (\nabla \eta_i)^2 \right] dV + \frac{1}{2} \sum_{p=1}^2 \sum_{q=1}^2 B'_{pq}(\vec{n}) \{ \Theta_p(\vec{r}) \} \{ \Theta_q(\vec{r}) \}^* \frac{d^3 g}{(2\pi)^3} \quad (5.67)$$

that includes the chemical free energy, the gradient energy term expanded in structural order parameters and the elastic energy term.

The chemical free energy density is constructed by the Kim-Kim-Suzuki method with the barrier term being an anisotropic function of interface direction in order to maintain a constant interface width:

$$f(c, \eta_1, \eta_2) = A \left[ c - c_\alpha^{eq} - (c_\beta^{eq} - c_\alpha^{eq}) h(\eta_1, \eta_2) \right]^2 + W(\theta) g(\eta_1, \eta_2) \quad (5.68)$$

The transition function used is

$$h(\eta_1, \eta_2) = 6(\eta_1^5 + \eta_2^5) - 15(\eta_1^4 + \eta_2^4) + 10(\eta_1^3 + \eta_2^3) \quad (5.69)$$

and the barrier function producing energy minima that distinguish the matrix ( $\eta_1 = 0, \eta_2 = 0$ ) from the two different orientations of  $\theta'$  at ( $\eta_1 = 1, \eta_2 = 0$ ) and ( $\eta_1 = 0, \eta_2 = 1$ ) is:

$$g(\eta_1, \eta_2) = (\eta_1^2 + \eta_2^2) - 2(\eta_1^3 + \eta_2^3) + (\eta_1^4 + \eta_2^4) + \eta_1^2 \eta_2^2 + \eta_1^2 \eta_2^4 + \eta_1^4 \eta_2^2 \quad (5.70)$$

The specific choice of coefficient  $A$  and barrier term height  $W(\theta)$  was explained previously in the section 5.6 “Typical parameters of the Al-Cu phase field model” and is based on the diffusion characteristics of the system, interfacial energy and desired interface width.

The variational derivatives of the free energy functional (5.67) with respect to composition and structural order parameters are:

$$\frac{\delta F}{\delta c} = \frac{\partial f(c, \eta_1, \eta_2)}{\partial c} = 2A \left[ c - c_\alpha^{eq} - (c_\beta^{eq} - c_\alpha^{eq})h(\eta_1, \eta_2) \right] \quad (5.71)$$

$$\begin{aligned} \frac{\delta F}{\delta \eta_i} = & -2A \left[ c - c_\alpha^{eq} - (c_\beta^{eq} - c_\alpha^{eq})h(\eta_1, \eta_2) \right] (c_\beta^{eq} - c_\alpha^{eq}) \frac{\partial h(\eta_1, \eta_2)}{\partial \eta_i} \\ & + W_0 \Psi_i(\theta_i) \frac{\partial g(\eta_1, \eta_2)}{\partial \eta_i} - k_0 \Psi_i(\theta_i) \Delta \eta_i \\ & - \left[ k_0 - \frac{2W_0 g(\eta_1, \eta_2)}{(\nabla \eta_i)^2} \right] \Psi_i'(\theta_i) |\nabla \eta_i \cdot \nabla \theta_i| \\ & - \left[ \frac{k_0}{2} + \frac{W_0 g(\eta_1, \eta_2)}{(\nabla \eta_i)^2} \right] \Psi_i''(\theta_i) |\nabla \eta_i \times \nabla \theta_i| \\ & + \frac{\partial \Theta(\eta_i)}{\partial \eta_i} \sum_{q=1}^2 \{ B'_{iq}(\vec{n}) \{ \Theta_q \} \} \end{aligned} \quad (5.72)$$

with the shape function (a function that is equal to 1 inside a precipitate of a particular type and 0 elsewhere) defined as

$$\Theta_i(\eta_i) = \begin{cases} 0 & ; \eta_i < 0 \\ 3\eta_i^2 - 2\eta_i^3 & ; 0 \leq \eta_i \leq 1 \\ 1 & ; \eta_i > 1 \end{cases} \quad (5.73)$$

The Cahn-Hilliard and Allen-Cahn equations for the evolution of the conserved and non-conserved fields respectively are given by:

$$\begin{aligned} \frac{\partial c}{\partial t} &= M_c \Delta \left( \frac{\delta F}{\delta c} \right) \\ \frac{\partial \eta_i}{\partial t} &= -L_{\eta_i}(\theta_i) \frac{\delta F}{\delta \eta_i} \end{aligned} \quad (5.74)$$

### 5.12.1. Semi-Implicit Fourier Spectral scheme for the Cahn-Hilliard equation

The explicit form of the Cahn-Hilliard equation in the case of the Kim-Kim-Suzuki free energy representation is particularly simple:

$$\frac{\partial c}{\partial t} = 2M_c A \left[ \nabla^2 c - (c_\beta^{eq} - c_\alpha^{eq}) \nabla^2 h(\eta_1, \eta_2) \right] \quad (5.75)$$

Because there is no gradient term associated with composition, the Cahn-Hilliard equation is of second order instead of fourth, which relaxes the time step constraints. Moreover, since all anisotropy contributions, interfacial and kinetic, are accounted for in the Allen-Cahn equations the evolution of composition becomes a diffusion problem with constant diffusivity. This allows one to take full advantage of spectral solvers. In this work the Semi-Implicit Fourier Spectral scheme [122] is applied for solving the Cahn-Hilliard equation. The Fourier transform of the evolution equation is taken and the Laplacian is treated implicitly for the concentration and explicitly for the non-linear terms:

$$\frac{\bar{c}_{n+1} - \bar{c}_n}{\Delta t} = -2M_c A k^2 \bar{c}_{n+1} + 2M_c A (c_\beta^{eq} - c_\alpha^{eq}) k^2 \bar{h}_n \quad (5.76)$$

$$\bar{c}_{n+1} = \frac{\bar{c}_n + 2M_c A (c_\beta^{eq} - c_\alpha^{eq}) k^2 \bar{h}_n \Delta t}{1 + 2M_c A k^2 \Delta t} \quad (5.77)$$

where  $k$  is the magnitude of a wave vector in Fourier space, a bar above a function represents its Fourier transform and index  $n$  corresponds to a step in time.

### 5.12.2. Alternating Direction Implicit scheme for the Allen-Cahn equation

The Allen-Cahn equation is more complicated due to the anisotropies in both the gradient coefficient and the interface mobility coefficient. Because of the location dependence of these coefficients, there is no benefit in using spectral methods, since conversion into Fourier space does not transform the initial partial differential equation into an ordinary differential equation.

Even partial linearisation by splitting the anisotropic terms into isotropic and anisotropic parts as in (5.78), proves to be problematic in practice.

$$\begin{aligned}\frac{\partial \eta(x, y)}{\partial t} &= a(\eta_x, \eta_y) \Delta \eta + u(\eta_x, \eta_y, \eta_{xx}, \eta_{xy}, \eta_{yy}) = \\ &= a_0 \Delta \eta + u_0(\eta_{xx}, \eta_{xy}, \eta_{yy}) + \delta a(\eta_x, \eta_y) \Delta \eta \\ &+ \delta u(\eta_x, \eta_y, \eta_{xx}, \eta_{xy}, \eta_{yy})\end{aligned}\tag{5.78}$$

The spectral determination of the derivatives is subject to the so-called Gibbs phenomenon, when the resulting approximation has fine oscillations, determined by the maximum frequency included in the spectrum. An exception to this effect is a perfectly harmonic function, with highest frequency below the maximum frequency included in the discretisation. Bulk phases are represented by regions of constant values for the phase variables and therefore of zero first spatial derivatives. Because the interface orientation angle is determined via first order spatial derivatives, oscillations in  $\eta_x$  and  $\eta_y$  result in chaotic changes of the anisotropic coefficients close to the interfaces and across the periodic boundaries of the simulation domain.

Therefore, the solver for the Allen-Cahn equation was taken in real-space, based on the finite difference technique. A simple Euler scheme for time stepping is usually sufficient, but the stability and maximum time step may be improved by using higher order schemes. In this work the Alternating Direction Implicit method [147] is used, which is of second-order accuracy both in space and in time.

The Allen-Cahn equation may be generalised from the form (5.78) where

$$a(\eta_x, \eta_y) = L(\theta) k_0 \Psi(\theta)\tag{5.79}$$

and the rest of the terms are collected under the combined non-linear function  $u(\eta_x, \eta_y, \eta_{xx}, \eta_{xy}, \eta_{yy})$ . Simple centred finite-difference stencils are used for the first and second order partial derivatives that enter into the determination of  $\theta(\eta_x, \eta_y)$  and the terms proportional to  $|\nabla \eta_i \cdot \nabla \theta_i|$  and  $|\nabla \eta_i \times \nabla \theta_i|$  are estimated as described in the previous section, via derivatives of the interface normal components.

ADI is a modification of the implicit Crank-Nicolson technique and the concept of operator splitting. In this method the time step is split into two equal sub-steps and in each sub-step only one direction is treated implicitly. The discretisation of the Allen-Cahn equation becomes:

$$\begin{aligned}
\eta_{i,j}^{n+\frac{1}{2}} &= \eta_{i,j}^n + u_{i,j} \frac{\Delta t}{2} + a_{i,j} \frac{\Delta t}{2\Delta x^2} \left( \delta_x^2 \eta_{i,j}^n + \delta_y^2 \eta_{i,j}^{n+\frac{1}{2}} \right) \\
\eta_{i,j}^{n+1} &= \eta_{i,j}^{n+\frac{1}{2}} + u_{i,j} \frac{\Delta t}{2} + a_{i,j} \frac{\Delta t}{2\Delta x^2} \left( \delta_x^2 \eta_{i,j}^{n+1} + \delta_y^2 \eta_{i,j}^{n+\frac{1}{2}} \right)
\end{aligned} \tag{5.80}$$

where index  $n$  identifies the time step and the indices  $i, j$  identify the grid point on the two-dimensional computational grid. Using the notation from [147] the finite differencing operators are:

$$\begin{aligned}
\delta_x^2 f &= f_{i+1,j} + f_{i-1,j} - 2f_{i,j} \\
\delta_y^2 f &= f_{i,j+1} + f_{i,j-1} - 2f_{i,j}
\end{aligned} \tag{5.81}$$

The splitting allows the utilisation of the stability of the second-order Crank-Nicolson scheme and simplifies the system of linear equations to be solved. Each sub-step requires the solution of a tridiagonal system of linear equations to obtain updated values of the structural variable field  $\eta_{i,j}^{n+\frac{1}{2}}$  and  $\eta_{i,j}^{n+1}$ .

Finally, an additional improvement of the overall numerical stability may be achieved if the concentration field is updated first and then the coefficients in (5.80) are estimated as

$$\begin{aligned}
a_{i,j}(c^{n+1}, \eta_1^n, \eta_2^n) \\
u_{i,j}(c^{n+1}, \eta_1^n, \eta_2^n)
\end{aligned}$$

In the next section the morphology of an isolated precipitate will be analysed and effects of various anisotropies introduced into the evolution equation will be considered.

### 5.13. Morphology of an isolated precipitate in two dimensions

The shape of the individual  $\theta'$  plates observed in an experiment is a complex product of several contributing factors, namely the influence of interfacial energy, coherency strains and kinetic anisotropies in the mobility of interfaces.

When only taking into account interfacial energy the simulated particle eventually evolves towards the shape corresponding to the Gibbs-Wulff equilibrium construction, see an example of elliptical anisotropy in Fig. 63:

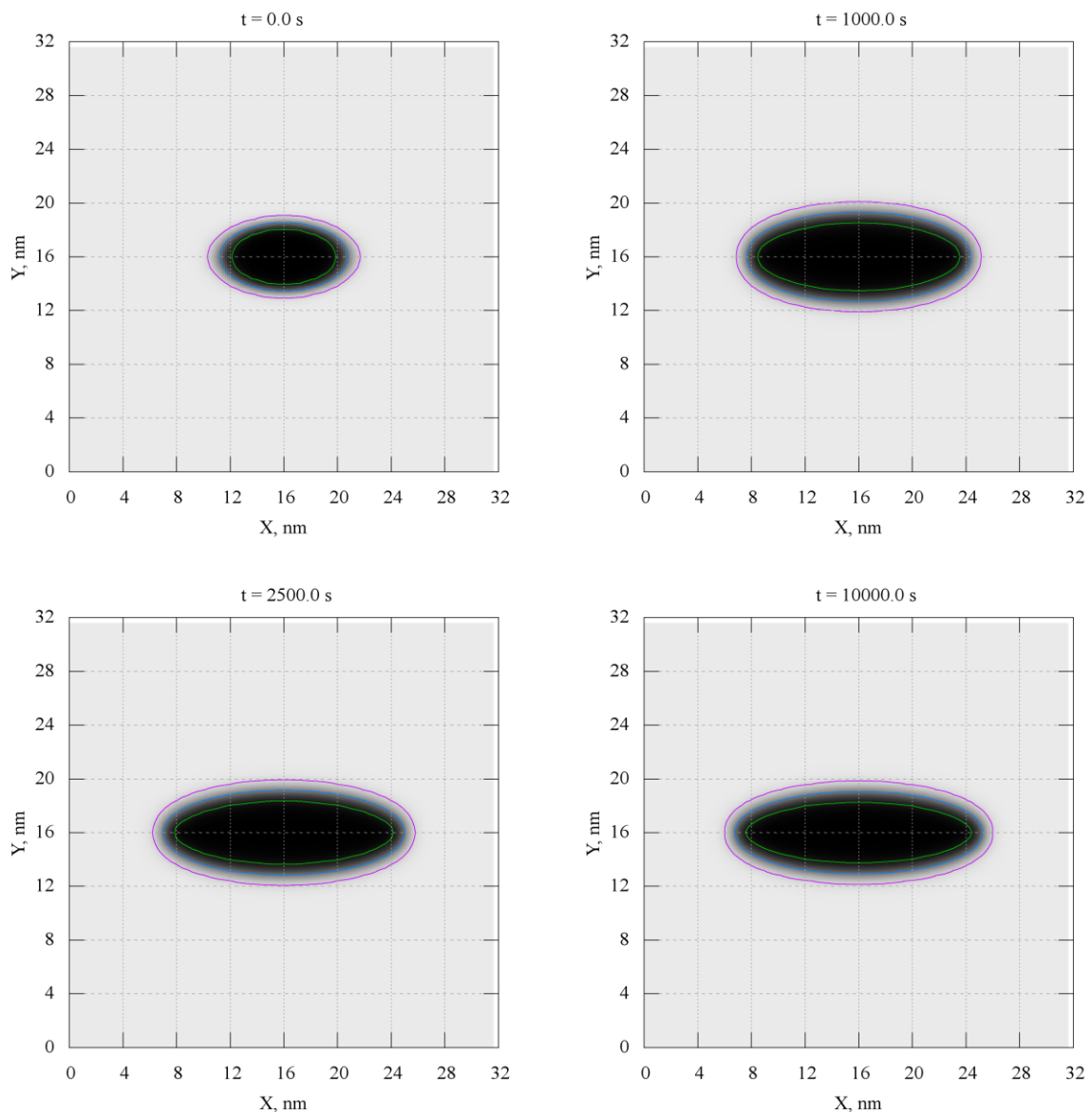


Fig. 63 Simulated evolution of the  $\theta'$  particle under the influence of the interfacial energy anisotropy (elliptic anisotropy is assumed).

Inclusion of strains into the free energy functional produces plates of higher aspect ratios, as demonstrated in Fig. 64. Since the strain energy is volume dependent the effect will be more pronounced for larger particles.

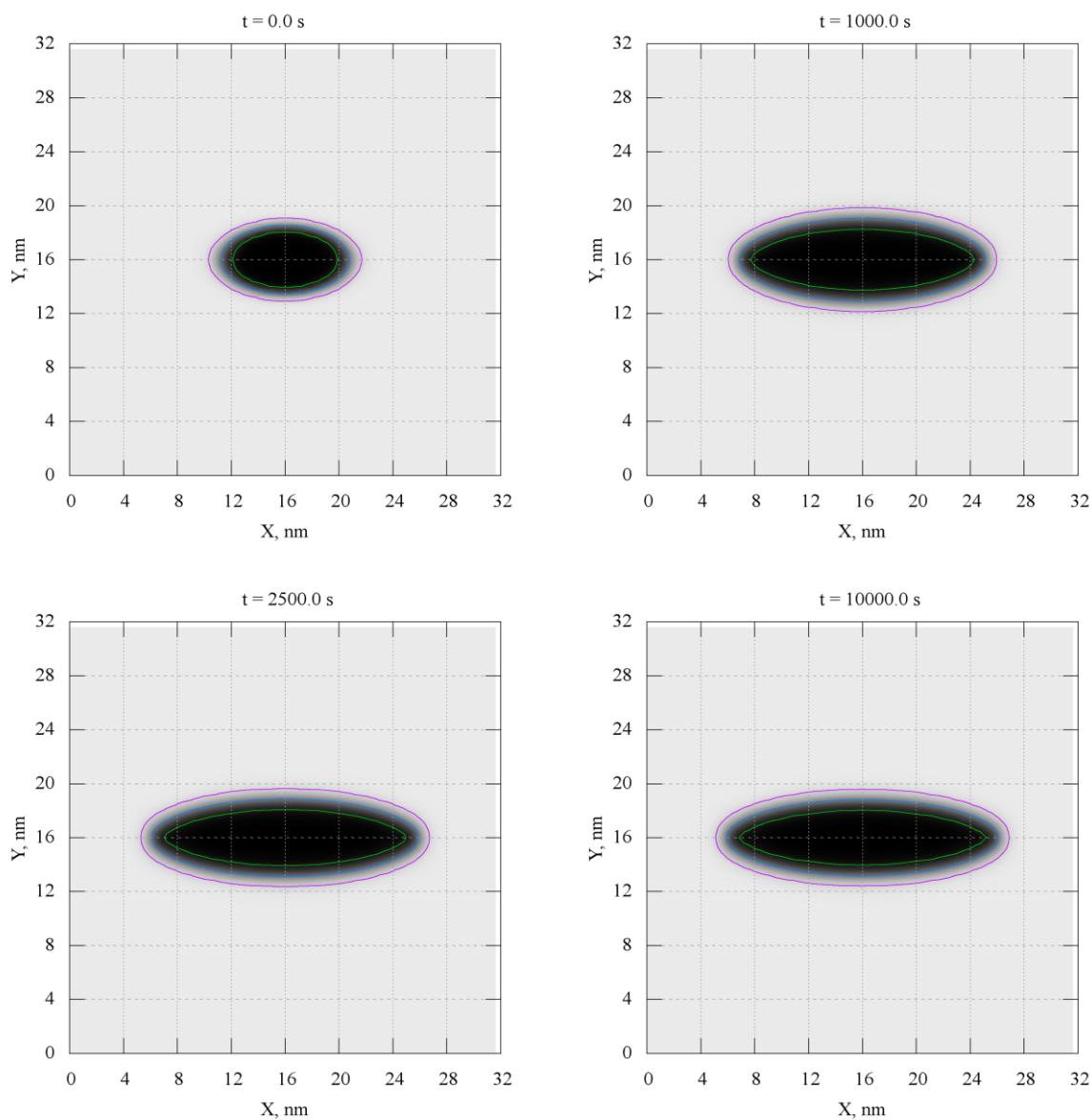


Fig. 64 Simulated evolution of the  $\theta'$  particle under the combined influence of the interfacial energy and the elastic energy.

The introduction of interface mobility anisotropy allows the reproduction of even higher aspect ratios. The effect of moderate anisotropy, with the non-dimensional mobility  $\tilde{L}_\eta=0.1$  corresponding to mixed mode of growth for the broad faces is demonstrated in Fig. 65:

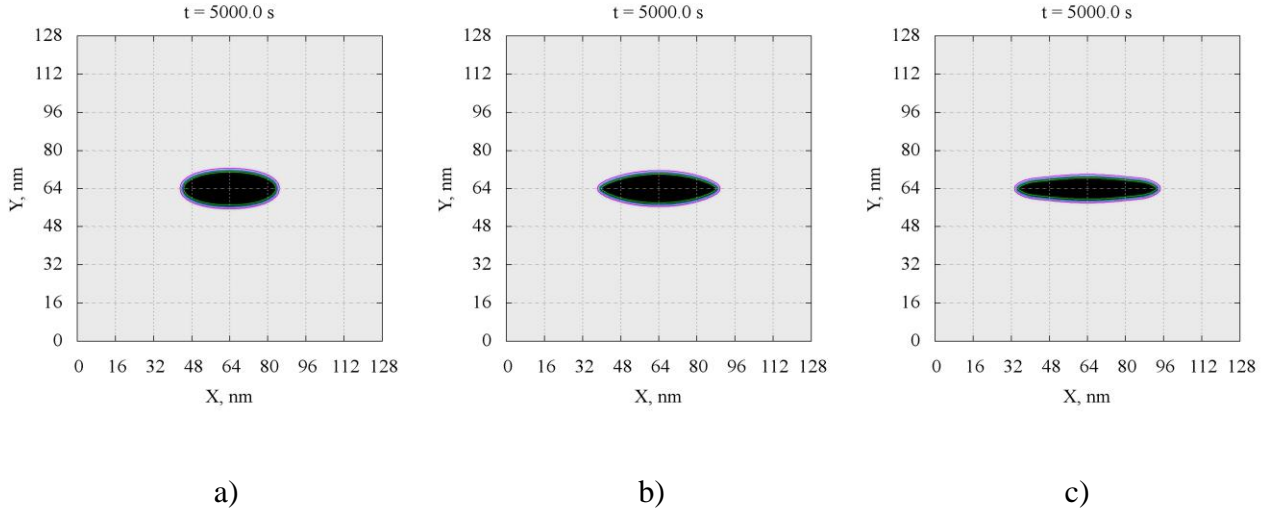


Fig. 65 Simulated evolution of the  $\theta'$  particle in the larger periodic system with a) only interfacial energy; b) interfacial and strain energies and c) interfacial, strain energies and anisotropy in the interfacial mobility.

A series of simulations was performed in order to look at the effects of the various approximations in the phase field model on the driving forces around growing plates. In each simulation an initial seed was placed in the centre of the square simulation domain of length and with periodic boundary conditions. The initial particle is approximately 5 nm thick and 10 nm wide. The matrix composition is 0.02 at. % Cu and the temperature is 500 K.

Fig. 66 demonstrates the evolution of the nucleation driving force for the formation of the sheared nucleus that is parallel to the large plate and with shear along positive  $x$ -direction. The nucleation driving force is assessed as a difference of the volumetric chemical driving force and the volumetric elastic interaction energy of a nucleus with the existing microstructure:

$$G_{Total} = G_V - \frac{\Delta E^{int}}{V_0} \quad (5.82)$$

The chemical driving force is extracted from COST507 light metal alloys database [102] and the volumetric contribution from elastic interaction is calculated by Shen's method [59], see equation (2.38).

In Fig. 66 two different approximations for the angular dependence of interfacial energy are compared side by side, smooth elliptic anisotropy  $\sigma = \sigma_0 \sqrt{9 \cos^2 \theta + \sin^2 \theta}$  on the left and the function (5.62) on the right. Both produce 3 to 1 anisotropy ratio of  $\sigma_x$  to  $\sigma_y$ , while the second function produces precipitates with sharp corners.

In spite of the significant difference in the morphology of the precipitates the driving force field around them is strikingly similar, both in symmetry and in magnitude. It appears that finer details of the balance between chemical driving forces and elastic interaction energy density are restricted to the regions of the matrix in immediate vicinity of the precipitate surface. When the distance from precipitate is comparable with its characteristic dimensions the difference produced by specific choice of anisotropy function is negligible.

This effect of similarity in the driving force for the different interfacial energy approximations is even more obvious if sizes and aspect ratios of elliptical and rectangular plates are closer, as for example in Fig. 67. In this case the effect of mobility anisotropy was taken into account as well. Initially identical precipitates are seeded in the centre of the simulation domain and allowed to grow. Two type of interfacial anisotropy are considered as before, and interfacial mobility of the broad faces is set at  $\tilde{L}_\eta=0.05$  to represent mixed interface control. Sharp corners in the case of the interfacial energy function (5.62) with “missing orientations” are associated with higher stress concentration at the edges; however, at medium distance from the precipitates the fields are almost identical, regardless of the anisotropy function used in the simulation.

Finally, the effect of numerical resolution of an interface on a computational grid was assessed. An artificial “pinning” of a poorly resolved interface has the same effect on kinetics as a decreasing interface mobility coefficient. Both lead to a slower motion and an elevated concentration of solute on both sides of an interface. In Fig. 68 interface-controlled growth is simulated differently: on the left – the fully anisotropic phase field model is considered, with anisotropic interfacial energy, constant interface width and anisotropic mobility with  $\tilde{L}_\eta=0.005$  for broad faces; on the right – similar interfacial anisotropy, variable interface width and grid step selected to make the sampling of thinner interface insufficient (dimensionless gradient coefficient is  $\tilde{k} \approx 2$ , producing maximum two grid points in the interface). The resulting fields of a driving force for the plates of comparable size are almost indistinguishable.

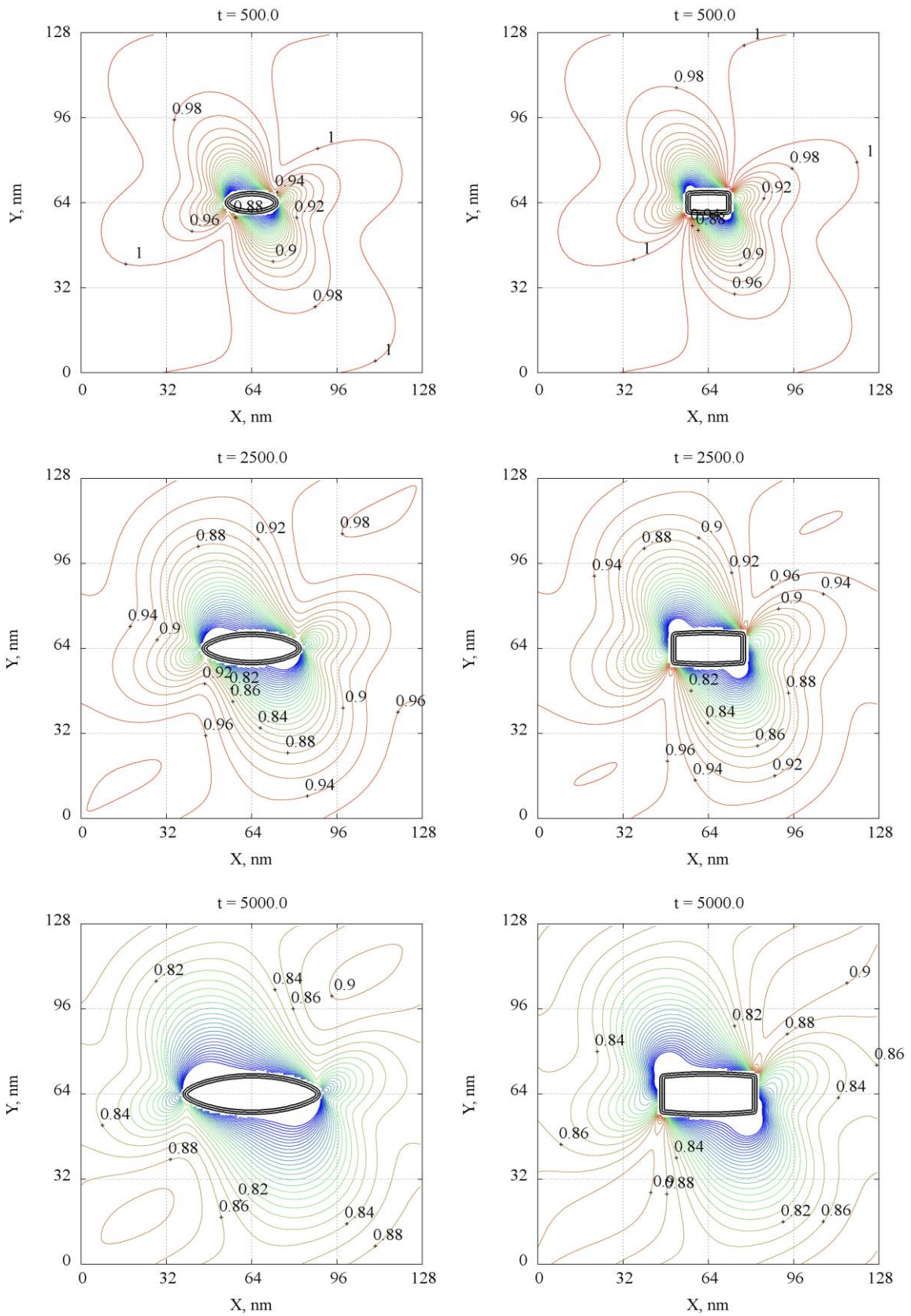


Fig. 66 Nucleation driving forces around the growing  $\theta'$  precipitate. On the left – smooth elliptical anisotropy, on the right – sharp corners rectangular anisotropy.



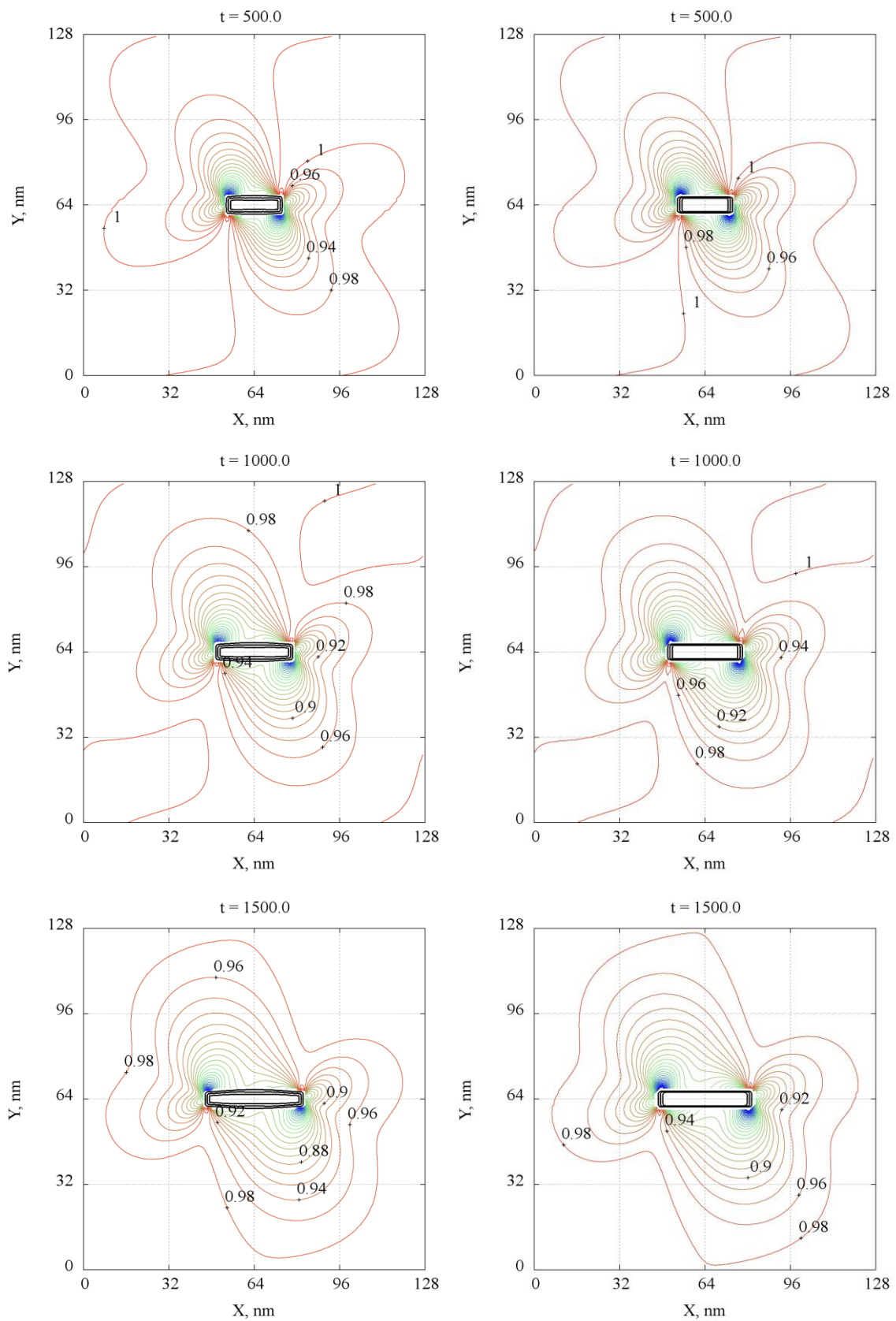


Fig. 68 Nucleation driving forces around  $\theta'$  plates modelled under different conditions: on the left fully resolved interfaces and anisotropic mobility, on the right – unresolved and numerically pinned habit planes.

The test cases discussed above led to the following conclusions:

- The specific choice of the function for the interfacial energy does not have a significant influence on the driving force for nucleation in the surroundings of the growing precipitate. Provided that the size and aspect ratio of the precipitates are similar the driving force around such plates appears to be approximately the same. This fact allows one to employ simple and computationally effective models of interfacial energy anisotropy, i.e. introducing different gradient coefficients along principle directions of a system [134]
- Furthermore, the exact growth conditions in the numerical scheme have no effect on the driving force field. Numerical pinning of a poorly resolved interface seems to be an adequate way to introduce kinetic anisotropy.

In light of these findings the remaining simulations are based on 3-to-1 elliptic interfacial anisotropy, variable interface width and a grid that restricts the motion of broad precipitate faces by limiting their resolution on a computational grid (the approach adopted in most of the phase field simulations of  $\theta'$  plates in Al-Cu [56, 134]). Simplifications in interfacial and kinetic anisotropies also allow taking full advantage of spectral methods in solving both the Cahn-Hilliard and Allen-Cahn equations. For the further simulations the Allen-Cahn equation was simplified to the form (5.83) with isotropic interface mobility  $L_\eta$  and principle direction gradient coefficients  ${}^x k_i$  and  ${}^y k_i$ :

$$\begin{aligned} \frac{\partial \eta_i}{\partial t} = & -L_\eta \left( -2A \left[ c - c_\alpha^{eq} - (c_\beta^{eq} - c_\alpha^{eq}) h(\eta_1, \eta_2) \right] (c_\beta^{eq} - c_\alpha^{eq}) \frac{\partial h(\eta_1, \eta_2)}{\partial \eta_i} \right. \\ & + W_0 \frac{\partial g(\eta_1, \eta_2)}{\partial \eta_i} - {}^x k_i \frac{\partial^2 \eta_i}{\partial x^2} - {}^y k_i \frac{\partial^2 \eta_i}{\partial y^2} \\ & \left. + \frac{\partial \Theta(\eta_i)}{\partial \eta_i} \sum_{q=1}^2 \{ B'_{iq}(\vec{n}) \{ \Theta_q \} \} \right) \end{aligned} \quad (5.83)$$

In the next chapter the phase field model is combined with an explicit nucleation algorithm and results of the simulations of strain induced transformation are presented.



## 6. Driving forces for nucleation in the environment of pre-existing $\theta'$ precipitates

In this chapter the results of the phase field simulations of the  $\theta'$  formation in Al-Cu are presented in detail. The system is simulated in two dimensions and nucleation is modelled by the explicit nucleation algorithm. The model of coherent precipitation developed here is sensitive to elastic interactions of the microstructure and potential nuclei and therefore applied to test the possibility of autocatalytic nucleation under several assumptions regarding the type of the transformation strain of the nuclei.

Autocatalytic nucleation may only be possible if the driving force for the formation of a nucleus is altered locally in the vicinity of a previously formed precipitate. An increase or decrease in the magnitude of the nucleation driving force (compared to that in the unperturbed matrix) results from the combination of two terms: the chemical driving force defined by a local matrix composition and the elastic interaction energy between the nucleus and the pre-existing precipitate. The distribution of the driving force in the vicinity of a growing  $\theta'$  plate is analysed systematically for two alloy compositions and the range of transformation temperatures.

The type of coherency strain between the matrix and the mature precipitate is considered to be tetragonal, as observed in experiments of Stobbs and Purdy [77] and Dahmen and Westmacott [90]. It is still consistent with the transformation mechanism that involves shear, because the sheared transformation blocks or layers are expected to form in combinations that minimise the total strain energy by mutually cancelling shear. The simulations are based on the magnitude of the remaining tetragonal misfit that is most often observed for  $\theta'$  plates. In the two scenarios considered here the central pre-existing  $\theta'$  plate has only tetragonal misfit of -4.3%.

On the other hand nuclei are assumed either of the same transformation strain as fully developed mature plates or having the combination of tetragonal misfit with the shear component of 0.3. The latter is representative of the diffusional-displacive transformation models by Nie and Muddle [64, 65] and Dahmen and Westmacott [90].

The difference in the distribution of the interaction energy and the total driving force is presented and analysed in detail. In the final section long term simulations with nucleation are presented and discussed.

## 6.1. Formation of a nucleus with tetragonal transformation strain

In this section the hypothesis of autocatalysis will be tested under the assumption that the stress-free transformation strain of a nucleus does not contain a shear component. This corresponds to the traditional model of  $\theta'$  formation, which assumes that precipitates have disordered edges and the transformation is diffusional in character. Elastic misfit exists only in the direction normal to a broad habit plane of a precipitate.

If arrays of precipitates that are occasionally observed in experiments are formed in a sequential chain of events, with the next plate stimulated by the formation of a previous one, it is necessary to monitor how the driving force around individual precipitate evolves during its growth from the critical nucleus size onwards. Since the elastic interaction is fairly localised, the influence of pre-existing microstructure is largely an influence of a nearest pre-existing plate.

In the following simulations a small  $\theta'$  nucleus is seeded in the centre of a simulation domain and its growth is monitored. The simulation domain is the square with 256 nm side with periodic boundary conditions employed. The small initial precipitate 2.5 nm thick and 7.5 nm wide is placed in the centre. Simulations are performed for two alloy compositions (2 and 4 wt. % Cu) and three ageing temperatures (200°C, 225°C and 250°C) for each composition in order to approximately cover the range where  $\theta'$  forms directly from solid solution.

In the series of figures from Fig. 69 to Fig. 74 the snapshots of nucleation driving forces are taken at the stages of growth when the length of the plate passes through 16 nm, 32 nm and 64 nm in order to monitor different stages of growth and matrix depletion. To see the effect of the elastic interaction the total driving force is plotted next to the distribution of the chemical driving force alone. In each case the total driving force is normalised by  $G_{chem}(c_0, T)$ , the magnitude of the chemical driving force in the matrix at the initial composition.

In all cases simulated and presented in Fig. 69 - Fig. 74 evolution of the nucleation driving force is essentially the same and is characterised by the following features:

- The elastic interaction of the pre-existing precipitate and the potential nucleus does affect the magnitude and symmetry of the driving force distribution. However, the strength of the interaction is not sufficient to create any localised regions of elevated driving force. Also, no specific directions, or “corridors” where the driving force remains significantly above other locations could be identified.

- The reduction of the chemical driving force due to the matrix depletion is invariably sufficient to suppress the stimulating effect of elastic interaction even at close distances from the growing precipitate, where the effect of interaction is most pronounced. The propagation of the depletion field also seems to be effective in compensating the elastic interaction contribution, which grows in magnitude as the plate gets bigger.
- Neither composition, nor ageing temperature has significant effect on the evolution of the normalised driving force. The variation of the nucleation driving force in the matrix at initial composition is quite pronounced and one might expect a stronger effect of elasticity at lower chemical driving forces (changing between  $2.5 \cdot 10^8 \text{ J/m}^3$  in 2 wt. % Cu alloy at 250°C and  $3.8 \cdot 10^8 \text{ J/m}^3$  in 4 wt. % Cu alloy at 200°C). The effect, however, is not readily obvious in the maps of the total driving force. As can be seen from a comparison of Fig. 71 with Fig. 72, a transformation that proceeds at lower level of overall driving force results in thinner plates that lead to weaker elastic interaction. The changes in magnitude of the chemical term and the elastic term are in the same direction and therefore normalised levels of the total driving force are very similar.

It is concluded that the nucleus with stress-free transformation strain without shear would generally not benefit from elastic interaction with pre-existing microstructure. The magnitude of such interaction is insufficient to significantly alter nucleation driving forces and is efficiently suppressed by reduction in chemical driving forces due to matrix depletion. The behaviour is similar in the wide range of matrix composition and transformation temperatures considered.

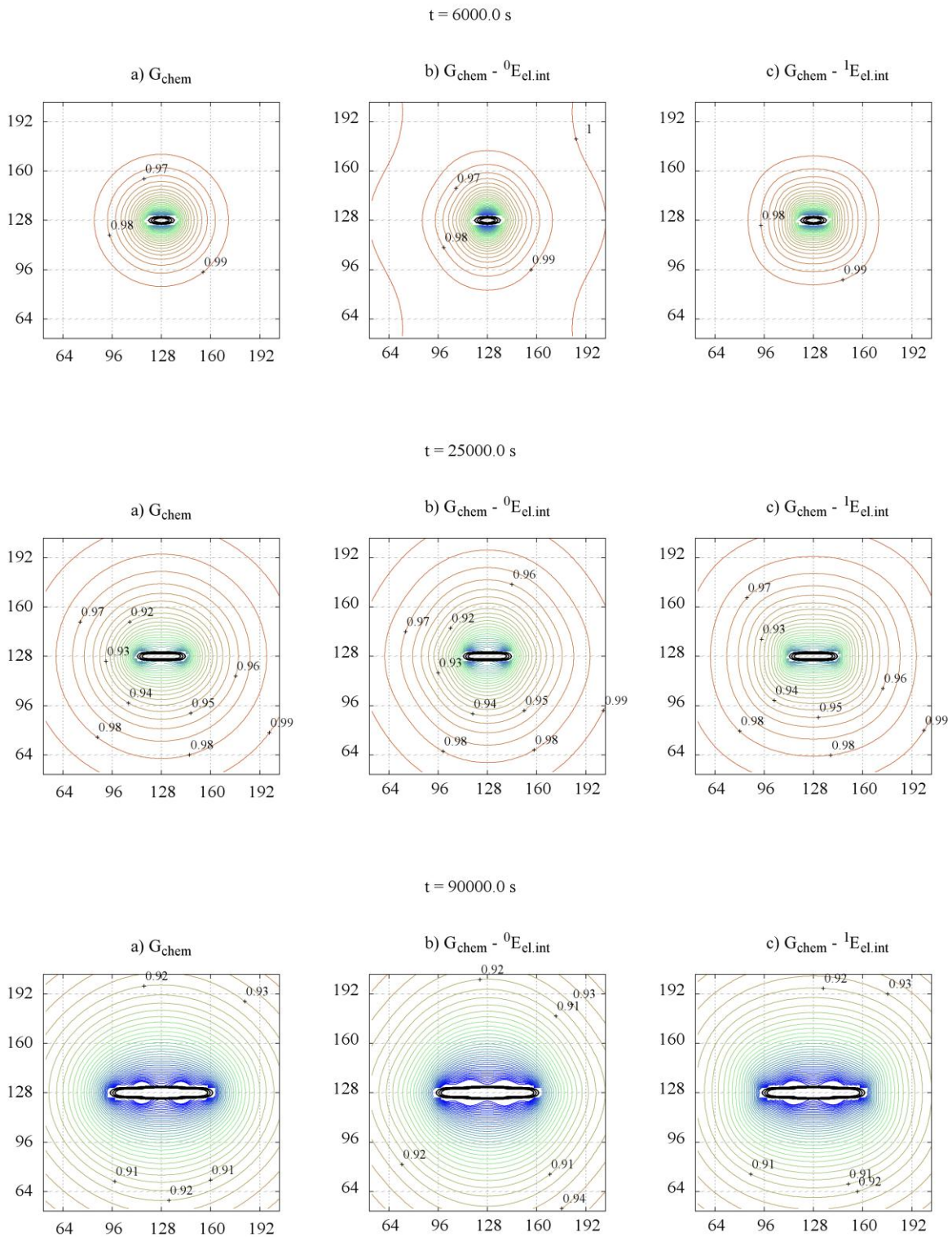


Fig. 69 Al-2 wt. % Cu,  $T = 200^\circ\text{C}$ . Distributions of a) chemical driving force, b) total driving force for the formation of a nucleus with a tetragonal misfit in the  $[01]$  direction and c) total driving force for the formation of the tetragonal nucleus with a  $[10]$  misfit.

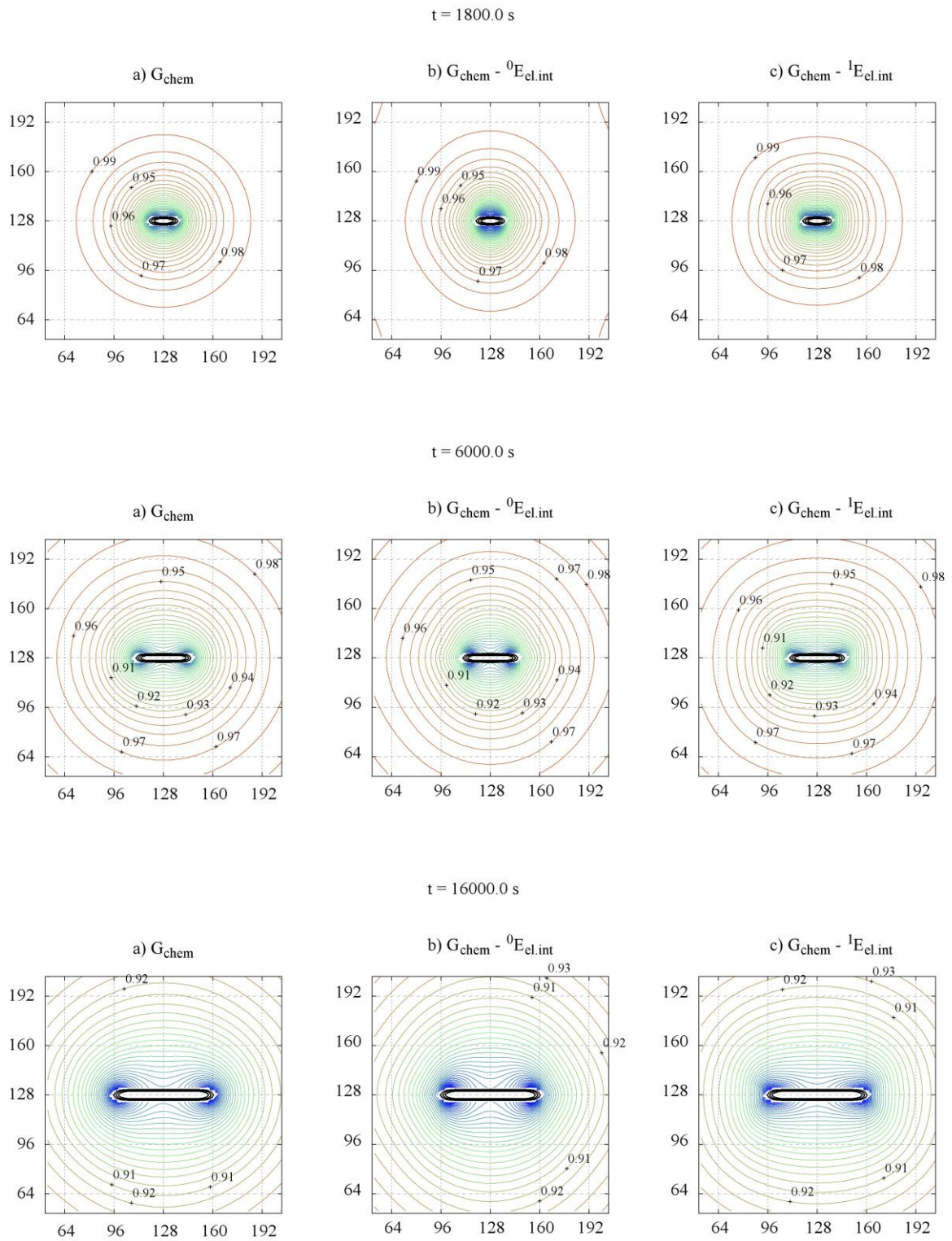


Fig. 70 Al-2 wt. % Cu,  $T = 225^\circ\text{C}$ . Distributions of a) chemical driving force, b) total driving force for the formation of a nucleus with a tetragonal misfit in the [01] direction and c) total driving force for the formation of the tetragonal nucleus with a [10] misfit.

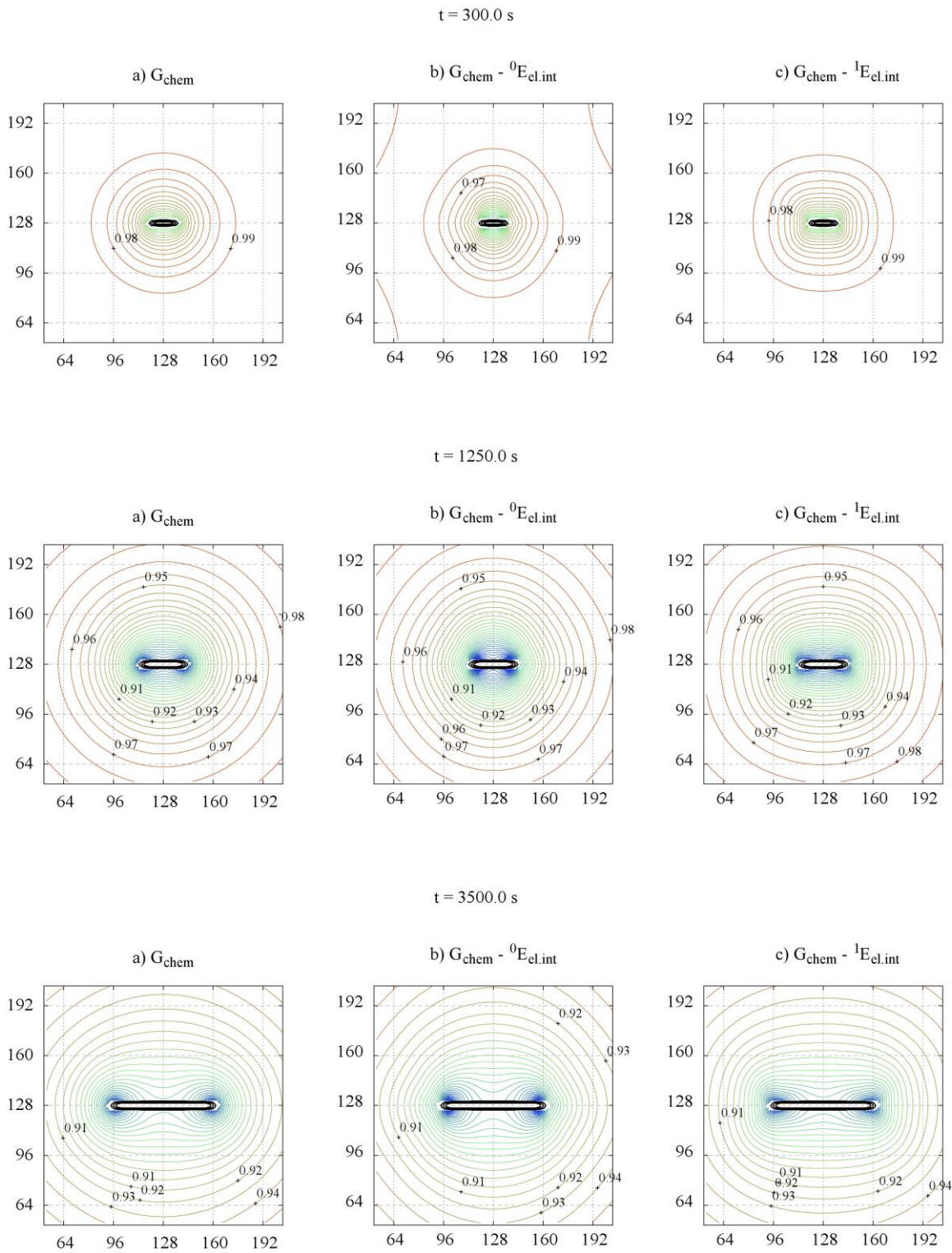


Fig. 71 Al-2 wt. % Cu,  $T = 250^{\circ}\text{C}$ . Distributions of a) chemical driving force, b) total driving force for the formation of a nucleus with a tetragonal misfit in the  $[01]$  direction and c) total driving force for the formation of the tetragonal nucleus with a  $[10]$  misfit.

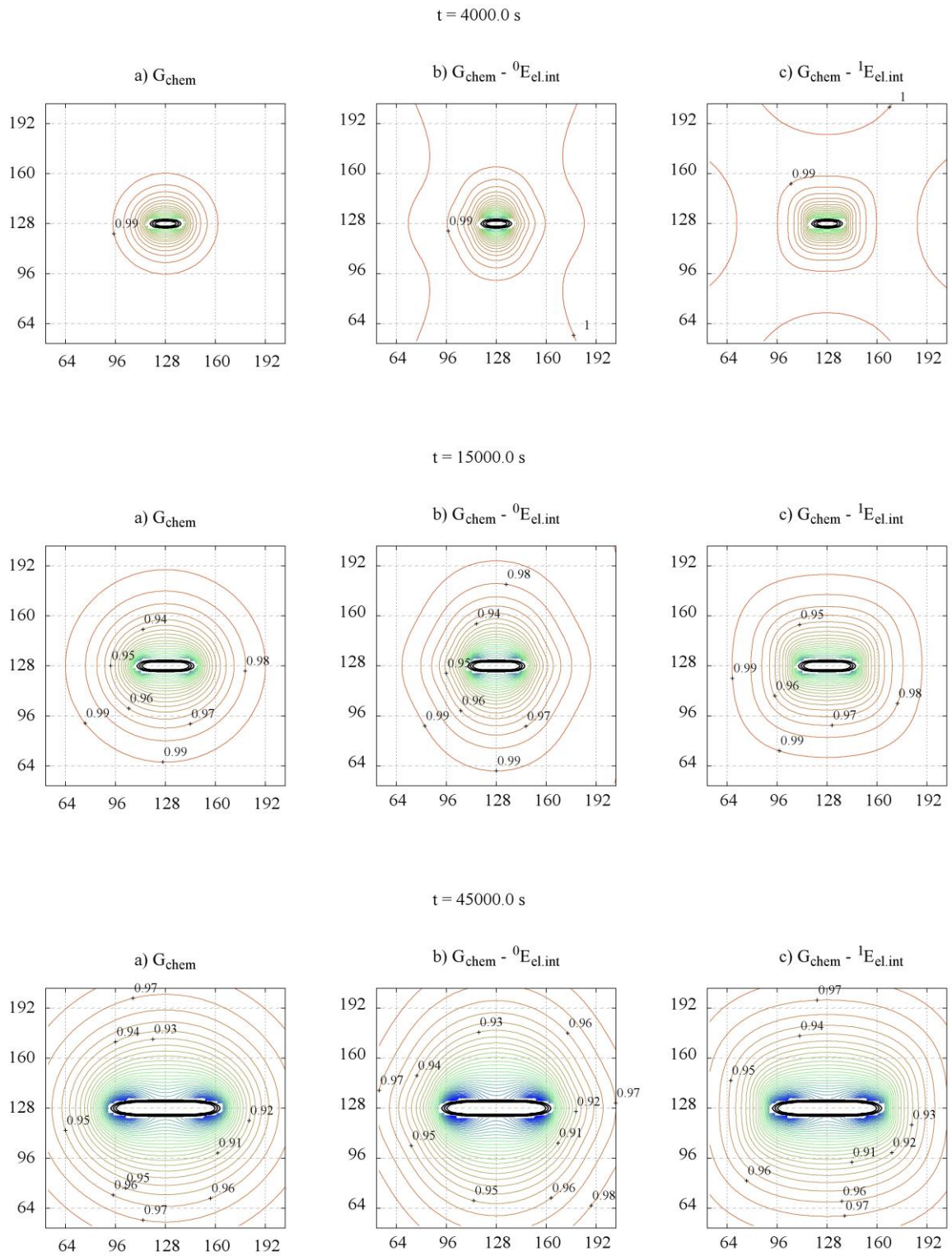


Fig. 72 Al-4 wt. % Cu,  $T = 200^\circ\text{C}$ . Distributions of a) chemical driving force, b) total driving force for the formation of a nucleus with a tetragonal misfit in the  $[01]$  direction and c) total driving force for the formation of the tetragonal nucleus with a  $[10]$  misfit.

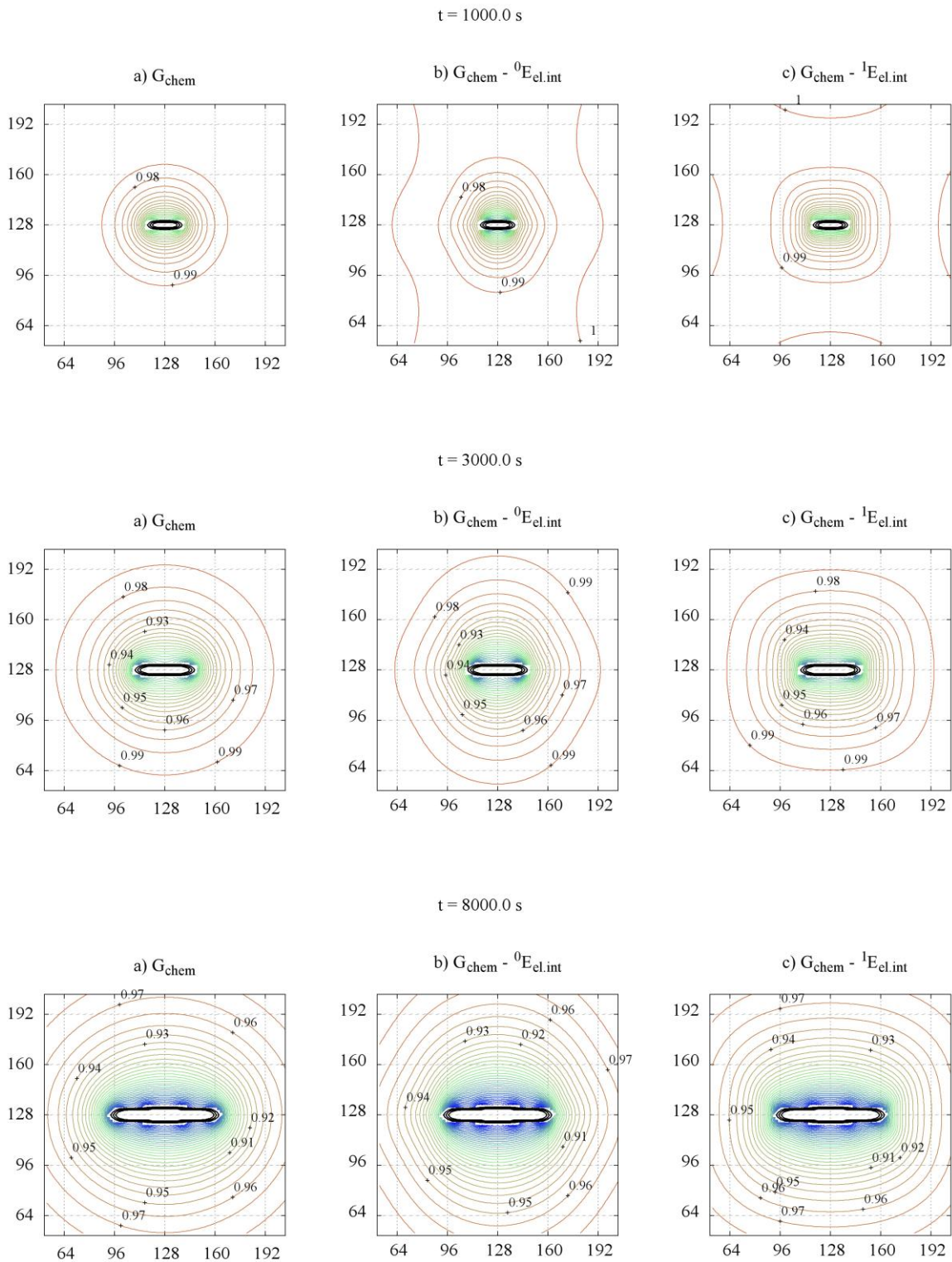


Fig. 73 Al-4 wt. % Cu,  $T = 225^\circ\text{C}$ . Distributions of a) chemical driving force, b) total driving force for the formation of a nucleus with a tetragonal misfit in the [01] direction and c) total driving force for the formation of the tetragonal nucleus with a [10] misfit.

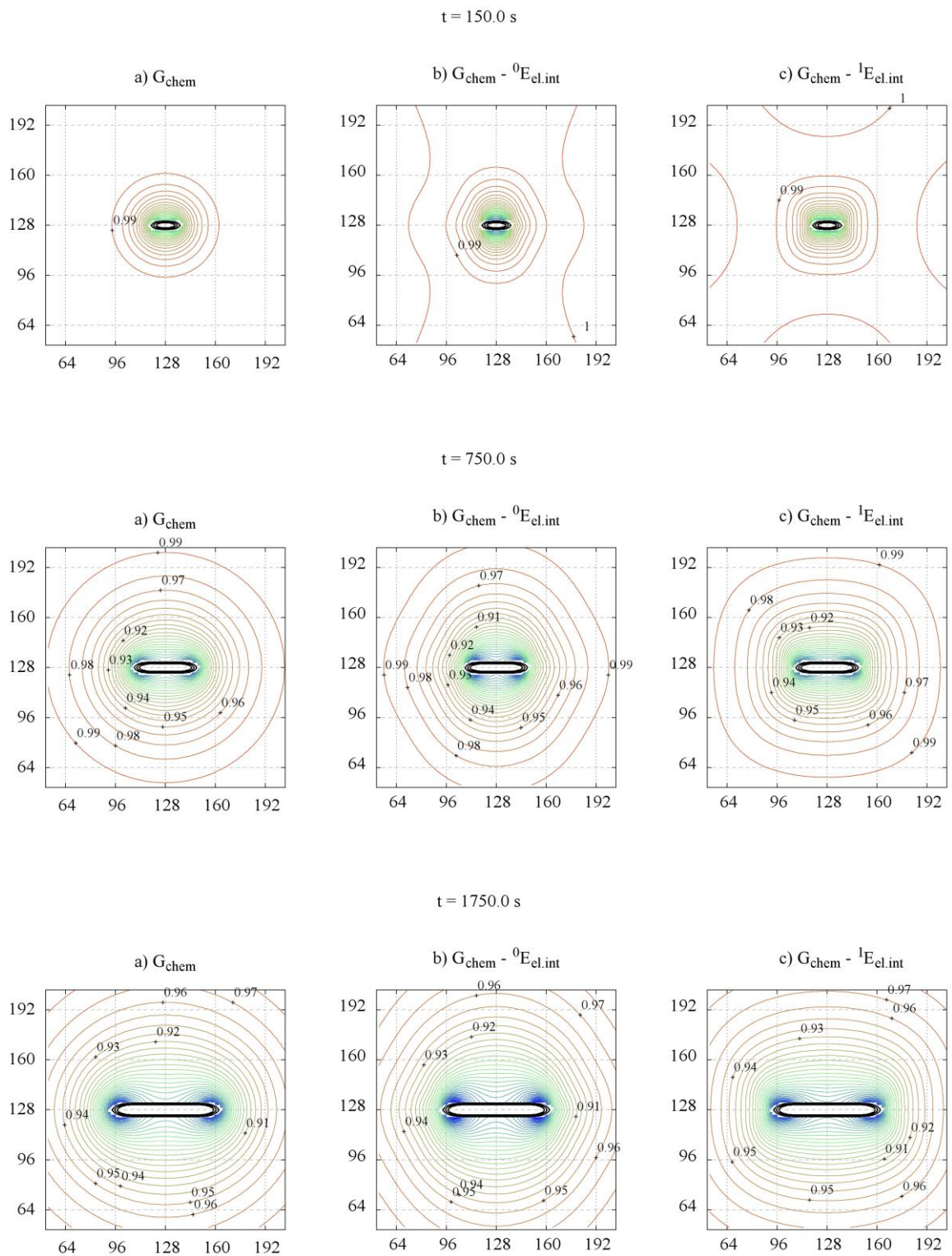


Fig. 74 Al-4 wt. % Cu,  $T = 250^\circ\text{C}$ . Distributions of a) chemical driving force, b) total driving force for the formation of a nucleus with a tetragonal misfit in the  $[01]$  direction and c) total driving force for the formation of the tetragonal nucleus with a  $[10]$  misfit.

## **6.2. Formation of a nucleus with shear component in the transformation strain**

A similar analysis is performed for the formation of the sheared nucleus. The series of figures from Fig. 75 to Fig. 80 illustrates the effect of the interaction between the growing plate and the nucleus with the shear component of 0.3. Only one orientation of tetragonal misfit is presented here, since the shear component primarily defines the strength and symmetry of interaction and the tetragonal misfit in other direction leads to very similar results.

Contrary to the case of the purely tetragonal misfit the level of elastic interaction is strong enough to change the distribution of the nucleation driving force significantly.

Most notably, the level of interaction is high enough to compensate for matrix depletion next to the tip of the plate at the early stages of growth. This should not, however, be interpreted as the definitive location for the nucleation of the new precipitate or a ledge on the surface, since the method of assessing the interaction energy is not valid in severely strained regions.

Nonetheless, even at intermediate stages in growth, when plates reach 32 nm or 64 nm in length, the balance of the reduced chemical driving forces and the elastic interaction creates well pronounced regions of total driving forces maintained at or even slightly above their initial level in the matrix. This is in spite of well developed depletion fields around the tips of the precipitate. The effect is especially strong for thicker plates that form in 4 wt. % Cu alloy, as demonstrated in Fig. 78 - Fig. 80.

The distribution of the driving force obtained in the simulations should promote the formation of nuclei in the regions close to the edges of pre-existing precipitates, above or below them depending on the sign of the shear in the nucleus. This geometry is consistent with the arrangement of precipitates into arrays of both Type IV and Type V observed in experiments and discussed previously in chapter 4 “Elastic interaction model of strain assisted nucleation”.

In the next section the explicit nucleation algorithm is used as a part of phase field simulation to dynamically simulate the microstructure that develops under the assumption that the nuclei are of sheared character.

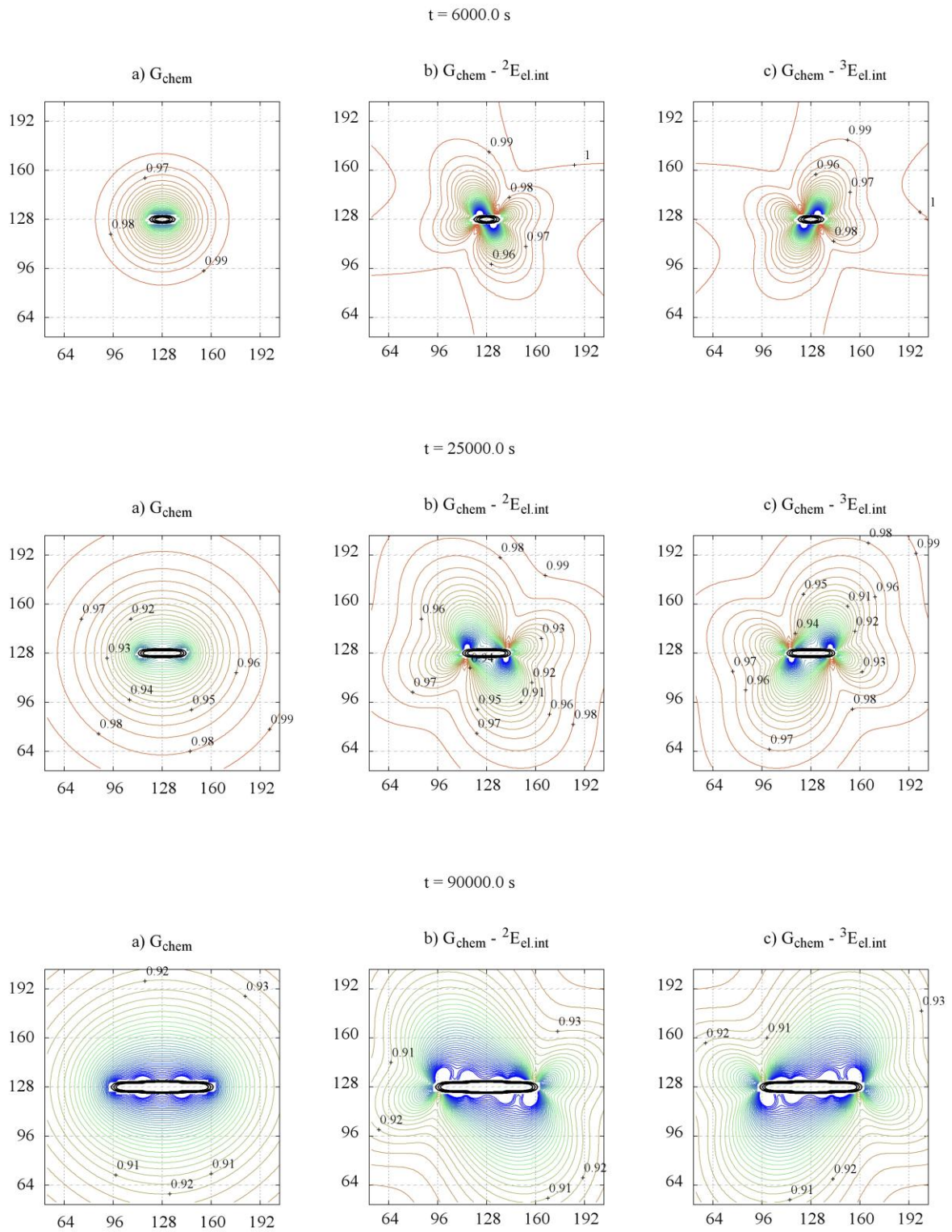


Fig. 75 Al-2 wt. % Cu,  $T = 200^\circ\text{C}$ . Distributions of a) chemical driving force, b) total driving force for the formation of a nucleus with tetragonal misfit in the [01] direction and positive shear along [10]; c) total driving force for the formation of a nucleus with tetragonal misfit in the [01] direction and negative shear along [10].

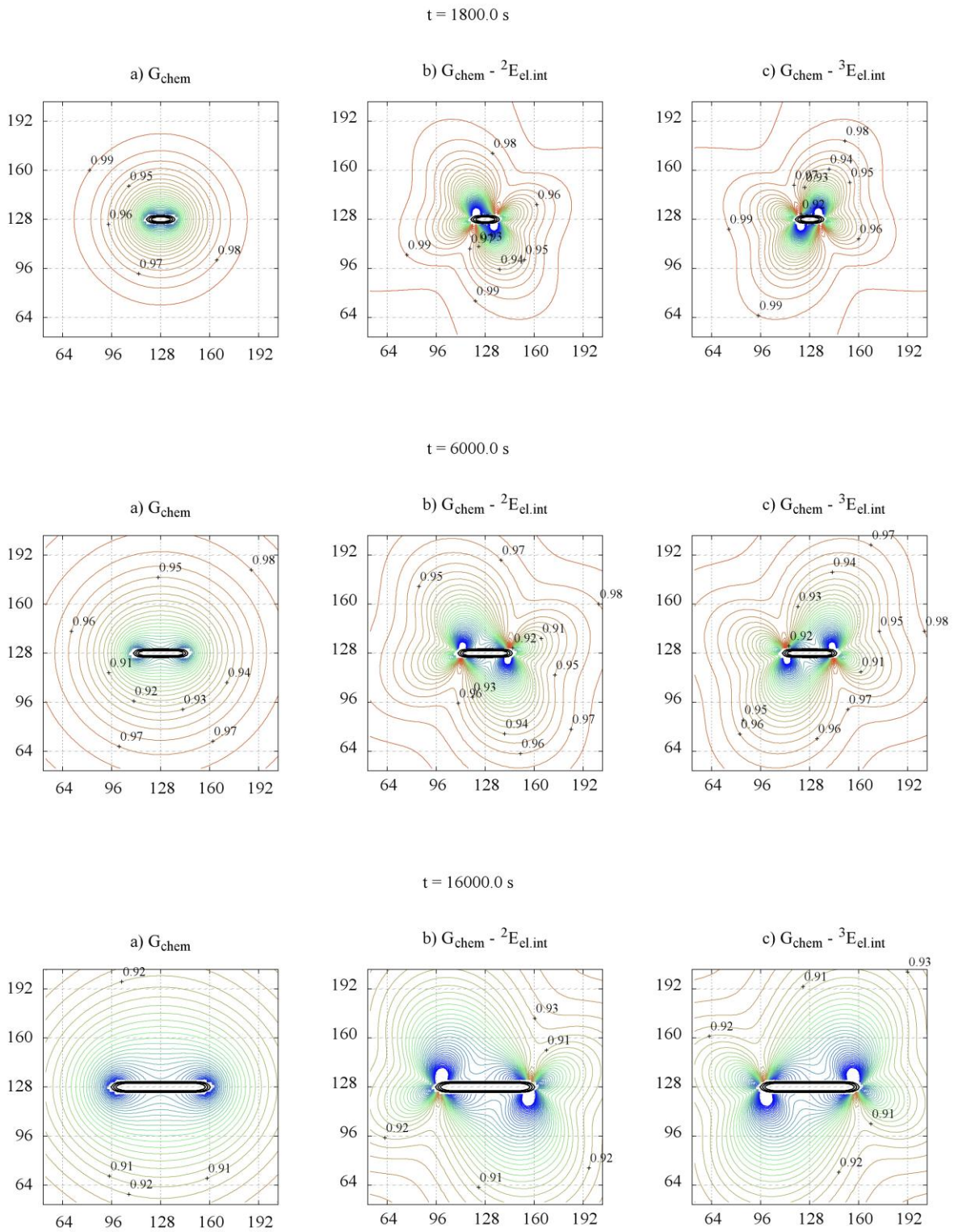


Fig. 76 Al-2 wt. % Cu,  $T = 225^\circ\text{C}$ . Distributions of a) chemical driving force, b) total driving force for the formation of a nucleus with tetragonal misfit in the [01] direction and positive shear along [10]; c) total driving force for the formation of a nucleus with tetragonal misfit in the [01] direction and negative shear along [10].

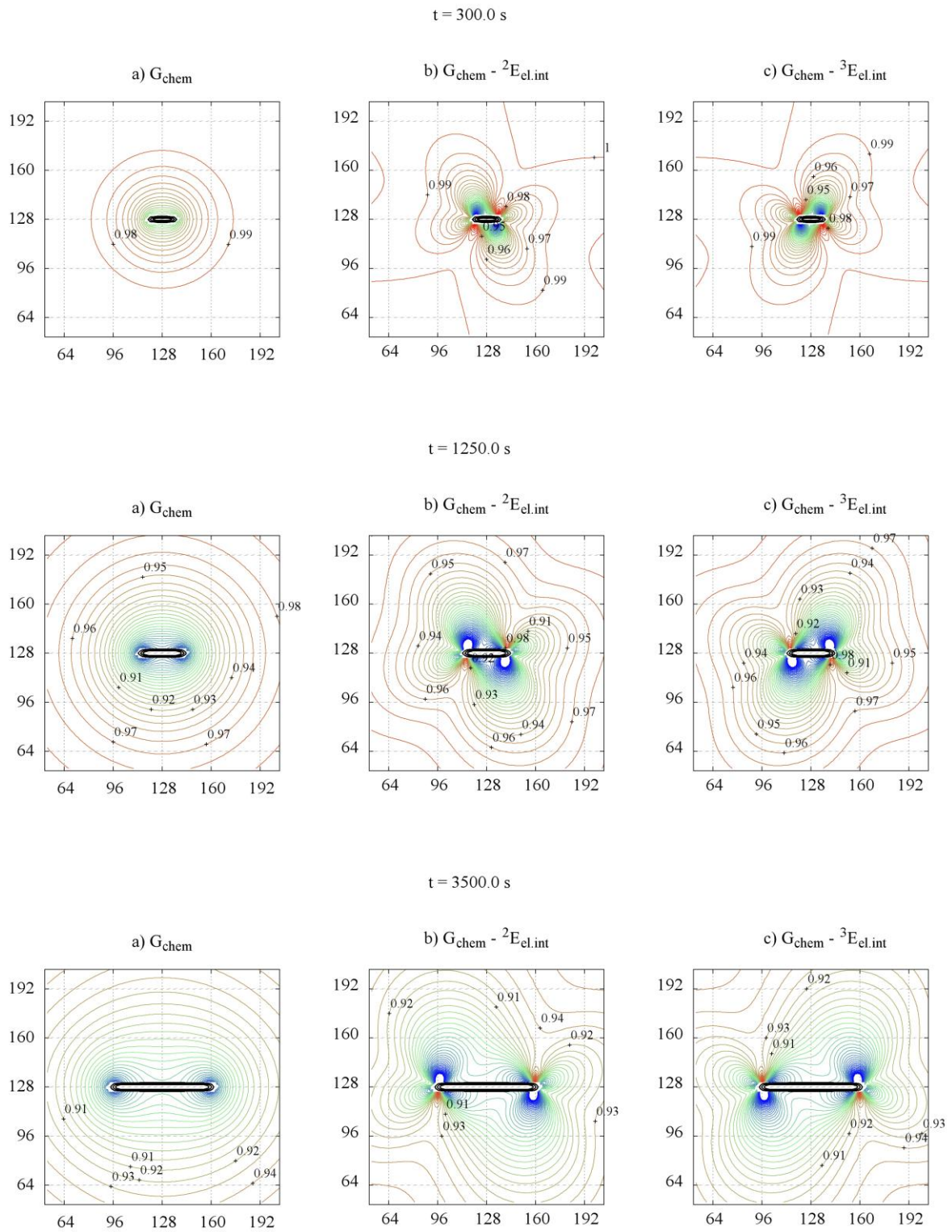


Fig. 77 Al-2 wt. % Cu,  $T = 250^\circ\text{C}$ . Distributions of a) chemical driving force, b) total driving force for the formation of a nucleus with tetragonal misfit in the [01] direction and positive shear along [10]; c) total driving force for the formation of a nucleus with tetragonal misfit in the [01] direction and negative shear along [10].

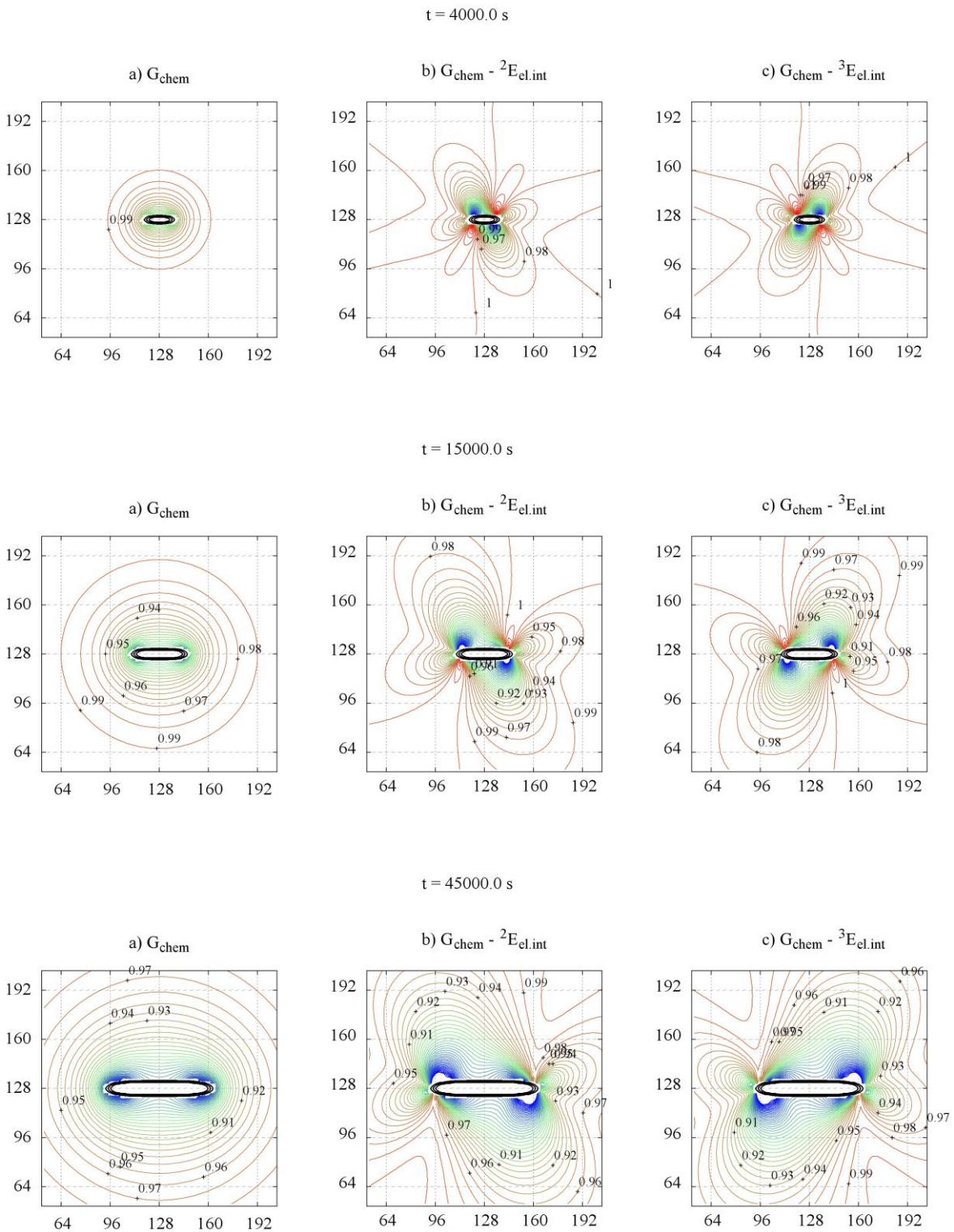


Fig. 78 Al-4 wt. % Cu,  $T = 200^{\circ}\text{C}$ . Distributions of a) chemical driving force, b) total driving force for the formation of a nucleus with tetragonal misfit in the [01] direction and positive shear along [10]; c) total driving force for the formation of a nucleus with tetragonal misfit in the [01] direction and negative shear along [10].

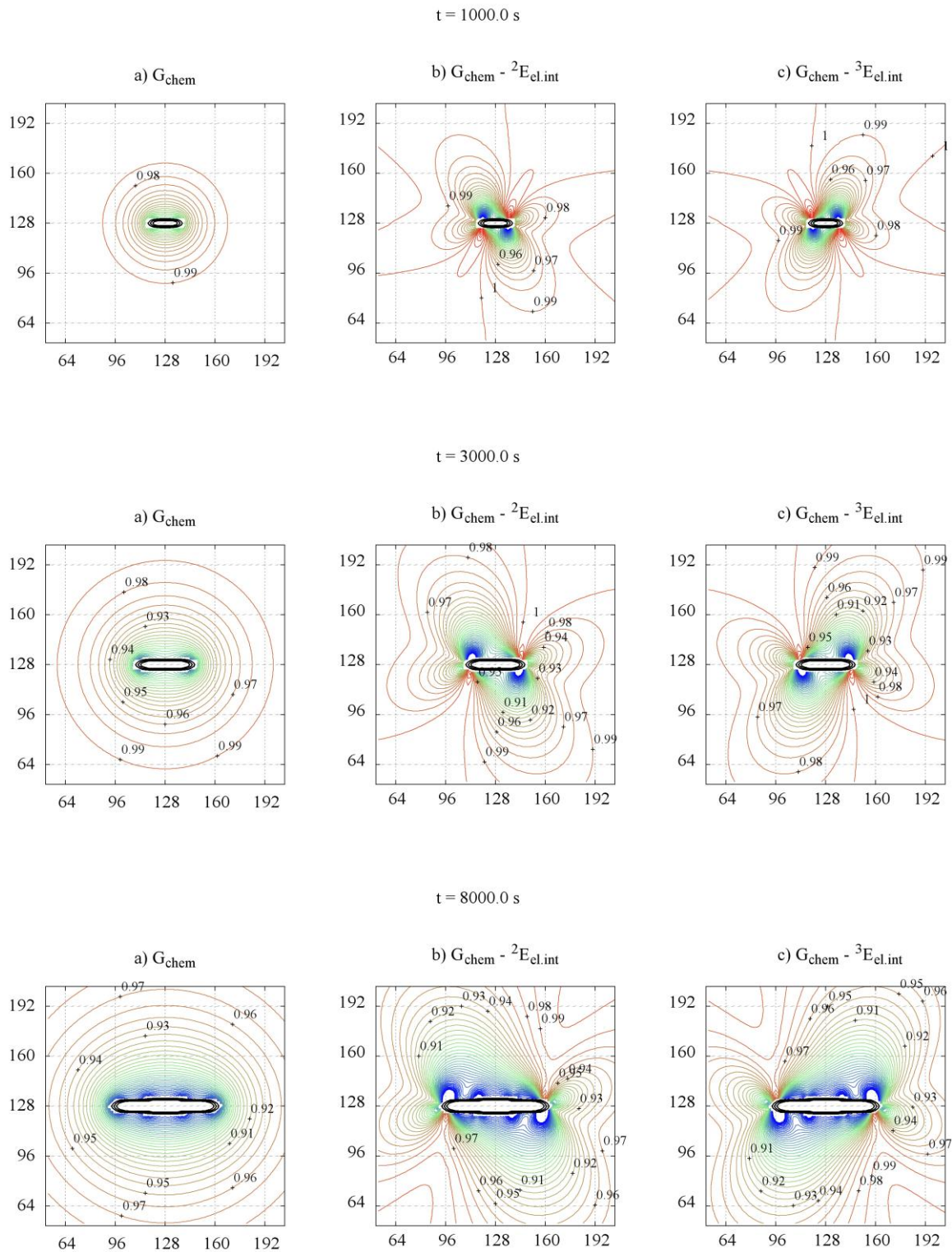


Fig. 79 Al-4 wt. % Cu,  $T = 225^\circ\text{C}$ . Distributions of a) chemical driving force, b) total driving force for the formation of a nucleus with tetragonal misfit in the [01] direction and positive shear along [10]; c) total driving force for the formation of a nucleus with tetragonal misfit in the [01] direction and negative shear along [10].

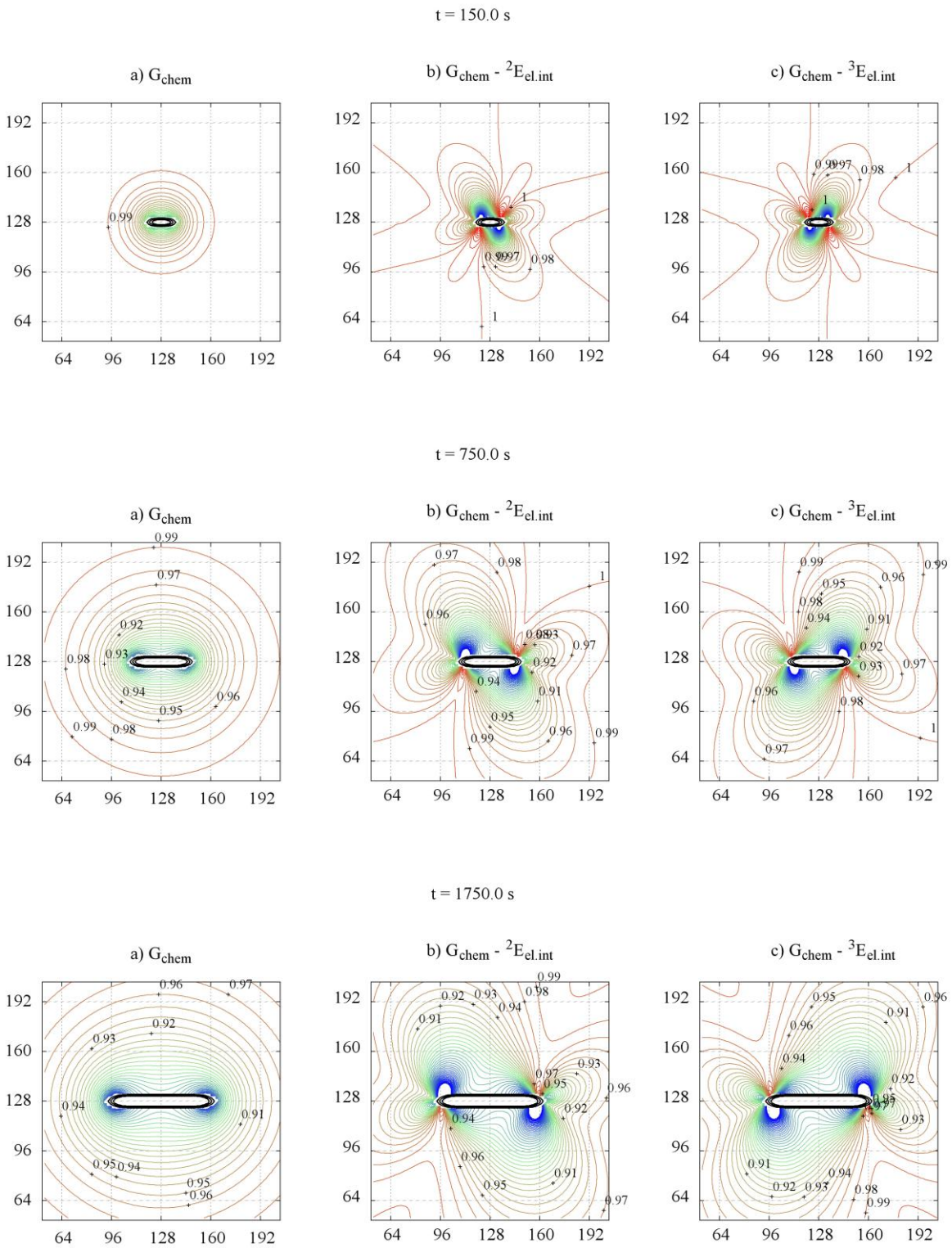


Fig. 80 Al-4 wt. % Cu,  $T = 250^\circ\text{C}$ . Distributions of a) chemical driving force, b) total driving force for the formation of a nucleus with tetragonal misfit in the [01] direction and positive shear along [10]; c) total driving force for the formation of a nucleus with tetragonal misfit in the [01] direction and negative shear along [10].

### 6.3. Strain assisted nucleation

As demonstrated in the previous section the elastic interaction between the sheared nucleus and the microstructure is sufficiently strong to affect the total driving force for nucleation. To analyse dynamically whether there is a potential for the autocatalytic formation of precipitate arrays a series of simulations was performed with nucleation modelled by the explicit nucleation algorithm.

In all simulations the system under consideration is Al-4 wt. % Cu aged at 225°C. The phase field simulation domain is a two dimensional square 768 by 768 nm in size with periodic boundary conditions employed. The initial solute distribution is homogeneous and precipitates are introduced in the random process handled by the explicit nucleation algorithm with the probability affected by local supersaturation and elastic interaction with the microstructure.

It is important to note that all simulations are semi-qualitative, since most of the rate controlling parameters, namely the interfacial energies and chemical driving forces, are estimates with varying degrees of reliability. Therefore, the overall nucleation rate is treated as parameter. According to classical nucleation theory the rate is expressed in the following form:

$$J = k_1 \exp \left( - \frac{k_2}{\left( G_{chem} - \frac{\Delta E^{int}}{V_0} \right)^{d-1}} \right) \quad (5.84)$$

where  $G_{chem}$  is a chemical driving force defined by composition and transformation temperature,  $\Delta E^{int}/V_0$  is the volumetric elastic interaction energy between the nucleus and the microstructure,  $d$  is dimensionality of the problem,  $k_1$  is a pre-exponential factor (constant for isothermal transformation, has the same temperature dependence as solute diffusion coefficient) and  $k_2 \sim \gamma^d / (k_B T)$  is a constant that combines the rest of the terms in the exponential factor.

In the following simulations the constant  $k_2$  is varied to produce barrier terms in the range from 30 to 60  $k_B T$ . The relative strength of the autocatalytic effect should depend on the sensitivity of the rate to changes in the magnitude of the nucleation barrier. For different values of  $k_2$  the same fractional change in the magnitude of the driving force will lead to different changes in the magnitude of the exponential term in the rate equation (5.84). Therefore, it is of interest to monitor the effects of strain at various levels of the barrier in the unperturbed matrix.

The pre-exponential factor is varied to check how strong the effect of elastic interaction is at different overall nucleation rates, since a high rate may produce dense homogeneous distribution that masks any autocatalytically linked nucleation events.

In the simulations presented in Fig. 81 - Fig. 96 the basis nucleation rate  $J_0$  is selected to produce a certain number  $N_{nuc}$  of nuclei per 512 nm square per 1000 seconds of transformation. Then constants  $k_1$  and  $k_2$  are adjusted to produce a specific barrier  $\tilde{G} = k_2/G_{chem}^{d-1}$  and to match the overall nucleation rate through the expressions below:

$$\begin{aligned} k_1 &= J_0 / \exp(-\tilde{G}) \\ k_2 &= \tilde{G} (G_{chem}(c_0, T))^{d-1} \end{aligned} \tag{5.85}$$

The ranges of input parameters covered are 1 to 8 for  $N_{nuc}$  and 30 to 60  $k_B T$  for the exponential barrier term.

In the next section effects of the nucleation rate level are analysed in detail. Then the influence of the transformation strain type is considered and analysis is presented for the differences in the microstructure between tetragonal and mixed type models of the nuclei. Finally, larger scale simulations are discussed and followed by general conclusions.

### 6.3.1. Effect of the nucleation rate

When the nucleation rate is low, precipitation events are rare and the distribution of  $\theta'$  is sparse. Precipitates have enough time for growth and their depletion fields develop faster than potential nuclei are able to take advantage of the catalytic effect of the elastic interaction.

The behaviour is quite similar for different levels of the barrier term – see examples for 30 and 50  $k_B T$  barriers in Fig. 81 and Fig. 82 respectively. Occasionally precipitates occur in small groups, as for example seen in the top right quadrants in both Fig. 81 and Fig. 82 between 5400 and 9000 s. Such grouping is usually restricted to several sequential events resulting in clusters of maximum three or four plates.

The formation of small secondary nuclei next to large precipitates may be detected, see for instance 18000 s snapshot in Fig. 81 that features two instances of the nucleus in the face-to-edge orientation in the vicinity of larger plates. Also the pair of parallel secondary and primary plates may be seen from 7200 s in the bottom left corner of Fig. 82. The grouping appears to be quite random and no sequential autocatalytic chains of multiple plates were detected.

The course of the transformation is different at a higher level of overall nucleation rate. In this case, illustrated in Fig. 83, the density of precipitates is significantly higher. It appears that the probability of the nucleation is high enough to generate new nuclei before the catalytic effect of the elastic interaction becomes suppressed by the matrix depletion. Multiple examples of linked events are evident in all possible mutual orientations of primary and secondary plates. Precipitates seem to be able to induce the formation of the next plate before they grow to large sizes. This is manifested in the high number of groups of relatively small plates.

The high density of both individual precipitates and their groups eventually results in a relatively homogeneous microstructure. It may be speculated that under conditions leading to high nucleation rate the autocatalysis would be harder to detect, since the groups of precipitates formed in autocatalytic sequences become masked by the dense precipitate distribution.

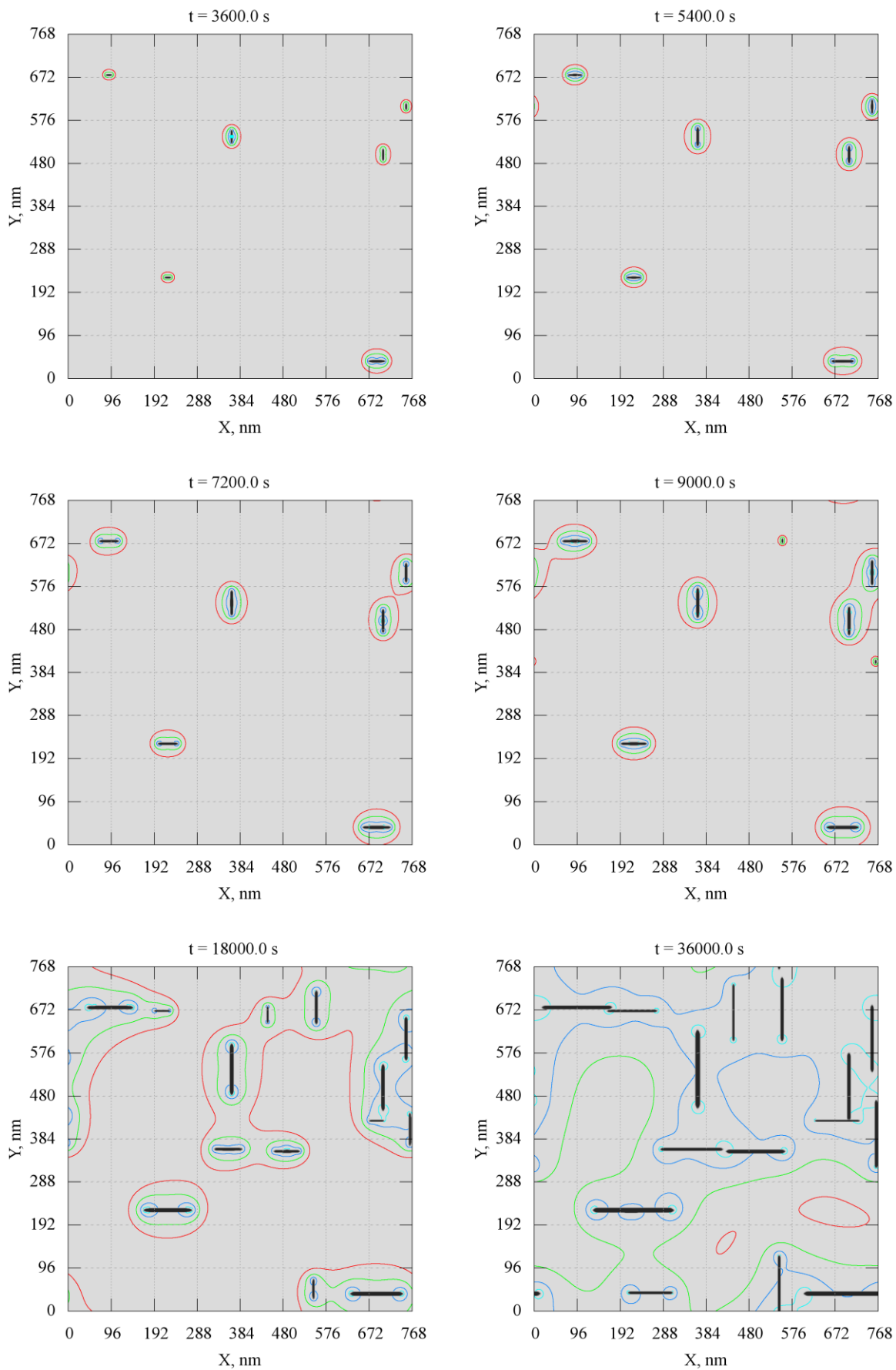


Fig. 81 Evolution of the system with nucleation barrier of  $30 k_B T$  and  $N_{nuc} = 0.5$ .

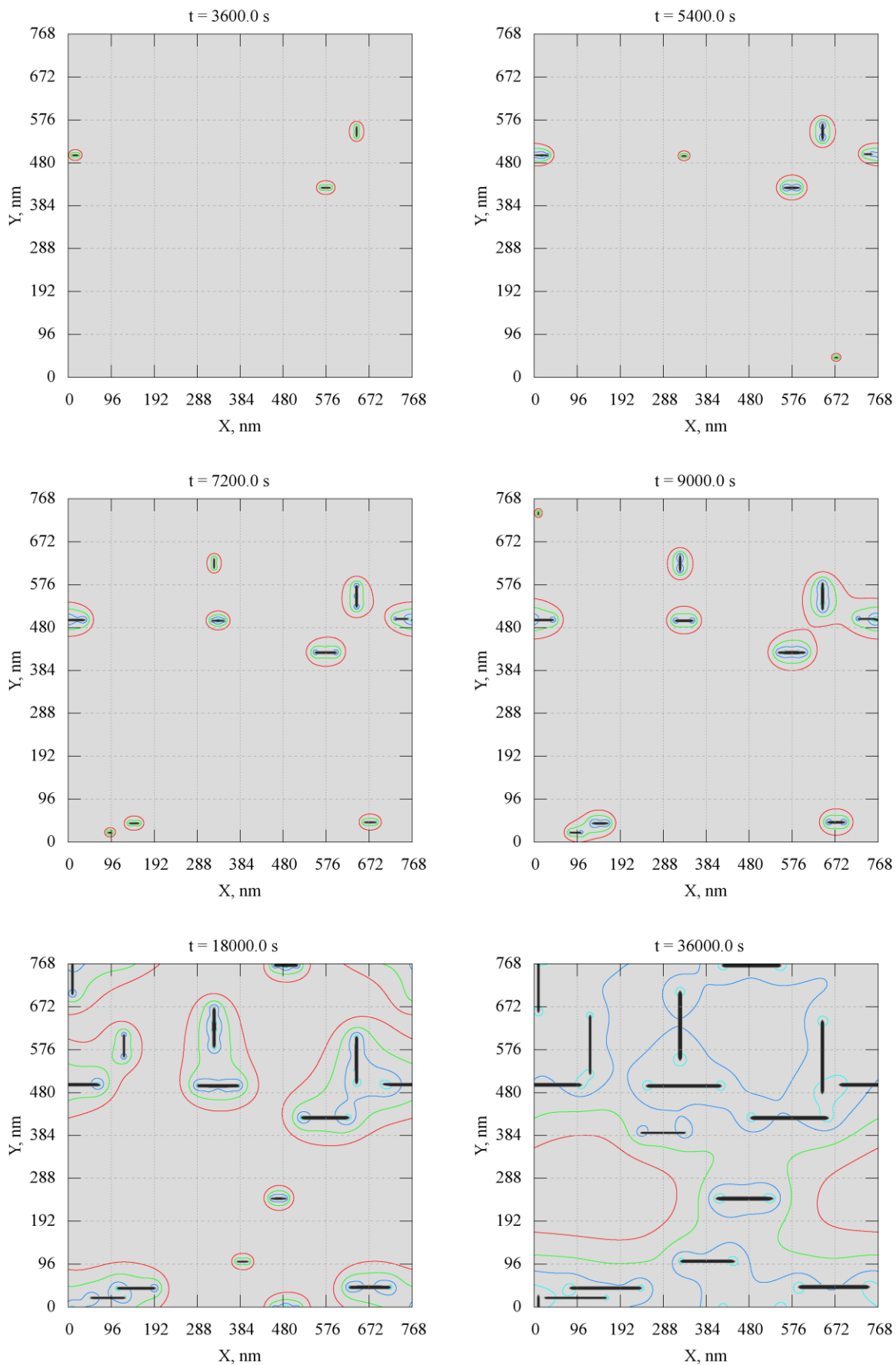


Fig. 82 Evolution of the system with nucleation barrier of  $50 k_B T$  and  $N_{nuc} = 0.5$ .

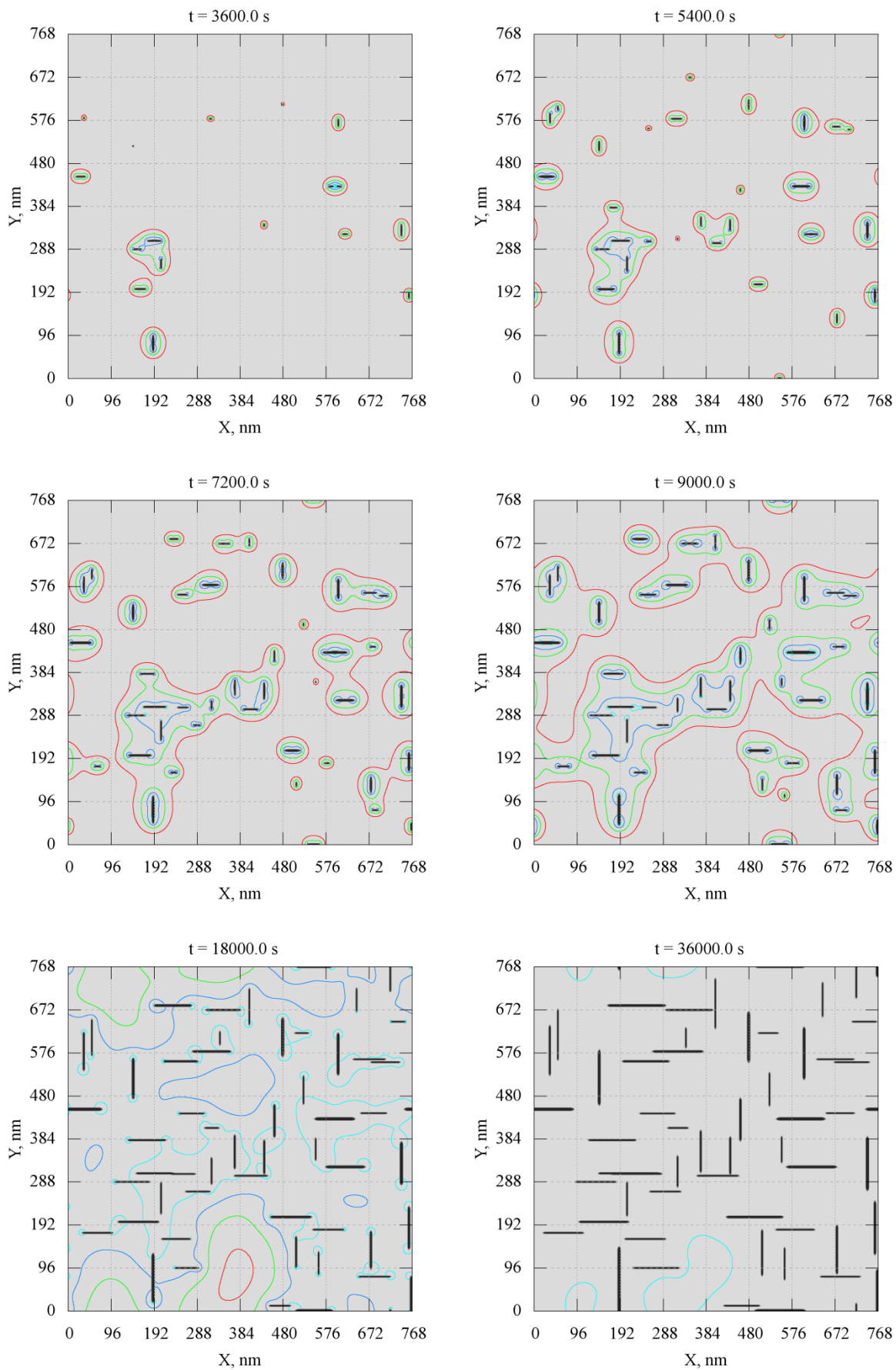


Fig. 83 Evolution of the system with nucleation barrier of  $30 k_B T$  and  $N_{nuc} = 4$ .

A series of simulations with intermediate nucleation rates characterised by values of the parameter  $N_{nuc}$  equal to 1 and 2 is presented in Fig. 84 - Fig. 90. The microstructure that develops is characterised by the abundance of precipitate clusters. These clusters comprise three or more precipitates forming in sequence one after the other. The majority of the clusters have both orientations of plates featured, although occasionally inclined stacks of one orientation are observed, as for example in Fig. 90.

As discussed in the previous section, the level of the nucleation rate has a strong effect on the appearance of the microstructure. For the  $N_{nuc}=2$  the clustering starts earlier in the course of the transformation. For example, at  $N_{nuc}=1$  grouping of the precipitates is limited mostly to agglomerations of two or three plates early in the transformation, and only by the time of 7200 or 9000 s larger clusters develop (see Fig. 84 to Fig. 87). For higher rates clusters of three plates are observed already by 3600 s (Fig. 88) and occasionally even groups of five plates have developed by 5400 s, as in Fig. 90.

The distribution of the precipitates within groups is relatively random, with no preference for one particular variant within a group. Generally the groups appear to be stretched diagonally, confirming the role of the elastic interaction energy in promoting the nucleation diagonally away from the edge of the pre-existing plate.

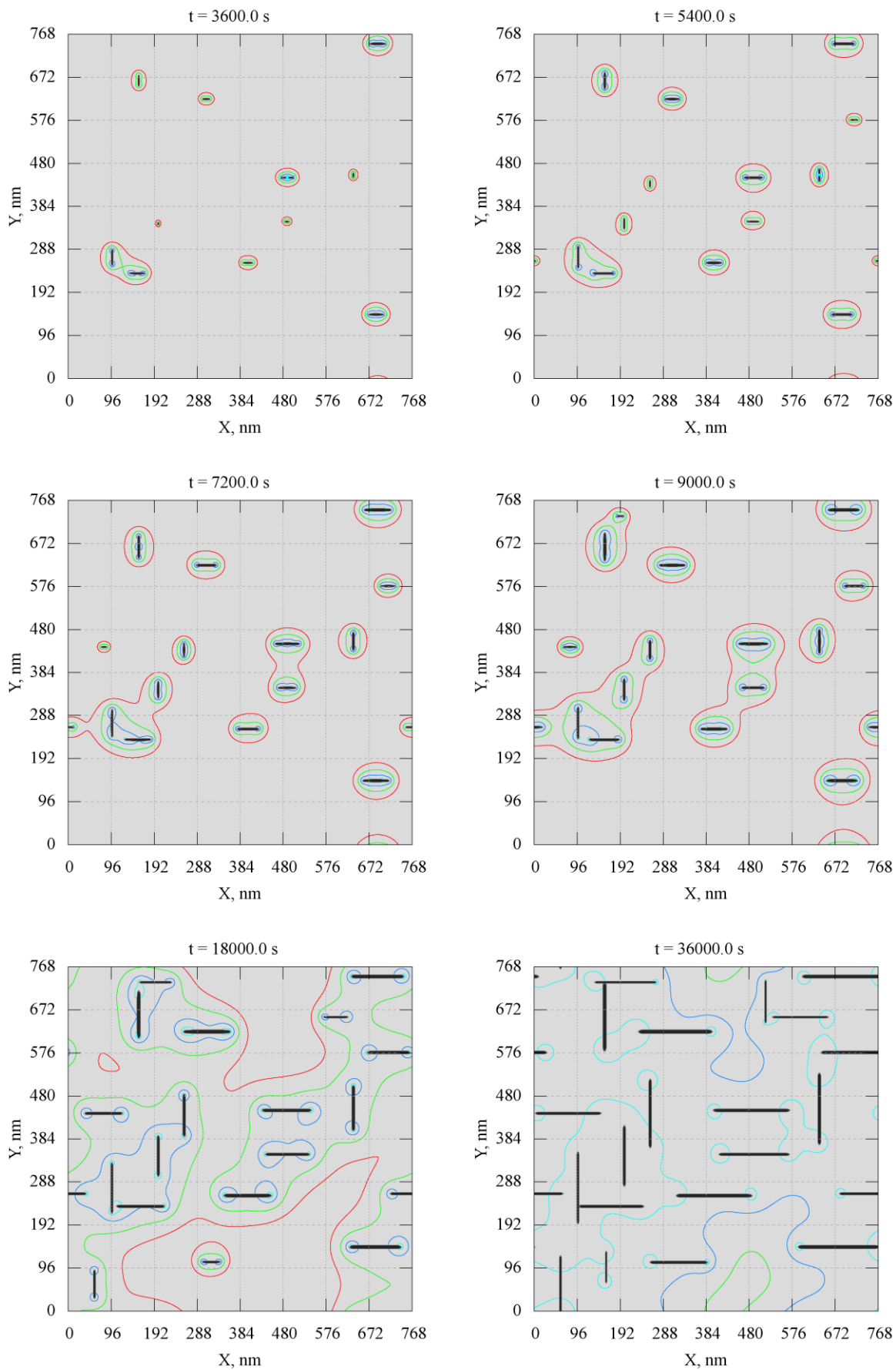


Fig. 84 Evolution of the system with nucleation barrier of  $30 k_B T$  and  $N_{nuc} = 1$ .

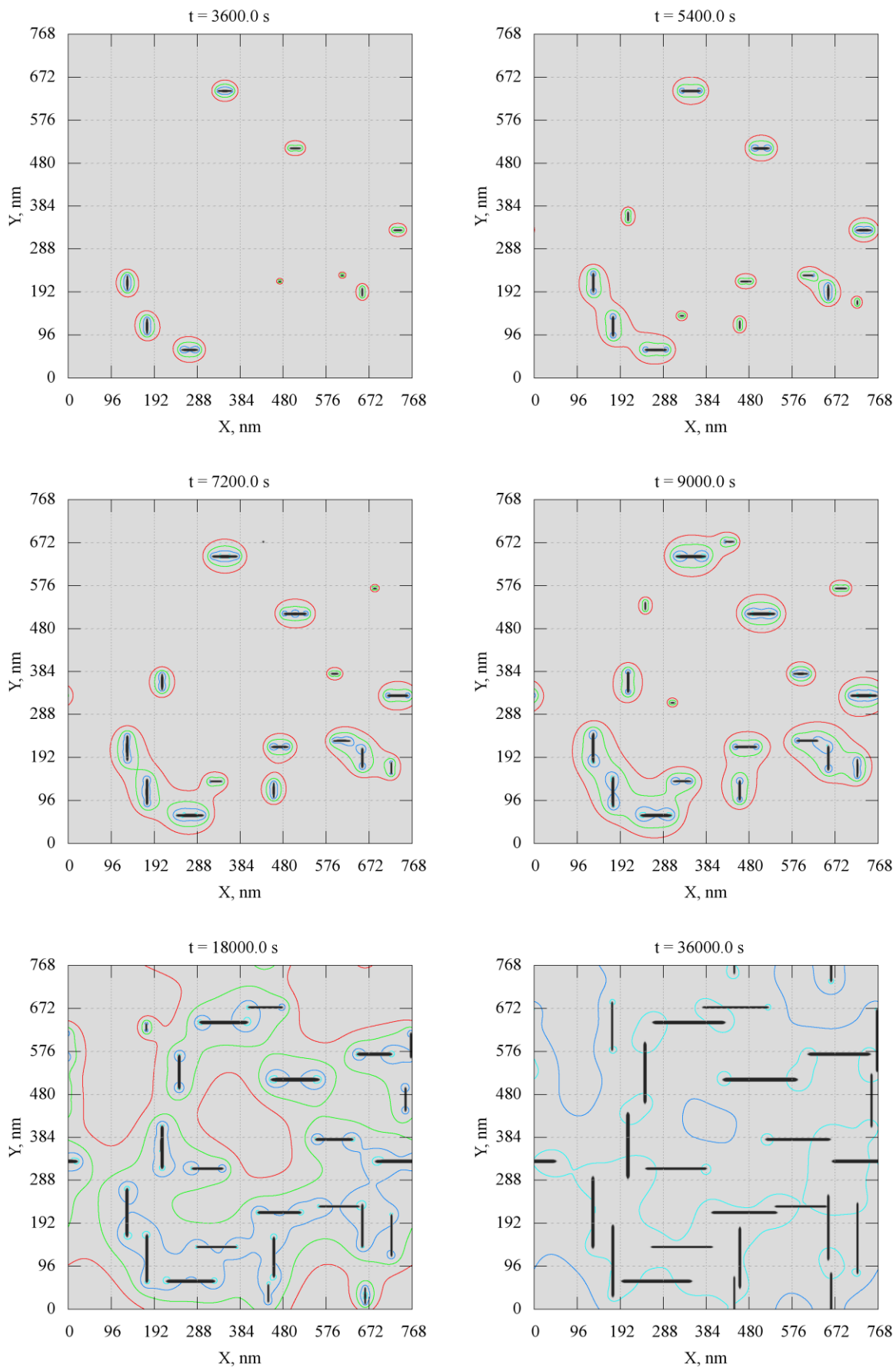


Fig. 85 Evolution of the system with nucleation barrier of  $40 k_B T$  and  $N_{nuc} = 1$ .

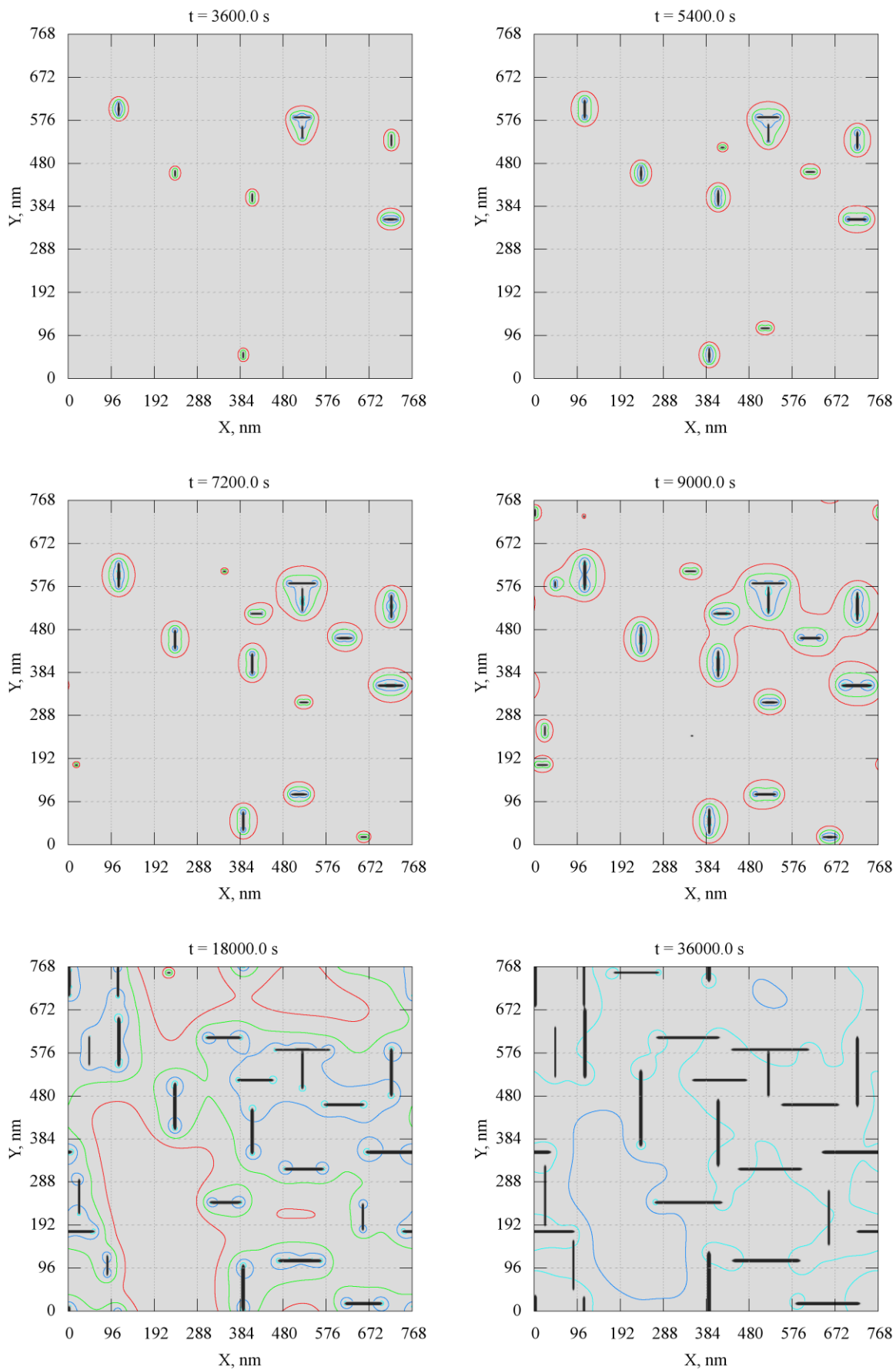


Fig. 86 Evolution of the system with nucleation barrier of  $50 k_B T$  and  $N_{nuc} = 1$ .

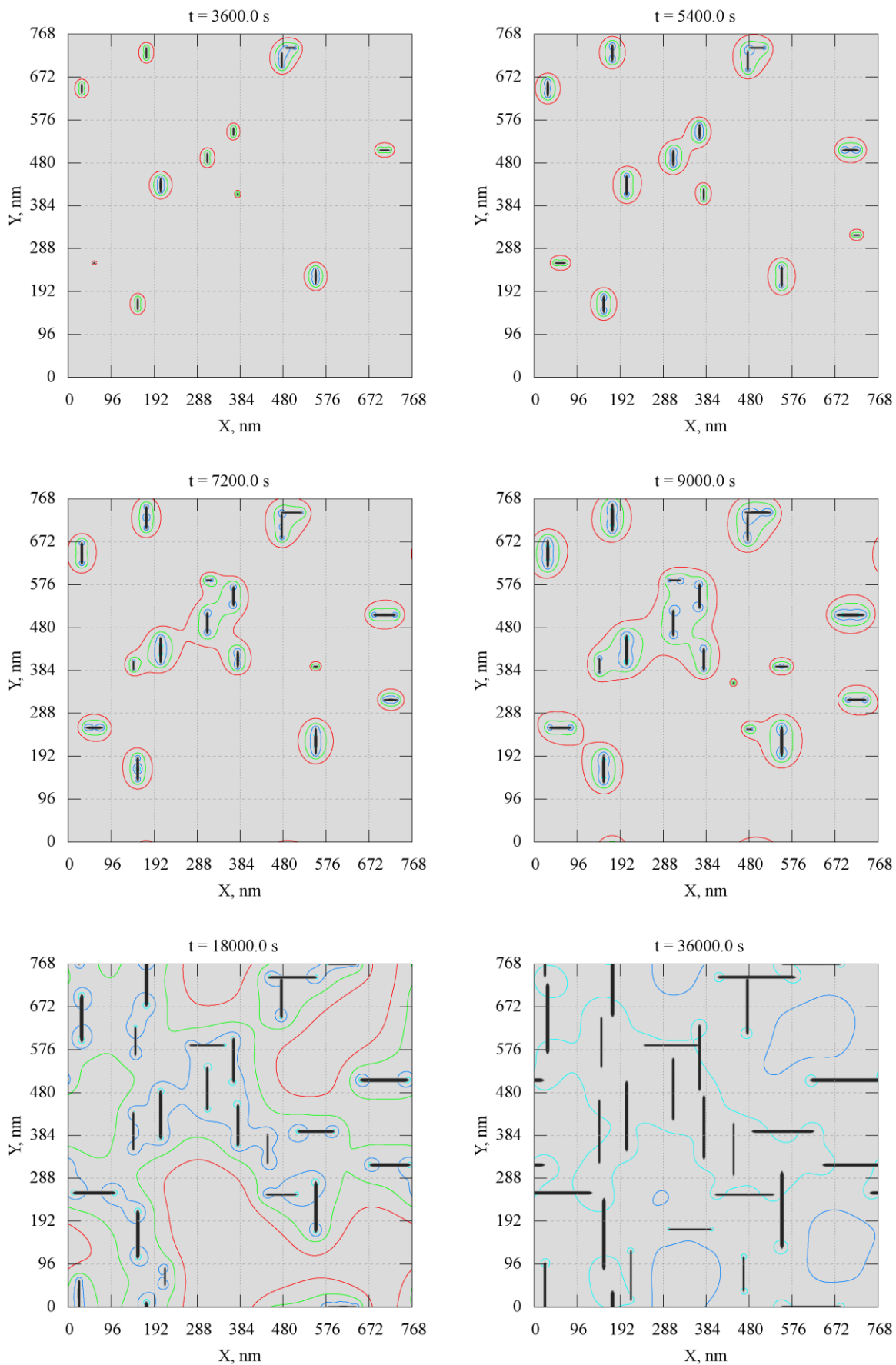


Fig. 87 Evolution of the system with nucleation barrier of  $60 k_B T$  and  $N_{nuc} = 1$ .

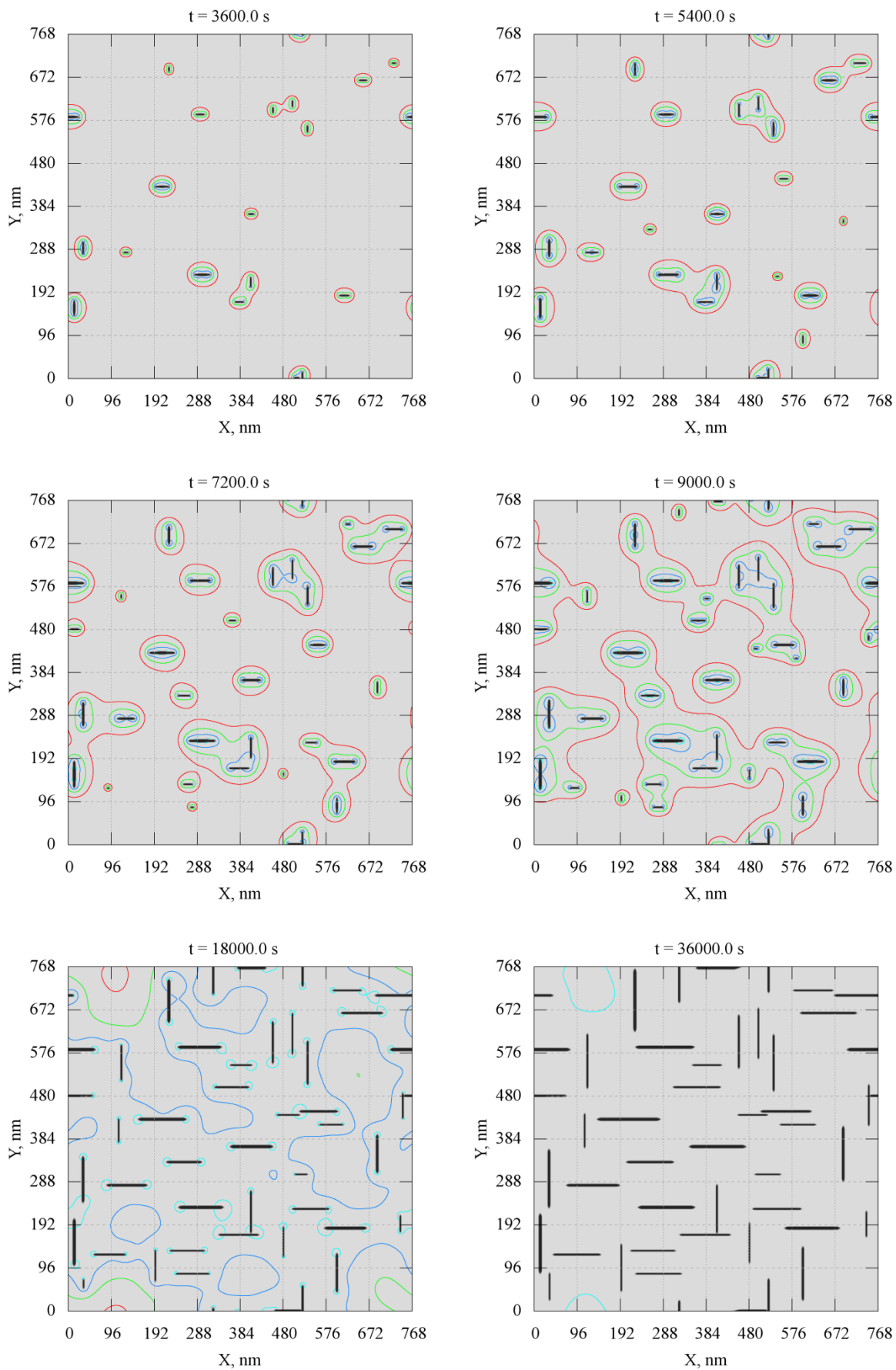


Fig. 88 Evolution of the system with nucleation barrier of  $30 k_B T$  and  $N_{nuc} = 2$ .

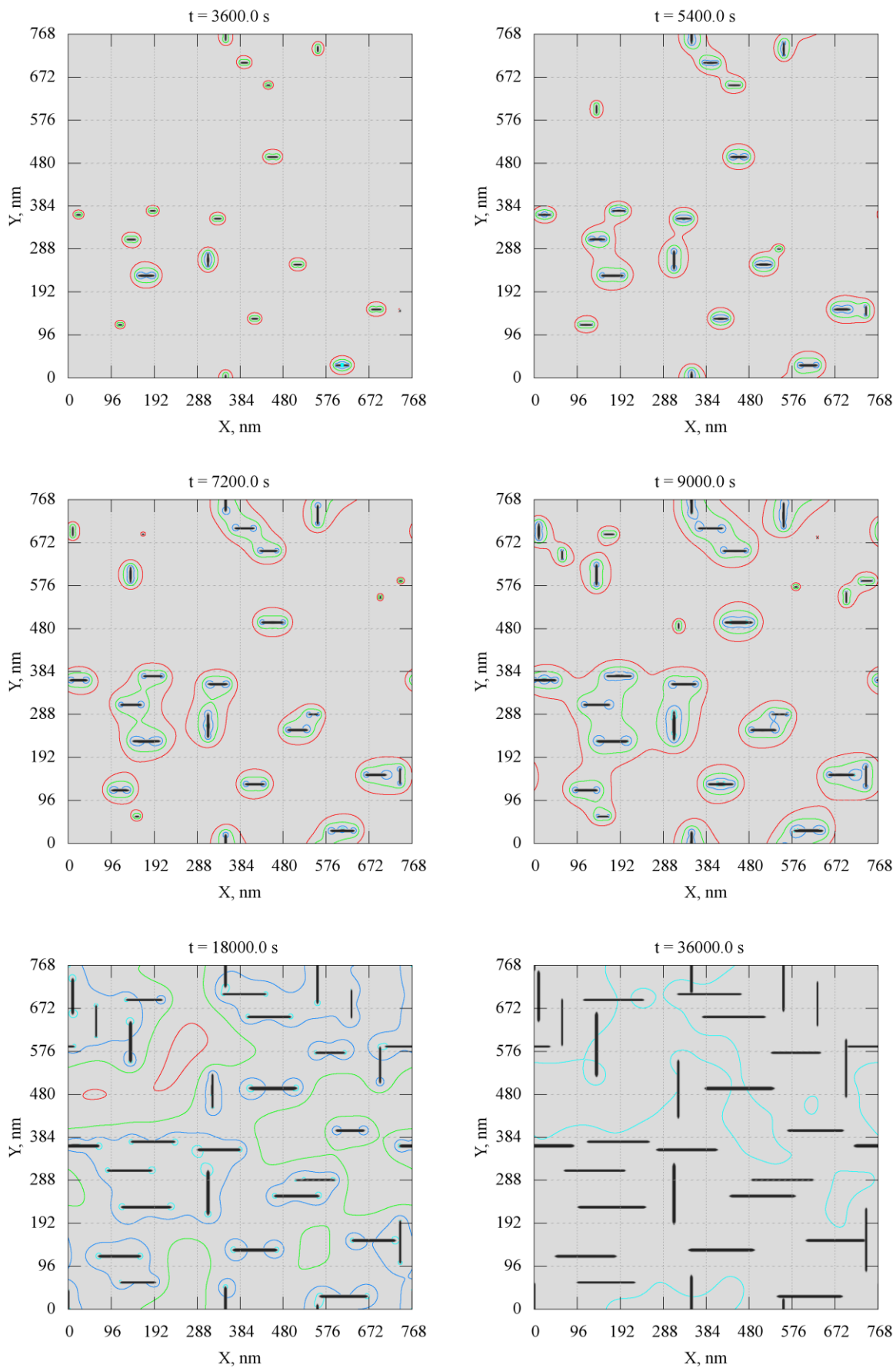


Fig. 89 Evolution of the system with nucleation barrier of  $40 k_B T$  and  $N_{nuc} = 2$ .

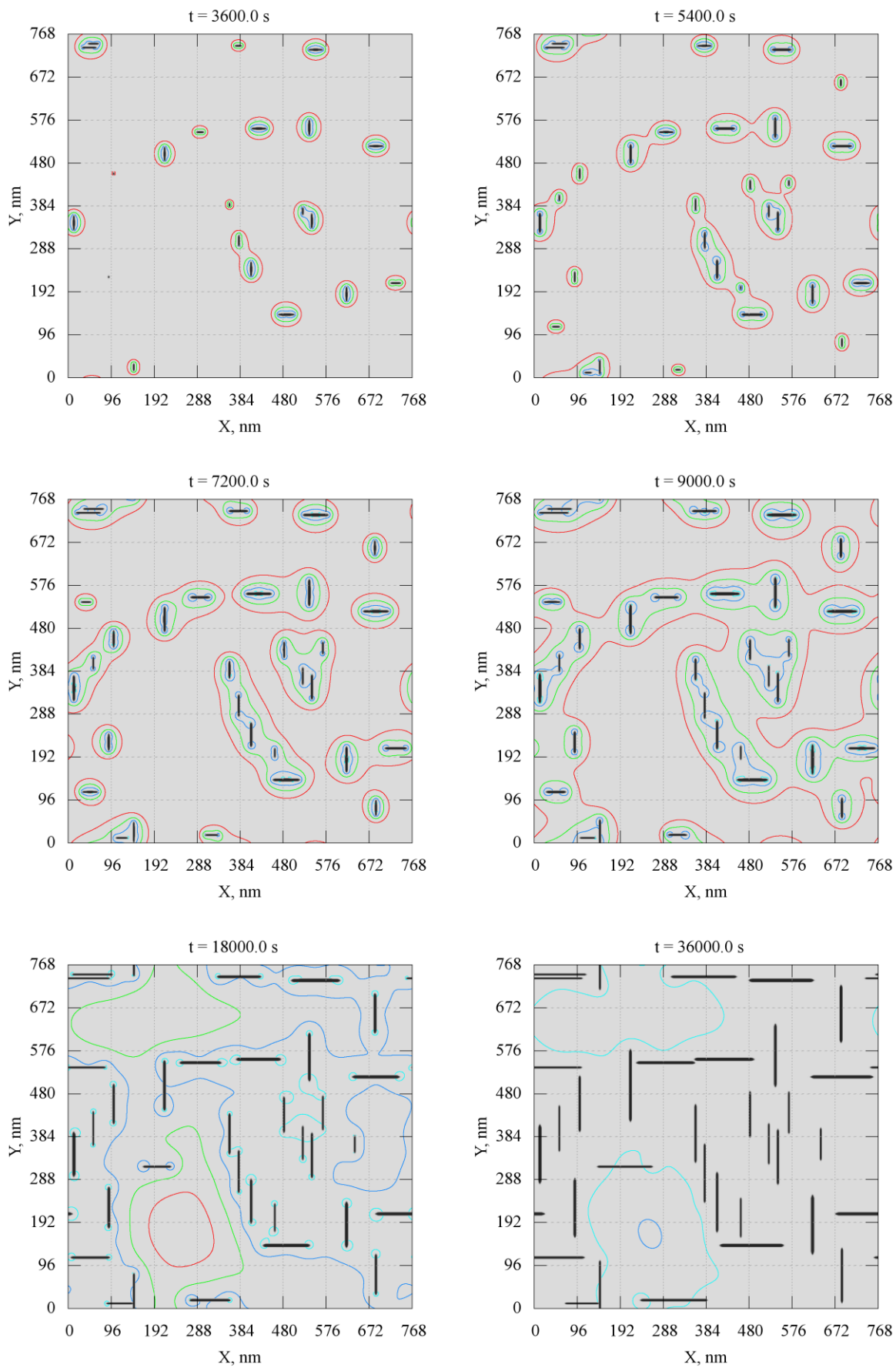


Fig. 90 Evolution of the system with nucleation barrier of  $50 k_B T$  and  $N_{nuc} = 2$ .

### 6.3.2. Effect of the type of the transformation strain. Tetragonal nucleus

The process of strain assisted nucleation was also simulated under the assumption that the transformation mechanism conforms to the traditional model, i.e. the stress free transformation strain contains only a tetragonal misfit component normal to the habit plane of  $\theta'$ .

It was demonstrated in the section 6.1 “Formation of a nucleus with tetragonal transformation strain” that the strength of the elastic interaction is relatively low. Therefore, in order to see if the interaction is sufficient to stimulate secondary nucleation, the combination of parameters that led to the most inhomogeneous distributions of sheared nuclei was used – the barrier of  $50 k_B T$  and rate parameter  $N_{nuc}=2$ . Two simulation runs are presented in Fig. 91 and Fig. 92.

In spite of the expected weakness of strain influence some autocatalytic effect is manifested. Three groups of precipitates may be observed in Fig. 91 starting as early as initial 3600 s snapshot. All of these groups start from two plates close to each other in the parallel orientation. Later in the transformation additional precipitates are formed in close proximity to the clusters. In another simulation illustrated in Fig. 92 there is an edge-face pair in the middle of the simulation domain evident from 3600 s onwards. There also couple of well spaced vertical plates in the middle vertical section of the system, which later stimulate the formation of secondary satellite nuclei.

There is one noticeable difference in clustering behaviour between the cases of generalised and tetragonal types of transformation strain. In the former the clustering on average leads to the arrangement of plates into diagonal or at least somewhat inclined agglomerations. In the latter groups of precipitates are more aligned along principle horizontal and vertical directions. This behaviour is generally consistent with the distribution of the elastic interaction energy described previously, which favours the coplanar formation of tetragonal nuclei and diagonal formation of sheared nuclei.

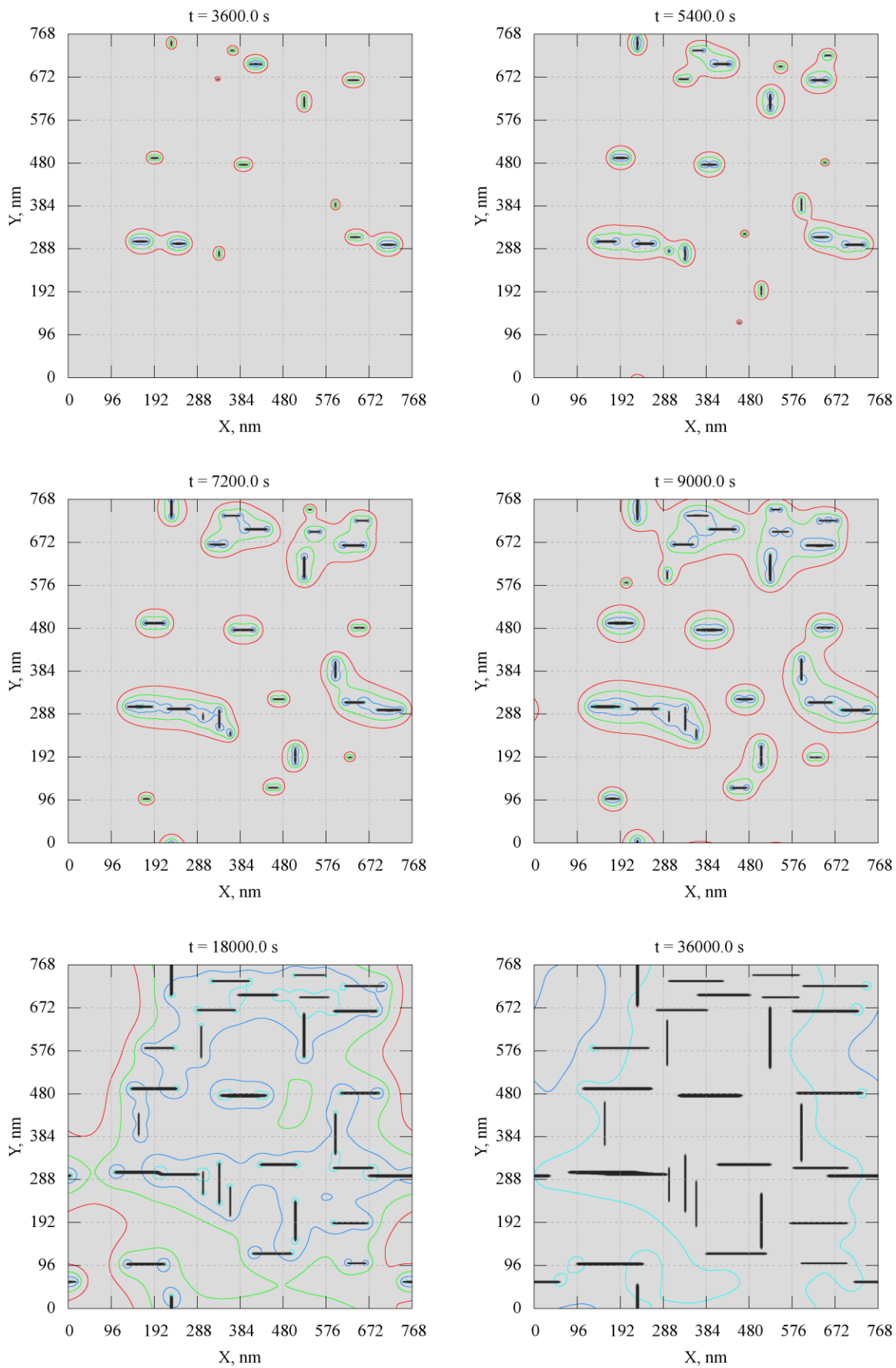


Fig. 91 Evolution of the system with nucleation barrier of  $50 k_B T$  and  $N_{nuc} = 2$ . Tetragonal nucleus.

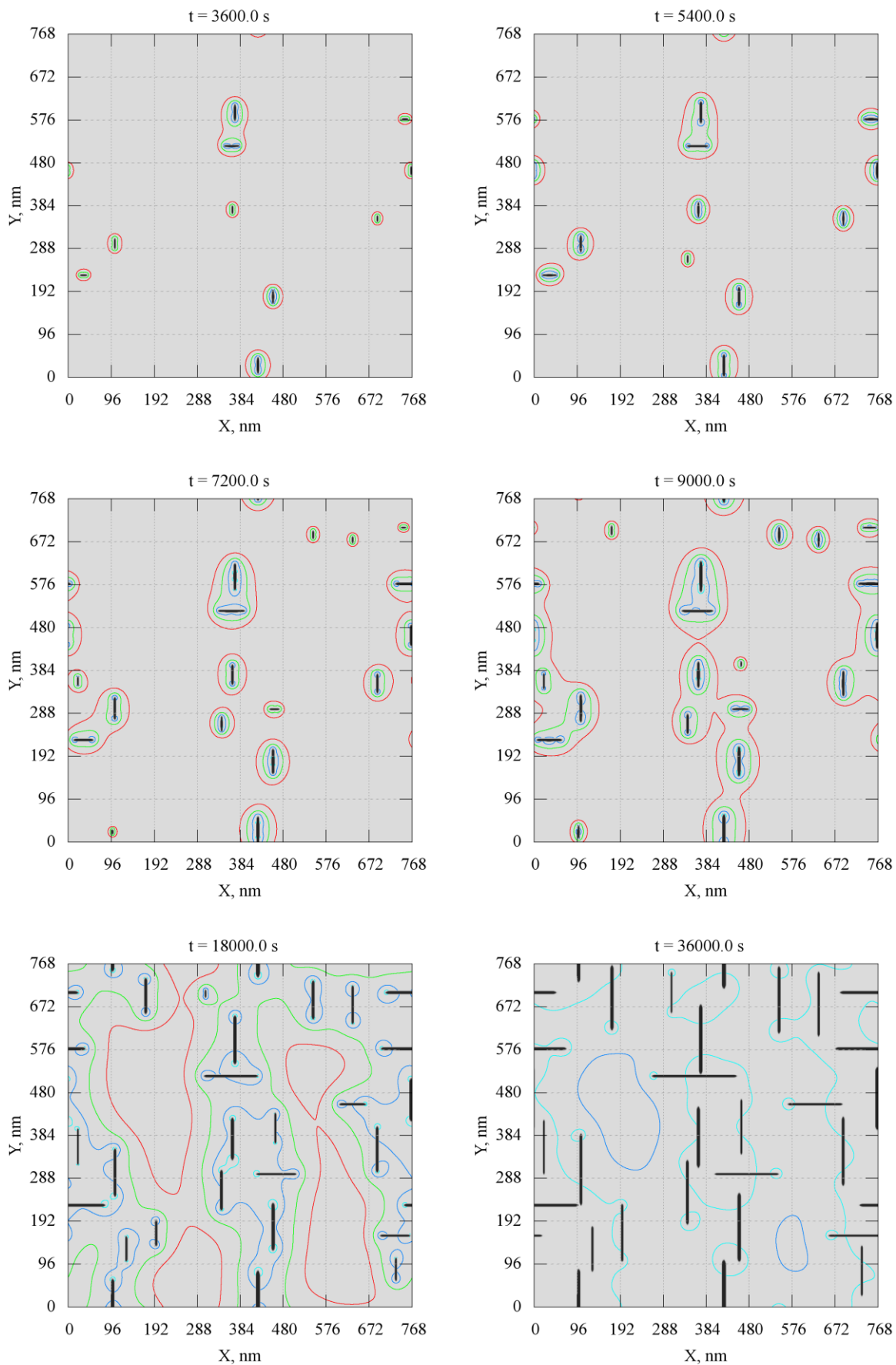


Fig. 92 Evolution of the system with nucleation barrier of  $50 k_B T$  and  $N_{nuc} = 2$ . Tetragonal nucleus.

### 6.3.3. Evolution at larger scale at low nucleation rates

Simulations of the microstructure evolution were also performed for a larger system and lower overall nucleation rates in an attempt to avoid the high density of precipitation that could mask the induced events. The system size is 1.536 by 1.536 microns and transformations in both 2 and 4 wt. % Cu alloys were modelled. The exponential barrier term is taken as  $50 k_B T$  and the scaling factor for overall nucleation is  $N_{nuc} = 0.2$ .

Results are presented in Fig. 93 - Fig. 96. A comparison between the generalised strain type simulations shown in Fig. 93 (4 wt. % Cu) and Fig. 95 (2 wt. % Cu) with the cases of tetragonal transformation strain in Fig. 94 (4 wt. % Cu) and Fig. 96 (2 wt. % Cu) shows that: both number density and clustering tendency is higher in the 4 wt. % Cu system; clustering is more evident in the case of generalised transformation strain. The latter could be attributed to the morphology of precipitates that develop in transformation, with thinner  $\theta'$  plates in the case of lower Cu content resulting in weaker stress produced in the matrix and therefore weaker interactions.

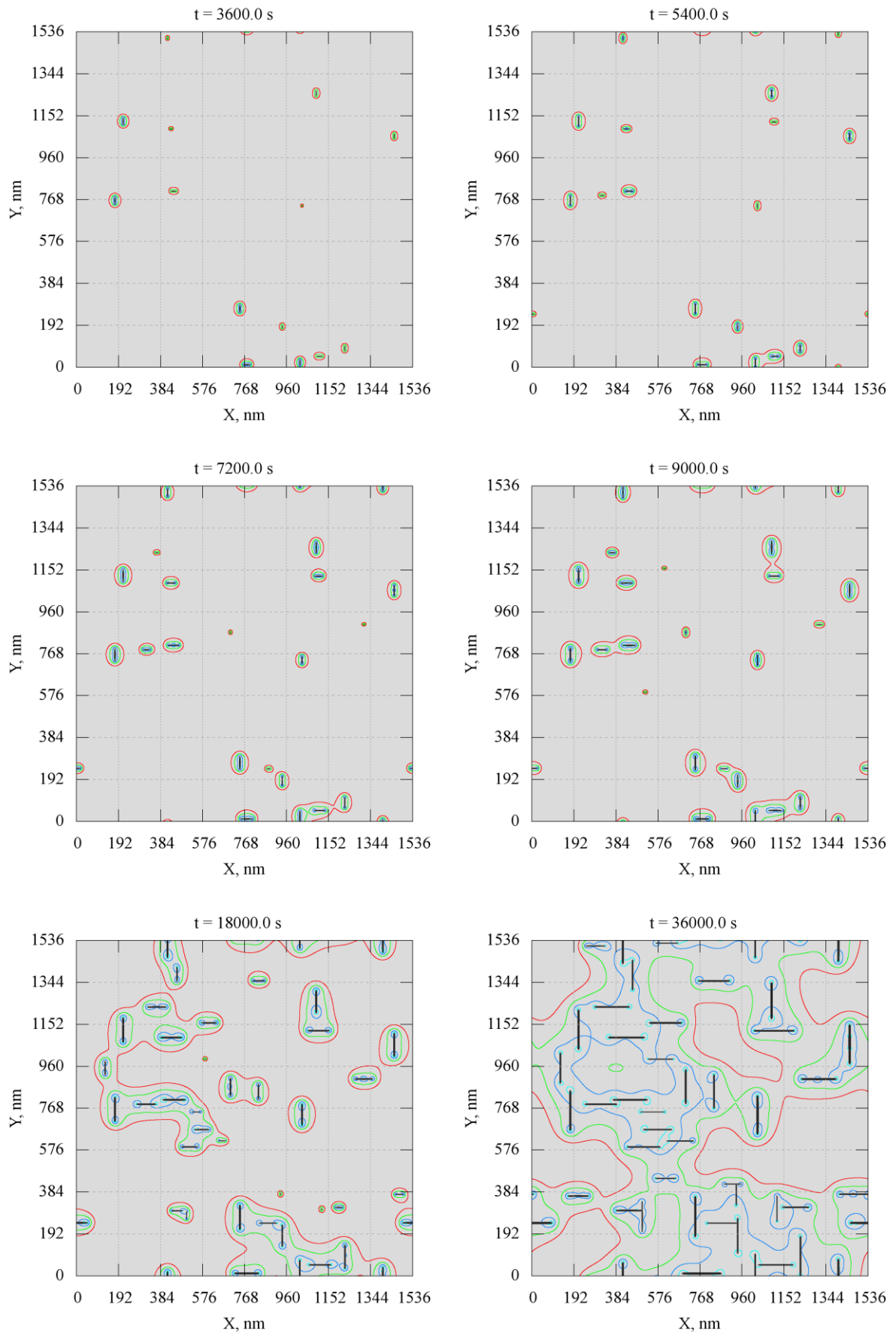


Fig. 93 Evolution of the Al-4 wt. % Cu system with nucleation barrier of  $50 k_B T$  and  $N_{nuc} = 0.2$ . Mixed type nucleus.

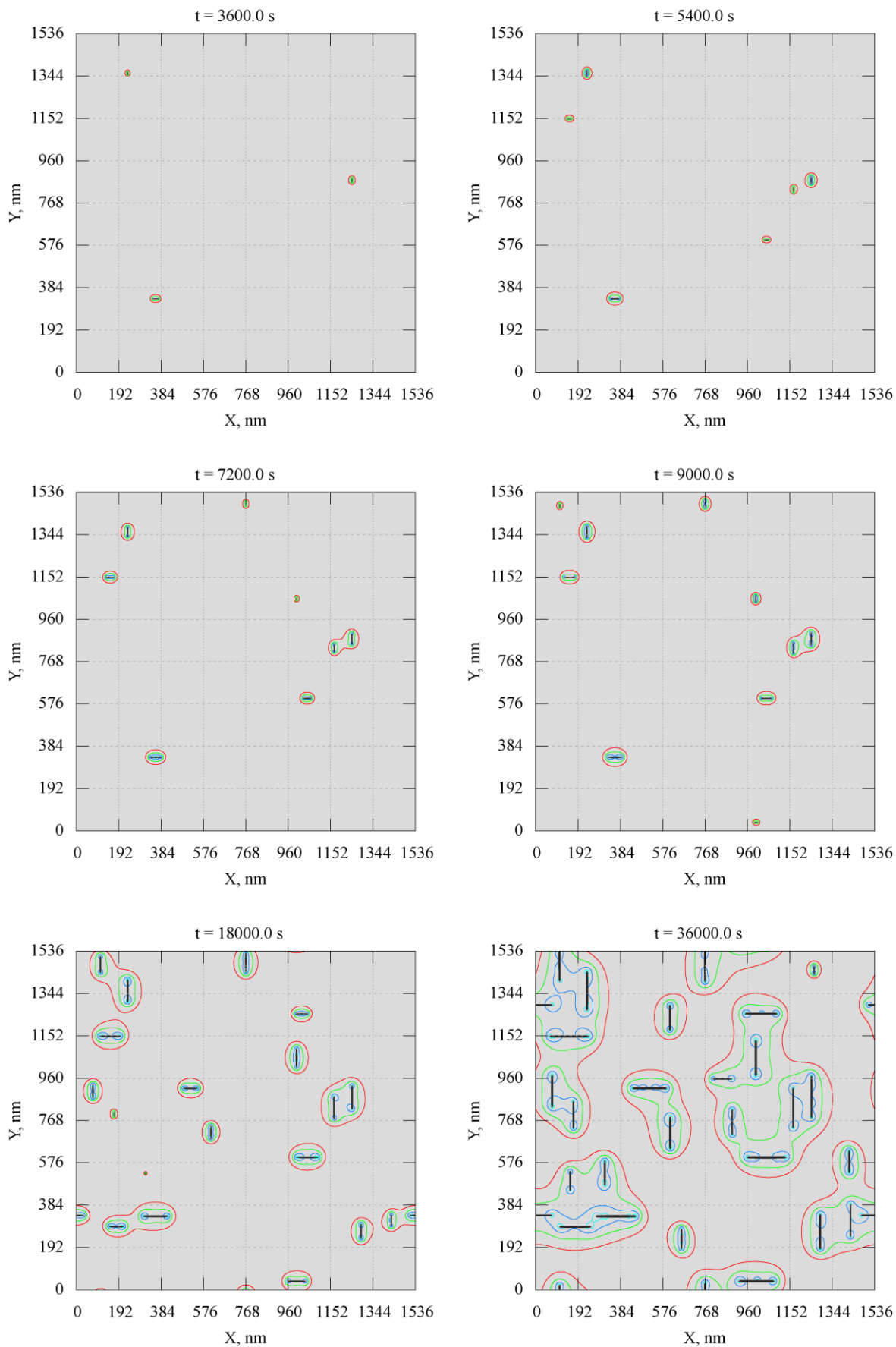


Fig. 94 Evolution of the Al-4 wt. % Cu system with nucleation barrier of  $50 k_B T$  and  $N_{nuc} = 0.2$ . Tetragonal nucleus.

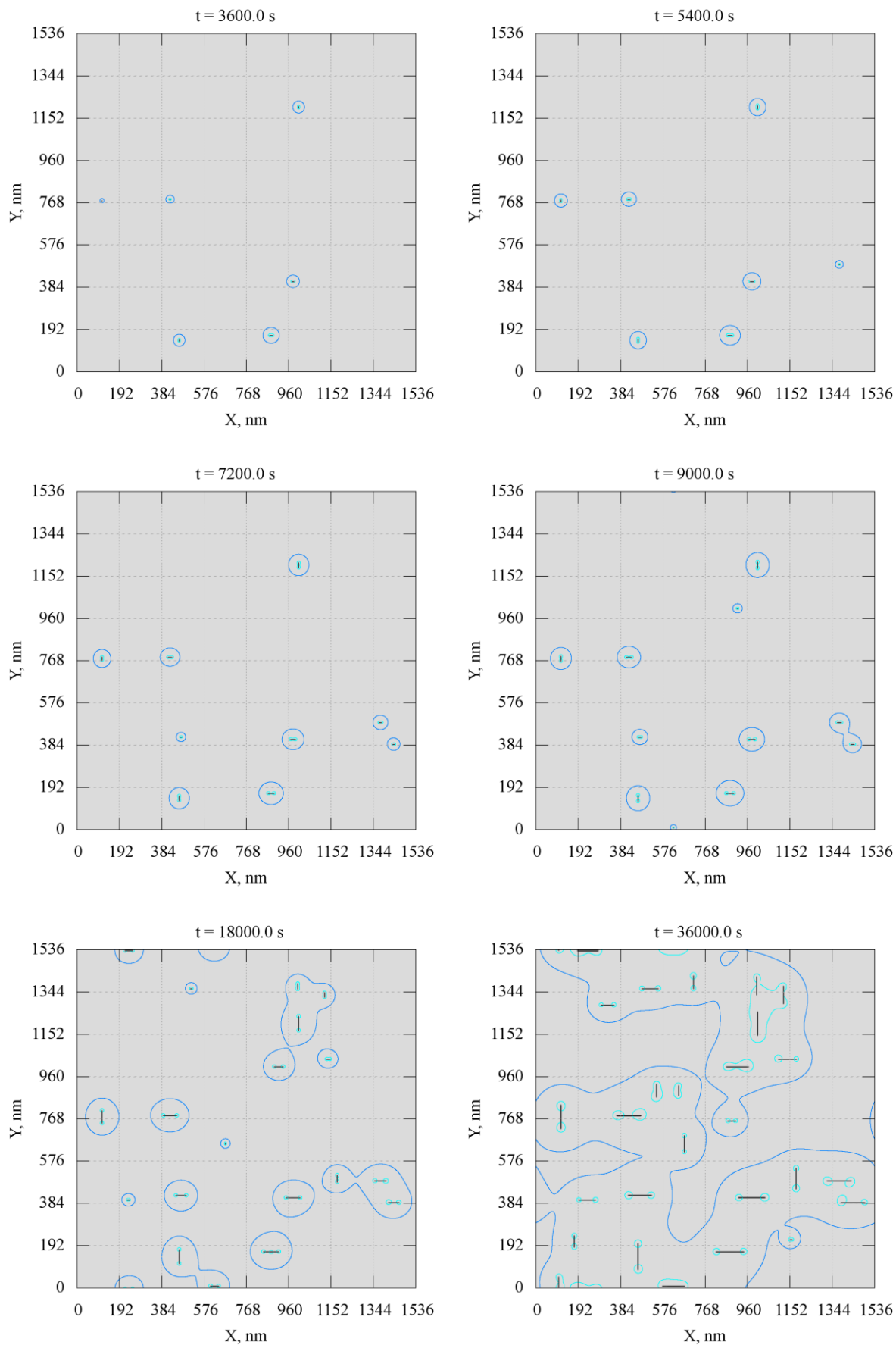


Fig. 95 Evolution of the Al-2 wt. % Cu system with nucleation barrier of  $50 k_B T$  and  $N_{nuc} = 0.2$ . Mixed type nucleus.

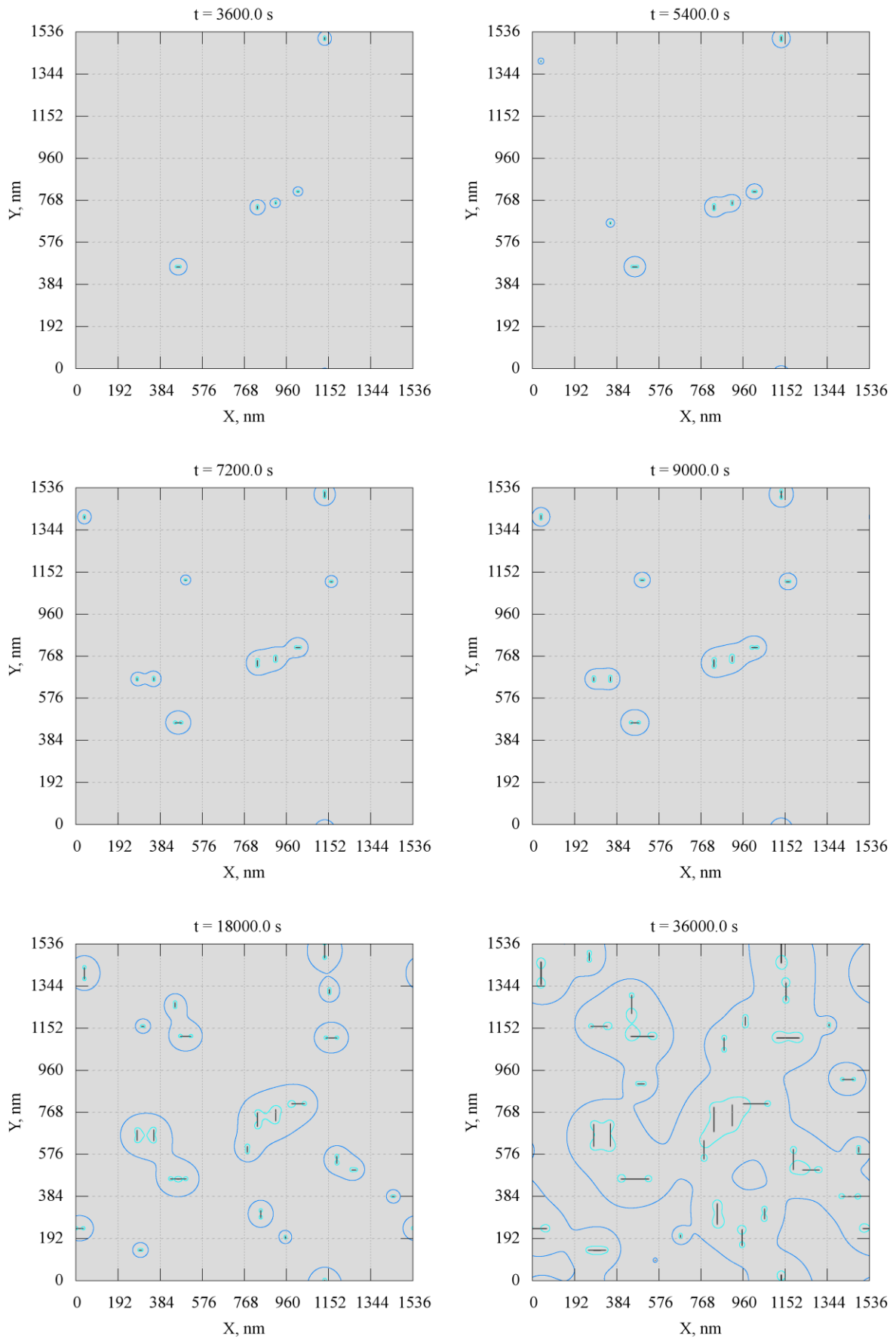


Fig. 96 Evolution of the Al-2 wt. % Cu system with nucleation barrier of  $50 k_B T$  and  $N_{nuc} = 0.2$ . Tetragonal nucleus.

#### 6.3.4. Discussion of results

The combination of the phase field microstructure evolution model and stochastic model of nucleation by the explicit nucleation algorithm proved to be a method capable of adequate description of coherent precipitation and strain induced nucleation. The results obtained allow several important conclusions to be drawn.

Firstly, it is obvious that details of the transformation mechanism, specifically the type of the transformation strain between the matrix and product phases, affect the distribution of coherent precipitates. Modelling successfully demonstrates that clustering behaviour is evident and the spatial distribution of precipitates in clusters is sensitive to the type of strain assumed for the nucleus.

Secondly, the strain induced formation of secondary precipitates is found to be dependent not only on the balance of chemical and elastic contributions to the nucleation driving force, but also on the level of nucleation rate. Modelling shows that even under assumption of strong elastic interaction of microstructure with sheared nuclei the clustering of precipitates may be insignificant. This occurs if the nucleation itself is rare and plates have sufficient time to develop depletion fields suppressing secondary nucleation. In the same way, provided that the nucleation rate is high, clustering may occur even for the case of the tetragonal nucleus with low elastic interaction energy.

Finally, the range of the nucleation barriers and overall rates considered here generally fails to reproduce the structures observed in experiments. For example arrays of Type IV (the clusters of parallel plates offset with respect to each other and forming inclined linear stacks of plates) appear just once in the simulations performed (see Fig. 90), and only under assumption of shear in the transformation strain of the nucleus. Cross-like arrays reported by Perovic et al. [92] were not reproduced at all. This leads to the conclusion that the structures previously assumed to appear autocatalytically may be associated with other type of defects, rather than explained by sequential strain induced nucleation.



## 7. Conclusions and directions for future research

Details of the transformation mechanism from the matrix to the product phase are of great technological importance in the design of precipitation hardenable alloys. An understanding of the nature and magnitude of the activation barrier components is crucial both for the explanation of transformation kinetics and technological control of the process. The study presented in this thesis attempts to look at the  $\theta'$  nucleation in Al-Cu system in light of suggestions of its diffusive-displacive nature, characterised both by the significant composition change and the existence of a lattice correspondence between matrix and product. As a test case for the influence of the shear component of the transformation strain an autocatalytic mode of transformation was studied.

Preliminary assessments of the magnitude of the nucleation barrier for the formation of platelike precipitates were performed. The range of estimates for the variables that control the nucleation rate, namely the interfacial energy and the chemical driving force, was covered parametrically. It was demonstrated that the uncertainty range existing in the estimates of these parameters does not explain the apparent difficulty of the transformation. Within the existing estimates of the interfacial energy and chemical driving forces barriers lower than  $60 k_B T$  were obtained. This makes relatively easy homogeneous nucleation of  $\theta'$  possible, provided that a shear is not present in the transformation strain. For the generalised transformation strain it was shown that the barrier increases dramatically and the strain energy due to the shear component becomes a major part of an activation barrier.

Autocatalysis in the Al-Cu system has been previously suggested to explain the inhomogeneous distributions of  $\theta'$  that sometimes appear in TEM micrographs. In this mode arrays of precipitates are formed, which are characterised by regular arrangement of plates without any obvious association with any type of defect. Early models of the phenomenon attempted to explain the array formation by the elastic interaction between precipitates. In this work these models were extended to the case of the generalised transformation strain, which includes both a tetragonal distortion normal to the habit plane and a shear component that lies in the plane of the plate. Three dimensional distributions of the elastic interaction energy demonstrated that the interaction between the tetragonally strained primary particle and the sheared nucleus has the symmetry consistent with the geometry of precipitate arrays observed in experiments. Since the potential location of the nucleus is sensitive to the chemical driving force,

the need for a model that simultaneously monitors the chemical composition and mechanical state of the matrix was identified.

To test the hypothesis that arrays are formed in a sequential manner due to the interaction between the existing precipitates and subsequent nuclei a dynamic model of the microstructure evolution and nucleation was employed. The model is based on a diffuse interface phase field approach and Explicit Nucleation Algorithm. Since the phenomenon is a result of a subtle balance between the chemical and mechanical energy contributions special care was taken to develop a model with the ability to reproduce precipitate morphologies and solute concentration fields in the matrix around it. The model includes high interfacial anisotropy with the ability to produce flat interfaces and sharp corners, and also a kinetic anisotropy to account for the different growth conditions of the coherent habit planes and semicoherent edges. A modification of the interfacial energy regularisation was developed in order to improve the stability of the numerical scheme. Full advantage of the Kim-Kim-Suzuki (KKS) approach was taken to simplify the Cahn-Hilliard equation. Also, stability analysis of the transitional behaviour of the KKS model allowed the establishing of practical limits of the double-well potential magnitude for the control of the simulation interface width. A special alternating direction implicit solver was implemented to allow for an efficient and discontinuity-tolerant scheme for solving the evolution equations. The modelling, however, showed that the field of the nucleation driving force is relatively insensitive to the fine structure of the precipitate morphology, and that a simple and computationally efficient model may be used as an adequate approximation for precipitate evolution.

Finally, a semi-quantitative explicit nucleation algorithm has been employed to simulate the assisted nucleation in the environment of the pre-existing precipitates. The modelling demonstrated that the elastic interaction of the nucleus with the tetragonal transformation strain and pre-existing microstructure is weak. The decrease in chemical driving force caused by the depletion of solute is sufficient to suppress any benefit created by the favourable elastic interaction. Therefore, precipitate clustering cannot be explained in terms of elastic interaction if the traditional model of transformation mechanism is assumed. Unfortunately the case of a generalised transformation strain with the shear component failed to produce conclusive results. Some clustering of precipitates was observed, but well-defined array structures were not.

The application of phase field modelling for the investigation of the atomic mechanism of precipitate formation has significant potential for development. The major directions can be broadly separated into two strategic areas: the extension of the experimental data available on the

thermodynamics and transformation kinetics of the systems of interest; the application of the phase field modelling for the investigation of precipitate-defect associations.

The first direction would require extensive experimental efforts in order to expand the base of the reliable quantitative information available on the systems of interest. This information includes the fundamental thermodynamical characteristics of the phases involved in the transformation, i.e. the interfacial energies of precipitating phases and the chemical driving forces for their formation. Also, more systematic data on precipitate sizes, morphologies and number densities are of crucial interest. Finally, the influence of quenched-in vacancies on diffusion rates, driving forces and stress relief requires more quantitative information. Data obtained for the range of homogenisation and ageing conditions would help to calibrate phase field models and make them truly quantitative and predictive.

The second direction would involve application of more complex phase field models, which incorporate a variety of defect types. This will allow studying the interaction of nuclei with dislocations and grain boundaries. Lastly, the influence of non-equilibrium vacancy population on microstructure evolution could be incorporated into the phase field formulation. The dependence on the decaying concentration of vacancies may be included into the free-energy functional and the mobility coefficients in order to study the effects of homogenisation temperature and quench regime.

Also, the model presented in the thesis could be potentially extended into three dimensions. It was demonstrated (see Fig. 24 - Fig. 26, section 4.5) that the elastic interaction between inclusions is strongest when the centres of the interacting plates belong to the same  $\{100\}_\alpha$  plane. However, some configurations also have relatively strong interactions in other mutual orientations (with a nucleus of a certain type at the corner of a larger plate for instance). Such configurations can only be studied in three dimensions. Unfortunately, the limitations imposed by computational power and the need to keep interfaces properly resolved restrict the simulation domain to the immediate environment of a single plate and preclude the study of complex spatial arrangements of any significant number of plates. Work in this direction would require development of sophisticated adaptive grid methods, with meshes that adapt according to the gradients in field variables and nucleation driving forces.

Provided that additional experimental data become available and is complemented by advances in computing power and adaptive grid algorithms, the phase field formalism promises to develop into an important technological tool in alloy design.



## References

1. M. Volmer and A. Weber, *Nuclei Formation in Supersaturated States*, Zeitschrift für Physikalische Chemie **119**, pp. 277-301, 1926.
2. M. von Smoluchowski, *Molekular-kinetische Theorie der Opaleszenz von Gasen im kritischen Zustande, sowie einiger verwandter Erscheinungen*, Annalen der Physik **330**(2), pp. 205-226, 1908.
3. A. Einstein, *Theory of the Opalescence of Homogeneous Liquids and Liquid Mixtures in the Neighbourhood of the Critical State*, Annalen der Physik **33**(6), pp. 1275-1298, 1910.
4. L. Farkas, *Rate of Nuclei Formation in Supersaturated Vapours*, Zeitschrift für Physikalische Chemie **125**, pp. 236-242, 1927.
5. R. Kaischew and I.N. Stranski, *Kinetic Derivation of the Nucleation Rate*, Zeitschrift für Physikalische Chemie B **26**, pp. 317-326, 1934.
6. R. Becker and W. Döring, *Kinetic Treatment of Nucleation in Supersaturated Vapours*, Annalen der Physik **24**(8), pp. 719-752, 1935.
7. J.B. Zeldovich, *On the Theory of a New Phase Formation. Cavitation.*, Journal of Experimental and Theoretical Physics (Russian) **12**, p. 525, 1942.
8. J. Frenkel, *A General Theory of Heterophase Fluctuations and Pretransition Phenomena*, Journal of Chemical Physics **7**, pp. 538-547, 1939.
9. R. Becker, *Die Keimbildung bei der Ausscheidung in metallischen Mischkristallen*, Annalen der Physik **32**(1-2), pp. 128-140, 1938.
10. R. Becker, *On the Formation of Nuclei during Precipitation*, Proceedings of the Physical Society **52**, pp. 71-76, 1940.
11. D. Turnbull and J.C. Fisher, *Rate of Nucleation in Condensed Systems*, Journal of Chemical Physics **17**, pp. 71-73, 1949.
12. K.C. Russell, *Nucleation in Solids: the Induction and Steady State Effects*, Advances in Colloid and Interface Science **13**, pp. 205-318, 1980.

13. J.W. Christian, "The Theory of Transformations in Metals and Alloys", 3rd ed., 2002: Elsevier.
14. D. Turnbull, *Transient Nucleation*, Metals Technology (American Institute of Mining and Metallurgical Engineers - Technical Publications), Technical Publication 2365, 1948.
15. J.C. Fisher, J.H. Hollomon and D. Turnbull, *Nucleation of Phase Transformations*, Metals Technology (American Institute of Mining and Metallurgical Engineers - Technical Publications), Technical Note 5, 1948.
16. J.H. Hollomon and D. Turnbull, *Nucleation*, Progress in Metal Physics **4**, pp. 333-388, 1953.
17. J.W. Cahn, *Nucleation on Dislocations*, Acta Metallurgica **5**(3), pp. 169-172, 1957.
18. K.C. Russell, *The Role of Excess Vacancies in Precipitation*, Scripta Metallurgica **3**(5), pp. 313-316, 1969.
19. R. Gomez-Ramirez and G.M. Pound, *Nucleation of a Second Solid Phase along Dislocations*, Metallurgical Transactions A **4**(6), pp. 1563-1570, 1973.
20. B.Y. Lyubov and V.A. Solov'ev, *The Possibility of Existence of Stable Segregations of Solute Atoms and Nucleation of Coherent Centres of a New Phase in the Elastic Stress Fields of Edge Dislocations*, Fizika Metallov i Metallovedenie **19**(3), pp. 333-342, 1965.
21. C.C. Dollins, *Nucleation on Dislocations*, Acta Metallurgica **18**(11), pp. 1209-1215, 1970.
22. D.M. Barnett, *On Nucleation of Coherent Precipitates near Edge Dislocations*, Scripta Metallurgica **5**(4), pp. 261-266, 1971.
23. F. Larche, *Nucleation and Precipitation on Dislocations*, pp. 135-153 in "Dislocations in Solids", Ed. F.R.N. Nabarro, 1979
24. J.W. Cahn, *Kinetics of Grain Boundary Nucleated Reactions*, Acta Metallurgica **4**(5), pp. 449-459, 1956.
25. J.W. Cahn and J.E. Hilliard, *Free Energy of a Nonuniform System. I. Interfacial Free Energy*, Journal of Chemical Physics **28**(2), pp. 258-267, 1958.

26. J.W. Cahn, *Free Energy of a Nonuniform System. II. Thermodynamic Basis*, Journal of Chemical Physics **30**(5), pp. 1121-1124, 1959.
27. J.W. Cahn and J.E. Hilliard, *Free Energy of a Nonuniform System. III. Nucleation in a Two-Component Incompressible Fluid*, Journal of Chemical Physics **31**(3), pp. 688-699, 1959.
28. K.C. Russell, *Linked Flux Analysis of Nucleation in Condensed Phases*, Acta Metallurgica **16**(5), pp. 761-769, 1968.
29. M. Volmer and H. Flood, *Drop Formation in Vapours*, Zeitschrift für Physikalische Chemie **170**(3-4), pp. 273-285, 1934.
30. H. Flood, *Drop Formation in Supersaturated Ethyl-Alcohol-Water Vapour Mixtures*, Zeitschrift für Physikalische Chemie **170**(3-4), pp. 286-294, 1934.
31. I.S. Servi and D. Turnbull, *Thermodynamics and Kinetics of Precipitation in the Copper-Cobalt System*, Acta Metallurgica **14**(2), pp. 161-170, 1966.
32. G. Wulff, *On the Question of Speed of Growth and Dissolution of Crystal Surfaces*, Zeitschrift für Kristallographie und Mineralogie **34**(5/6), pp. 449-530, 1901.
33. D.A. Porter and K.E. Easterling, "Phase Transformations in Metals and Alloys", 2nd ed., 1992: Chapman & Hall.
34. D. Turnbull, *Role of Structural Impurities in Phase Transformations*, Impurities and Imperfections, pp. 121-144, 1955.
35. H.I. Aaronson, J.B. Clark and C. Laird, *Interfacial Energy of Dislocation and of Coherent Interphase Boundaries*, Metal Science Journal **2**, pp. 155-158, 1968.
36. J.H. van der Merwe, *On the Stresses and Energies Associated with Inter-Crystalline Boundaries*, Proceedings of the Physical Society. Section A **63**, pp. 616-637, 1950.
37. E.D. Hondros, *Energetics of Solid-solid Interfaces*, pp. 77-100 in "Interfaces Conference Melbourne 1969: Review Papers and Abstracts of Research Papers" (Melbourne, 1969), Ed. R.C. Gifkins: The Australian Institute of Metals & Butterworth.

38. F.R.N. Nabarro, *The Strains Produced by Precipitation in Alloys*, Proceedings of the Royal Society of London, Series A (Mathematical and Physical Sciences) **175**, pp. 519-538, 1940.
39. E. Kröner, *On the Calculation of the Strain Energy Associated with the Nucleation of a New Phase within a Crystal*, Acta Metallurgica **2**(2), pp. 302-309, 1954.
40. J.D. Eshelby, *The Determination of the Elastic Field of an Ellipsoidal Inclusion, and Related Problems*, Proceedings of the Royal Society of London, Series A (Mathematical and Physical Sciences) **241**(1226), pp. 376-396, 1957.
41. J.D. Eshelby, *The Elastic Field Outside an Ellipsoidal Inclusion*, Proceedings of the Royal Society of London, Series A (Mathematical and Physical Sciences) **252**, pp. 561-569, 1959.
42. J.W. Christian, *Accommodation Strains in Martensite Formation, and the use of a Dilatation Parameter*, Acta Metallurgica **6**(5), pp. 377-379, 1958.
43. J.W. Christian, *Discussion of "Comments on Accommodation Strains in Martensite Formation and the use of a Dilatation Parameter"*, Acta Metallurgica **7**(3), pp. 218-219, 1959.
44. L. Kaufman, *Comments on "Accommodation Strains in Martensite Formation and the use of a Dilatation Parameter"*, Acta Metallurgica **7**(3), pp. 216-218, 1959.
45. D.M. Barnett, J.K. Lee, H.I. Aaronson and K.C. Russell, *The Strain Energy of a Coherent Ellipsoidal Precipitate*, Scripta Metallurgica **8**(12), pp. 1447-1450, 1974.
46. J.K. Lee, H.I. Aaronson and D.M. Barnett, *The Elastic Strain Energy of Coherent Ellipsoidal Precipitates in Anisotropic Crystalline Solids*, Metallurgical Transactions A **8**(6), pp. 963-970, 1977.
47. S.L. Sass, T. Mura and J.B. Cohen, *Diffraction Contrast from Non-spherical Distortions - in particular a Cuboidal Inclusion*, Philosophical Magazine **16**, pp. 679-690, 1967.
48. G. Faivre, *Coherence Deformations of a Quadratic Precipitate*, Physica Status Solidi **35**(1), pp. 249-259, 1969.

49. R. Sankaran and C. Laird, *Deformation Field of a Misfitting Inclusion*, Journal of the Mechanics and Physics of Solids **24**(4), pp. 251-262, 1976.
50. J.K. Lee and W.C. Johnson, *Calculation of the Elastic Strain Field of a Cuboidal Precipitate in an Anisotropic Matrix*, Physica Status Solidi A **46**(1), pp. 267-272, 1978.
51. S. Onaka, T. Fujii and M. Kato, *The Elastic Strain Energy of a Coherent Inclusion with Deviatoric Misfit Strains*, Mechanics of Materials **20**(4), pp. 329-336, 1995.
52. A.G. Khachaturyan, *Some Questions Concerning the Theory of Phase Transformations in Solids*, Fizika Tverdogo Tela **8**(9), pp. 2709-2717, 1966.
53. A.G. Khachaturyan and G.A. Shatalov, *Elastic-interaction Potential of Defects in a Crystal*, Fizika Tverdogo Tela **11**(1), pp. 118-123, 1969.
54. A.G. Khachaturyan, "Theory of Structural Transformations in Solids", 1983: John Wiley & Sons.
55. A.G. Khachaturyan, S. Semenovskaya and T. Tsakalakos, *Elastic Strain Energy of Inhomogeneous Solids*, Physical Review B **52**(22), pp. 15909-15919, 1995.
56. D.Y. Li and L.Q. Chen, *Computer Simulation of Stress-oriented Nucleation and Growth of  $\theta$  Precipitates in Al-Cu Alloys*, Acta Materialia **46**(8), pp. 2573-2585, 1998.
57. D.Y. Li and L.Q. Chen, *Morphological Evolution of Coherent Multi-variant  $Ti_{11}Ni_{14}$  Precipitates in Ti-Ni Alloys under an Applied Stress - a Computer Simulation Study*, Acta Materialia **46**(2), pp. 639-649, 1998.
58. Y.U. Wang, Y.M. Jin and A.G. Khachaturyan, *Phase Field Microelasticity Theory and Modeling of Elastically and Structurally Inhomogeneous Solid*, Journal of Applied Physics **92**(3), pp. 1351-1360, 2002.
59. C. Shen, J.P. Simmons and Y. Wang, *Effect of Elastic Interaction on Nucleation: I. Calculation of the Strain Energy of Nucleus Formation in an Elastically Anisotropic Crystal of Arbitrary Microstructure*, Acta Materialia **54**(20), pp. 5617-5630, 2006.
60. B.C. Muddle, J.F. Nie and G.R. Hugo, *Application of the Theory of Martensite Crystallography to Displacive Phase Transformations in Substitutional Nonferrous Alloys*, Metallurgical and Materials Transactions A **25**(9), pp. 1841-1856, 1994.

61. H.I. Aaronson and M.G. Hall, *A History of the Controversy over the Roles of Shear and Diffusion in Plate Formation above  $M_d$  and a Comparison of the Atomic Mechanisms of These Processes*, Metallurgical and Materials Transactions A **25**(9), pp. 1797-1819, 1994.
62. H.I. Aaronson, J. Hirth, B. Rath and C.M. Wayman, *General Discussion Sessions of the "Pacific Rim Conference on the Roles of Shear and Diffusion in the Formation of Plate-Shaped Transformation Products"*, Metallurgical and Materials Transactions A **25**(12), pp. 2655-2673, 1994.
63. J.W. Christian, *Lattice Correspondence, Atomic Site Correspondence and Shape Change in "Diffusional-Displacive" Phase Transformations*, Progress in Materials Science **42**(1-4), pp. 101-108, 1997.
64. J.F. Nie and B.C. Muddle, *The Lattice Correspondence and Diffusional-Displacive Phase Transformations*, Materials Forum **23**, pp. 23-40, 1999.
65. B.C. Muddle and J.F. Nie, *Characteristics of Diffusional-Displacive Transformation Products*, pp. 1128-1135 in "Proceedings of an International Conference on Solid-Solid Phase Transformations (JIMIC-3)" (Sendai, 1999), Eds. M. Koiwa et al.: Japan Institute of Metals.
66. H.K. Hardy and T.J. Heal, *Report on Precipitation*, Progress in Metal Physics **5**, pp. 143-278, 1954.
67. A. Kelly and R.B. Nicholson, *Precipitation Hardening*, Progress in Materials Science **10**(3), pp. 149-391, 1963.
68. G.W. Lorimer, *Precipitation in Aluminium Alloys*, p. 87 in "Precipitation Processes in Solids" (Niagara Falls, 1978): Metallurgical Society of AIME.
69. G.D. Preston, *The Diffraction of X-Rays by Age-Hardening Aluminium Copper Alloys*, Philosophical Magazine **28**, pp. 855-871, 1938.
70. A. Guinier, *Le mécanisme de la précipitation dans un cristal de solution solide métallique. - Cas des systèmes aluminium-cuivre et aluminium-argent*, Journal de Physique et le Radium **3**(7), pp. 122-136, 1942.

71. J.M. Silcock, T.J. Heal and H.K. Hardy, *Structural Ageing Characteristics of Binary Aluminum-Copper Alloys*, Journal of the Institute of Metals **82**(Part 6), pp. 239-248, 1954.
72. J.M. Silcock and T.J. Heal, *The  $\theta$  Structure in Aluminium Copper Alloys*, Acta Crystallographica **9**, p. 680, 1956.
73. H.I. Aaronson and C. Laird, *Structures and Migration Kinetics of  $\alpha/\theta$  Boundaries in Al-4%Cu: Part 2 - Kinetics of Growth*, Transactions of Metallurgical Society of American Institute of Mining, Metallurgical and Petroleum Engineers **242**(7), pp. 1437-1448, 1968.
74. C. Laird and H.I. Aaronson, *Direct Observations of Thinning of  $\theta$  Plates in Al-4%Cu by Lateral Movement of Ledges*, Journal of the Institute of Metals (London) **96**(Part 7), pp. 222-223, 1968.
75. C. Laird and H.I. Aaronson, *Structures and Migration Kinetics of  $\alpha/\theta$  Boundaries in Al-4%Cu: Part 1 - Interfacial Structures*, Transactions of Metallurgical Society of American Institute of Mining, Metallurgical and Petroleum Engineers **242**(7), pp. 1393-1403, 1968.
76. G.C. Weatherly and C.M. Sargent, *Electron Diffraction Contrast from Ledges at the Interfaces of Faceted  $\theta$  Precipitates*, Philosophical Magazine **22**(179), pp. 1049-1061, 1970.
77. W.M. Stobbs and G.R. Purdy, *The Elastic Accommodation of Semicohherent  $\theta$  in Al-4 wt.%Cu Alloy*, Acta Metallurgica **26**(7), pp. 1069-1081, 1978.
78. Y. Bouazra and R. Reynaud, *Determination of the Heights of Ledges on  $\theta$  Plates in Al-4wt% Cu by Convergent Beam Electron Diffraction and Lattice Plane Imaging*, Acta Metallurgica **32**(4), pp. 529-534, 1984.
79. G. Thomas and M.J. Whelan, *Helical Dislocations in Quenched Al-4%Cu Alloys*, Philosophical Magazine **4**(40), pp. 511-527, 1959.
80. R.B. Nicholson, *The Interaction of Solute Atoms and Dislocations in Aluminium Alloys*, pp. 375-378 in "European Regional Conference on Electron Microscopy" (Delft, 1960)
81. R.B. Nicholson, G. Thomas and J. Nutting, *Electron-Microscopic Studies of Precipitation in Aluminium Alloys*, Journal of the Institute of Metals **87**, pp. 429-438, 1959.

82. J.M. Silcock, *A Study of Elongation and Ageing in Al-4%Cu and Al-4%Cu-0.05% In Crystals*, *Acta Metallurgica* **8**(9), pp. 589-597, 1960.
83. W.F. Hosford and S.P. Agrawal, *Effect of Stress during Aging on the Precipitation of  $\theta'$  in Al-4 wt % Cu*, *Metallurgical Transactions A* **6**(3), pp. 487-491, 1975.
84. J.M. Silcock, T.J. Heal and H.K. Hardy, *Structural Ageing Characteristics of Ternary Aluminium-Copper Alloys with Cadmium, Indium, or Tin*, *Journal of the Institute of Metals* **84**(Part 1), pp. 23-31, 1955.
85. J.M. Silcock, *Intermediate Precipitates in Aged Binary Alloys of Aluminium with Cadmium, Indium, or Tin*, *Journal of the Institute of Metals* **84**(Part 1), pp. 19-22, 1955.
86. X. Gao, J.F. Nie and B.C. Muddle, *Heterogeneous Nucleation of Precipitate Phase  $\theta'$  in Microalloyed Al-Cu based Alloys*, pp. 225-228 in "Proceedings of an International Conference on Solid-Solid Phase Transformations (JIMIC-3)" (Sendai, 1999), Eds. M. Koiwa et al.: Japan Institute of Metals.
87. L. Bourgeois, J.F. Nie and B.C. Muddle, *Assisted Nucleation of  $\theta'$  Phase in Al-Cu-Sn: The Modified Crystallography of Tin Precipitates*, *Philosophical Magazine* **85**(29), pp. 3487-3509, 2005.
88. J.F. Nie, H.I. Aaronson and B.C. Muddle, *The Role of Microalloying Elements in the Formation of Precipitate Plates in Aluminium Alloys*, pp. 157-160 in "Proceedings of an International Conference on Solid-Solid Phase Transformations (JIMIC-3)" (Sendai, 1999), Eds. M. Koiwa et al.: Japan Institute of Metals.
89. J.F. Nie, B.C. Muddle, H.I. Aaronson, S.P. Ringer and J.P. Hirth, *On the Roles of Clusters during Intragranular Nucleation in the Absence of Static Defects*, *Metallurgical and Materials Transactions A* **33**(6), pp. 1649-1658, 2002.
90. U. Dahmen and K.H. Westmacott, *Ledge Structure and the Mechanism of  $\theta'$  Precipitate Growth in Al-Cu*, *Physica Status Solidi A* **80**(1), pp. 249-262, 1983.
91. G.W. Lorimer, *The Sympathetic Nucleation of  $\theta'$  and  $\gamma'$* , pp. 491-494 in "Proceedings of Fourth European Regional Conference on Electron Microscopy" (Rome, 1968): Tipografia Poliglotta Vaticana.

92. V. Perovic and G.R. Purdy, *Autocatalytic Nucleation and Elastic Stabilization of Linear Arrays of Plate-Shaped Precipitates*, Acta Metallurgica **29**(5), pp. 889-902, 1981.
93. J.K. Lee and W.C. Johnson, *Influence of Transformation Strain Energy upon Diffusional Nucleation and Growth*, pp. 127-150 in "Proceedings of an International Conference on Solid-Solid Phase Transformations" (Pittsburgh, 1982), Eds. H.I. Aaronson et al.: Metallurgical Society of AIME.
94. G.J. Shiflet, K.C. Russell and H.I. Aaronson, *Homogeneous Nucleation Kinetics of Parallelepipeds*, Surface Science **62**(1), pp. 303-307, 1977.
95. J.D. Boyd and R.B. Nicholson, *A Calorimetric Determination of Precipitate Interfacial Energies in two Al-Cu Alloys*, Acta Metallurgica **19**(10), pp. 1101-1109, 1971.
96. V. Vaithyanathan, C. Wolverton and L.Q. Chen, *Multiscale Modeling of Precipitate Microstructure Evolution*, Physical Review Letters **88**(12), pp. 125503(1-4), 2002.
97. V. Vaithyanathan, C. Wolverton and L.Q. Chen, *Modeling Precipitate Microstructure Evolution in Alloys With First-Principles Energetic Information*, Material Science Forum **449-452**, pp. 19-24, 2004.
98. S.Y. Hu, M.I. Baskes, M. Stan and L.Q. Chen, *Atomistic Calculations of Interfacial Energies, Nucleus Shape and Size of  $\theta'$  Precipitates in Al-Cu Alloys*, Acta Materialia **54**(18), pp. 4699-4707, 2006.
99. C. Wolverton and V. Ozolins, *Entropically Favored Ordering: The Metallurgy of  $Al_2Cu$  Revisited*, Physical Review Letters **86**(24), pp. 5518-5521, 2001.
100. R.V. Ramanujan, J.K. Lee and H.I. Aaronson, *A Discrete Lattice Plane Analysis of the Interfacial Energy of Coherent fcc:hcp Interfaces and its Application to the Nucleation of  $\gamma$  in Al-Ag Alloys*, Acta Metallurgica et Materialia **40**(12), pp. 3421-3432, 1992.
101. H.I. Aaronson and C. Laird, Ford Motor Co. Scientific Laboratory Report, 1967.
102. *COST 507, Thermochemical Database for Light Metal Alloys*, Eds. I. Ansara, A.T. Dinsdale and M.H. Rand, 1998: Office for Official Publications of the European Communities.

103. A.T. Dinsdale, *SGTE Data for Pure Elements*, CALPHAD **15**, pp. 317-425, 1991.
104. V.T. Witusiewicz, U. Hecht, S.G. Fries and S. Rex, *The Ag–Al–Cu System. Part I: Reassessment of the Constituent Binaries on the Basis of New Experimental Data*, Journal of Alloys and Compounds **385**, pp. 133-143, 2004.
105. R. Baur and V. Gerold, *The Existence of a Metastable Miscibility Gap in Aluminium-Silver Alloys*, Acta Metallurgica **10**(6), pp. 637-645, 1962.
106. A.J. McAlister, *Ag-Al (Silver-Aluminium)*, pp. 8-9 in "Binary Alloy Phase Diagram", Eds. T. Massalski et al., 1990
107. L.M. Brown, R.H. Cook, R.K. Ham and G.R. Purdy, *Elastic Stabilization of Arrays of Precipitates*, Scripta Metallurgica **7**(8), pp. 815-820, 1973.
108. V. Perovic, G.R. Purdy and L.M. Brown, *On the Stability of Arrays of Precipitates*, Acta Metallurgica **27**(6), pp. 1075-1084, 1979.
109. P. Eurin, J.M. Penisson and A. Bourret, *Study of the Periodic Array of Ordered Nuclei in Equiatomic Co-Pt Alloy by Electron Microscopy and Optical Diffraction*, Acta Metallurgica **21**(5), pp. 559-570, 1973.
110. V. Perovic, G.R. Purdy and L.M. Brown, *The Role of Shear Transformation Strains in the Formation of Linear Arrays of Precipitates*, Scripta Metallurgica **15**(2), pp. 217-221, 1981.
111. F. Kroupa, *The Interaction between Prismatic Dislocation Loops and Straight Dislocations. I*, Philosophical Magazine **7**, pp. 783-801, 1962.
112. S.M. Allen and J.W. Cahn, *A Microscopic Theory for Antiphase Boundary Motion and its Application to Antiphase Domain Coarsening*, Acta Metallurgica **27**(6), pp. 1085-1095, 1979.
113. J.W. Cahn, *On Spinodal Decomposition*, Acta Metallurgica **9**(9), pp. 795-801, 1961.
114. P.C. Hohenberg and B.I. Halperin, *Theory of Dynamic Critical Phenomena*, Reviews of Modern Physics **49**(3), pp. 435-479, 1977.
115. E.W. Hart, *Thermodynamics of Inhomogeneous Systems*, Physical Review **113**(2), pp. 412-416, 1959.

116. J.S. Langer, *Statistical Theory of the Decay of Metastable States*, Annals of Physics **54**(2), pp. 258-275, 1969.
117. J.S. Langer, *Theory of Spinodal Decomposition in Alloys*, Annals of Physics **65**(1-2), pp. 53-86, 1971.
118. C. Shen, PhD thesis: *The Fundamentals and Applications of Phase Field Method in Quantitative Microstructural Modeling*, Department of Materials Science and Engineering, The Ohio State University, Columbus, 2004.
119. L.Q. Chen, *Phase-Field Models for Microstructure Evolution*, Annual Review of Materials Science **32**, pp. 113-140, 2002.
120. Y. Wang, D. Banerjee, C.C. Su and A.G. Khachaturyan, *Field Kinetic Model and Computer Simulation of Precipitation of  $L1_2$  Ordered Intermetallics from fcc Solid Solution*, Acta Materialia **46**(9), pp. 2983-3001, 1998.
121. D.Y. Li and L.Q. Chen, *Shape Evolution and Splitting of Coherent Particles under Applied Stresses*, Acta Materialia **47**(1), pp. 247-257, 1998.
122. L.Q. Chen and J. Shen, *Applications of Semi-Implicit Fourier-spectral Method to Phase Field Equations*, Computer Physics Communications **108**(2-3), pp. 147-158, 1998.
123. J.D. Gunton, M. San Miguel and P.S. Sahni, *The Dynamics of First-order Phase Transitions*, p. 289 in "Phase transitions and critical phenomena", Eds. C. Domb and J.L. Lebowitz, 1983
124. L.D. Landau and E.M. Lifshitz, "Statistical Physics", 3rd ed., 1976: Science.
125. C. Shen, J.P. Simmons and Y. Wang, *Effect of Elastic Interaction on Nucleation: II. Implementation of Strain Energy of Nucleus Formation in the Phase Field Method*, Acta Materialia **55**(4), pp. 1457-1466, 2007.
126. T.M. Rogers, K.R. Elder and R.C. Desai, *Numerical Study of the Late Stages of Spinodal Decomposition*, Physical Review B **37**(16), pp. 9638-9649, 1988.
127. J.P. Simmons, C. Shen and Y. Wang, *Phase Field Modeling of Simultaneous Nucleation and Growth by Explicitly Incorporating Nucleation Events*, Scripta Materialia **43**(10), pp. 935-942, 2000.

128. S.G. Kim, W.T. Kim and T. Suzuki, *Phase-Field Model for Binary Alloys*, Physical Review E **60**(6), pp. 7186-7197, 1999.
129. S.Y. Hu, PhD thesis: *Phase-field Models of Microstructure Evolution in a System with Elastic Inhomogeneity and Defects*, Department of Materials Science and Engineering, Pennsylvania State University, 2004.
130. S.Y. Hu, J. Murray, H. Weiland, Z.K. Liu and L.Q. Chen, *Thermodynamic Description and Growth Kinetics of Stoichiometric Precipitates in the Phase-Field Approach*, CALPHAD: Computer Coupling of Phase Diagrams and Thermochemistry **31**(2), pp. 303-312, 2007.
131. J.L. Murray, *The Aluminium-Copper System*, International Metals Reviews **30**(1), pp. 211-234, 1985.
132. Y. Du, Y.A. Chang, B. Huang, W. Gong, Z. Jin, H. Xu, Z. Yuan, Y. Liu, Y. He and F.Y. Xie, *Diffusion Coefficients of Some Solutes in fcc and Liquid Al: Critical Evaluation and Correlation*, Materials Science and Engineering A **363**(1-2), pp. 140-151, 2003.
133. C. Zener, *Theory of Growth of Spherical Precipitates from Solid Solution*, **20**(10), pp. 950-953, 1949.
134. V. Vaithyanathan, C. Wolverton and L.Q. Chen, *Multiscale Modeling of  $\theta'$  Precipitation in Al-Cu Binary Alloys*, Acta Materialia **52**(10), pp. 2973-2987, 2004.
135. T.A. Abinandanan and F. Haider, *An Extended Cahn-Hilliard Model for Interfaces with Cubic Anisotropy*, Philosophical Magazine A **81**(10), pp. 2457 - 2479, 2001.
136. G. Caginalp and P. Fife, *Higher-order Phase Field Models and Detailed Anisotropy*, Physical Review B **34**, pp. 4940-4943, 1986.
137. G.B. McFadden, A.A. Wheeler, R.J. Braun, S.R. Coriell and R.F. Sekerka, *Phase-Field Models for Anisotropic Interfaces*, Physical Review E **48**(3), pp. 2016-2024, 1993.
138. N. Ma, Q. Chen and Y. Wang, *Implementation of High Interfacial Energy Anisotropy in Phase Field Simulations*, Scripta Materialia **54**(11), pp. 1919-1924, 2006.
139. D.W. Hoffman and J.W. Cahn, *A Vector Thermodynamics for Anisotropic Surfaces: I. Fundamentals and Application to Plane Surface Junctions*, Surface Science **31**, pp. 368-388, 1972.

140. J.W. Cahn and D.W. Hoffman, *A Vector Thermodynamics for Anisotropic Surfaces. II. Curved and Faceted Surfaces*, Acta Metallurgica **22**(10), pp. 1205-1214, 1974.
141. W.W. Mullins, *Proof that the Two-Dimensional Shape of Minimum Surface Free Energy is Convex*, Journal of Mathematical Physics **3**(4), pp. 754-759, 1962.
142. J.J. Eggleston, G.B. McFadden and P.W. Voorhees, *A Phase-Field Model for Highly Anisotropic Interfacial Energy*, Physica D **150**(1-2), pp. 91-103, 2001.
143. J.M. Debierre, A. Karma, F. Celestini and R. Guerin, *Phase-Field Approach for Faceted Solidification*, Physical Review E **68**(4), pp. 041604(1-13), 2003.
144. A.A. Wheeler and G.B. McFadden, *On the Notion of a  $\xi$ -vector and a Stress Tensor for a General Class of Anisotropic Diffuse Interface Models*, Proceedings of the Royal Society of London, Series A (Mathematical, Physical and Engineering Sciences) **453**(1963), pp. 1611-1630, 1997.
145. A.A. Wheeler, *A  $\xi$ -vector Formulation of Anisotropic Phase-Field Models: 3D Asymptotics*, European Journal of Applied Mathematics **7**(04), pp. 367-381, 1996.
146. A.A. Wheeler, *Phase-Field Theory of Edges in an Anisotropic Crystal*, Proceedings of the Royal Society A **462**(2075), pp. 3363-3384, 2006.
147. W.H. Press, S.A. Teukolsky, W.T. Wetterling and B.P. Flannery, "Numerical Recipes: The Art of Scientific Computing", 3rd ed., 2009: Cambridge University Press.